FINAL TECHNICAL REPORT

C1 Chemistry for the Production of Ultra-Clean Liquid Transportation Fuels and Hydrogen

Final Technical Report for DOE Contract No. DE-FC26-02NT41594
Prepared by the Consortium for Fossil Fuel Science
Submitted April 10, 2006

Gerald P. Huffman, Director
CFFS / University of Kentucky
533 S. Limestone Street, Suite 107
Lexington, KY 40506
Phone: (859) 257-4027
FAX: (859) 257-7215
E-mail: huffman@engr.uky.edu

Consortium for Fossil Fuel Science
University of Kentucky
West Virginia University
University of Pittsburgh
University of Utah
Auburn University

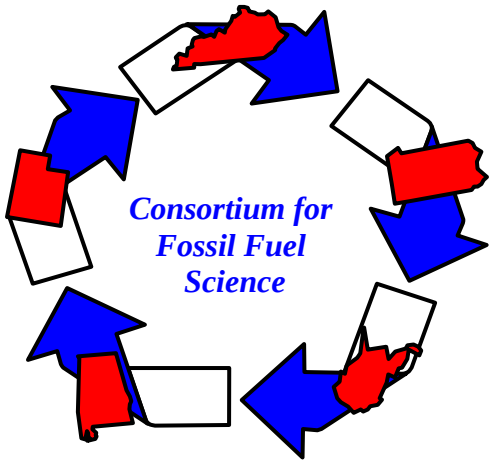

Table of Contents

C1 Chemistry for Production of Ultra-Clean Liquid Transportation Fuels and Hydrogen

U.S. Department of Energy (Fossil Energy) Contract No. DE-FC26-02NT41594

Contact: Gerald P. Huffman, Director, Consortium for Fossil Fuel Science, University of Kentucky, Suite 107 Whalen Building, 533 S. Limestone St., Lexington, KY 40506-0043
(859) 257-4027; FAX: (859)257-7215; **huffman@engr.uky.edu**

Abstract

Professors and graduate students from five universities – the University of Kentucky, University of Pittsburgh, University of Utah, West Virginia University, and Auburn University - are collaborating in a research program to develop C1 chemistry processes to produce ultra-clean liquid transportation fuels and hydrogen, the zero-emissions transportation fuel of the future. The feedstocks contain one carbon atom per molecular unit. They include synthesis gas (syngas), a mixture of carbon monoxide and hydrogen produced by coal gasification or reforming of natural gas, methane, methanol, carbon dioxide, and carbon monoxide. An important objective is to develop C1 technology for the production of liquid transportation fuel and hydrogen from domestically plentiful resources such as coal, coalbed methane, and hydrocarbon gases and liquids produced from coal. An Advisory Board with representatives from Chevron-Texaco, Eastman Chemical, Conoco-Phillips, the Air Force Research Laboratory, the U.S. Army National Automotive Center, and Tier Associates provides guidance on the practicality of the research. The current report summarizes the results obtained in this program during the period October 1, 2002 through March 31, 2006. The results are presented in detailed reports on 16 research projects headed by professors at each of the five CFFS Universities and an Executive Summary. Some of the highlights from these results are given below.

- Small (~1%) additions of acetylene or other alkynes to the Fischer-Tropsch (F-T) reaction increases its yield, causes chain initiation, and promotes oxygenate formation.
- The addition of Mo to Fe-Cu-K/AC F-T catalysts improves catalyst lifetime and activity.
- The use of gas phase deposition to place highly dispersed metal catalysts on silica or ceria aerogels offers promise for both the F-T and the water-gas shift WGS reactions.
- Improved activity and selectivity are exhibited by Co F-T catalysts in supercritical hexane.
- Binary Fe-M (M=Ni, Mo, Pd) catalysts exhibit excellent activity for dehydrogenation of gaseous alkanes, yielding pure hydrogen and carbon nanotubes in one reaction. A fluidized-bed/fixed-bed methane reactor was developed for continuous hydrogen and nanotube production.
- A process for co-production of hydrogen and methyl formate from methanol has been developed.
- Pt nanoparticles on stacked-cone carbon nanotubes easily strip hydrogen from liquids such as cyclohexane, methylcyclohexane, tetralin and decalin, leaving rechargeable aromatic phases.
- Hydrogen volume percentages produced during reforming of methanol in supercritical water in the output stream are ~98%, while CO and CO_2 percentages are <2 %.

Executive Summary

Prepared by Gerald P. Huffman, Director, Consortium for Fossil Fuel Science

(859) 257-4027; huffman@engr.uky.edu

Introduction

The Consortium for Fossil Fuel Science (CFFS), a five university research consortium, is conducting a program of basic research aimed at developing innovative and economical technology for producing clean liquid transportation fuels and hydrogen from coal, coalbed methane, natural gas, and other hydrocarbons using C1 chemistry. The research program is made up of 16 separate but coordinated research projects being conducted at the five CFFS universities, all contributing towards achieving the goal of producing clean, economical transportation fuel from domestic resources. The current report summarizes progress made toward that goal during the current DOE research contract. This Executive Summary provides a very brief summary of the principal results obtained over the duration of the contract. The appended individual project reports provide more details and contain all the required elements of DOE research contract reports: an introduction, experimental procedure, results and discussion, conclusions, and references. Lists of all publications and presentations resulting from this research contract during this period are also given in these project reports.

Experimental

A discussion of experimental procedures is provided in each of the individual project reports that constitute the bulk of this report.

Results

Liquid fuels from Fischer-Tropsch (F-T) synthesis

Co-feeding acetylene and other alkynes greatly increases the amount of F-T products at various temperatures for both Co and Fe catalysts. Incorporation becomes stable at temperatures above 180˚C. About 60% of acetylene is incorporated into higher products with both catalysts. Incorporation of terminal alkynes produces straight chain hydrocarbons while incorporation of internal alkynes produces both branched- and straight-chain hydrocarbons. Oxygenates are formed with incorporation of alkynes in the F-T on cobalt and iron catalysts. Oxygenates formed on cobalt catalysts are limited to the aldehyde and alcohol with one carbon more than the probe.

The addition of Mo to Fe-Cu-K/AC F-T catalysts improves Fe dispersion after catalysts are reduced at 400°C for 12 h. Iron carbide (Fe_2C_5) and magnetite (Fe_3O_4) are detected on spent catalysts by XRD. These are postulated to be active phases for the FTS and WGS reactions. Mo addition prevents agglomeration of the iron particles during reduction and reaction, leading to improved catalyst stability.

Mössbauer spectroscopy indicates that the Fe in these catalysts is present as superparamagnetic ferrihydrite prior to reaction, while Mo x-ray absorption near-edge spectroscopy (XANES) suggests that the Mo oxidation state is principally as Mo(VI) in

molybdate. After reaction, the Fe and Mo are primarily present as carbides. The Mössbauer spectra resemble those of ε and χ carbide. The question of whether the Mo and Fe are present in the same carbide or oxide phase or form distinct carbide and oxide phases is less clear. The preliminary TEM study was inconclusive; Mo-free Fe-rich particles, Fe-free Mo particles, and some Fe-Mo mixed particles were observed.

Six different SBA-15 supported cobalt and iron catalysts were prepared to study the impact of different impregnation methods, active metals, and aluminum incorporation in SBA-15 on catalytic activity in Fischer-Tropsch (FT) synthesis. The cobalt impregnation method had a significant effect on catalytic activity and selectivity because of differences in reducibility of cobalt oxides. Aluminum added to an iron-based catalyst is also advantageous.

Iron-containing silica-based aerogel (SBA) F-T catalysts were examined by iron XAFS and Mössbauer spectroscopies. The iron in the as-prepared catalyst samples was found to be present as a mixture of hematite and ferrihydrite. The ratio of these two phases varies systematically with potassium content and the nature of the SBA support. Various methods of estimating the ratio of Fe as hematite to Fe as ferrihydrite in the as-prepared catalysts have been tested and good agreement was found among the different methods. The Fe/SBA-15 catalysts consist of a mixture of iron carbides and oxides after reaction.

The high surface areas and highly porous nature of silica aerogels offer promise for both the F-T reaction and for the WGS. The use of gas phase deposition generates catalyst centers in highly dispersed form on the aerogel supports. It also appears that a silica aerogel structure can be of value in providing a robust framework onto which more fragile support species, such as ceria, can be anchored. New ^{13}C NMR techniques are being developed to investigate metal-ligand complexes in these catalysts.

Production of light olefins (C_2-C_4) from methanol or syngas over silicoaluminophosphate (SAPO) catalysts provides an indirect way of converting fossil resources to industrially valuable olefins and other value-added products such as polymers and fine chemicals. Catalytic activity and selectivity for light olefins can be influenced by many catalyst parameters such as silicon content, acid site density, acid strength, crystallite size, and nature of template. Excellent results were observed for the methanol to olefins (MTO) reaction using the SAPO-34 catalyst.

In supercritical hexane (SCH) F-T conditions, the in situ reduction of Co_3O_4 produced both hcp and fcc Co^0 that were stable for long times-on-stream (TOS). As a result, the activity and selectivity of the catalyst in the SCH medium is more stable and recoverable than that under gas-phase F-T conditions.

XRD and magnetic characterization of the used Co/Al_2O_3 catalysts indicate that cobalt oxide is reduced in situ during the both gas-phase and supercritical hexane (SC) F-T reactions. In SCH-F-T conditions, the in situ reduction of Co_3O_4 produced both hcp and fcc Co^0 that were stable for long times-on-stream (TOS). As a result, the activity and selectivity of the catalyst in the SCH medium is more stable and recoverable than that under gas-phase F-T conditions.

Hydrogen

There are several advantages of carrying out reforming reactions of hydrocarbons in supercritical water over the conventional processes. The density of supercritical water is higher than that of steam, which results in a high space-time yield. The higher values of thermal

conductivity and specific heat of supercritical water are beneficial for the endothermic reforming reaction. H_2 is available at a high pressure and can be stored directly, avoiding the problems associated with compression. Hydrogen volume percentages produced during reforming of methanol in supercritical water in the output stream are ~98%, while CO and CO_2 percentages are <2 %. CH_4 formation can be suppressed by (1) operating at a low residence time, (2) using a Ni-Cu reactor or (3) adding K_2CO_3 or KOH in the feed.

Thermodynamically, co-production of hydrogen and methyl formate from methanol is favored at temperatures below 220˚C. At temperatures higher than 250˚C, complete methanol decomposition is favored to form syngas with a ratio of H_2/CO=2. The presence of steam favors hydrogen but decreases methyl formate production. A Cu/MgO catalyst produced more hydrogen but less methyl formate. The Cu/TiO_2 catalyst has a higher selectivity to methyl formate but lower activity. The Cu/Al_2O_3 produced less hydrogen and methyl formate but high dimethyl ether. Cu/ZrO_2 show good activity for coproduction of hydrogen and methyl formate and will be pursued in future. This catalyst shows high promise and is being more thoroughly investigated.

Experiments on the aqueous-phase reforming of ethylene glycol and of glycerol in a continuous system have shown that significant amounts of hydrogen are produced with low CO content. This method for producing hydrogen appears promising for use with PEM fuel cells.

Binary Fe-based catalysts on alumina have been found to exhibit excellent activity for dehydrogenation of methane, ethane, and propane to produce pure hydrogen and carbon nanotubes (CNT). In an attempt to make the reaction continuous, a fluidized-bed reactor was developed. However, an alternating fluid and stationary bed (mixed-mode) reactor was found to be much more efficient. Work has now begun on Fe-Ni and Ni catalysts supported on a Mg(Al)O support. This support is much more easily dissolved to produce clean multi-walled nanotubes (MWNT) and will be tried in the fluid-bed and mixed-mode reaction schemes. Another approach to be investigated is the use of Fe and Ni nanoparticles as catalysts in an continuous down-flow reactor with spooling collection of the CNT.

The sol-gel synthesis followed by supercritical CO_2 drying leads to ceria aerogel-based catalysts with much higher surface area than impregnated or precipitated catalysts. The catalysts are active towards the production of hydrogen through the WGSR. Gas-phase loading of palladium resulted in more active catalysts than the incorporation of either copper or zero-valent gold nanoparticles.

Partial oxidation and autothermal reforming processes have more promise for hydrogen production than steam reforming system because they do not require external heating. Partial oxidation of propane was investigated using Pt/CeO_2 catalysts, with CeO_2 prepared by different techniques. It was found that Pt catalyzes the reduction of surface CeO_2 but has little effect on reduction of bulk CeO_2. Pt on CeO_2 prepared by a decomposition method exhibited the highest BET surface area, reducibility, and catalytic activity for partial oxidation of propane at 700ºC. The optimum O_2/C_3H_8 ratio is 2.0 for moderately high conversion and high selectivity.

Several CFFS investigators have studied the dehydrogenation-hydrogenation of cyclic hydrocarbons such as cyclohexane, methylcyclohexane, tetralin, decalin, etc., as a possible technology to store, transport, and locally produce hydrogen. Some advantages of this approach are that no CO or CO_2 are produced, reaction reversibility, relatively high hydrogen content (6-8 wt.%), and convenient liquid phase transportability. Pt catalysts supported on mesoporous SBA

appears to offer good potential for this reaction. Excellent results have also been obtained using Pt nanoparticles supported on stacked-cone nanotubes.

Conclusions

Liquid fuels from Fischer-Tropsch (F-T) synthesis

1. Small (~1%) additions of acetylene or other alkynes to the F-T reaction increases its yield, causes chain initiation, and promotes oxygenate formation. Terminal alkynes promote straight chain initiation while internal alkynes also initiate branched hydrocarbons.

2. The addition of Mo to Fe-Cu-K/AC F-T catalysts prevents agglomeration of catalyst particles during reduction and reaction, leading to improved catalyst stability. Mössbauer and XAFS spectroscopy indicate that the Fe and Mo are primarily present as carbides.

3. A method to synthesize light olefins (C_2-C_4) from methanol or syngas over SAPO catalysts has been developed.

4. The use of gas phase deposition to place highly dispersed metal catalysts on high surface areas and high porosity aerogels offers promise for both the F-T and the WGS reactions. ^{13}C NMR techniques are being developed to investigate metal-ligand complexes in these catalysts.

5. The activity of F-T catalysts consisting of Co and Fe supported on SBA-15 supports prepared by different impregnation methods is being investigated.

6. The activity and selectivity of Co F-T catalysts in supercritical hexane is better than that under gas-phase conditions.

7. XRD, magnetic studies, Mössbauer spectroscopy, XAFS spectroscopy, and TEM have been used to obtain detailed structural information for F-T, WGS, and dehydrogenation catalysts.

Hydrogen

1. Hydrogen volume percentages produced during reforming of methanol in supercritical water in the output stream are ~98%, while CO and CO_2 percentages are <2 %.

2. Binary Fe-M (M=Ni, Mo, Pd) catalysts exhibit excellent activity for dehydrogenation of gaseous alkanes, yielding pure hydrogen and carbon nanotubes in one reaction. A fluidized-bed/fixed-bed methane reactor was developed for continuous hydrogen and nanotube production.

3. Several copper catalysts have been shown to be active for the co-production of hydrogen and methyl formate from methanol.

4. Partial oxidation of propane was investigated using Pt/CeO_2 catalysts.

5. Aqueous-phase reforming of ethylene glycol and of glycerol in a continuous system have produced significant amounts of hydrogen with low CO content.

6. Pt nanoparticles on stacked-cone carbon nanotubes easily strip hydrogen from liquids such as cyclohexane, methylcyclohexane, tetralin and decalin, leaving rechargeable aromatic phases.

CHAIN INITIATION OF FISCHER-TROPSCH WITH ACETYLENE INCORPORATION

Yulong Zhang, Li Hou, John W. Tierney and Irving Wender
Department of Chemical Engineering, University of Pittsburgh

Introduction

The Fischer-Tropsch (F-T) synthesis converts syngas (CO and H_2), which can be produced from coal, natural gas, biomass and any carbonaceous material, into long chain hydrocarbons which can be transformed to fuels and chemicals. The mechanism of the F-T reaction is still under debate although it has been investigated for many years. It is difficult to distinguish among the many complex intermediates formed during F-T reactions. Schulz[1] has pointed out that the F-T regime is established during the synthesis by restructuring the catalyst surface and suppressing undesired reactions. The use of probe molecules has been shown to be an effective way to study the F-T mechanism[2].

The F-T synthesis is a stepwise growth of hydrocarbon chains by addition of monomeric units. Unlike usual polymerization processes, the reaction proceeds by addition of monomers formed in-situ. In previous studies, we found that long chain alkynes are incorporated more easily than corresponding alkenes[3]. It has been reported that ethylene is 10 to 40 times more easily incorporated into the F-T synthesis than are higher olefins. We have reported incorporation of long chain alkynes, phenylacetylenes and preliminary results of incorporation of acetylene on F-T cobalt and iron catalysts. In this work, the effects of operating variables such as temperature and pressure on co-feeding of acetylene were investigated. A rhodium catalyst is also studied due to its characteristics in hydroformylation. Possible pathways of F-T synthesis are discussed and a chain initiation mechanism with a two-carbon entity is proposed.

Experimental

Supported cobalt catalysts were prepared by incipient-wetness impregnation of cobalt nitrate on alumina. A rhodium catalyst was prepared by incipient wetness impregnation of rhodium (III) chloride hydrate on alumina. A precipitated iron catalyst with a composition of 100Fe/4.4Si/1.25K was obtained from Dr. B. Davis of the University of Kentucky.

The F-T reaction was carried out in a computer controlled fixed bed reactor (stainless-steel with i.d. 3/8 inches). Acetylene was introduced from a tank of premixed gas containing (mol): 1% acetylene, 10% Ar, 44% CO, and 45% H_2 obtained from Praxair. H_2 was added when the H_2/CO ratio needed to be adjusted. Co catalysts were activated by H_2 at a rate of 50 ml/min, with a temperature program ramping from room temperature to 350^{o}C at 1^{o}C /min, holding at 350^{o}C for 10 hours. Fe catalysts were activated similarly but kept at 350^{o}C for 5 hours and 450^{o}C for 2 hours. The F-T reaction was started by gradually increasing the CO and H_2 flow rate to avoid a temperature surge due to active sites present in the fresh catalysts. Products were analyzed by two online GCs (HP6890 and HP5890).

Results and Discussion

The addition of acetylene on cobalt catalysts increases the yield of C_2^+ products up to about C_{10}. It can be seen from Figure 1 that C_3 has a three fold increase upon addition of 1% acetylene. Compared to 1-hexyne, acetylene is 3 to 4 times easier to incorporate into the F-T products. As shown in Table 1, a significant amount of acetylene is dimerized to C_4 on Co and Rh catalysts but very little on the Fe catalyst. Dimerization is not a part of the F-T reaction since it is not sensitive to sulfur poisoning. It is most likely due to the acidic Al_2O_3 support used in cobalt and rhodium catalysts. C_4 products are mainly internal olefins; however, they are also capable of chain initiation. As with co-feeding of internal acetylenes reported earlier[3], isomers such as 2-methylbutane and 3-methylpentane are produced when acetylene is co-fed.

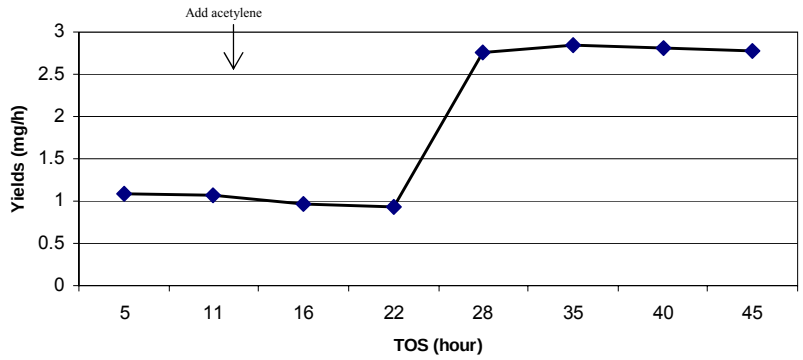

Figure 1. Yield of C_3 hydrocarbons with TOS on a cobalt catalyst ($10Co/90Al_2O_3$) at 100 psi., 180°C, H_2/CO=1, 1% acetylene.

The effects of temperature and pressure on F-T without/with acetylene were investigated. Compared to the base reaction (without acetylene), co-feeding acetylene greatly increases the amount of F-T products at various temperatures for both Co and Fe catalysts. Incorporation is lower at very low temperatures, e.g. at 120˚C, but becomes stable at temperatures above 180˚C, as shown in Table 1. About 60% of acetylene is incorporated into higher products with both catalysts. The rhodium catalyst shows a low incorporation rate, probably due to its low F-T activity. Increase in pressure from 100 to 700 psi has little effect on the incorporation ratio on Co and Fe catalysts, but it enhances oxygenate formation.

Table 1. Comparison of incorporation of acetylene on several F-T catalysts

	Temperature (˚C)	Hydrogenation (%)	Dimerization (%)	Incorporation (%)
$10Co/90Al_2O_3$	120	40	28	32
	180	8	36	56
	220	14	27	59
100Fe/4.4Si/1.25K	180	30	7	63
	220	33	7	60
	260	34	5	61
$5Rh/95Al_2O_3$	220	20	65	15

A striking effect of co-feeding acetylene is initiation of the F-T chain growth at lower temperatures. At 120°C, appreciable amounts of F-T products can still be obtained on cofeeding of 1% of acetylene; the FT reaction does not take place at such a low temperature. Incorporation of acetylene on a Co catalyst only produces C_3 and a small amount of C_5 oxygenates, apparently by hydroformylation of adsorbed unsaturated C_2 and C_4 species. Iron catalysts, however, produce a spectrum of oxygenates which follows the Anderson-Schultz-Flory (ASF) distribution as shown in Figure 2.

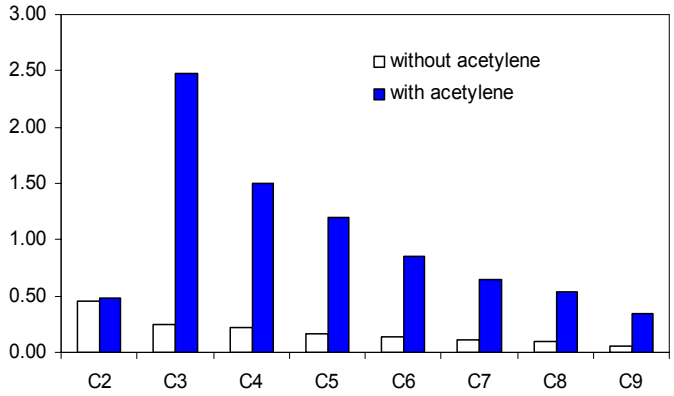

Figure 2. Oxygenated product distribution without/with acetylene incorporation on an iron catalyst (100Fe/4.4Si/1.25K) at 300psi, 180°C, H_2/CO=1, 1% acetylene.

CO hydrogenation with acetylene over a Rh catalyst was carried out at 220°C and 100psi. In contrast to Fe and Co catalysts, only 15% of acetylene is incorporated into higher molecular weight hydrocarbons. Dimerization of acetylene to C_4 hydrocarbons (65%) is very active with a Rh catalyst, which is similar to that with a cobalt catalyst. Acidity of the alumina support of cobalt and rhodium may play an important role for the dimerization reaction of acetylene.

With rhodium, in the absence of acetylene, a large amount of ethanol was produced from the CO hydrogenation reaction. With incorporation of acetylene, the amount of 1-propanol was increased greatly, while the amount of ethanol was not affected. This indicates that 1-propanol was produced by a different pathway than F-T reactions. Similar to reactions of acetylene with Co catalyst, 1-propanol was formed by a hydroformylation type reaction. The yield of ethanol with Rh was much greater than that with Co.

Acetylenes initiate the chain but are not incorporated into the growing chain. The alpha value of the F-T reaction declines with co-fed acetylene due to the increasing number of chain initiators. There are many studies on the nature of the species formed from two-carbon entities added to an F-T reaction[2,4-6]. These include ethylene, vinyl ethylidene, ethylidyne and, undoubtedly, a variety of other similar adsorbates. Zaera[7-8] has provided surface science evidence that two-carbon entities interconvert on the surface of a metal catalyst; our work with acetylene has corroborated his results, as shown in Figure 3.

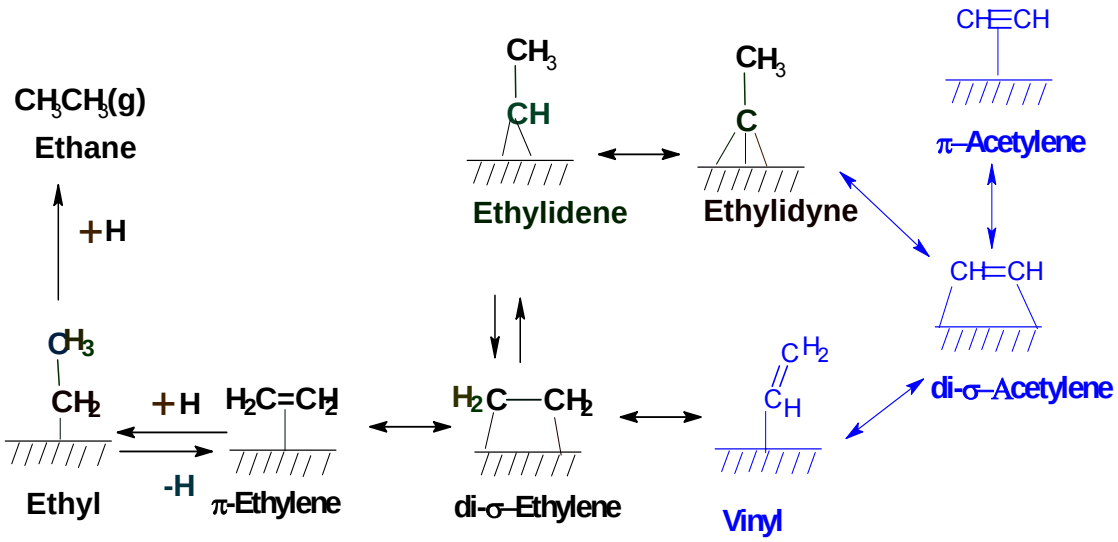

Figure 3. Reaction mechanisms for the conversion of ethylene on Pt (111)

Alkylidyne species are well-known in adsorption studies on metal atoms. It is possible that terminal acetylenic compounds are adsorbed at low temperature on F-T catalysts to form alkylidynes which initiate the reaction. Stable alkylidyne compounds have been reported in organometallic complexes having one and two metal centers; however, the most stable alkylidyne species is that in which nests in the center of three metal atoms. This has been substantiated by the synthesis of an organometallic compound, ethylidyne tricobalt nonacarbonyl ($CH_3CCo_3(CO)_9$). There is undoubtedly a close relation between unsaturated hydrocarbon ligands in organometallic compounds and those on metal surfaces.

Conclusions

Our work with acetylenic compounds can be summarized as follows: Acetylenic compounds can initiate the cobalt-catalyzed F-T synthesis at temperatures too low for normal F-T reactions. Alkynes initiate chain growth more effectively than olefins. When acetylenic probe molecules are added to the F-T synthesis, both the probe-initiated and the conventional F-T synthesis proceed simultaneously and their products overlap. The use of phenylalkyne probes allows the probe-initiated products to be easily distinguished from the conventional F-T products by GC-MS analysis. It is possible that the acetylenic molecule is hydrogenated to the corresponding olefin which then initiates chain growth. The possibility exists that the triple bond in the acetylenic molecule plays a special role in the initiation of the synthesis by inducing a surface restructuring of the cobalt surface before or as it is reduced to an olefin.

Incorporation of terminal alkynes produces straight chain hydrocarbons while incorporation of internal alkynes produces both branched- and straight-chain hydrocarbons. Part of the internal triple bond in the alkyne can isomerize to the terminal position and then start chain growth to produce straight chain products.

Oxygenates are formed with incorporation of alkynes in the F-T on cobalt and iron catalysts. Oxygenates formed on cobalt catalysts are limited to the aldehyde and alcohol with one carbon more than the probe. Incorporation of alkynes on iron catalysts produces a series of oxygenates; cobalt and iron apparently produce oxygenates by different mechanisms. Oxygenates formed on

cobalt catalysts are probably the result of a hydroformylation type of reaction: oxygenates formed on iron catalysts are produced according to the ASF distribution by an F-T reaction.

Acetylene is incorporated into the F-T reaction much more effectively than are higher acetylenes, a finding similar to results reported with addition of olefins. Alpha values decrease upon addition of acetylene, indicating that acetylene, a two-carbon entity, serves as a chain initiator.

References

(1) Schulz, H.; Nie, Z. Q.; Ousmanov, F. *Catal. Today* **2002**, *71*, 351-360.
(2) Turner, M. L.; Marsih, N.; Mann, B. E.; Quyoum, R.; Long, H. C.; Maitlis, P. M. *J. Am. Chem. Soc.* **2002**, *124*, 10456.
(3) Zhang ,Y.; Hou, L.; Tierney, J. W.; Wender, I. *Top. Catal.* **2005**, 33.
(4) Slivinskii, E. V.; Rumyantsev, V. Y.; Voitsekhovskii, Y. P.; Zvezdkina, L. I.; Loktev, S. M. *J. Catal.* **1990**, *123*, 333-40.
(5) Loktev, S. M. *J. Mol. Catal.* **1982**, *17*, 225-30.
(6) Long, H. C.; Turner, M. L.; Fornasiero, P.; Kaspar, J.; Graziani, M.; Maitlis, P. M. *J. Catal.* **1997**, *167*, 172.
(7) Zaera, F.; Bernstein, N. *J. Am. Chem. Soc.* **1994**, *116*, 4881.
(8) Zaera, F. *Chem. Rev.* **1995**, *95*, 2651.

SBA-15 Supported Cobalt and Iron Catalysts for Fischer-Tropsch Synthesis

Dae Jung Kim, Brian C. Dunn, and Edward M. Eyring

Department of Chemistry, University of Utah Salt, Lake City, UT 84112

Introduction

Fischer-Tropsch (FT) synthesis is a promising pathway to very clean alternative fuels derived from coal syngas. It is important to develop active catalysts with high selectivity for production of long chain hydrocarbons. The activity of catalysts for FT synthesis depends primarily on the overall amount of exposed metal atoms. Thus, a highly active catalyst requires a high dispersion of cobalt metal. Mesoporous silica materials such as SBA-15 have been recently used as supports for cobalt.[1-4] The high surface area (500 - 1500 m^2/g) of the mesoporous materials gives higher metal dispersions at higher cobalt loadings compared with conventional amorphous silicas. Furthermore, the uniform pore diameters (2 - 30 nm) of the mesoporous silica materials permit better control of the cobalt particle size and the distribution of hydrocarbon products from the FT synthesis.[5] We have proposed that surface modification of SBA-15 via silylation increases the catalytic activity and hydrocarbon selectivity in FT synthesis.[6]

The objectives of this present study are to determine the relative merits of impregnation methods, advantages of iron over cobalt and the consequences of aluminum incorporation in SBA-15 on catalytic activity in Fischer-Tropsch synthesis. Six different catalysts were prepared. The physical and chemical properties of the catalysts were obtained from N_2 adsorption/desorption, XRD and TPR experiments. The catalytic performance in FT synthesis was evaluated with a fixed-bed reactor.

Experimental

Catalyst preparation. SBA-15 was obtained by a procedure described elsewhere.[6,7] Triblock polymer Pluronic P123 ($EO_{20}PO_{70}EO_{20}$, M_{av} = 5800, BASF) was used as the structure-directing agent of SBA-15. Anhydrous sodium metasilicate (Na_2SiO_3, Aldrich) was used as the silica source of SBA-15. Aluminum incorporation in SBA-15 was achieved using the following post-synthesis procedure. 1.0 g of calcined pure SBA-15 was added to a 50 mL ethanol solution containing $AlCl_3$ (Aldrich). The mixture was stirred at ambient temperature overnight, and filtered using a glass membrane filter. The filtered sample was dried in air at 100 ^oC overnight, and then calcined in air at 550 ^oC overnight. The amount of incorporated aluminum was analyzed by ICP-AES.

SBA-15 supported cobalt catalysts were prepared by three different cobalt impregnation methods: incipient wetness, post-synthesis and supercritical solvent. The cobalt post-synthesis impregnation was similar to that used to graft aluminum on SBA-15. The impregnation of the SBA-15 with cobalt using a supercritical solvent proceeded as follows: The SBA-15 was added to a 250 mL ethanol solution of $Co(NO_3)_2 \cdot 6H_2O$, and stirred at ambient temperature for 1 h. The suspension was transferred to an autoclave placed inside a furnace. The autoclave was purged ten times with 200 psi N_2 to remove any oxygen trapped in the system. The autoclave was heated to 350 ^oC at 5 ^oC/min, then held at 350 ^oC for 3h. The pressure inside the autoclave was maintained at 2000 psi by controlled venting through a high-pressure valve. The system was cooled to 200 ^oC ,and the gas inside the autoclave was

Table 1. Specifications of SBA-15 supported cobalt and iron catalysts.

Catalyst	Silica	Precursor	Co loading (Wt %)	Loading method
CAT1	SBA15	$Co(NO_3)_2$	6	IW
CAT2	SBA-15	$Co(ac)_2$[b]	6	PS
CAT3	SBA-15	$Co(NO_3)_2$	6	SS
CAT4	SBA-15	$Co(NO_3)_2$	20	IW
CAT5	SBA-15	$Fe(NO_3)_3$	20	IW
CAT6	AlSBA-15	$Fe(NO_3)_3$	20	IW

[a] IW: incipient wetness, PS: post synthesis, SS: Supercritical solvent

[b] $Co(ac)_2$ is anhydrous cobalt acetate

vented for 1 h. The system was then cooled to ambient temperature. The cobalt impregnated sample was calcined in air at 550 ^oC overnight. In this study, iron impregnated SBA-15 samples were prepared by incipient wetness impregnation using $Fe(NO_3)_3 \cdot 9H_2O$ dissolved in ethanol solution. All calcined samples were reduced under hydrogen at 500 ^oC for 10 h to obtain active metallic cobalt or iron for the FT synthesis. Specifications of SBA-15 supported cobalt and iron catalysts used in this study are shown in Table 1.

Catalyst characterization. To evaluate the pore structure of the catalyst samples, nitrogen adsorption isotherms were measured using an Autosorb-1 instrument (Quantachrom). The isotherms were used to calculate the BET specific surface area (S), total pore volume (V_t), and average pore diameter (D_p). The pore structure of the samples was also evaluated using XRD patterns. The reduction of cobalt oxides in the sample was evaluated by temperature programmed reduction (TPR, Micromeritics). The H_2 consumption of the sample was calculated using the reduction of CuO as the standard.

FT synthesis and product analysis. The FT synthesis was carried out in a fixed-bed stainless steel reactor (5 mm I.D. and 168 mm length) at 100 psi and 265 ^oC. An H_2/CO molar ratio of 2 was used, and a ratio of sample weight to total gas flow rate (W/F) was 0.47 - 0.91. The gas flow rates for reactant gases (CO, H_2) and internal standard (Ar) were controlled by mass flow controllers (MKS). Iron carbonyl impurities in the CO reactant stream were removed by a PbO_2/Al_2O_3 trap. The test for the FT synthesis was carried out for 36 h on stream. Reactants and hydrocarbon products were analyzed by gas chromatography (Shimadzu). The GC oven was heated using a heating program as follows: 10 ^oC for 4 min, then heating from 10 to 350 ^oC with the heating rate of 20 ^oC/min and holding at 350 ^oC for 10 min. Reactants were separated on a capillary column (CarboPlot, 0.53 mm I.D. and 30 m length) with a TCD detector. Hydrocarbon products were separated on a capillary column (DB-5, 0.25 mm I.D. and 10 m length) with an FID detector.

Results and Discussion

The results of XRD patterns and nitrogen adsorption/desorption isotherms revealed that all cobalt catalysts having 6 wt% cobalt had the 2-D hexagonal structure of pure SBA-15. Pore structural parameters calculated from nitrogen adsorption/desorption isotherms for the cobalt SBA-15 catalysts are listed in Table 2. The BET surface area, pore volume and pore diameter of SBA-15 are decreased by cobalt impregnation. However, the three cobalt catalysts prepared by three different impregnation methods have similar pore structural values. This implies that the impregnation method does not have a significant impact on the pore structure of SBA-15.

Table 2. Physical and chemical properties of SBA-15 supported cobalt catalysts.

Catalyst	S[a] (m^2/g)	Vt[b] (cc/g)	D_p[c] (nm)	Co_3O_4 [d] Diameter (nm)	Reduction [e] (%)
Pure SBA-15	724	1.243	8.09	-	-
CAT1	465	0.811	8.08	11.1	49
CAT2	472	0.858	8.08	-	18
CAT3	461	0.815	8.08	11.6	63

[a] BET Surface area, [b] Total pore volume, [c] average pore diameter, [d] Co_3O_4 crystallite diameter calculated from the widths of XRD peaks using the Scherrer equation (2 theta = 36.68°), [e] reduction degree of cobalt oxides during TPR at 30 – 500 °C.

The mean Co_3O_4 crystallite sizes deduced from the XRD data using the Scherrer equation and the reduction percentage of the cobalt oxides at temperatures less than 500 °C are presented in Table 2. The XRD peak at 36.68° for CAT2 was not detected. This suggests that most of cobalt oxides are present as cobalt silicates in the framework of the SBA-15, and the average crystallite size of Co_3O_4 on the surface of the SBA-15 is very small. The mean Co_3O_4 crystallite size on CAT3 is slightly larger than on CAT1. This result indicates that the crystallite size of Co_3O_4 is clearly dependent on the impregnation method.

Figure 1 shows TPR profiles of three cobalt catalysts, CAT1, CAT2 and CAT3. CAT1 and CAT3 show similar TPR profiles with three typical peaks. However, the TPR profile of CAT2 with two peaks is significantly different. For CAT1 and CAT3, the first peak at temperatures less than 380 °C can be assigned to the reduction of Co_3O_4, and the second peak in the 380 - 600 °C range corresponds to the reduction of cobalt oxides strongly interacting with the SBA-15. The third peak in the 600 - 760 °C range can be attributed to the reduction of cobalt oxides very strongly interacting with the SBA-15. The maximum temperatures of the three peaks for CAT3 are located at lower temperatures than for CAT1. In particular, the intensity of the third peak for CAT3 is very low. This suggests that highly irreducible cobalt oxides on CAT3 are less prevalent than on CAT1. CAT2 shows two peaks in its TPR profile. The first peak is at temperatures in the

range of 200 – 500 ^{o}C, and the second peak is located at temperatures above 760 ^{o}C, corresponding to the reduction of cobalt oxides in the framework of SBA-15. The reduction percentage of the cobalt oxides at temperatures less than 500 ^{o}C are presented in Table 2. CAT3 shows the highest reducibility of cobalt oxides among the

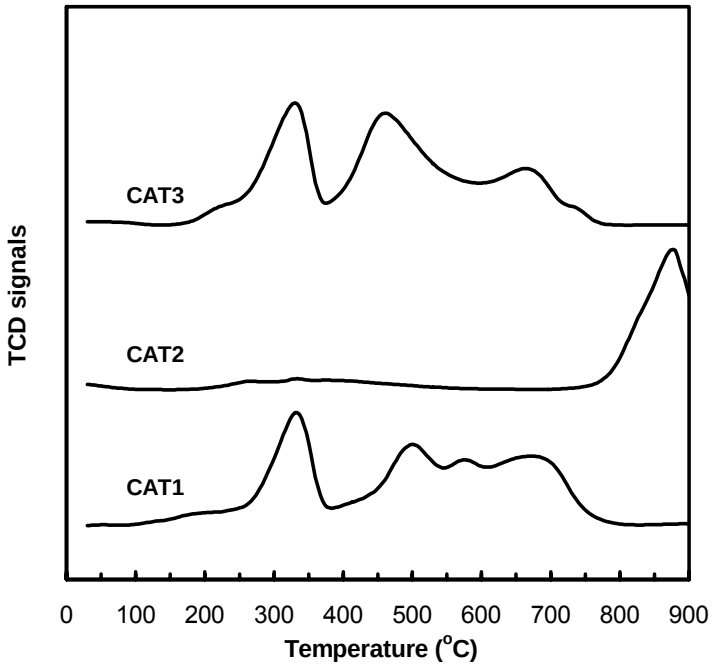

Fig.1 TPR profiles of three cobalt catalysts

three catalysts prepared by different impregnation methods. According to the TPR results, undesireable cobalt oxides (those not easily converted to active cobalt metal at lower temperature) were abundantly produced in CAT1. Catalytic activities of SBA-15 supported cobalt and iron catalysts in FT synthesis are summarized in Table 3.

Table 3. CO conversion, hydrocarbon selectivity and chain growth probability of SBA-15 supported cobalt and iron catalysts

Catalyst	W/F (g h/mol)	CO conversion (%)	Product selectivity (C mol%)				α [a]
			C_1	C_2-C_4	C_5-C_{10}	C_{10+}	
CAT1	0.73	15.7	8.6	38.6	39.0	13.8	0.86
CAT2	0.91	4.6	15.8	56.8	24.2	3.2	0.82
CAT3	0.67	21.1	7.3	32.4	45.3	15.0	0.88
CAT4	0.55	22.2	7.2	32.3	46.5	14.0	0.88
CAT5	0.47	23.8	6.2	6.5	32.8	54.5	0.95
CAT6	0.47	32.5	4.9	6.1	27.3	61.7	0.98

[a] chain growth probability obtained from Anderson-Schulz-Flory equation

CO conversion and higher hydrocarbon selectivity can be related to the reducibility of the cobalt oxides and pore structure of a cobalt catalyst. The three samples (CAT1, CAT2, CAT3) having the same loading of cobalt showed similar values in BET surface area, pore volume and average pore size. However, the three samples showed differences in the reducibility of cobalt oxides. CAT3 shows the highest CO conversion, C_{5+} selectivity and chain growth probability among the three catalysts obtained by three different cobalt impregnation methods. This result is quite consistent with the TPR result.

In this study, to investigate the effect of active metal and aluminum incorporation of SBA-15 on catalytic activity, we prepared a cobalt catalyst (CAT4) and two iron catalysts (CAT5, CAT6). The three samples have the same metal loading. CAT5 shows higher CO conversion, C_{5+} selectivity and chain growth probability than CAT4. This indicates that iron in the SBA-15 is more effective than cobalt for FT synthesis.

As the results of TPR and EXAFS tests, after aluminum incorporation of SBA-15, reducible iron oxides such as Fe_2O_3 on CAT6 were greatly increased compared to CAT5. This indicates that the increase of reducible iron oxides leads to an increase in catalytic activity of the iron catalyst.

Conclusions

The cobalt impregnation method has a significant effect on catalytic activity and selectivity through differences in reducibility of cobalt oxides. Aluminum added iron-based catalyst is also advantageous.

References

1. J.S. Girardon, A.S. Lermontov, L. Gengembre, P.A. Chernavskii, A. Griboval-Constant and A.Y. Khodakov, J. Catal., **2005**, 230, 339-352.
2. K. Okabe, M. Wei and H. Arakawa, Energy & Fuels, **2003**, 17, 822-828.
3. A. Martinez, C. Lopez, F. Marquez and I. Diaz, *J. Catal*., **2003**, 220, 486-499.
4. J. Panpranot, J. G. Goodwin Jr. and A. Sayari, *Catal. Today*, **2002**, 77, 269-284
5. Y. Wang, M. Noguchi, Y. Takahashi and Y. Ohtsuka, *Catal. Today*, 2001, **68**, 3-9.
6. D. J. Kim, B. C. Dunn, P. Cole, G. Turpin, R. D. Ernst, R. J. Pugmire, M. Kang, J. M. Kim, and E. M. Eyring, *Chem. Commun*., **2005**, 1462-1464.
7. J. M. Kim and G. D. Stucky, *Chem. Commun*., **2000**, 1159-1160.

DEVELOPMENT OF MOLYBDENUM-PROMOTED CATALYSTS SUPPORTED ON ACTIVATED CARBON FOR DIESEL FUEL SYNTHESIS

Wenping Ma, Edwin L. Kugler, James Wright and Dady B. Dadyburjor

Department of Chemical Engineering
West Virginia University
Morgantown, WV 26505-6102

I. Introduction

It is well known that the Fischer-Tropsch Synthesis (FTS) provides an alternative way to convert coal indirectly to transportation fuels. The traditional industrial catalysts used for this reaction are precipitated iron and silica-supported cobalt catalysts, which initially appeared in the FTS plants in South Africa and Malaysia [1-2]. These two types of FTS catalysts have been famous for optimal production of high-molecular-weight hydrocarbons, which need to be further treated (by isomerization and hydrocracking) to yield liquid diesel fuels. In order to simplify the conventional FTS technology and to lower the capital cost of the diesel fuels, selective FTS catalysts have been suggested, on which medium-molecular weight hydrocarbons (mainly diesel fuels) expect to be directly formed from syngas [3-4]. Hydrocarbon chain growth can be limited over iron and cobalt catalysts supported on activated carbon (AC) and on carbon nanotube supports, indicating that carbon material may be a good choice for limiting hydrocarbon chain length to a certain range.

We have been working on AC-supported Mo catalysts since 1993. Mo-Ni/AC catalysts have been successfully used for synthesis of high-molecular-weight alcohols [5, 6]. These studies also demonstrated that AC-supported catalysts are able to produce hydrocarbons with limited carbon numbers, e.g. less than C_6, and that the nature of the activated carbon plays a role in the product distribution. In the present study, we have investigated physico-chemical properties of AC- supported Mo- promoted Fe-Cu-K catalysts as a function of Mo loading (0-12%). The catalysts have been characterized by N_2 adsorption, x-ray diffraction (XRD), temperature-programmed reduction (TPR), CO chemisorption and isothermal reduction. The influence of Mo loading on the degree of reduction of iron, iron dispersion, and the particle size of iron containing active sites are discussed.

II. Experimental

Catalyst Synthesis. The catalysts were prepared as described earlier [7], except that the only support used was activated carbon from peat, as obtained from Sigma Aldrich. The final catalyst contains 0-12% Mo, 15.7 % Fe, 0.8 wt% Cu and 0.9 wt% K. The catalysts were characterized before and after reaction.

BET surface area measurement. The BET surface area and pore volume of the peat-AC support and catalysts before and after FTS reactions were determined by isothermal adsorption of N_2 at

77 K in a Coulter Omnisorp 360 system. Prior to the adsorption measurements, the samples were degassed under vacuum at 300ºC for 10 h.

EDS measurement. The supports and catalysts were analyzed by energy-dispersive spectroscopy (EDS) in order to confirm the elements and the relative ratio of iron to carbon on the catalyst surface. The sample was placed on double-stick adhesive tape and placed in the instrument.

XRD measurement. Powder x-ray diffraction (XRD) analysis of the catalysts after reaction was carried out at room temperature using a Rigaku Diffractometer (DMAX-B) and Cu K_α radiation (1.5418 Å). The samples were mounted on a silicon plate for x-ray measurements. The identification of different phases was conducted using Jade software and the ICDD-PDF4 library. The average particle sizes of iron oxide and iron carbide in the different catalysts were estimated by the Scherrer equation using the most intense reflection at 2 θ = 35.5º and 43.1°, respectively.

TPR study. Temperature-programmed reduction (TPR) of the catalysts was conducted in a mixture of 5% hydrogen-95% argon at a total flow rate of 50 cm /min. About 50 mg of the catalyst was placed in a quartz U-tube (5 mm × 300 mm) and heated from room temperature (RT) to 915°C at a constant rate of 10°C/min, and then it was held at 915°C for 30 mins before quenching. The H_2 consumption rate was monitored in a thermal conductivity detector (TCD). The TCD was calibrated previously by reduction of 14 mg of ultra-high purity CuO (99.9999%) between RT and 500°C at the same heating rate. The peak areas in the TPR patterns of the catalysts were deconvoluted using PeakFit software, and the corresponding H_2 consumption at each deconvoluted peak was precisely quantified (H_{exp}). The total theoretical H_2 consumption (H_{tot}) was calculated assuming that Fe and Mo are in the forms of Fe_2O_3 and MoO_3 before reduction, and that they are completely reduced to Fe and Mo metals. Then the degree of reduction of the metal, R_T, corresponding to the deconvoluted TPR peak, can be calculated as:

$$R_T = (H_{exp}) / (H_{tot}) \quad (1)$$

CO pulse chemisorption / Isothermal Reduction. CO adsorption behavior on partially reduced catalysts was studied in order to estimate the Fe and Mo metal dispersion on the catalyst surface. About 200 mg of the AC support or catalyst was pretreated at 400°C for 12 hours using 5%H_2 in Ar. After that, the reactor was cooled to room temperature by flowing Ar. CO chemisorption was conducted by injection of 10 μl of CO in a stream of Ar. The quantity of CO not chemisorbed on the catalyst was recorded by a TCD. The injections were continued until CO saturates the surface and peak size does not change with subsequent injections. The number of iron sites on the surface, [Fe_s], was estimated from the CO chemisorbed, [CO], using

$$[CO] / [Fe_s] = 2 \quad (2)$$

The dispersion (D) is determined by:

$$D (\%) = 100* [Fe_s] / (\text{total number of Fe atoms}) \quad (3)$$

Finally, the chemisorbed sample was reduced at 400°C for 12 h and the amount of hydrogen required for that was determined. The degree of reduction of the metals during this isothermal reduction, R_I, was estimated using (1).

III. Results and Discussion

BET-based Properties of support and supported catalysts. BET surface areas, total pore volumes, and average pore diameters of the peat-AC support and the catalysts before and after FTS reaction are shown in Table 1. After addition of Fe, Cu and K to the support, the BET surface area of the fresh catalysts is reduced by 42%, and the total pore volume by about 50%. Correspondingly, the average pore diameter of the fresh catalyst is decreased by 30%. Addition of 6 wt% Mo does not further decrease the surface area, pore volume or average pore diameter appreciably. When the catalyst contains 12 wt% Mo, the surface area decreases by another 30%, while the pore volume does not decrease appreciably, but the average pore diameter increases to approximately the value of AC alone. It might be that more micro-pores on the 12 % Mo catalyst are filled or blocked by metal precursors, leading to a relatively greater loss of surface area in comparison with its pore volume and larger average pore diameter.

The decrease in BET surface area and pore volume for the fresh catalysts might arise from two factors. One could be metal precursors filling and blocking a fraction of micro- and meso-pores of the AC support; another could be lower mass concentration of the AC support after impregnation (25-42% less). For the spent catalysts, the BET surface areas of all the catalysts decrease by 95%, and the pore volumes by 40 – 70%, but the average pore diameters increase to 102 -152 Å. This indicates that the pores of the spent catalysts are collapsed partially after FTS and/or some of the FTS products remain in the micro-pores of the catalyst.

EDS. Table 2 gives the EDS results for the AC support and the three fresh catalysts. The catalysts are characterized by slightly higher mole ratios of iron to carbon than the bulk values, and slightly lower amount of Mo, but probably within the range of experimental error. EDS also detects oxygen and trace amounts of Si, Ca and Mg elements on surface of the carbon support.

XRD. Figure 1 shows the patterns of the three spent Fe-Mo-Cu-K/AC catalysts after 72-396 h FTS reaction at 310-320°C. All three catalysts show qualitatively similar XRD patterns between $2\theta = 30° - 80°$. The diffraction peaks match very well with the standard Fe_5C_2 phase and magnetite (Fe_3O_4) phase. This is in good agreement with previous studies on precipitated-iron FTS catalyst [8-10]. Some metallic iron may not be carbonized and may be present on the catalyst surface during reaction. But the current XRD patterns cannot reveal this phase, since the catalyst sample was exposed to air after reaction and any metallic iron would be oxidized.

Figure 1 also shows that the diffraction peaks become smaller and less sharp (particularly at $2\theta = 35.5°$ and 43.8°) when the Mo loading increases. This suggests that the particles of iron oxide and iron carbide become smaller with increasing Mo content. This is quantified by using the Scherrer equation and the results are shown in Table 3. Apparently, the dispersions of Fe_5C_2 and Fe_3O_4 phases on the catalyst are improved after addition of the Mo promoter.

Further, note that the values of the average crystal sizes of Fe_5C_2 and Fe_3O_4 (8-29 nm) in Table 3 are larger than those of the average pore diameters of the spent catalysts in Table 1 (10-15 nm). This suggests that the Fe_5C_2 and Fe_3O_4 particles are outside the micropores and mesopores.

Also, no Mo crystalline phase (oxide or carbide) is observed in the XRD pattern of the 6% Mo catalyst, probably indicating that the Mo precursor is highly dispersed on the AC support. Similar results on a 10wt% Mo/AC catalyst after H_2 treatment at 600°C were reported by Liang *et al*. [11]. However, when the Mo loading is increased to 12wt%, two additional peaks occur. The new peaks (at 21.4° and 23.7°) do not fit any form of molybdenum carbides or molybdenum oxides. But a new Mo-Fe oxide or Mo-Fe carbide phase might be formed for the 12wt % Mo catalysts during reduction or FTS reaction.

TPR. Patterns for 0, 6 and 12 wt% Mo catalysts are shown in Figure 2. All three patterns have similar shapes and can be characterized by five distinct structures in the temperature range of RT to 915°C. The first peak (Peak A, 200 - 300°C) could be assigned to the reduction of Fe_2O_3 to Fe_3O_4 and CuO to Cu [12,13]. However, the calibration results with pure CuO, as described earlier, indicate that the contribution of Cu in Peak A is negligible, relative to the contribution of Fe. The second peak, B, is observed in the temperature range of 300-400°C. Peak B may be assigned to the subsequent reduction of Fe_3O_4 to FeO. Peak C, observed at 400-700°C, may be assigned to the reduction of FeO to metallic Fe or, if Mo is present, to the reduction of MoO_3 to an oxide of Mo with low chemical valence, i.e. MoO_2, or to Mo [14]. Peak C is much broader than Peaks A and B; it demonstrates that the reduction of iron in the third stage (FeO to metallic Fe) is a slow process [9,12]. The fourth peak, D, (700 - 800°C) is relatively small and could be attributed to reduction of smaller Fe_3O_4 or FeO crystallites located in micro-pores to metallic Fe, since smaller particles are more difficult to reduce [15]. Alternatively, Peak D might be assigned to the reduction of a Mo-Fe oxide species formed at high temperature during TPR. The last peak, E (800 - 915°C), is negative. This has been ascribed [14,16] to CO effusion due to the decomposition of oxygen-containing groups present on the surface of the AC support, and/or to the reaction between partially reduced metal oxides such as MoO3 and Fe2O3 with H2 and active carbon species on the AC surface [11,17].

The effect of Mo addition on the reduction behavior of the catalysts can also be seen in Figure 2. Peaks A and B for the 0% Mo catalyst are much larger and sharper than those of the 6 and 12% Mo catalysts, apparently indicating that Mo addition significantly inhibits iron reduction. This suggests that a strong interaction between Mo and Fe oxides exists during the reduction process. The areas in Peak C for the 6% and 12% Mo catalysts are larger than that of the 0% Mo catalyst. This is due to the additional reduction of Mo oxide to MoO_2 or to Mo between 400 and 750°C.

The H_2 consumed in each reduction stage in the TPR patterns was analyzed quantitatively, following calibration of TCD peak areas by pure CuO, as described earlier. The corresponding results for the three catalysts are summarized in Table 4 in terms of the degree of reduction R_T, as defined in Eqn (1) above. The total R_T and the R_T values of iron in the first and the second reduction stages (peaks A and B respectively) decrease with increasing Mo loading, indicating that Mo addition inhibits greatly the first-step and the second-step reductions of Fe_2O_3 ($Fe_2O_3 \rightarrow Fe_3O_4$ and $Fe_3O_4 \rightarrow FeO$ respectively). The values of R_T of the three catalysts in the third reduction stage (peaks C and D) change less after addition of Mo than do the values in the first and second stages.

CO chemisorption and Isothermal Reduction. The results of CO uptake on the catalysts are shown in Table 5. The CO uptake on the 6%Mo/AC alone (i.e. without Fe, Cu, and K) is also listed in Table 5 for comparison. CO uptakes increase monotonically with the addition of Mo into the catalyst. The incremental CO uptake with addition of 6%Mo to the Fe-Cu-K catalyst is approximately 1 μmol/g-cat, less than the CO uptake for the 6%Mo/C. However, it is unlikely that the increase in CO uptake for the 6%-Mo catalyst is due only to Mo and not by a change in the particle size of Fe, since Mo peaks are not seen on the XRD patterns of the catalyst. On the other hand, with 12% Mo on the Fe catalyst, the incremental CO uptake is greater than that which can be ascribed to Mo, and is clearly due to an increase in dispersion, D (or a decrease in average crystallite size, d). The calculated values of D and d are also shown in Table 5. The decrease in particle size with increasing Mo as determined by CO chemisorption is less than the decease using XRD (Table 3) but qualitatively consistent. Finally, the values of the degrees of reduction, R_I, in Table 5 are comparable with those in Table 4.

IV. Conclusions

The effects of Mo addition on the physico-chemical properties of Fe-Cu-K/AC were studied for the Fischer–Tropsch synthesis reaction over catalysts. The addition of Mo improves Fe dispersion after catalysts are reduced at 400°C for 12 h. Iron carbide (Fe_2C_5) and magnetite (Fe_3O_4) are detected on spent catalysts by XRD. These are postulated to be active phases for the FTS and WGS reactions. The addition of Mo prevents iron particles from agglomerating at reduction and reaction conditions, leading to improved catalyst stability of the catalysts.

TPR studies indicate a three-step reduction process of iron oxide on AC, $Fe_2O_3 \rightarrow Fe_3O_4 \rightarrow FeO \rightarrow Fe$, in three distinctive temperature ranges, 200 - 300°C, 300 - 400°C and 400 - 800°C. The reducibility of Fe-Cu-K/AC catalysts is affected greatly by the Mo promoter. The addition of Mo creates a strong interaction between Fe and Mo oxides. As a result, the extents of reduction of Mo-containing Fe-Cu-K/AC catalysts decrease. Quantitative TPR analysis confirms the results and shows the greater influence of the first and second stage reductions of iron oxide. Preliminary analysis of the reaction results, presented earlier [7], indicate that both the 6% and 12% Mo catalysts show much greater stability than the catalyst without Mo and that catalyst activity on the 6% Mo catalyst is higher than that of the 12% Mo catalyst. This might be due to the higher degree of reduction of iron oxide on the 6%Mo catalyst, which allows more reduced Fe to be carbonized to active sites for the FTS reaction.

V. Papers Presented or Published

W.P. Ma, J.H. Wright, E.L. Kugler, and D.B. Dadyburjor, "Effect of Molybdenum Loading on Iron-Based Fischer-Tropsch Catalyst," AICHE Annual Meeting, Cincinnati, OH, October 30, 2005

W.P. Ma, E.L. Kugler, J.H. Wright and D.B. Dadyburjor, "Effect of Mo promoter on reducibility, activity and hydrocarbon selectivity over activated-carbon supported Fe-Cu-K catalysts for Fischer-Tropsch synthesis," CFFS Annual Meeting, Stonewall Jackson Resort, WV, August 1-3, 2005

W.P. Ma, E.L. Kugler, J.H. Wright and D.B. Dadyburjor, "Effect of Mo Promoter on Reducibility, Activity and Hydrocarbon selectivity over Activated-Carbon Supported Fe-Cu-K Catalysts for Fisher-Tropsch Synthesis," Pittsburgh-Cleveland Catalysis Society Spring Symposium, Pittsburgh, June 17, 2005

W.P. Ma, E.L. Kugler, and D.B. Dadyburjor, "Effect of Mo loading and support type on oxygenates produced during Fischer-Tropsch Synthesis Over Fe-Mo-Cu-K catalyst supported on Activated Carbon", ACS National Meeting, San Diego, March 2005.

W.P. Ma, E.L. Kugler, and D.B. Dadyburjor, "Effect of Mo loading and support type on oxygenates produced during Fischer-Tropsch Synthesis Over Fe-Mo-Cu-K catalyst supported on Activated Carbon", *Prepr Pap. – Am. Chem. Soc., Div. Pet. Chem.* 2005 50(2), 161.

Wenping Ma, Edwin L. Kugler, James Wright and Dady B. Dadyburjor, "Activated Carbon Supported Mo-Fe Catalysts for Liquid Fuel Synthesis via Fischer-Tropsch Synthesis: Impact of Mo Addition on Reducibility, Activity and Hydrocarbon Selectivity," in preparation.

Article I.

VI. References

[1] Dry M. E. *Catal. Lett.* 1991, 7: 241.

[2] Eilers J., Posthuma S. A., Sie S. T. *Catal. Lett.* 1991, 7: 253.

[3] Venter J. J., Kaminsky M., Geoffroy G. L., Vannice M. A. *J. Catal.* 1987, 103: 450.

[4] Steen E. van, Prinsloo F. F. *Catal. Today* 2002, 71: 327.

[5] Kugler, E.L., Feng, L., Li, X., Dadyburjor, D.B. *Studies in Surface Science and Catalysis*. 2000, 130A: 299-304.

[6] Li, X.G., Feng, L.J., Liu, Z.Y., Zhong, B., Dadyburjor, D.B., Kugler, E.L. *Ind. Eng. Chem. Res.* 1998, 37, 3853.

[7] Ma, W., Kugler, E.L., Shao H., Wright, J. and Dadyburjor, D.B. Development Of Activated-Carbon-Supported, Molybdenum-Promoted Catalysts For Diesel Fuel Synthesis, Annual Report (2004).

[8] Bukur, D.B., Koranne, M., Lang, X.SRao, ., K.R.P.M., Huffman, G.P., Appl. Catal. 126 (1995) 85.

[9] Lox, E.S., Marin, G.B., DeGrave, E., Bussiere, P., Appl. Catal. 40 (1988) 197.

[10] Rao, K.R.P.M., Huggins, F.E., Huffman, G.P., Gormley, R.J., O'Brien, R.J., Davis, B.H., Energy & Fuels 10 (1996) 546.

[11] Liang, C.H., Ying, P.L., Li, C., Chem. Mater. 14 (2002) 3148.

[12] Bukur, D.B., Sivaraj, C., Appl. Catal. 231 (2002) 201.

[13] Obrien, R.J., Xu, L.G., Spicer, R.L., Bao, S.Q., Milburn, D.R., Davis, B.H., Catal. Today 36 (1997) 325.

[14] Feng, L.J., Li, X.G., Dadyburjor, D.B., Kugler, E.L., J. Catal. 190 (2000) 1.

[15] Jacobs, G., Das, T.K., Zhang, Y.Q., Li, J.L., Racoillet, G., Davis, B.H., Appl. Catal. 233 (2002) 263.

[16] Sayag, C., Benkhaled, M., Suppan, S., Trawczynski, J., Djega-Mariadassou, G., Appl. Catal. 275 (2004) 15.

[17] Liang, C.H., Ma, W.P., Feng, Z.C., Li, C., Carbon 41 (2003) 1833.

Table 1. BET Measurements of Peat-AC support and Fe-Mo-Cu-K/AC Catalysts.

Support and Catalyst	Surface Area [m^2/g]		Pore Volume [cm^3/g]		Ave Pore Size [nm]	
	Fresh	Spent	Fresh	Spent	Fresh	Spent
Peat AC	606	-	0.48	-	5.92	-
15.7% Fe / 0.8% Cu / 0.9% K/AC (a)	350	48	0.24	0.15	4.18	10.2
6 %Mo / 15.7% Fe / 0.8% Cu / 0.9% /AC (b)	347	34	0.25	0.16	4.06	15.2
12% Mo /15.7 Fe / 0.8% Cu / 0.9% K/AC (c)	280	32	0.22	0.06	5.73	10.4

(a) Spent catalyst evaluated after 72 h, 3Nl/gcat/h/300 psig, $H_2/CO = 0.9$.
(b) Same as above but evaluated after 396 h.
(c) Same as above but evaluated after 216 h.

Table 2 EDS Measurements of Peat-AC support and Fresh Fe-Mo-Cu-K/AC Catalysts.

Support and Catalyst	Fe/C Mole ratio		Mo [wt%]	
	Bulk	Measurement	Bulk	Measurement
Peat AC	-	-	-	-
15.7% Fe / 0.8% Cu / 0.9% K/AC (a)	0.045	0.053	-	-
6 %Mo / 15.7% Fe / 0.8% Cu / 0.9% /AC (a)	0.051	0.056	6	4.7
12% Mo /15.7 Fe / 0.8% Cu / 0.9% K/AC(a)	0.058	0.063	11.8	8.9

Table 3. Active Phases and Particle Sizes of Spent Catalysts from XRD

Mo Loading, wt%	Fe_5C_2 [nm]	Fe_2O_3 [nm]
0	21.2	28.4
6	13.6	12.2
12	8.4	8.2

Table 4. H_2 Consumption and Degree of Reduction from TPR Measurements.

Mo Loading [wt%]	Measured H_2 Consumption [mmol/gcat] (a)				Theoretical H_2 Consumption [mmol/gcat]	Degree of Reduction, R_T [%]				
	Peak A	Peak B	Peak C	Peak D		Peak A	Peak B	Peak C	Peak D	Total
0	0.81	1.44	1.56	0.12	4.34	19	33	36	2.8	90
6	0.54	1.14	2.57	0.10	6.22	8.6	18	41	1.6	70
12	0.52	1.00	2.87	0.11	8.04	6.5	12	36	1.4	56

(a) AC Support contributions have been subtracted to obtain these values.

Table 5. Results of CO Chemisorption. Catalysts contain 15.7% Fe / 0.8% Cu / 0.9% K/AC unless otherwise specified.

Mo Loading [wt%]	CO adsorbed [μmol/gcat]	Dispersion, D [%] (a)	Particle Size, D [nm] (b)	Degree of Reduction, R_I [%]
0	24.7	1.9	37.9	89.0
6	25.6	2.4	31.2	71.2
12	28.0	3.6	20.8	49.1
6Mo/AC only	1.6	-	-	-

Figure 1. X-Ray Diffraction Patterns of Spent Fe-Mo-Cu-K/AC Catalysts

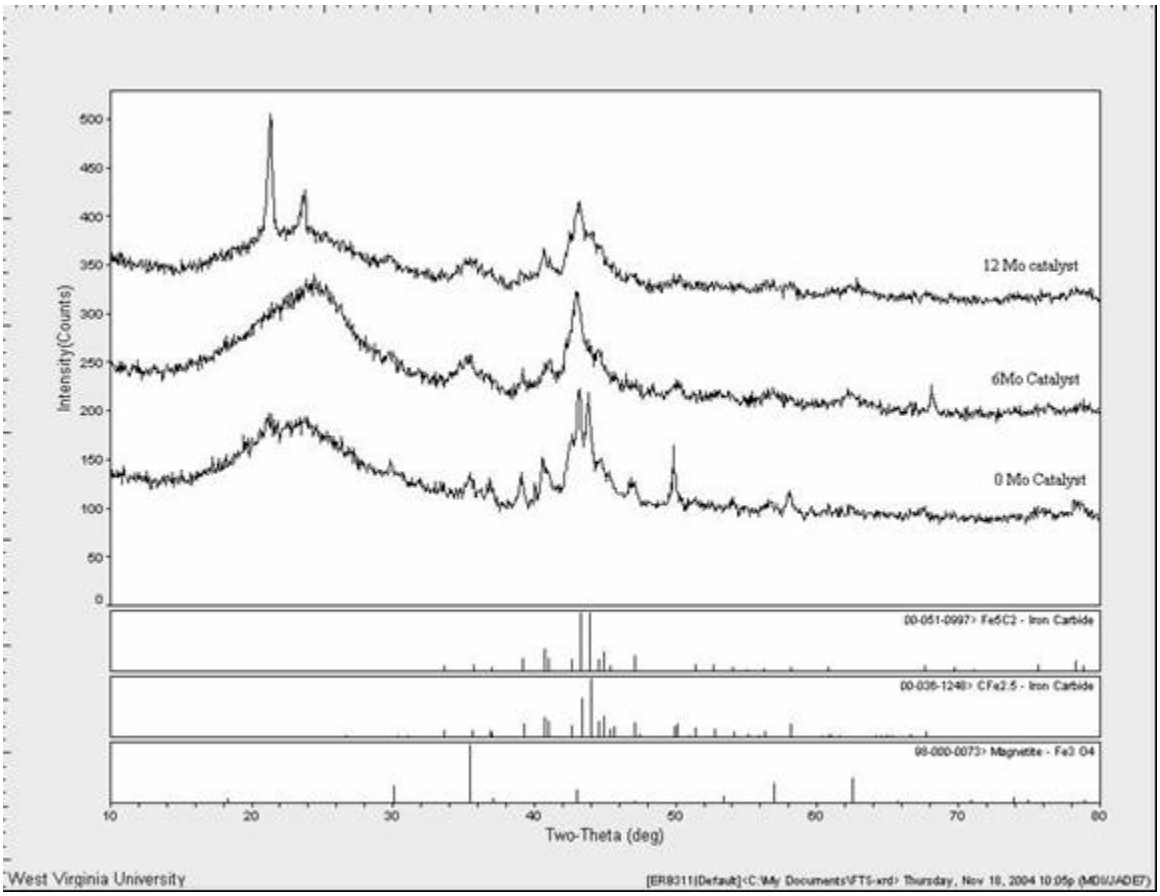

Figure 2. TPR Profiles of Fe-Mo-Cu-K/AC Catalysts.

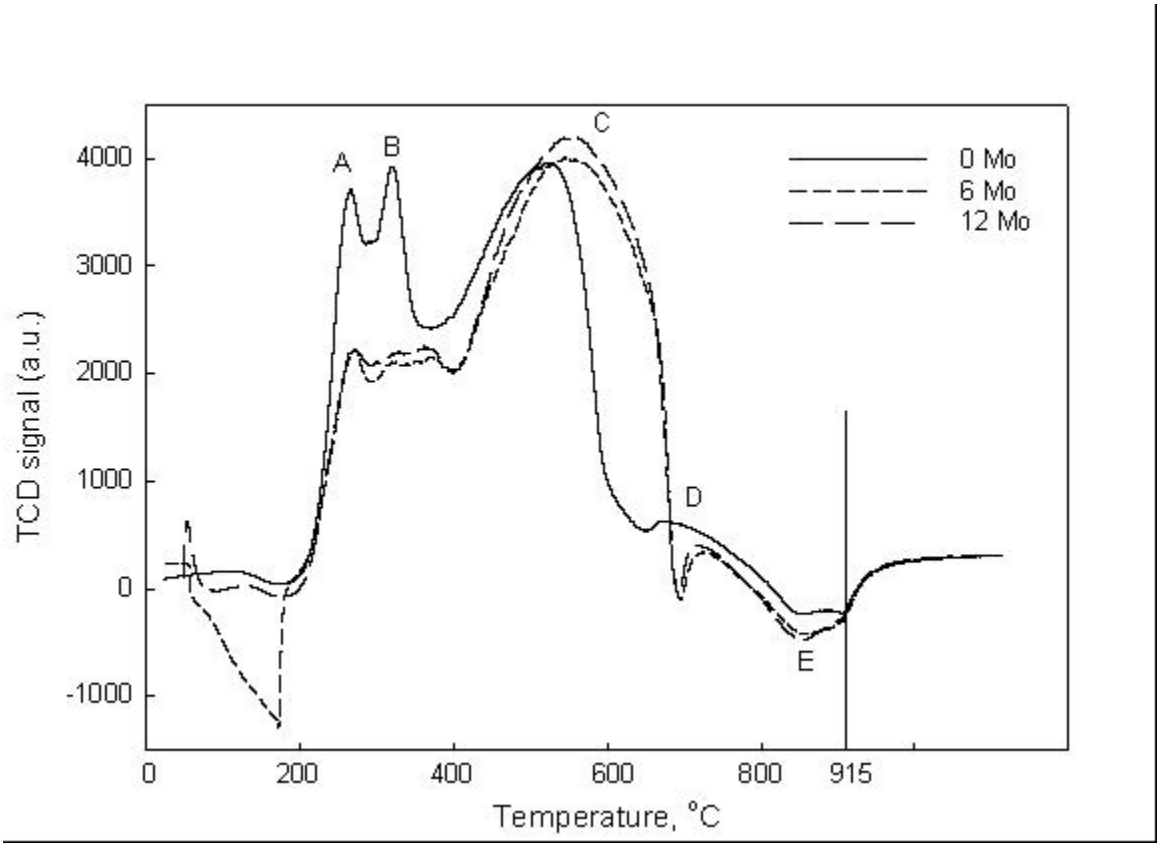

Spectroscopic Characterization of Catalysts for C1 Chemistry and H_2 Generation Applications

*Frank Huggins, *Y. Chen, *N. Shah, †E.M. Eyring, †D.J. Kim, and *G.P. Huffman
*CFFS/CME, University of Kentucky and †Chemistry Department, University of Utah

I. Introduction:

Many of the reactions of interest to C1 chemistry and hydrogen generation from coal and other fossil fuels involve catalysis. This project provides support for those researchers within the Consortium who desire to understand the reaction mechanisms and active species involved in the various reactions under investigation in the Consortium program. The Principal Investigators supply the catalysts they are preparing (see other individual reports in this Report and recent previous Consortium reports for details of the preparations) to the University of Kentucky and the materials are then analyzed by iron Mössbauer spectroscopy or XAFS spectroscopy, as appropriate, or by electron microscopy, if needed.

In this report, we describe new results from ^{57}Fe Mössbauer, X-ray absorption fine-structure (XAFS) and TEM investigations of key metal species involved in two different experimental investigations. These included:

(a) Development of silica-based zeolitic-like (SBA-15) catalysts that incorporate Fe or Co (Kim, Dunn, and Eyring, pp. 11-15, this report);
(b) Mo-promoted, Fe-based water-gas-shift catalysts (Ma, Kugler, Wright, and Dadyburjor, pp. 16-26, this report).

II. Experimental Methods

(a) Mössbauer spectroscopy

Mössbauer spectroscopy was carried out using Halder, GmbH, Mössbauer control and driving units interfaced by means of MCS/PHA boards from Canberra Nuclear, Inc., to a personal computer running MS-DOS. The Mössbauer spectra were collected over two regions of 512 channels (1,024 total channels) in mirror image mode using a symmetric constant acceleration waveform. Collection times were ~100 μs per channel and the data collection and driving unit oscillations were synchronized by means of a start pulse from the Halder control unit, which occurred at a rate of ~9 Hz. Data were accumulated in the MCS mode at a rate of about 10,000-20,000 cts/sec and continued until at least 10^6 counts had been collected in each channel. An Ar/CH_4 filled proportional counter, operating at 1750 V, was used to record the counts. This signal was amplified by means of a pre-amplifier and an amplifier before reaching the MCS/PHA boards. To calibrate the unknown spectrum, the Mössbauer spectrum of a thin (6 um) metallic Fe foil was accumulated at the opposite end of the drive using a similar proportional counter and signal amplification system. The gamma-ray source material at each end of the driving unit consisted of radioactive ^{57}Co doped into a thin Rh foil. This isotope of Co decays by electron capture to an excited state of ^{57}Fe, which then emits the gamma-ray of 14.4 keV that is used for the Mössbauer experiment. Samples of the catalysts for Mössbauer spectroscopy consisted of approximately 50 to 100 mg of crushed material held in a compression

holder that exposed a thin disc of material approximately 1.5 cm in diameter and 0.1 cm in thickness to the gamma-ray beam.

Mössbauer data analysis consists of least-squares fitting of the catalyst Mössbauer spectra to various combinations of 2-line quadrupole and 6-line magnetic components. A pure lorentzian line-shape is assumed for the individual peaks in the different components. A minimization of the statistic, χ^2, is the desired target of the least-squares fitting procedure. Ideally, the value for this parameter should be ~1 per channel in the spectrum, or ~500 for a fully acceptable fit to the data. From the least squares fitting, various Mössbauer parameters, such as the isomer shift (I.S. in mm/s, relative to the isomer shift of metallic iron at room temperature), the quadrupole splitting (Q.S. in mm/s), full width at half peak height (width in mm/s). and the magnetic hyperfine splitting (H0 in kGauss) are derived for the different quadrupole and magnetic components. The values for these parameters are used to identify the iron-bearing phase that gives rise to the particular component in the spectrum. The area under the peaks in the various components is then used to quantify the distribution of Fe among the different iron-bearing components in the catalyst.

(b) XAFS spectroscopy

XAFS spectroscopy is used to investigate other elements in the catalyst formulations. XAFS spectroscopy is performed at beam-line X-18B at the National Synchrotron Light Source (NSLS), Brookhaven National Laboratory. The X-ray absorption spectra are collected over an energy range that includes one of the characteristic absorption edges of the element of interest. The spectrum is collected as a function of energy by means of the rotation of a Si(111) channel-cut crystal from typically about 100 eV below the absorption edge to as much as 1000 eV above the absorption edge. Spectra are recorded in either absorption or fluorescence geometry, depending on the concentration of the element in the catalyst, using gaseous ionization detectors or solid state detectors such as a PIPS detector or a multi-element germanium detector. The spectral data acquired at NSLS are transferred to the University of Kentucky for detailed analysis.

Data analysis is initiated by first calibrating the catalyst's Mo XAFS spectrum relative to the zero point of the XAFS spectrum of metallic Mo foil, then normalizing the spectrum to the edge-step, and finally dividing the Mo XAFS spectra into separate X-ray absorption near-edge structure (XANES) and extended X-ray absorption fine structure (EXAFS) regions. As is well described in the literature [1-3], the XANES region is used without further modification as a "fingerprint" of how the Mo exists in the catalyst materials; it largely reflects the oxidation state of the Mo and the immediate bonding of the Mo atom or ion to its nearest neighbor ligands. In contrast, the EXAFS region is converted to a reciprocal space (k-space) representation and weighted by k^3 to yield the k^3(chi) spectrum. This spectrum is then subjected to a Fourier transform, which converts it to a radial structure function (RSF). Additional processing of both the XANES and EXAFS/RSF spectral regions is then possible. This can take the form of least-squares fitting the unknown catalyst to various combinations of standard XANES or EXAFS spectra of Mo compounds, principal component analysis with standard spectra, or FEFF fitting of individual atom shells in the EXAFS/RSF spectra.

(c) Transmission Electron Microscopy

Transmission electron microscopy (TEM) was performed on a 200 kV field emission analytical transmission electron microscope (JEOL-2010F) equipped with an Oxford energy-dispersive X-ray spectrometer, a scanning (STEM) unit, and a Gatan imaging filter (GIF) system. The GIF provides both energy-filtered imaging and diffraction and parallel detection EELS. All images and spectra were recorded with a slow-scan charge coupled device (CCD) camera with a 1024 x 1024 pixel array and processed with Gatan Digital Micrograph software.

The analysis consisted of finding various interesting particles within the catalyst mass of the right thickness for TEM. Particles were then investigated according to one or more of the various analytical methods available on the TEM to the microscopist. Images and spectra were recorded digitally.

II. Results and Discussion

(a) Characterization of silica-based aerogel F-T catalysts that incorporate Fe or Co (in cooperation with Eyring and Kim, University of Utah)

At the University of Utah, Drs. Kim and Eyring have been developing catalysts based on mesoporous silica-based aerogels (SBA-15) doped with Fe or Co ions. As discussed in the previous Annual Report, these catalyst materials may have potential for use as Fischer-Tropsch (F-T) catalysts. SBA-15 is a mesoporous silica aerogel, in which other elements, notably Al, can be substituted for Si and the Al/Si ratios in the current samples vary from is 0 to as much as 1/30. In the previous year, a detailed study of six formulations (Set 1) was carried using XAFS and Mossbauer spectroscopic methods to investigate the relationship between K added as a promoter and the ratio of hematite to ferrihydrite, the two principal iron-bearing phases generated in the catalyst formulation. Over the last year, two new batches of 5 (Set 2) and 3 (Set 3) samples were submitted by Kim and Eyring for Mössbauer and XAFS analyses in order to elucidate the iron-bearing phases present in new formulations of the catalysts and to determine the iron-bearing phases formed after reaction. The first batch (Set 2) consisted of five samples; as described in Table 1, three of these catalysts were after reaction while two were as prepared. In the second batch (Set 3) of samples, minor amounts of Co, Mn and Ni, were also incorporated in the SBA-15 formulations. A description of all samples is included in Table 1.

Table 1: Sample Identification (Sets 1, 2 and 3)

Identification	%Fe, form	%K, form	Support	Status
Set1				
Utah 1-1	20 Fe^{3+} nitrate	--	100SBA-15	As Prepared
Utah 1-2	20 Fe^{3+} nitrate	--	Al-SBA-15; Si:Al = 60	As Prepared
Utah 1-3	20 Fe^{3+} nitrate	0.5 KCl	100SBA-15	As Prepared
Utah 1-4	20 Fe^{3+} nitrate	0.5 K_2CO_3	100SBA-15	As Prepared
Utah 1-5	20 Fe^{3+} nitrate	3.0 K_2CO_3	100SBA-15	As Prepared
Utah 1-6	20 Fe^{3+} nitrate	0.5 K_2CO_3	Al-SBA-15; Si:Al = 60	As Prepared
Set 2				

Utah 2-1	20 Fe^{3+} nitrate	--	100 SBA-15, no Al	After FT Reaction
Utah 2-2	20 Fe^{3+} nitrate	--	Al-SBA-15; Si:Al = 100	After FT Reaction
Utah 2-3	20 Fe^{3+} nitrate	K_2CO_3	100 SBA-15, no Al	After FT Reaction
Utah 2-4	20 Fe^{3+} nitrate	--	Al-SBA-15; Si:Al = 100	As Prepared
Utah 2-5	20 Fe^{3+} nitrate	--	Al-SBA-15; Si:Al = 30	As Prepared
Set 3				
Utah 3-1	20 Fe^{3+} nitrate	--	Co-100 SBA-15	As prepared
Utah 3-2	20 Fe^{3+} nitrate	--	Mn-100 SBA-15	As prepared
Utah 3-3	20 Fe^{3+} nitrate	--	Ni-100 SBA-15	As prepared

Results for Set 1 were described in the previous Annual Report and will not be repeated in this Report. However, some data for these as-prepared catalysts will be included in this report, where they contribute to establishing correlations between the different techniques.

(i) Spectroscopic characterization of Set 2 of Fe SBA Calatlysts

For the samples of Set 2, the Fe XANES spectra (Figure 1) clearly show a division of the five samples into two groups, depending on whether or not the catalyst was fresh or obtained after reaction. The spectra of the fresh catalysts are very similar to those obtained for the Set 1 samples. The three after-reaction samples show a much different pre-edge feature (Figure 2) in that the small pre-edge peak has been replaced by a much larger, but less resolved shoulder and the white line peak is not nearly as pronounced. Indeed the spectra of the after-reaction samples appear flattened compared to those of the fresh samples. All of these differences are compatible with a significant amount of Fe^0 phases present in the after-reaction samples that are not present in the fresh samples.

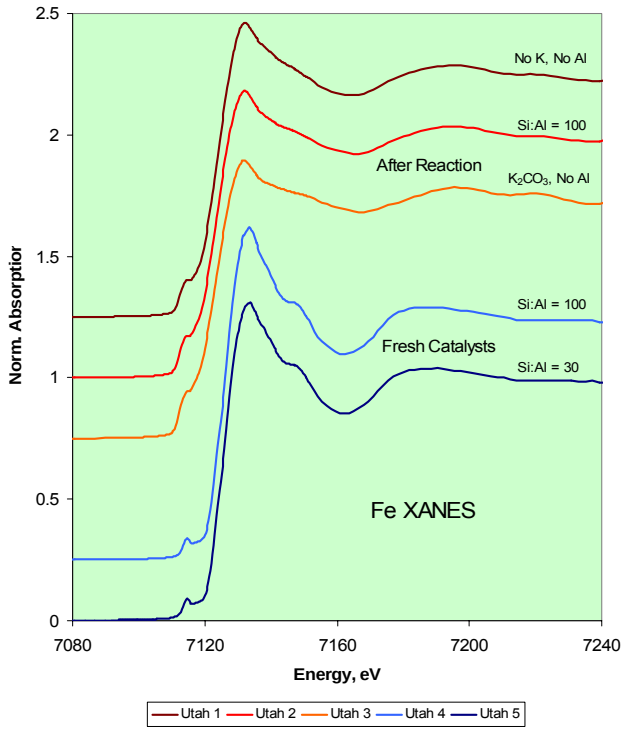

Figure 1: Fe XANES spectra of five 20Fe/xK/SBA catalysts in Set 2: three were obtained after FT reaction, whereas the other two were obtained as prepared, before reaction.

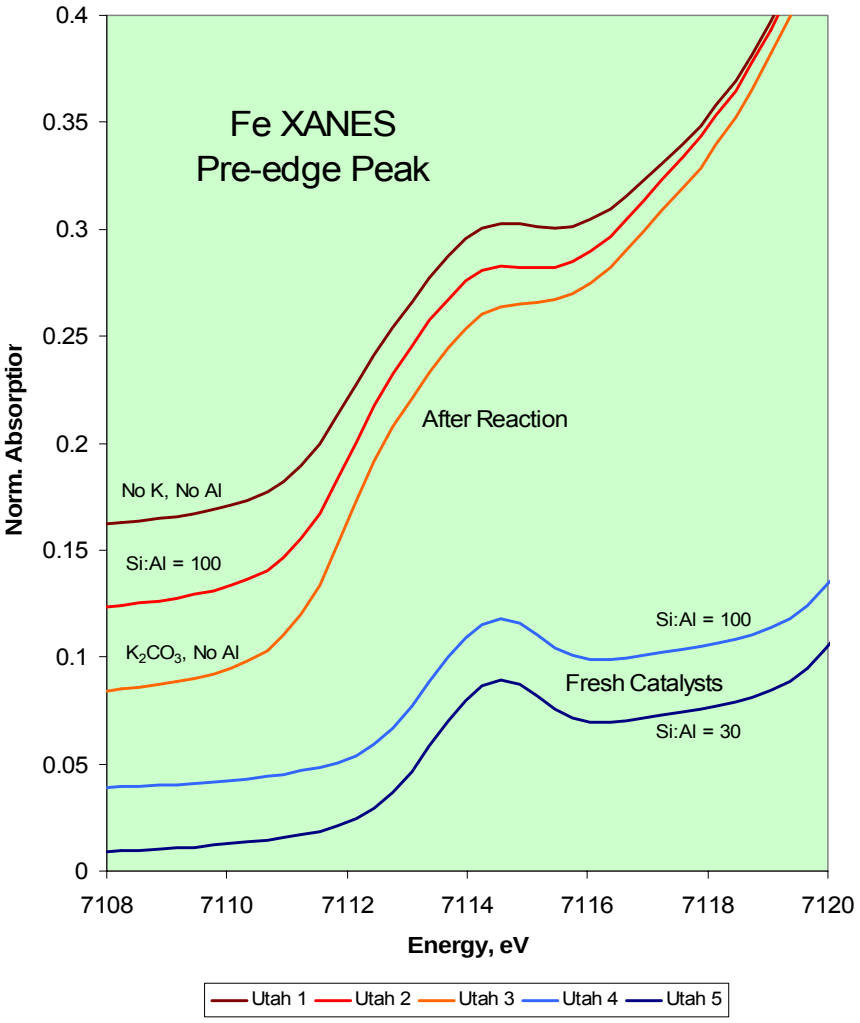

Figure 2: Expansion of pre-edge Fe XANES peak for the five catalyst samples

The EXAFS/RSFs, shown in Figure 3, also show a similar division of the set 2 samples. The three after reaction samples give a more complex RSF than the fresh samples, with at least five identifiable peaks compared to three for the fresh samples. These peaks are identified with increasing distance as follows: Fe-O; Fe-Fe; Fe-O; Fe-Fe; and Fe-Fe and are indicated in Figure 3 by different colored arrows. Only the Fe-O peaks are present in the RSFs of the fresh samples.

Figures 4 and 5 show Mössbauer spectra representative of the two different types of samples. Figure 4 shows the Mössbauer spectrum of one of the fresh samples (Sample 4, set 2); it is similar to some of those in Set 1, consisting of hematite (α-Fe_2O_3) and ferrihydrite components. However, in addition, some additional very weak magnetic peaks can be observed; these peaks have been attributed to maghemite (γ-Fe_2O_3), although it is possible that they could also arise from magnetite (Fe_3O_4). The same peaks were also present in Sample 5, set 2, although somewhat weaker. However, these very minor contributions to the spectra were not apparent in

the spectra of the six fresh samples in set 1, reported previously. Results of the Mossbauer analyses are summarized in Table 2.

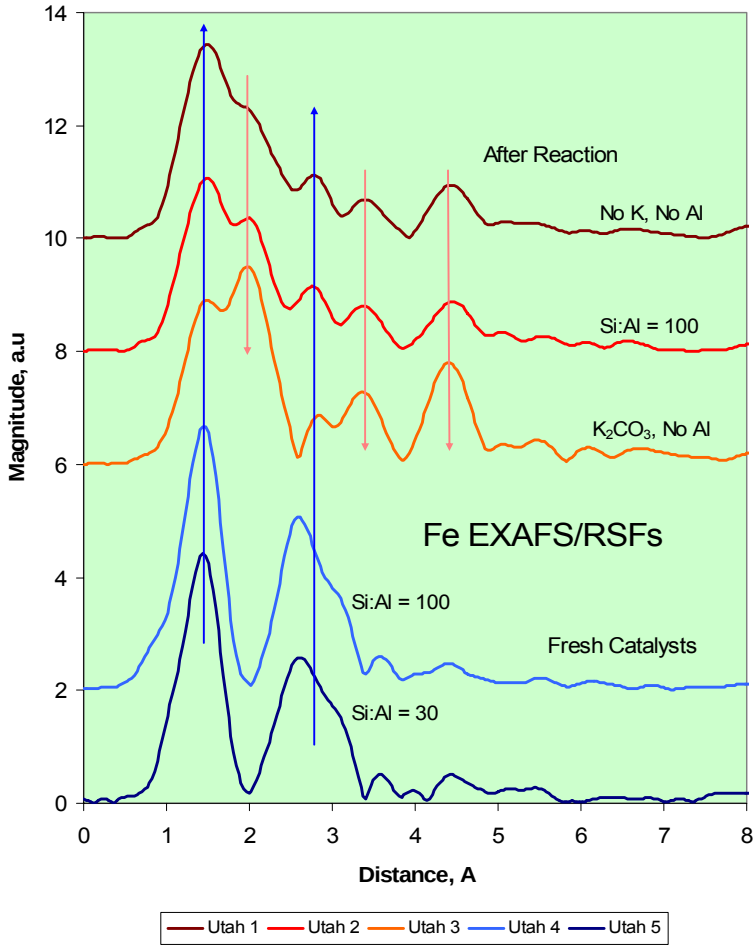

Figure 3: EXAFS/RSFs of the five Set 2 catalyst samples

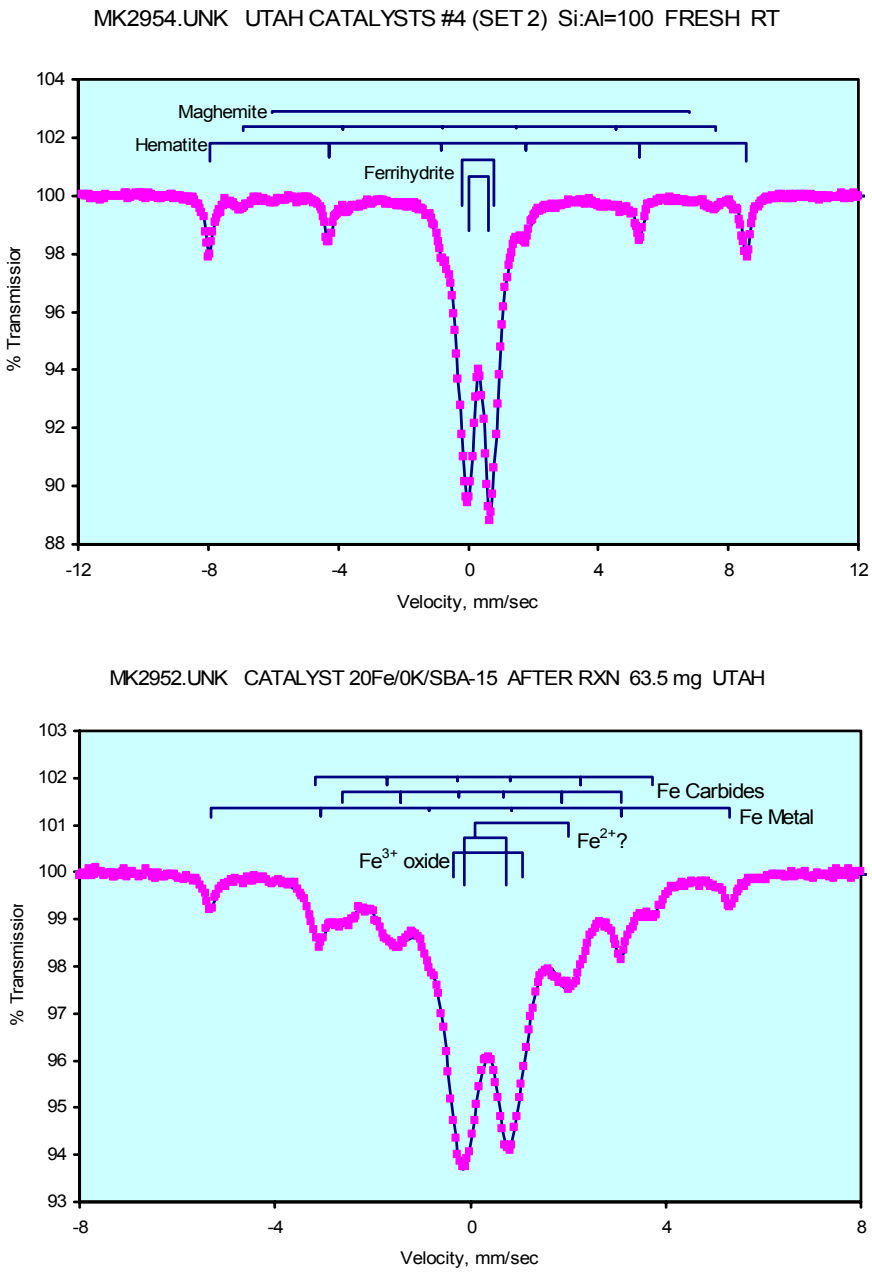

Figures 4 and 5: Mössbauer spectra of samples #4 (top) and #1 (bottom) from Set 2. Note the difference in scale on the abscissas of the plots.

Table 2: Tabulation of Results from Mössbauer Experiments on Sets 2 and 3 catalysts

Sample ID	*Comp*	*IS*	*QS*	*H0*	*Width*	*%Fe*	*I.D.*
Catalyst #1, SET 2	1 QS	0.32	0.86		0.62	17.5	Fe^{3+}
20Fe/100 SBA-15	2 QS	0.35	1.41		0.62	36	Fe^{3+}
No K	3 QS	1.05	1.92		0.62	10	Fe^{2+}
After RXN	1 H0	0.01		329.5	0.28	7	Fe metal

	2 H0	0.22		177	0.71	20.5	Fe carbide
	3 H0	0.28		213.5	0.41	9	Fe carbide
Catalyst #2, SET 2	1 QS	0.33	0.66		0.36	6.5	Fe^{3+}
20Fe/Al-SBA-15	2 QS	0.35	1.16		0.85	42.5	Fe^{3+}
No K, Si:Al=100	3 QS	1.11	1.68		0.5	7	Fe^{2+}
After RXN	1 H0	0		330	0.28	4	Fe metal
	2 H0	0.22		179	0.63	28	Fe carbide
	3 H0	0.29		216	0.41	12.5	Fe carbide
Catalyst #3, SET 2	1 QS	0.33	0.97		0.78	36	Fe^{3+}
20Fe/K_2CO_3/SBA-15	2 QS	0.75	1.73		1.19	11	Fe^{3+}?
After RXN	3 QS	0.17	3.81		0.31	2.5	Fe carbide?
	1 H0	0		329.5	0.28	14	Fe metal
	2 H0	0.24	0.02	177	0.63	15	Fe carbide
	3 H0	0.27		211	0.41	22	Fe carbide
Catalyst #4, SET 2	1 QS	0.33	0.58		0.39	35.5	Ferrihydrite
20Fe/0K/Al-SBA-15	2 QS	0.31	0.97		0.51	39.5	Ferrihydrite
No K, Si:Al=100	1 H0	0.39	-0.09	512	0.29	16.5	Hematite
Fresh	2 H0	0.34		450	0.65	6.5	γ-Fe_2O_3/Fe_3O_4
	3 H0	0.39		397	0.41	2	γ-Fe_2O_3/Fe_3O_4
Catalyst #5, SET 2	1 QS	0.33	0.56		0.36	24.5	Ferrihydrite
20Fe/0K/Al-SBA-15	2 QS	0.32	0.93		0.52	47.5	Ferrihydrite
No K, Si:Al=30	1 H0	0.39	-0.1	511	0.3	19	Hematite
Fresh	2 H0	0.34		456	0.94	6.5	γ-Fe_2O_3/Fe_3O_4
	3 H0	0.44		400	0.44	2.5	γ-Fe_2O_3/Fe_3O_4
Catalyst #1 SET 3	1 QS	0.34	0.56		0.39	38	Ferrihydrite
20Fe/0K/Co-SBA-15	2 QS	0.32	0.91		0.39	31	Ferrihydrite
No K	3 QS	0.32	1.33		0.39	9.5	Ferrihydrite
	1 H0	0.4	-0.09	513	0.28	21.5	Hematite
Catalyst #2, SET 3	1 QS	0.34	0.59		0.44	46	Ferrihydrite
20Fe/0K/Mn-SBA-15	2 QS	0.32	1.01		0.51	40	Ferrihydrite
No K	1 H0	0.39	-0.09	513	0.31	13	Hematite
Catalyst #3 SET 3	1 QS	0.33	0.56		0.4	27	Ferrihydrite
20Fe/0K/Ni-SBA-15	2 QS	0.32	0.91		0.4	21.5	Ferrihydrite
No K	3 QS	0.33	1.35		0.4	6	Ferrihydrite
	1 H0	0.4	-0.09	513.5	0.27	41	Hematite
	2 H0	0.4	-0.06	499	0.27	4.5	Hematite

Both Mössbauer and Fe XAFS spectroscopies indicate that Fe/SBA-15 catalysts undergo significant reaction and modification when exposed to the Fischer-Tropsch reaction. The fresh catalysts start off as either 100% pure ferrihydrite or as mixtures of ferrihydrite and magnetic iron oxides (mostly hematite, with very minor amounts of maghemite or magnetite). As discussed previously, the ratio of ferrihydrite to magnetic iron oxides appears to depend on the K

and Al contents of the catalyst formulations. After exposure to the conditions of the FT reaction, the iron phases consist of metallic iron (Fe^0), iron carbides, and non-magnetic iron oxides. Mössbauer spectral data suggests that the iron carbides are a mixture of epsilon (ε) and chi (χ) carbides, rather than cementite, Fe_3C. These phases are frequently observed after iron-based catalysts have been used in FT reactions, regardless of how they have been made and their support material. The non-magnetic iron oxides probably derive from the ferrihydrite present in the original catalyst formulation; however, the Mössbauer parameters are significantly altered and it would not be correct to describe this component as ferrihydrite in the after-reaction samples. More correctly, they should be referred to as superparamagnetic (spm) iron oxides.

(ii) Spectroscopic characterization of Set 3 of Fe SBA Catalysts

The three as-prepared Fe/SBA-15 catalyst formulations in Set 3 (Table 1) have also been examined by iron Mossbauer and XAFS spectroscopies. The XAFS and Mossbauer spectra of these new formulations exhibited virtually identical spectra to those shown in Figures 1-3 and 4, respectively, for the as-prepared catalysts of Set 2, except that the minor maghemite or magnetite phases observed in the Mossbauer spectra of the as-prepared formulations in Set 2 were not observed for the Set 3 catalysts. In this last respect, the Mossbauer spectra of the Set 3 catalyst formulations are more closely similar to those of the Set 1 catalysts, reported previously, than to those of the Set 2 as-prepared catalysts. Hence, figures will not be shown for these catalysts; however, the data derived for these samples are included in the Tables and the correlations between the data from the two techniques.

(iii) Correlation between Mossbauer and XAFS determinations of iron phases in as-prepared SBA-15 Catalyst Formulations

An alternative method of quantifying the iron XANES spectra into %Fe as hematite (magnetic iron oxides) and %Fe as ferrihydrite was invoked for analysis of the as-prepared Fe-based SBA-15 catalysts. This method is based on least-squares fitting of the k^3(chi) spectral data for the fresh catalysts using spectra for hematite and ferrihydrite (sample 5, set 1). As can be seen from Figure 6, the k^3(chi) vs. k spectra for these two iron oxides are quite different and the least-squares analysis using this method is therefore reasonably robust.

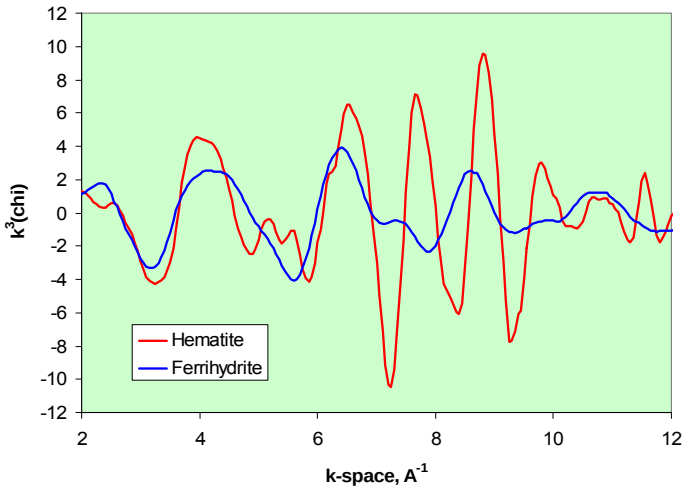

Figure 6: Comparison of the k^3(chi) EXAFS spectra for hematite and ferrihydrite (sample 5, Set 1). Note the significant differences between the two spectra.

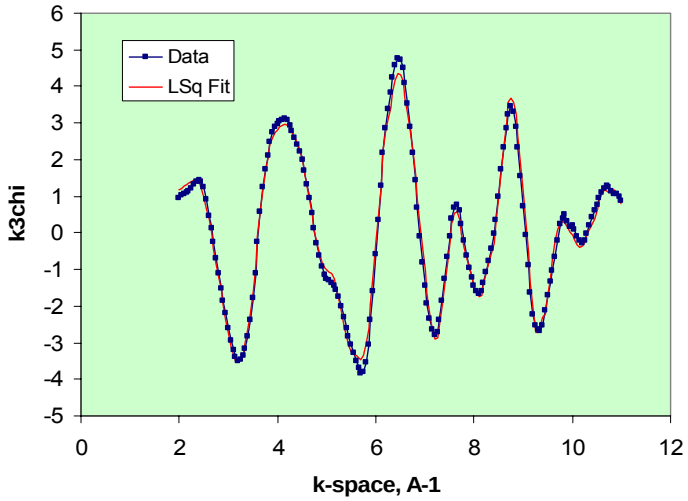

Figure 7: Example of least-squares fitting of the iron k^3(chi) vs. k EXAFS spectrum for sample 6, Set 1, based on linear combination of the corresponding spectra for hematite and ferrihydrite (sample 5, Set 1) shown in Figure 6.

Figure 7 is an example of a k^3(chi) vs. k spectrum least-squares fitted as a weighted combination of the spectra for hematite and ferrihydrite shown in Figure 6. The spectra of the fresh catalysts are fit surprisingly well by this method, which implies that the structural integrity of the individual end-member components is maintained in such mixtures of the two phases. Results based on this method are summarized in Table 3 for fresh samples from all three sample Sets. The results of least-squares fitting of the iron EXAFS data are also compared to similar estimates based on analysis of Mössbauer spectra. The agreement is satisfactory, within experimental errors of ±5% in most instances (Figure 8), and a linear correlation exists between the sets of data, with a correlation coefficient of 0.97. Furthermore, it should be noted that at least one possible minor source of bias has been ignored in the analysis of the Mössbauer data (variation in the recoil-free fraction for the two iron-bearing phases).

Table 3: Comparison of results from least-squares fitting of k^3(chi) vs. k EXAFS spectra with data from Mössbauer spectra for as prepared Fe-based/SBA-15 catalysts.

Sample	EXAFS %Fhyd	EXAFS % Hem	Eshift eV	Red. χ^2	MOSS %Fhyd	MOSS %Hem
Set 1						
1	63	37	0.07	0.067	63	37
2	52	48	-0.01	0.13	46	54
3	90	10	0.07	0.134	96	4
4	97	3	0.03	0.038	100	0
5	100	0	---	---	100	0
6	76	24	0.08	0.043	71	29
Set 2						
4	76	24	0.07	0.148	72	28
5	79	21	0.08	0.213	75	25

Set 3						
1 (Co)	83	17	-0.02	0.197	79	21
2 (Mn)	86	14	0.1	0.178	87	13
3 (Ni)	62	38	0	0.168	55	45

Eshift is the amount of shift in eV that was applied to align the data and fit in the EXAFS fitting. As can be seen in all cases it is less than ±0.1 eV. Red χ^2 is a statistical goodness of fit parameter.

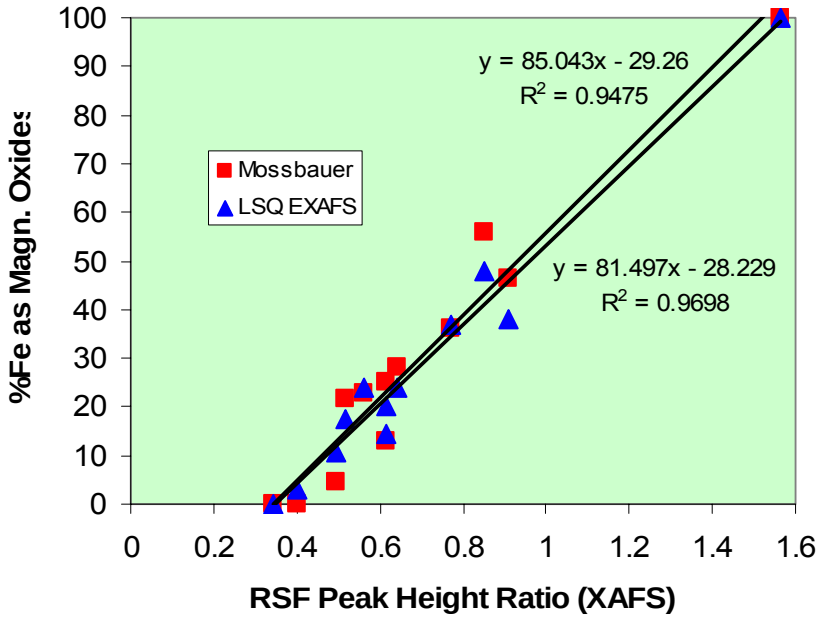

Figure 8: Correlation between Mössbauer, Fe EXAFS least squares fitting, and RSF peak-height ratio data for the phase constitution of all 11 as-prepared Fe/SBA-15 catalysts.

(b) Mössbauer, XAFS and TEM Analysis of Fe-Mo catalysts (in cooperation with Dadyburjor and Ma, West Virginia University)

Mössbauer spectra of the six samples of Fe-Mo catalysts are shown in Figure 9. The spectra vary significantly from sample to sample, although samples 2 and 4 appear very similar to each other, as do samples 1, 3, and 6. Samples 2 and 4 do not contain any magnetic phases, whereas the other four spectra contain a significant fraction of iron in magnetic form. The various components contributing to the spectra are indicated by the 2-line and 6-line diagrams above the spectral data. The magnetic six-line patterns arise from χ and έ Fe-carbides, while the central doublet arises from iron oxides. Note that the spectrum of sample 2 is shown at a reduced velocity setting compared to the other spectra. It and the closely similar spectra for sample 4 arise entirely from iron present as ferrihydrite. The results of the data analysis by least-squares fitting for various Mössbauer parameters are summarized in Table 4.

The data show that the outermost magnetic component has I.S. values between 0.24 – 0.27 mm/s and H_0 values between 213 – 216 kGauss for the four samples that exhibit magnetic components. Such variation is relatively small and not much greater than experimental errors. Although there is reasonable agreement for samples 1 and 3 for the other two inner magnetic components, the same components in samples 5 and 6 show rather more variation, particularly in

the hyperfine magnetic splitting parameter. Based on published data for iron carbides [4-6], the magnetic components appear to arise from χ-carbide and έ-carbide. Furthermore, an additional component with a large quadrupole splitting has been added to make these fits more statistically robust. It would appear that there is some superparamagnetic (spm) behavior in the carbides in these two samples. Again, similar behavior has been reported previously for iron-based catalysts used in the commercial manufacture of acetonitrile [4] and for Fischer-Tropsch catalysts [5,6]. Samples 2 and 4 do not exhibit any magnetic components; all of the iron in these samples appears to be present as iron oxides, in particular, as ferrihydrite, a small particle iron oxyhydroxide. Mössbauer spectra of similar phases have been described in the literature [7-9], including a Mo-substituted ferrihydrite in which the Mo was located at the particles' surfaces as the molybdate anion (MoO_4^{2-}) [10].

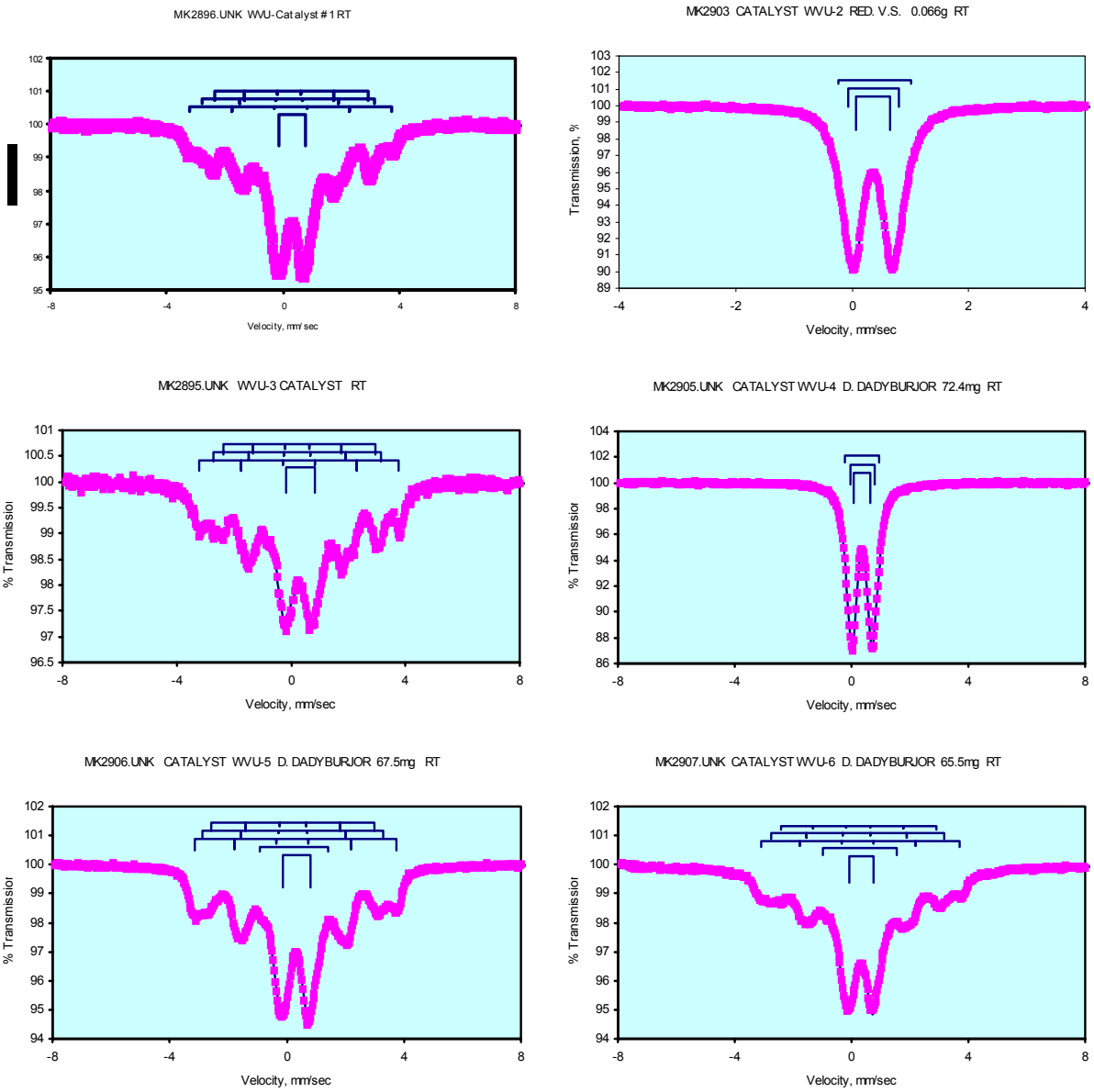

Fgure 1: Mössbauer spectra of the six Fe-Mo catalyst samples received from Dr. Dadyburjor.

Table 4: Results of Mössbauer Least-squares Fitting of Fe-Mo Catalyst Samples

Sample	Comp.[1]	I.S.	Q.S.	H_0	Width	%Fe	I.D.
		mm/s	mm/s	kGauss	mm/s		
MK2896	1 QS	0.33	0.92		0.81	56	Fe^{3+} Oxide
WVU-1	1 H0	0.26	0	215	0.49	13	χ-carbide
	2 H0	0.22	-0.01	183	0.51	14	χ-carbide
	3 H0	0.25	0.04	165	0.36	17	ε, χ-carbide
MK2903	1 QS	0.36	0.59		0.33	60	Ferrihydrite
WVU-2	2 QS	0.36	0.87		0.33	33	Ferrihydrite
	3 QS	0.38	1.25		0.33	7	Ferrihydrite
MK2895	1 QS	0.34	0.99		1.05	49	Fe^{3+} Oxide
WVU-3	1 H0	0.27	0	216	0.5	23	χ-carbide
	2 H0	0.21	0	182	0.37	14	χ-carbide
	3 H0	0.25	0.04	165	0.36	14	ε, χ-carbide
MK2905	1 QS	0.36	0.59		0.33	55	Ferrihydrite
WVU-4	2 QS	0.37	0.83		0.33	35	Ferrihydrite
	3 QS	0.37	1.16		0.33	10	Ferrihydrite
MK2906	1 QS	0.34	0.94		0.69	45	Fe^{3+} Oxide
WVU-5	2 QS	0.25	2.35		0.69	6	spm carbide?
	1 H0	0.24	0.04	213	0.45	22	χ-carbide
	2 H0	0.22	0	191	0.36	11	χ-carbide
	3 H0	0.22	0.01	173	0.42	16	ε, χ-carbide
MK2907	1 QS	0.32	0.88		0.70	52	Fe^{3+} Oxide
WVU-6	2 QS	0.15	3.16		0.70	8	spm carbide?
	1 H0	0.25	0.06	213	0.40	10	χ-carbide
	2 H0	0.25	0	174	0.83	30	ε, χ-carbide

[1]*Quadrupole components are indicated as QS; magnetic components as H0.*

Mo K-edge XAFS spectra were recorded and divided into separate XANES and EXAFS regions. The XANES region spectral data are shown in Figure 10. They consist of an abrupt edge that reflects the Mo 1s (K-edge) absorption process to the continuum upon which various peaks are superimposed that arise from electronic and other transitions within individual Mo atoms. The most obvious feature is the relatively sharp inflection point that occurs about half-way up the absorption edge; it is most prominent for samples 2 and 4, but is present, albeit somewhat less obviously, in all other samples as well. This feature is characteristic of the Mo(VI) oxidation state, especially the molybdate anion species, MoO_4^{2-}. Other peaks occur on

top of the absorption edge; as shown in Figures 11 and 12, there are a minimum of three peaks that contribute to the edge structure, up to about 70 eV above the absorption edge.

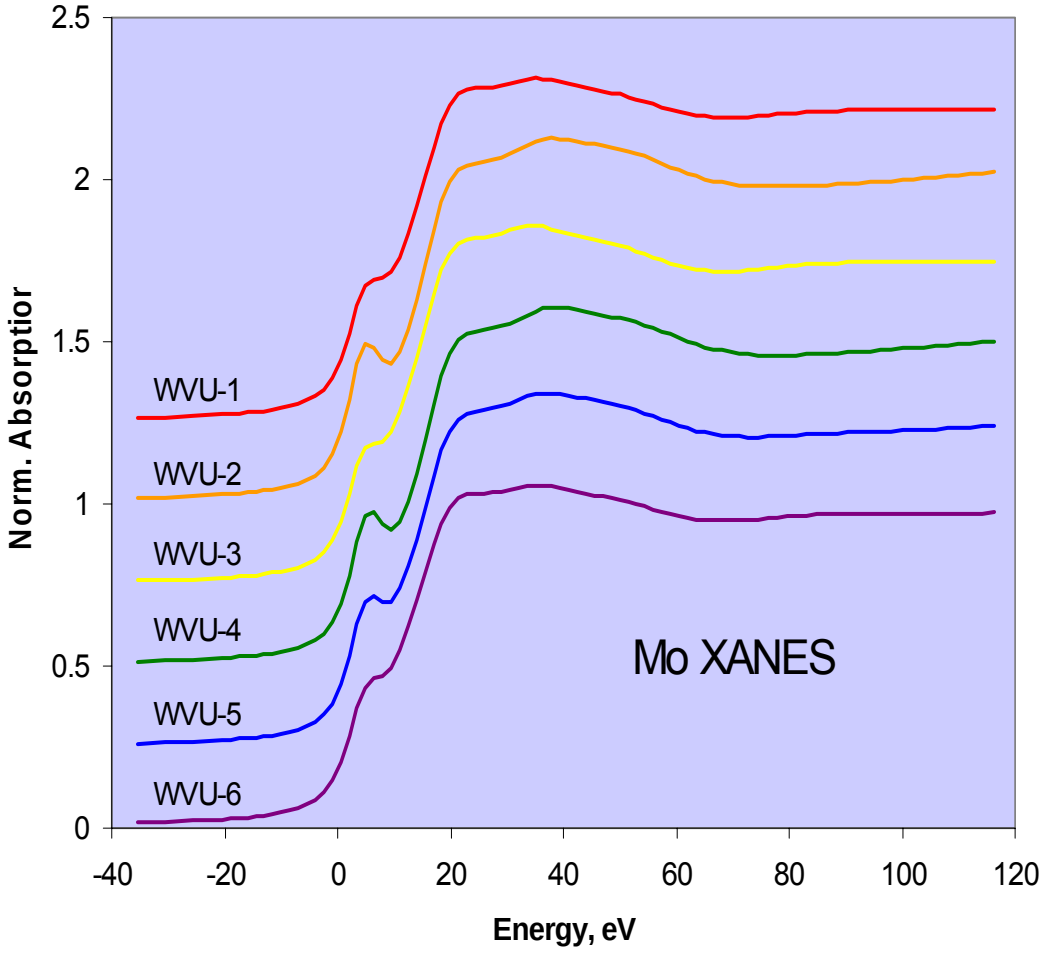

Figure 10: Mo XANES spectra of the six Fe-Mo catalysts from WVU.

There are systematic changes that occur with the 4 individual peaks upon comparing the XANES spectra. These are best demonstrated and quantified by least-squares fitting of the XANES spectra, according to the fitting model shown in Figures 11 and 12, and detailing the variation of the parameters derived from the least-squares analysis. These data are summarized in Table 5 and will be discussed in the subsequent section of this report.

Attempts were made to analyze the EXAFS/RSF region as well; but to date these have not been too successful. It is not clear why the EXAFS region is so recalcitrant in releasing information for the k^3(chi) spectra did not appear overly complex. Most RSF showed a phase-shift uncorrected peak at about 1.35 – 1.40 A; such a peak is consistent with the Mo-O bonds in molybdate anions. However, there were a number of large apparently spurious peaks in the RSF spectra making more detailed analysis impossible.

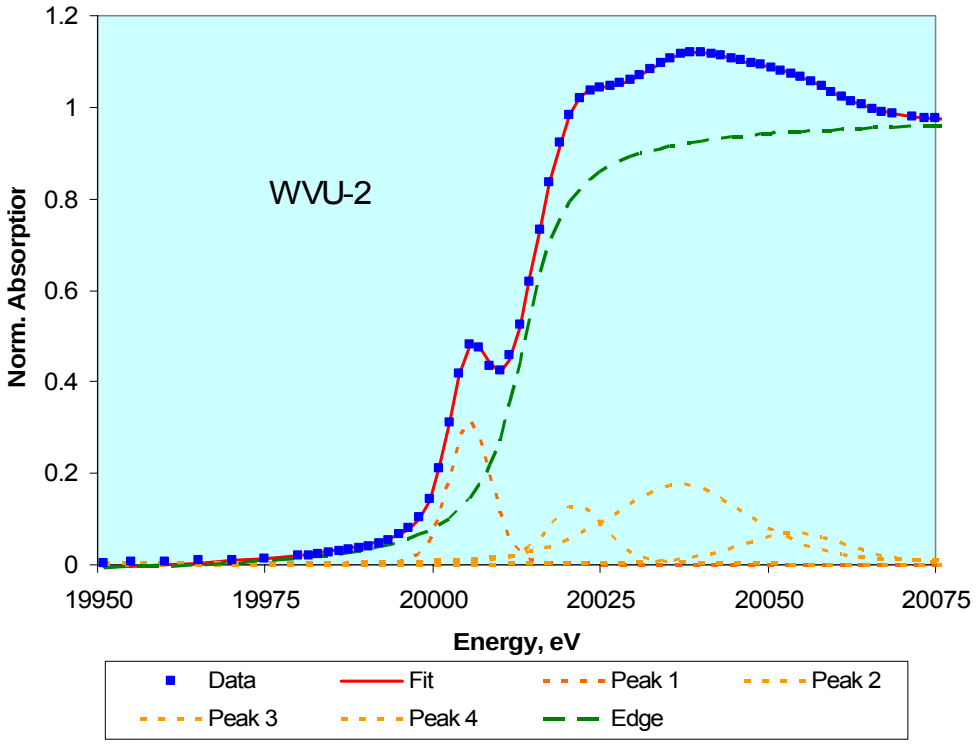

Figure 11: Least-squares fitted Mo XANES spectrum of catalyst sample WVU-2.

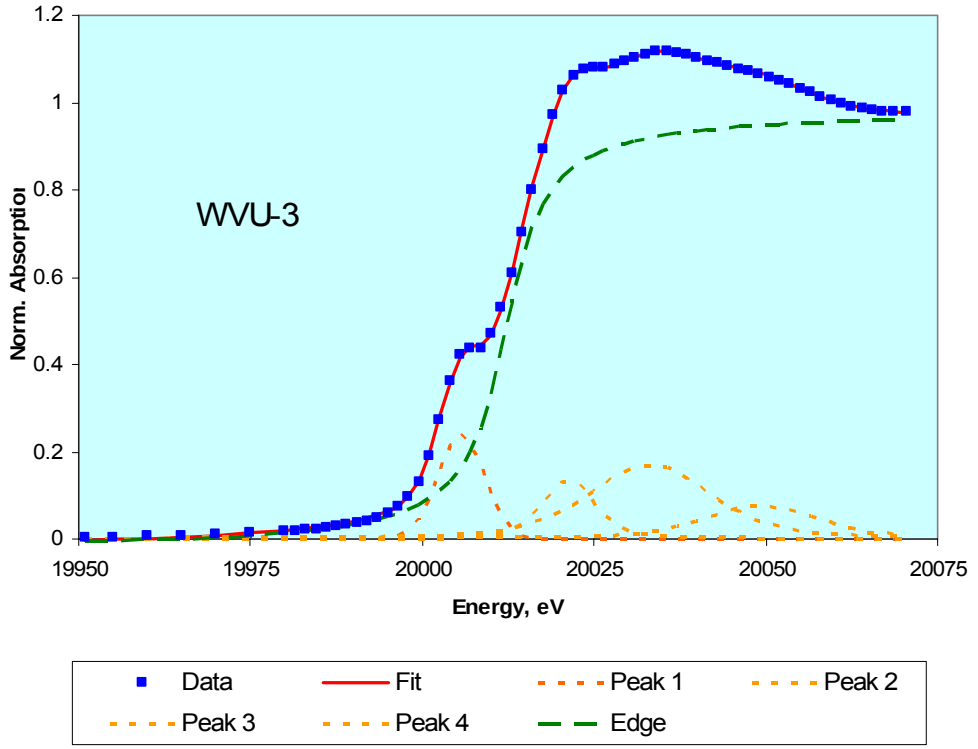

Figure 12: Least-squares fitted Mo XANES spectrum of catalyst sample WVU-3.

Table 5: Results from Least-Squares Analysis of Mo XANES of 6 samples from Dr. Dadyburjor

	MOCAT.157A WVU-1	*MOCAT.160A WVU-2*	*MOCAT.163A WVU-3*	*MOCAT.166A WVU-4*	*MOCAT.169A WVU-5*	*MOCAT.172A WVU-6*
Total Area	65.76	73.94	65.63	73.57	70.32	64.6
1. Height	0.265	0.315	0.239	0.307	0.282	0.26
1. Position	6.05	5.54	5.67	5.92	5.9	5.8
1. Width	8.5	7.34	7.91	7.37	7.77	8.37
1. Area	2.42	2.61	2.01	2.54	2.345	2.32
2. Height	0.127	0.131	0.133	0.135	0.115	0.132
2. Position	21.4	21.4	21.4	21.8	21.6	21.3
2. Width	9.94	9.94	9.06	10.1	9.13	9.7
2. Area	1.6	1.66	1.545	1.74	1.34	1.625
3. Height	0.147	0.176	0.17	0.179	0.1655	0.159
3. Position	34.1	36.9	33.1	37.16	34.9	33.6
3. Width	22.8	24.6	20.8	24.2	24.3	22.15
3. Area	4.06	5.23	4.315	5.235	4.865	4.26
4. Height	0.05	0.071	0.076	0.072	0.069	0.062
4. Position	50.8	53.7	49.2	54.2	51.4	50.4
4. Width	18.3	19.1	20.1	19.35	19.8	19.6
4. Area	1.08	1.625	1.8	1.66	1.63	1.422
Edge Height	1.02	1.015	1.013	1.013	1.019	1.016
Edge Position	12.18	13.5	12.1	13.8	12.9	12.3
Edge Width	13.5	15	13.6	14.9	14.45	13.53
Edge Area	59.7	66.8	59.34	66.4	63.89	58.13
% Area Peak 1	3.7	3.5	3.1	3.5	3.3	3.6
% Area Peak 2	2.4	2.2	2.4	2.4	1.9	2.5
% Area Peak 3	6.2	7.1	6.6	7.1	6.9	6.6
% Area Peak 4	1.6	2.2	2.7	2.3	2.3	2.2
% Area Edge	86.1	85.0	85.3	84.8	85.5	85.1

N.B. All positions are given relative to the zero-point of energy at 20,000 eV.

A brief TEM investigation was conducted on samples WVU-1 and WVU-2 as these two samples appeared to differ the most according to the spectroscopic data. Some observations made with the TEM, based on the micrographs and the EDS and EELS spectra shown in Figures 13-18, are described.

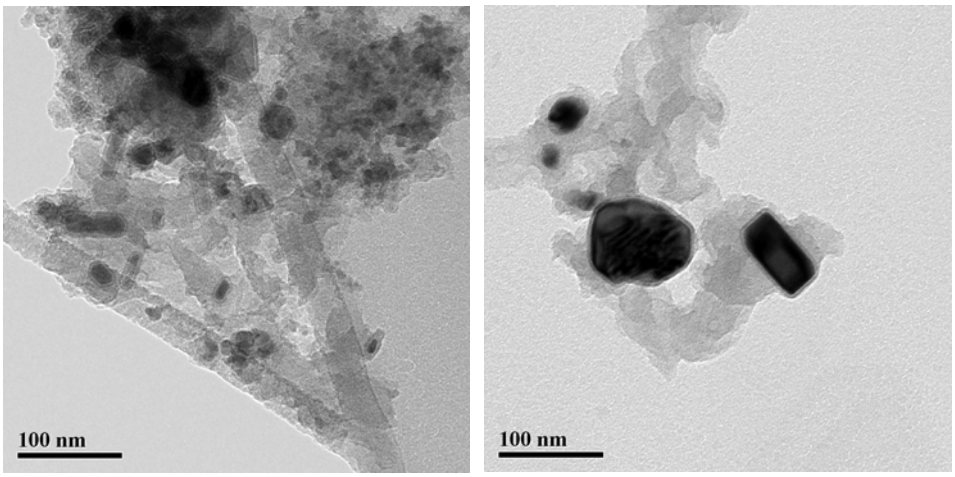

Figure 13: TEM micrograph of WVU-1 catalyst particles.

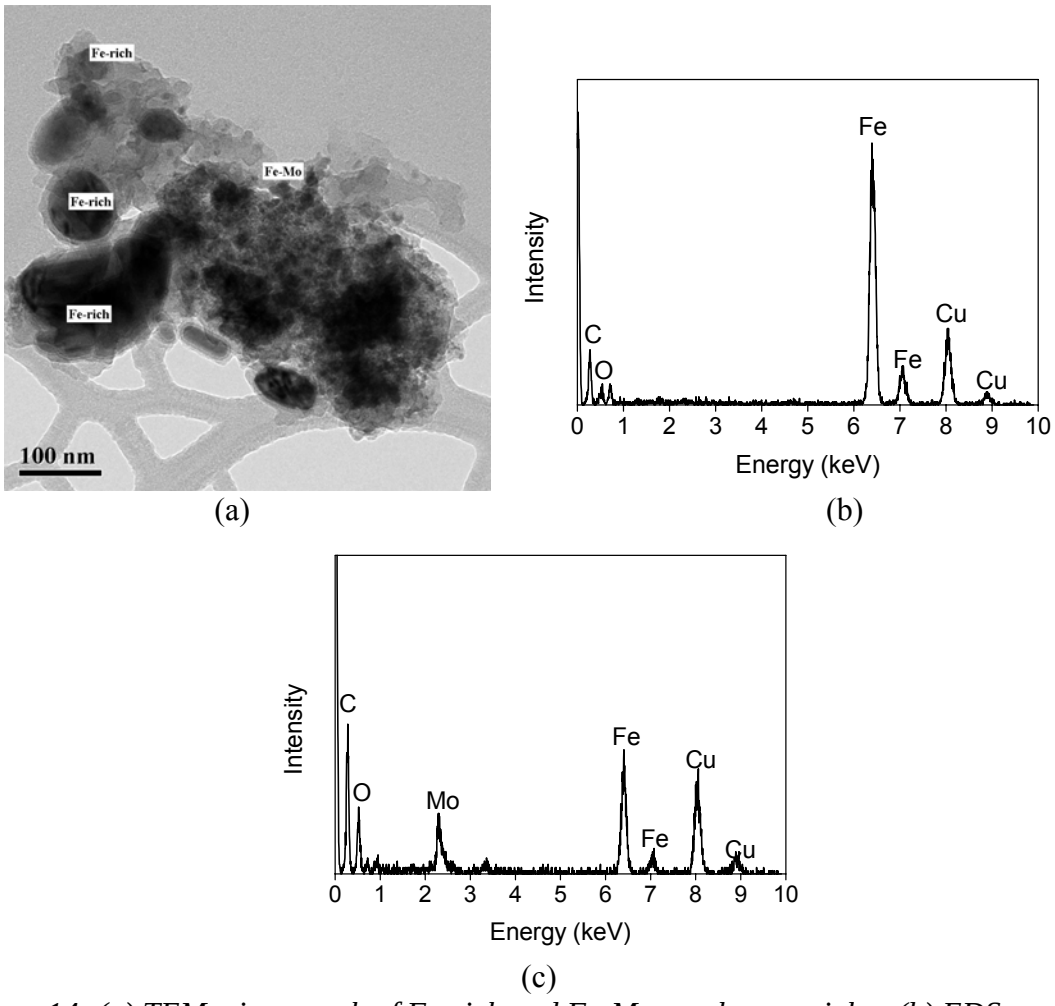

Figure 14: (a) TEM micrograph of Fe-rich and Fe-Mo catalyst particles. (b) EDS spectrum recorded from the Fe-rich particles. (c) EDS spectrum recorded from the Fe-Mo particles. Cu peaks are from TEM grids.

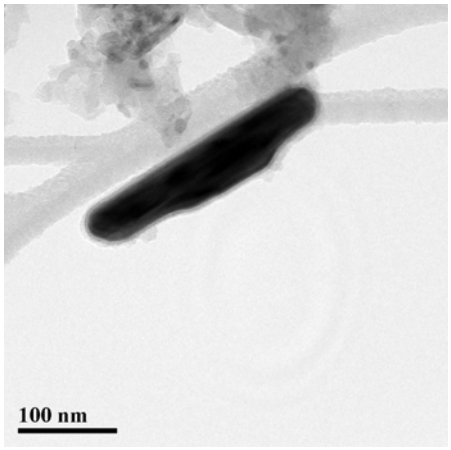

(a)

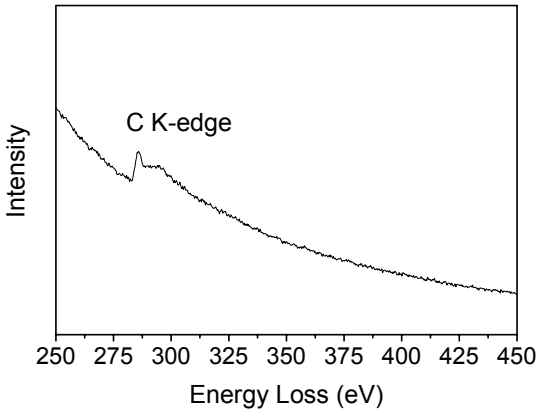

(b)

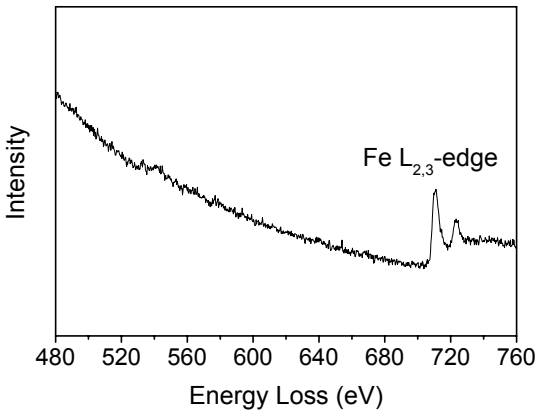

(c)

Figure 15: TEM micrograph (a), carbon K-edge (b) and iron L-edge EELS spectrum (c) of a rod-like iron carbide particle.

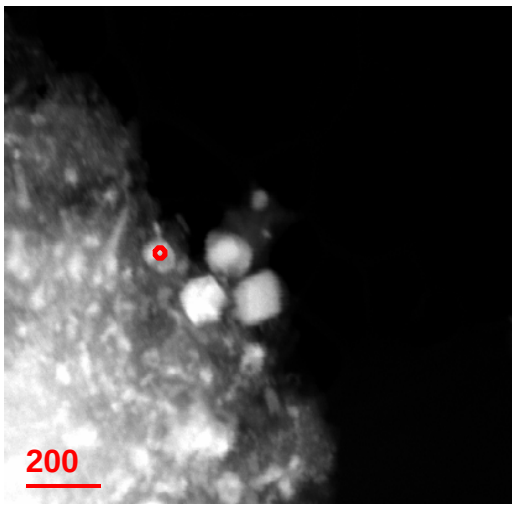

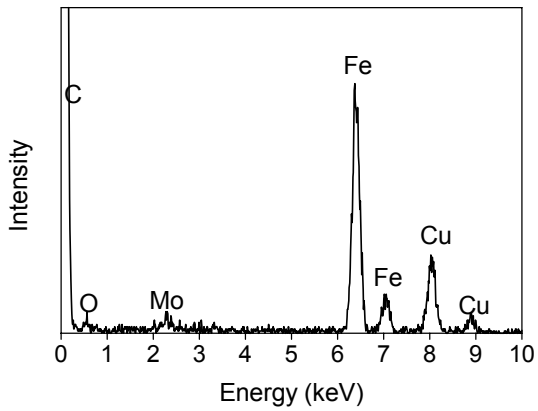

Figure 16, left: HAADF (high-angle annular dark-field) image of several Fe-Mo catalyst particles; right: EDS spectrum recorded from the particle indicated by the red spot. Cu peaks are from TEM grids.

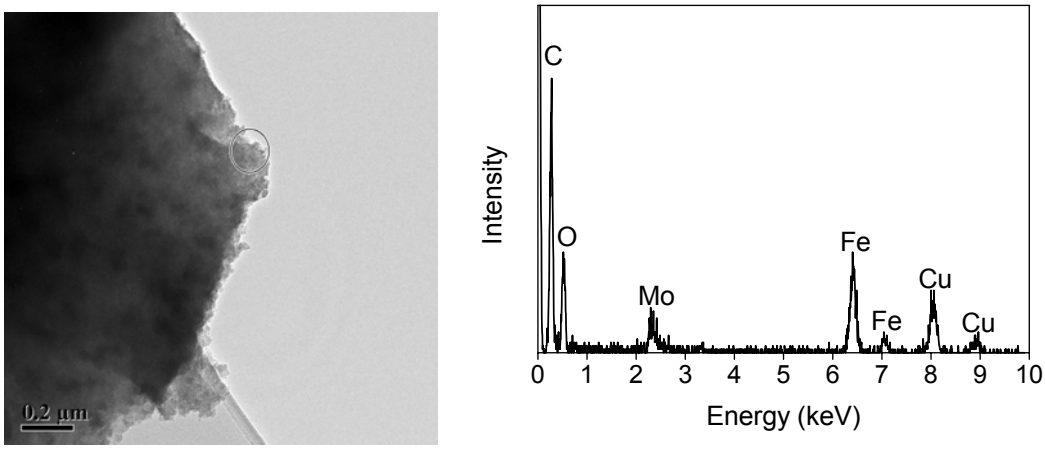

Figure 17. Sample WVU-2: left: TEM micrograph of a large carbonaceous particle; right: EDS spectrum recorded from the circled region shown in left image shows C, Fe, Mo and O peaks. Cu peaks are from TEM grids.

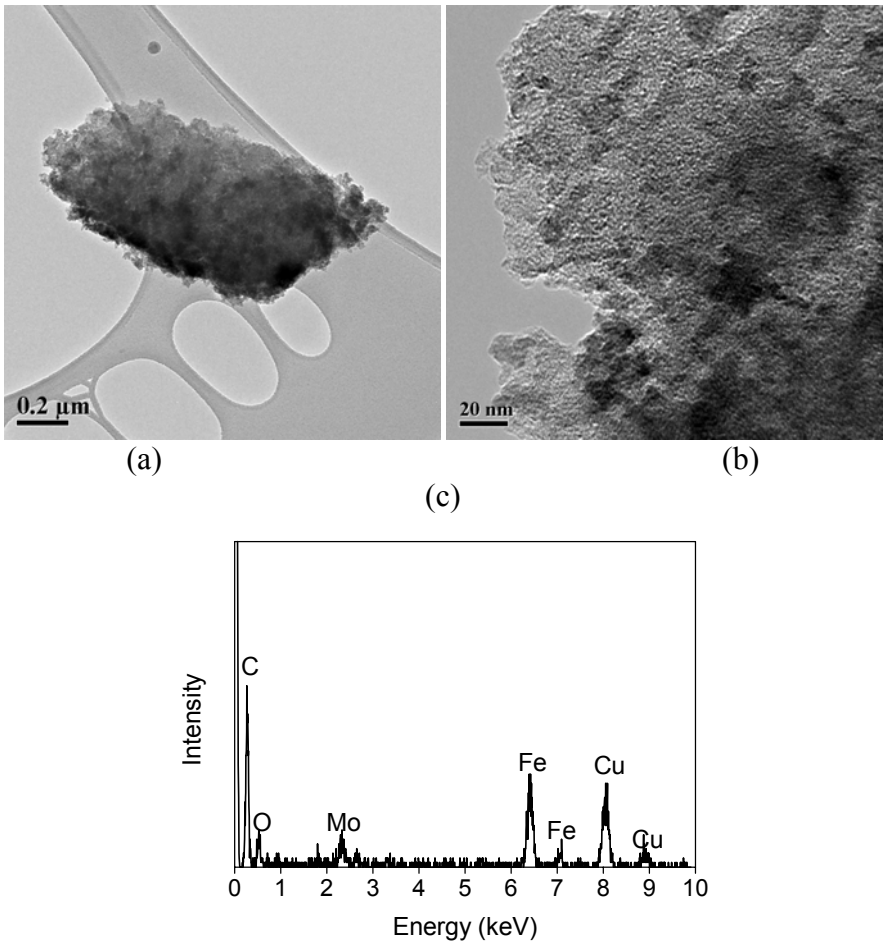

Figure 18: (a) low-mag. TEM micrograph, (b) higher-mag. TEM micrograph, and (c) EDS spectrum of a carbonaceous particle. Fe and Mo signals can be detected from the carbonaceous matrix. However, it seems that separate catalyst particles haven't fully developed.

The catalyst particles in sample WVU1 have typical sizes varying from 15-150 nm. Iron tends to exist in the form of separate crystals with larger sizes, while Mo tends to exist in the form of smaller aggregated particles. Both Fe-rich and Fe-Mo mixed catalyst particles have been observed. Many of the catalyst particles seem to be in the form of carbides.

The catalyst particles in sample WVU2 seem not to be very well developed. Carbonaceous supports have been observed that contain both Fe and Mo (probably in the form of salt?).

The Mo-Fe catalyst samples divide clearly into two distinct sets of samples: set 1, consisting of WVU-2 and WVU-4, and set 2 consisting of WVU-1, WVU-3, WVU-5 and WVU-6. As indicated by the Mössbauer data, Figure 19, the former set of samples do not contain any iron carbides, whereas the latter set of 4 samples contain significant iron carbide.

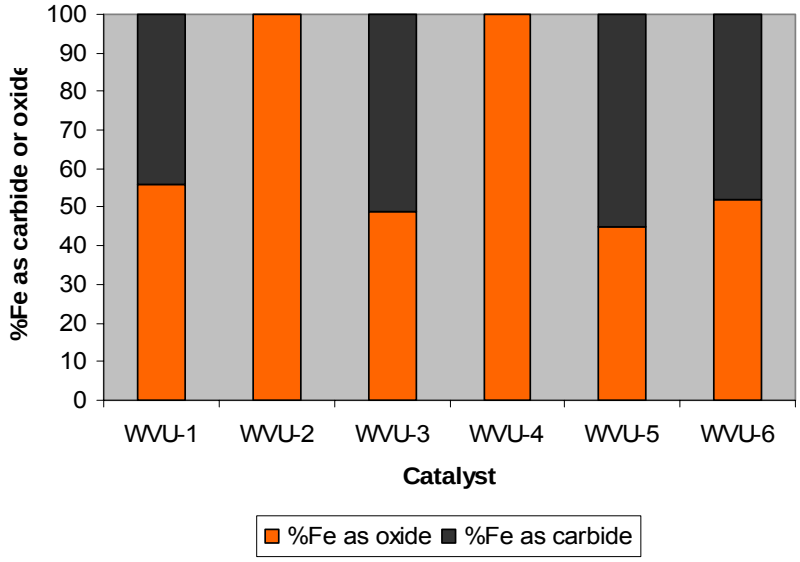

Figure 19: Histogram showing the distribution of Fe between oxide and carbide forms for the six samples, as obtained from the Mössbauer data.

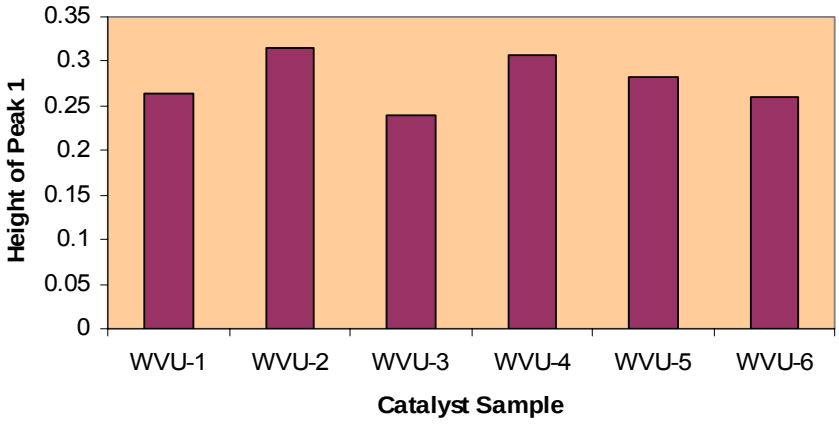

Figure 20: Histogram of the height of peak 1 for the six catalyst samples normalized to the edge step, as obtained from the Mo XAFS data.

A similar separation is also apparent in the Mo XAFS data. Figure 12 shows the height of the inflection peak (peak 1) relative to the edge step. Samples 2 and 4 have significantly more height (and resolution – q.v. Figure 4) for Peak 1 than the other four samples. A very similar separation can also be seen in Figure 13, which shows the variation among the six catalyst samples in the positions of the four least-squares fitted peaks. Data for peaks 2 and 4 occur at distinctly higher energy than for the other four samples. Sample 5 appears transitional on the basis of the Mo XAFS data.

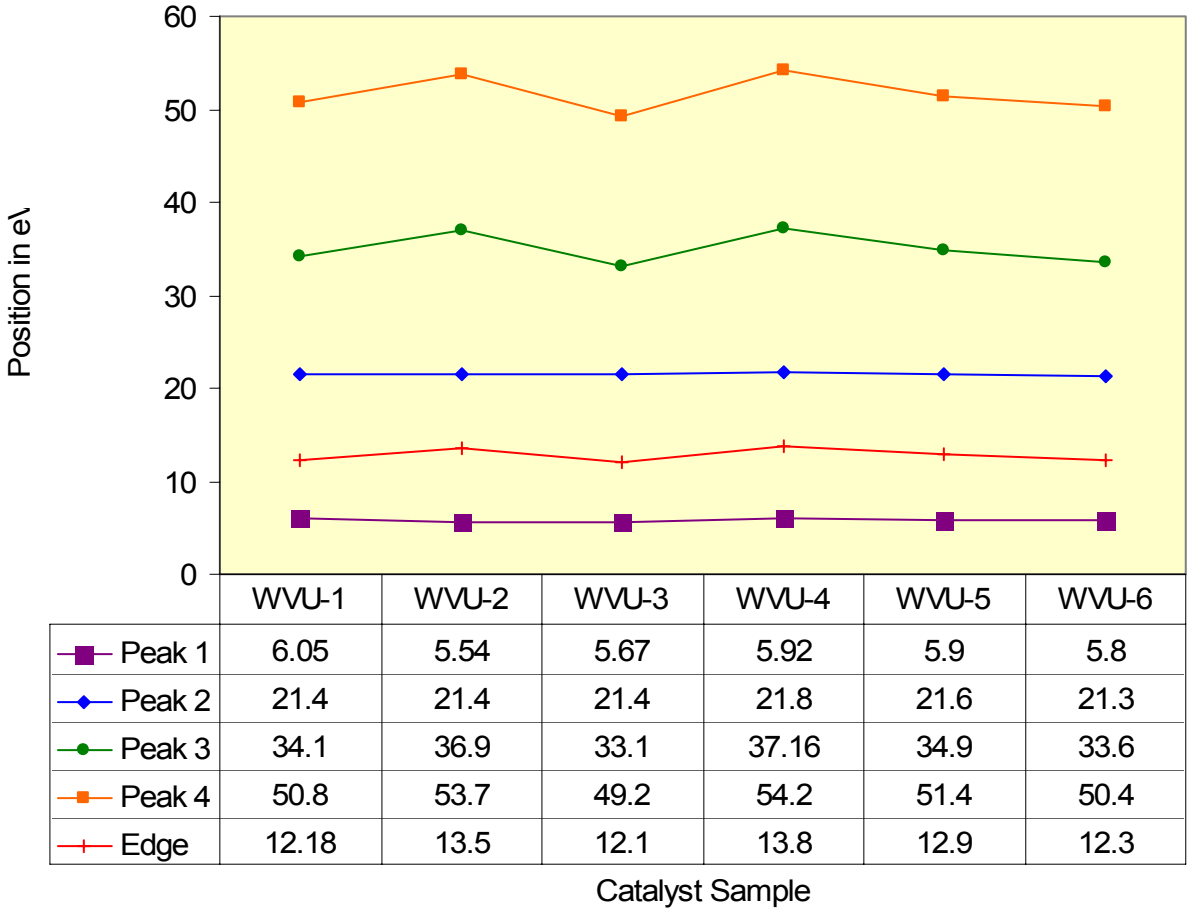

Figure 21: Variation of peak position in eV, relative to the Mo K-edge at 20,000 eV, of the four least-squares fitted peaks (q.v. Figures 3 and 4) in the Mo XANES region. Note that the peak positions of Peaks 3 and 4 and the edge are shifted to higher energy compared to the positions of the same peak for the other four samples. As before, data for sample WVU-5 appears to be transitional.

Both the Mössbauer and XAFS data indicate that samples WVU-2 and WVU-4 are significantly different to the other four samples. The data for the K edge position and for peaks in the Mo XANES spectra suggest that the Mo oxidation state is, on average, higher (principally as Mo(VI) in molybdate) in WVU-2 and WVU-4 than in the other four samples, which appear to be a mixture of Mo(VI) and Mo(IV). Similarly, the Mössbauer data indicate that the iron oxidation state is entirely Fe^{3+} for samples WVU-2 and WVU-4, but a mixture of Fe^{3+} (in oxide

forms) and Fe^0 (in carbide forms) for the other four samples. Hence, we conclude that samples WVU-2 and WVU-4 represent largely unreacted catalyst materials, in which the formal oxidation states of Fe and Mo are +3 and +6, respectively. The other four samples represent samples that have been exposed to the WGS reaction and have been partially converted to mixtures of iron and molybdenum carbides. The question of whether the Mo and Fe are present in the same carbide or oxide phase or form distinct carbide and oxide phases is less clear. The preliminary TEM study was inconclusive; Mo-free Fe-rich particles, Fe-free Mo particles, and some Fe-Mo mixed particles were observed. Similarly, the Mössbauer parameters for the ferrihydrite phase in samples WVU-2 and WVU-4 appear quite similar to those in 100% Fe systems, as do the Mössbauer parametric data for the carbides in the other four samples. However, the oxide phase has clearly changed between the two sets of samples; the simple apparent 2-peak spectrum in samples WVU-2 and WVU-4 has clearly given way to something more complex with significantly different Mössbauer parameters (slightly lower isomer shift and larger average quadrupole splitting) suggesting that the ferrihydrite phase may be undergoing a transformation to superparamagnetic iron oxides before being reduced to carbide.

IV Conclusions

Mössbauer and XAFS spectroscopic methods have been successfully used to characterize key elements present in various catalyst formulations under development by Consortium researchers for use in C1 or hydrogen-related reactions.

Fourteen iron containing silica-based aerogel (SBA) catalyst samples prepared by Kim and Eyring at the University of Utah for possible use in F-T synthesis have been examined by iron XAFS and Mössbauer spectroscopies over the last two years. The iron in the as-prepared catalyst samples was found to be present as a mixture of hematite and ferrihydrite. In the previous year, it was established that the ratio of these two phases varies systematically with the potassium content and the nature of the support in the formulations of the catalysts. This year, additional as-prepared Fe/SBA-15 catalysts and related catalyst materials after reaction have been examined by the same methods. Various methods of estimating the ratio of Fe as hematite to Fe as ferrihydrite in the as-prepared catalysts have been tested and good agreement was found among the different methods. These Fe/SBA-15 catalysts consist basically of a mixture of iron carbides and oxides after reaction.

Six Fe-Mo catalysts supported on activated carbons prepared from biomaterials by Ma and Dadyburjor at West Virginia University were also examined by iron Mossbauer and Mo XAFS spectroscopies. The two as-prepared samples consisted of 100% ferrihydrite; after exposure to F-T reaction conditions for up to 300 hours, the ferrihydrite had converted into a mixture of iron carbides and superparamagnetic iron oxides. At the same time, the Mo present initially as Mo(VI) in molybdate anions (MoO_4^{2-}) had become reduced somewhat.

V. Papers presented or published (include submitted and in-press papers)

Papers on both types of catalyst are in preparation.

VI. Future Work

Additional work is planned for both types of catalyst in 2005-2006 to complete the studies. For the Fe/SBA-15 catalysts, a low-temperature Mossbauer study will be conducted to determine magnetic transitions in the iron phases. If the ferrihydrite phase behaves superparamagnetically, it should be possible to derive a size distribution for this phase. Additional samples of the Fe-Mo activated carbon catalysts have already been received and have been analyzed by both Mo XAFS and Fe Mossbauer spectroscopies. These samples consist of similar catalyst formulations but have only been exposed to reaction conditions for a short time (90 mins). The goal is to provide an indication of the rapidity of the conversion of the ferrihydrite to magnetic oxide and carbide phases.

In the coming year, similar XAFS characterization work will be extended to new catalyst systems as they are developed within the Consortium. Already, we have received several novel noble metal (Pt, Pd) promoted, Ce-doped aerogel catalyst systems that are being prepared at the University of Utah under the direction of Prof. Ernst.

References:

[1] G.E. Brown, Jr., G. Calas, G.A. Waychunas and J. Petiau, in: F.C. Hawthorne (Ed.), **Spectroscopic Methods in Mineralogy and Geology**; Rev. in Mineral. Vol. 18, Mineralogical Society of America, Washington, DC, 1988, Chapter 11, pp. 431-512.

[2] P.A. Lee, P.H. Citrin, P. Eisenberger and B.M. Kincaid, **Rev. Mod. Phys**. 53 (1981) 769-808.

[3] D.C. Koningsberger and R. Prins, **X-ray Absorption. Principles, Applications, Techniques of EXAFS, SEXAFS, and XANES**, J. Wiley & Sons, New York, 1988.

[4] M.V. Badani and W.N. Delgass, *The active phase of iron catalysts for acetonitrile synthesis.* **J. Catalysis** 187 (1999) 506-517.

[5] K.R.P.M. Rao, F.E. Huggins, G.P. Huffman, R.J. Gromley, R.J. O'Brien, and B.H. Davis, *Mössbauer study of iron Fischer-Tropsch catalysts during activation and synthesis.* **Energy & Fuels** 10 (1996) 546-551.

[6] K.R.P.M. Rao, F.E. Huggins, V. Mahajan, G.P. Huffman, V.U.S. Rao, B.L. Bhatt, D.B. Bukur, B.H. Davis, and R.J. O'Brien, *Mössbauer spectroscopy study of iron-based catalysts used in Fischer-Tropsch synthesis.* **Topics in Catalysis**, 2 (1995) 71-78.

[7] U. Schwertmann and U. Cornell, **Iron oxides in the laboratory.** VCH, Weinham, Germany, 1991.

[8] E. Murad, and U. Schwertmann, *The Moessbauer spectrum of ferrihydrite and its relations to those of other iron oxides.* **American Mineralogist***;* 65 (1980) 1044-1049.

[9] J. Zhao, F.E. Huggins, Z. Feng, and G.P. Huffman, *Surface-induced superparamagnetic relaxation in nanoscale ferrihydrite particles.* **Phys. Rev B.** 54 (1996) 3403-3407.

[10] J. Zhao, Z. Feng, F.E. Huggins, N. Shah, G.P. Huffman, and I. Wender, *Role of molybdenum at the iron oxide surface.* **J. Catalysis**, 148 (1994) 194-197.

Gas-Phase Incorporation of Organometallic Compounds within Aerogels for Synthesis of Fischer-Tropsch and Water-Gas Shift Catalysts

Gregory C. Turpin, Yifan Shi, and Richard D. Ernst

Department of Chemistry, University of Utah, Salt Lake City, Utah 84112

I. Introduction

The Fischer-Tropsch and Water Gas Shift reactions each offer the potential for providing solutions to important future energy concerns. In each case, catalysts employed for these processes tend to be late transition metals deposited on typical supports such as silica, alumina, titania, zirconia, or ceria. While numerous studies have addressed the roles played by various catalyst and support combinations, far less attention has been devoted to studies involving aerogel supports, whose highly porous natures should promote more effective catalyst dispersal and enhanced mass transport of reactant and product molecules through the aerogel pores.[1] Additionally, catalytic studies utilizing aerogel supports may be carried out either under gas-phase or supercritical conditions, leading to additional control over the nature of the reaction.[2]

The unique structures and properties of aerogels allow for the preparation of very new catalyst/support motifs. In one application, the highly porous aerogel backbone can serve as a framework onto which a more desirable support material may be deposited. This approach could be advantageous in cases in which the more desirable support either may be costly, or does not form a reasonable aerogel structure on its own. As will be described, this approach has been successfully applied to the preparation of a ceria-coated silica aerogel. A second opportunity for aerogels relates to the catalyst incorporation step. Since partial wetting of an aerogel structure can lead to drastic collapse of the pore structure, gas phase incorporation processes could offer some advantages, including the potential of effecting single site metal incorporation and of delivering one metal selectively to another on the support surface.

II. Experimental

Catalyst Supports. Silica aerogels were prepared as previously described.[3] Solution phase loading of cerium(IV) alkoxide[4] was accomplished by first replacing the solvents in a 10.0 mL solid monolithic alcogel sample through 4-5 equilibrations with 20-25 mL volumes of THF, after which the external solvent was replaced by a solution of the cerium alkoxide in THF. Solution phase incorporation of ceric ammonium nitrate (CAN) was accomplished by first replacing the solvents in a 11.0 mL solid monolithic alcogel through 1 equilibration with ethanol (35 mL) and 3 equilibrations with acetone (35 mL each), after which the external solvent was replaced by an acetone solution of CAN. In either case, subsequent equilibration led to an even distribution of cerium throughout the entire solution volume, within and outside of the alcogel. The alcogel monolith was then removed and subjected to two similar equilibrations with acetone, after which the monolith was placed in a CO_2 atmosphere, pressurized and heated to supercritical conditions, and dried to yield the aerogel. The cerium-laden aerogel was sieved to 45-100 mesh, and then calcined in air at 450 ^{o}C.

Catalyst Preparations. The metal pentadienyl compounds were prepared according to literature methods,[5-7] as were the cobalt catalyst precursors.[8,9] A volatile organometallic palladium compound, (η^3-allyl)(η^5-cyclopentadienyl)palladium, was chosen as the palladium precursor; it is readily synthesized by a well-established literature procedure[10] and is appreciably

air-stable. For gas-phase incorporation of the metal precursor, an appropriate mass of the compound and the ceria-laden aerogel were combined under a nitrogen atmosphere in a Schlenk tube which was generally placed under static vacuum and rotated constantly until the separate organometallic phase was no longer visible. However, for the palladium compound, simple mixing under 1 atm. of nitrogen led to the gradual disappearance of the compound as it was homogenously adsorbed by the ceria-laden aerogel. The ceria- and palladium-laden aerogel was calcined again at 450 ºC, or otherwise as indicated, while for the other metals, oxygen gas was passed over the doped aerogel, beginning at 25 ºC, with the temperature thereafter slowly brought to 25-300 ºC, depending on sample. For the Fischer-Tropsch studies, the supported metal oxide was heated to 480 ºC, and reduced in a hydrogen stream. Surface area determinations were made by nitrogen desorption (BET) measurements.

Catalytic Studies. Fischer-Tropsch reactions were carried out in a laboratory-scale packed bed reactor, as previously described,[3] except that C_1-C_{13} hydrocarbon products were analyzed by gas chromatography on a capillary column (DB-5, 0.53 mm I.D. and 30 m length) with an FID.

Water-gas shift reactions were investigated in a laboratory-scale, packed-bed, 6-channel microreactor, as previously described.[11] Catalysts (~100 mg) were tested from 150 ºC up to 350 ºC in 50 ºC increments, and once again at 250 ºC to test for catalyst degradation. Water, CO, and nitrogen were passed over the catalyst at rates of 47 μL/min, 32 sccm, and 190 sccm at approximately 1 atm. pressure. Hydrogen, CO_2, as well as unreacted CO and water were analyzed by gas chromatography on a capillary column (HP-PLOT Q, 0.53 mm I.D., and 30 m length) and a TCD.

III. Results and Discussion

In the last year, a substantial backlog of Fischer-Tropsch catalysts to be tested has developed. Some effort, particularly by Dr. Brian Dunn, has therefore been expended to remove a GC/MS analyzer and make modifications to allow for simultaneous monitoring of up to six reactors, which should greatly facilitate our future studies. Some significant progress has been achieved over the past 6 months. Together with the Eyring and Pugmire groups, a number of zeolite-supported Fischer-Tropsch (FT) catalysts have been studied, and a publication of some of the results has appeared.

Calcination Temperature	Activity (g-CO/g-cat·h)	CO Conversion	Ru particle size (nm)
"room temperature"	4.2	31%	no crystalline peaks (finely dispersed)
150 ºC	1.5	13%	no crystalline peaks (finely dispersed)
250 ºC	1.2	8%	10 nm
300 ºC	0.6	4%	14 nm
500 ºC	0	0%	n/a

Further reactivity studies of aerogel-supported cobalt and ruthenium FT catalysts have been carried out, and the results are summarized in Table 1. Particle sizes were determined by the Seehra group at WVU using XRD. For the most part, these data mirror the preliminary

results described in last year's report. One especially intriguing result has been obtained, however, for a 2% ruthenium catalyst. While our other ruthenium catalysts were air-oxidized, subsequently calcined at ca. 350 ºC, and thereafter reduced by hydrogen, the most recent sample was simply air-oxidized at room temperature, and then reduced. Unlike all of our other ruthenium and cobalt catalysts, which did not show an induction period prior to the onset of activity, this one at first was nearly inactive, but after ca. 16 hours, its activity began to increase, and by ca. 30 hours, it had become even more active than our previous 10% ruthenium catalyst. It could be that by avoiding the high temperature calcinations process, the extent of ruthenium aggregation was reduced, leading initially to a lower activity catalyst, but with time agglomeration might have taken place to yield a more optimal metal distribution than obtained via higher temperature calcination. Clearly this preliminary result needs to be checked for reproducibility, and appropriate microscopic studies should help establish the natures of the metal particles at the key stages of preparation and use. If this preliminary observation holds up, it will clearly impact significantly on our future studies with hydrogen. It has also been observed that the initially incorporated ruthenium reacts directly with hydrogen, which provides another alternative to calcination.

While we have developed a gas-phase "redox targeting" approach that appears to selectively deliver cobalt to supported ruthenium on an aerogel surface (described in our last yearly report), it was also of interest to devise a strategy for achieving this via solution methods. A number of other groups have studied a variety of mixed Co/Ru carbonyl complexes, which can be incorporated via gas or solution phase methods, but the carbonyls clearly have cost and convenience issues. We have therefore turned our attention to the utilization of pyridazine and pyrazole, as ligands with the potential to link cobalt and ruthenium. One possibly useful result has been obtained, from the reaction of pyridazine with (1,5-COD)$RuCl_2$ (readily obtained from commercial "$RuCl_3$ hydrate" with 1,5-cyclooctadiene[12]). In the presence of H_2, the COD ligand is hydrogenated to cyclooctane, and rather surprisingly, six pyridazines coordinate to the ruthenium center, giving $[Ru(1,2\text{-}C_4N_2H_4)_6]^{2+}$ (see previous six month report). Previously, no more than three pyridazines could be incorporated into a ruthenium complex. Further work to attach cobalt to the uncoordinated ends of the pyridazines is underway.

Collaborative results with the Roberts and Guin groups have been described in the previous six month report.

Studies of the Water Gas Shift (WGS) Reaction. Copper, gold, and palladium catalysts supported on ceria have recently been reported to yield very active catalysts for the WGS reaction.[13, 14] One of our goals from the 2003-2004 yearly report was therefore to develop a means to prepare the equivalent of a ceria aerogel, whose large pores and surface area should offer substantial advantages as a support. Unfortunately, ceria aerogels undergo collapse at higher temperatures.[15] Hence, it was of interest to see if silica aerogel could be used as something of a scaffold on which ceria could be deposited, yielding the equivalent of a more robust ceria aerogel. This approach not only would yield a stronger, yet still highly porous support structure, it would also reduce the amount of the more expensive ceria required for a given amount of support.

Indeed, we have found that the very hydrolytically sensitive $Ce(O\text{-}i\text{-}C_3H_7)_4{\cdot}(i\text{-}C_3H_7OH)$ seems to incorporate very well, to at least 10%, into silica aerogel via standard solution methods, while cerium ammonium nitrate (CAN) can be used to achieve incorporations of at least 40%. The resulting aerogel-supported ceria takes advantage of the high surface area of aerogel to yield

surface areas for ceria-based catalysts that have previously not been achieved. Aerogel surface areas above 600 m^2/g were achieved with Ce loadings of 10% and well above 350 for loadings of 40% Ce (see Figure below). Undoped aerogel prepared similarly has surface areas around 700 m^2/g, while traditional ceria catalysts tend to have surface areas in the range of only 30 to 215 m^2/g.[16] There is every reason to believe that significantly higher surface areas can be obtained for our composites by starting with even more porous silica aerogels.

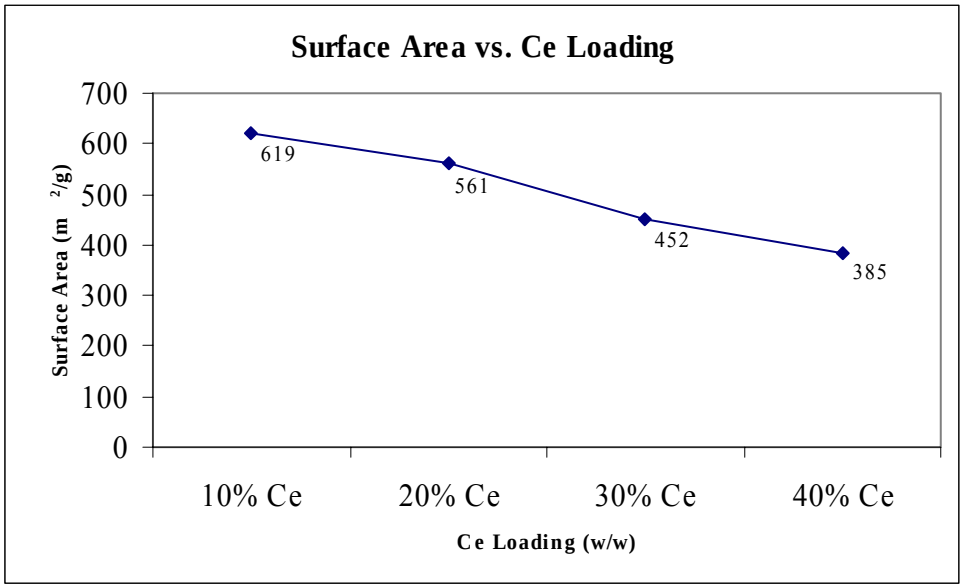

As important as high surface area is the ability of a ceria-based catalyst to maintain its surface area at high temperatures. It has been previously shown that ceria itself undergoes a dramatic loss of surface area even around 300 ºC.[15] Notably, our aerogel-supported ceria doesn't show the same decrease in surface area. For a series of 20% ceria catalysts, calcinations up to 650 ºC still yield substantially the same high surface areas (see Figure below). The activities of the aerogel-supported ceria catalysts compare favorably with traditional ceria-based catalysts, thereby demonstrating substantial potential for both cost savings and reactivity increases with our composite catalysts.

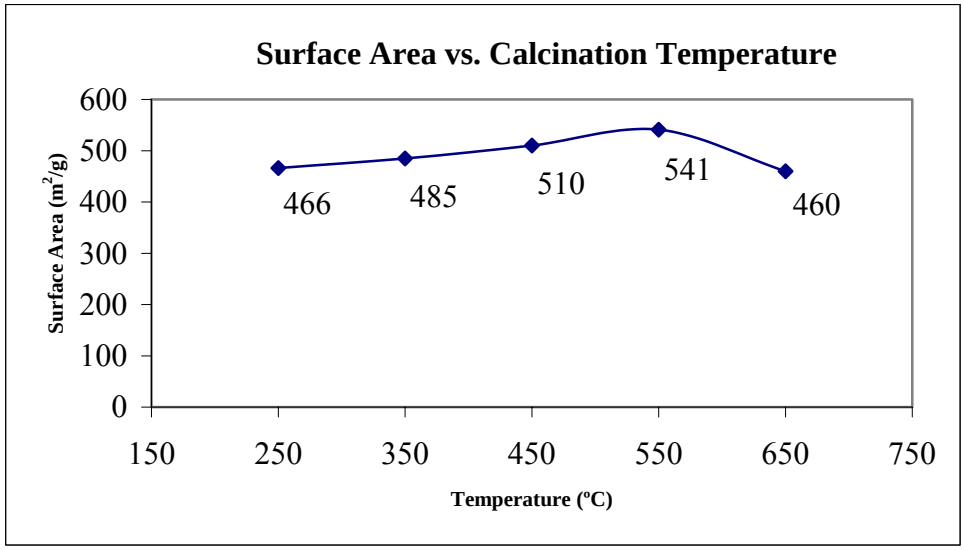

Calcination Effects. Samples with 1% Pd and 20% Ce were calcined at different temperatures in order to determine the optimal calcination conditions and to investigate the framework stability as a function of temperature (see Figure below). Whereas traditional ceria-based catalysts lose considerable activity and surface area on heating, our composite aerogel-supported catalysts lose neither appreciable surface area nor activity with higher calcination temperatures. Activities for catalysts calcined at either 450, 550, or 650 ºC are 1.5, 1.6, and 1.5 g-CO/g-cat/h at a reaction temperature of 350 ºC (see Figure below). Catalysts calcined below 450 ºC, at either 350 ºC or 250 ºC, have lower activities; this is possibly due to incomplete oxidation of the organic fragment of the organometallic Pd precursor, thereby reducing the number of catalytically active metal sites.

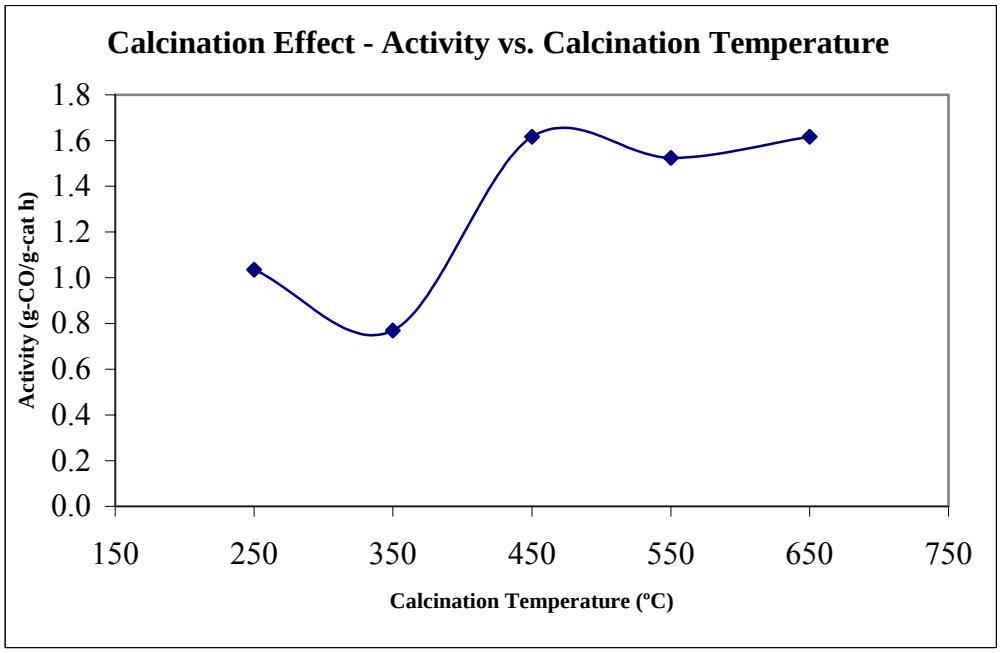

Ce Loading Effects. Samples with 1% Pd and 10, 20 and 30% Ce were prepared and, as might be expected, activity was found to correlate with Ce loading, as illustrated below.

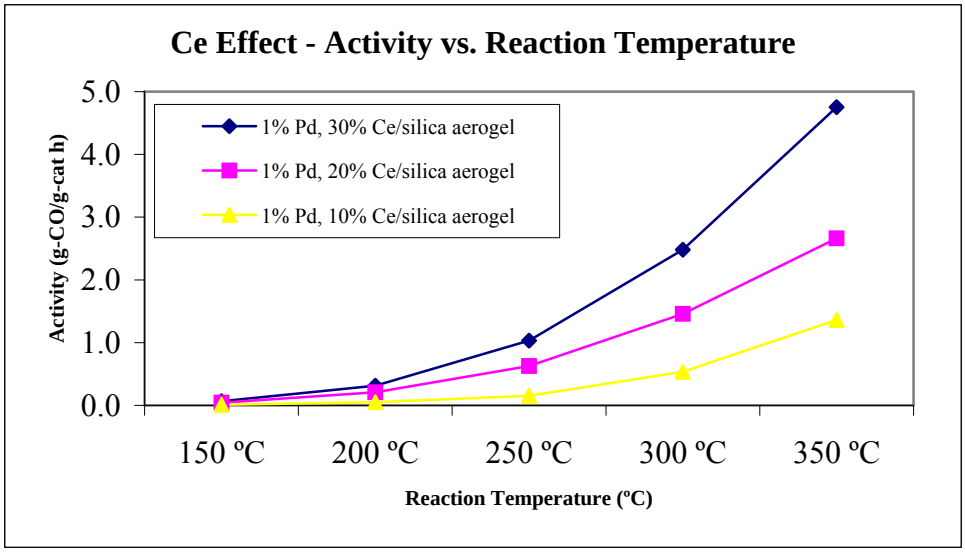

The Figure below provides tentative support for the proposal that the observed reactivity is nearly related to the combined quantity of the active metal species, specifically the amount of Pd and Ce. As can be seen, the normalized activities increase quite similarly with these quantities. This provides evidence that not only is the underlying aerogel support inert, but also that just a small fraction of the ceria, likely that at the surface, is critical to the chemistry involved and that bulk ceria is not necessary. However, further data will be required, particularly with varying Pd contents (*vide infra*) in order to conclusively resolve this issue.

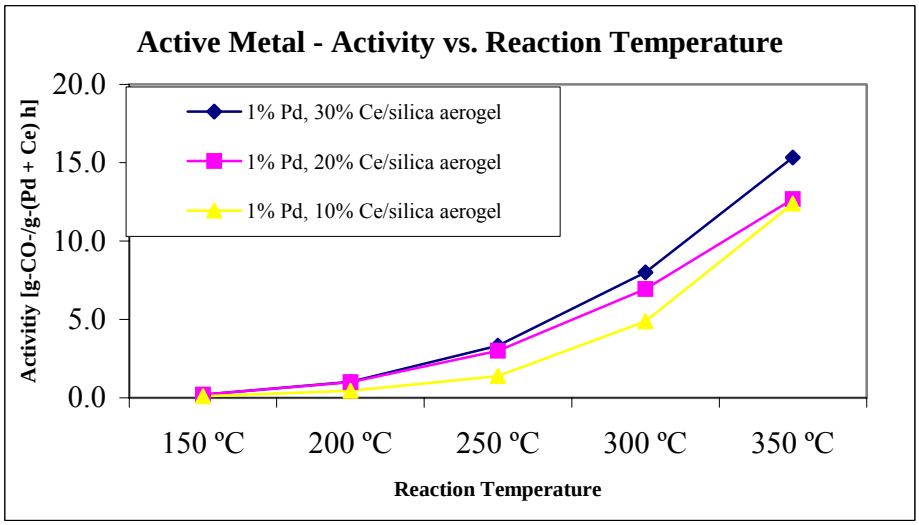

Pd Loading Effects. A previous report for a ceria- and palladium-based catalyst demonstrated that loadings of Pd in excess of ca. 1% did not correlate to increased activities.[16] In fact, samples with additional Pd were not appreciably active. Possibly,

traditional solution-phase incorporation of Pd precursors led to significant agglomeration at higher concentrations, yielding decreasing amounts of Pd that actually could interact with the ceria located at the surface. In our composite aerogels, samples with 1, 2, and 5% Pd, as well as 20% Ce, were prepared to investigate the effects of gas-phase Pd loading, which would be expected to yield a well-dispersed metal on the surface of the support. Indeed, as can be seen in the Figure below, loadings of up to at least 5% Pd do lead to increased activities.

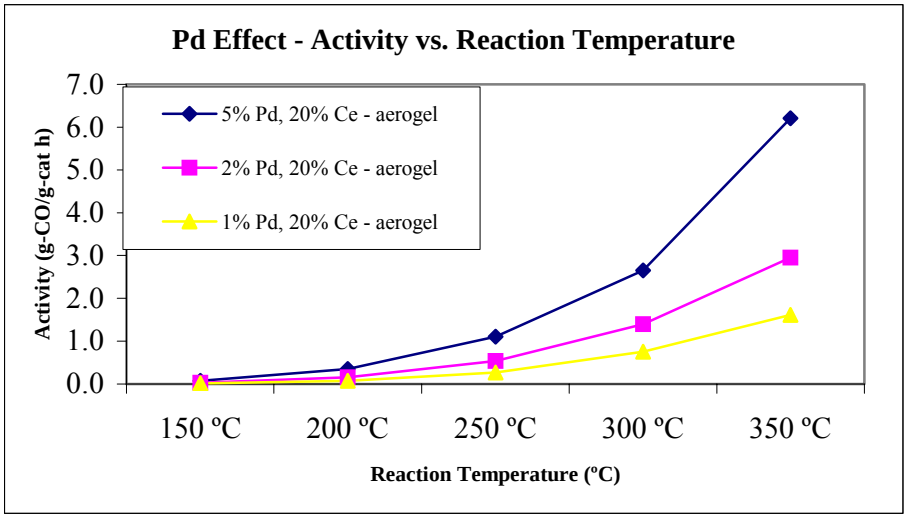

Other Observations. Preliminary results also suggest that these aerogel-supported catalysts have very promising activity for oxygen-assisted water-gas shift chemistry. The oxygen-assisted WGS reaction has attracted considerable interest for fuel cell applications.

Activation Parameters. Differential reaction rates as a function of temperature and the resulting energies of activation were determined for the catalysts. Activation energies were found to range from 44 and 53 kJ/mol. These values are similar to those found for traditional Pd-ceria catalysts.[17] One of several sets of these data is shown below.

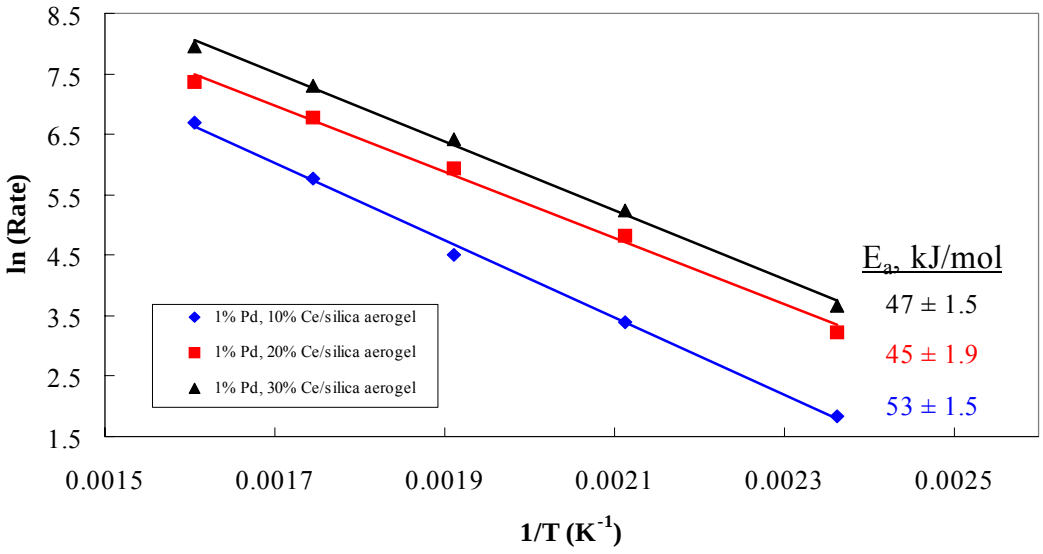

IV. Conclusions

The high surface areas and highly porous nature of aerogels offer promise not just for the FT reaction, but also WGS and certainly others as well. The gas-phase approach likely generates catalyst centers in very highly dispersed form, whether for aerogels, zeolites, or some other support. It also appears that a silica aerogel structure can be of value in providing a robust framework onto which more fragile species such as ceria can be anchored.

V. Papers Presented or Published

1. "Silica Aerogel Supported Catalysts for Fischer-Tropsch Synthesis," Dunn, B.C.; Cole, P.; Covington, D.J.; Webster, M.C.; Pugmire, R.J.; Ernst, R.D.; Eyring, E.M.; Shah, N.; Huffman, G.P. *Appl. Catal. A* **2005**, *278*, 233-238.
2. "Silica Xerogel Supported Cobalt Metal Fischer-Tropsch Catalysts for Syngas to Diesel Range Fuel Conversion," Dunn, B.C.; Covington, D.J.; Cole, P; Pugmire, R.J.; Muezelaar, H.L.C.; Ernst, R.D.; Heider, E.C.; Eyring, E.M.; Shah, N.; Huffman, G.P.; Seehra, M.S.; Manivannan, A.; Dutta, P. *Energy & Fuels* **2004**, *18*, 1519-1521.
3. "Enhancement in Reducibility of Cobalt Oxides and Catalytic Activity of a Mesoporous Silica Supported Cobalt Catalyst by Silylation," Kim, D.J.; Dunn, B.C.; Cole, P.; Turpin, G.C.; Ernst, R.D.; Pugmire, R.J.; Kang, M.; Kim, J.M.; Eyring, E.M. *J. Chem. Soc., Chem. Commun.* **2005**, 1462-1464.
4. "Reactions of SF_6 with Organotitanium and Organozirconium Complexes: The 'Inert' SF_6 as a Reactive Fluorinating Agent," Basta, R.; Harvey, B.G.; Arif, A.M.; Ernst, R.D. *J. Am. Chem. Soc.* **2005**, *127*, 11924-11925.
5. "Aerogel-supported Transition Metal Catalysts for Fischer-Tropsch and Related Reactions," Turpin, G.C.; Dunn, B.C.; Shi, Y.; Ma, Z.; Pugmire, R.J.; Eyring, E.M.; Ernst, R.D. 230th ACS National Meeting, Division of Fuels Chemistry, #84, Washington, DC, Aug. 30, 2005.
6. "Use of Organometallic Compounds for the Synthesis of Fischer-Tropsch Catalysts," Turpin, G.C.; Dunn, B.C.; Ma, Z; Pugmire, R.J.; Eyring, E.M; Ernst, R.D. Poster, Gordon Research Conference (Hydrocarbon Resources), January 9-14, 2005, Ventura, CA.

In addition, a US Patent application has been filed for the redox targeting process, while a patent disclosure has been filed for the composite ceria aerogels.

VI. Future Work

In addition to completing our FT studies, as described in our six month report, the recent successes with composite ceria/silica aerogel frameworks will be vigorously pursued by the Eyring, Ernst, and Pugmire groups, and studies to characterize the natures of these composites are underway with a number of our CFFS collaborators. Of initial interest will be attempts to increase the surface areas of our composites at the initial aerogel formation phase. An examination of the relative catalytic abilities of other metals, such as copper, gold, and platinum, will also be pursued.

VII. References

(1) Husing, N.; Schubert, U. *Angew. Chem. Int. Ed.* **1998**, *37*, 22-45.
(2) Elbashir, N.O.; Roberts, C.B. *Ind. Eng. Chem. Res.* **2005**, *44*, 505-521.

(3) Dunn, B.C.; Cole, P.; Turpin, G.C.; Ma, Z.; Pugmire, R.J.; Ernst, R.D.; Eyring, E.M.; Shah, N.; Huffman, G.P. Preprints of Symposia - American Chemical Society, Division of Fuel Chemistry **2004**, *449(1)*, 329-330.
(4) Vaartstra, B.A.; Huffman, J.C.; Gradeff, P.S.; Hubert-Pfalzgraf, L.G.; Daran, J.-C.; Parraud, S.; Yunlu, K; Caulton, K.G. *Inorg. Chem*. **1990**, *29*, 3126-3131.
(5) Wilson, D.R.; Stahl, L.; Ernst, R.D. *Organometallic Syntheses* **1986**, *3*, 136.
(6) Elschenbroich, C.; Bilger, E.; Ernst, R.D.; Wilson, D.R.; Kralik, M.S. *Organometallics* **1985**, *4*, 136.
(7) Gleiter, R.; Hyla-Kryspin, I.; Ziegler, M.L.; Sergeson, G.; Green, J.C.; Stahl, L.; Ernst, R.D. *Organometallics* **1989**, *8*, 298.
(8) Otsuka, S.; Rossi, M. *J. Chem. Soc. A.* **1968**, 2630.
(9) Eisch, J.J.; King, R.B. *Organometallic Syntheses* **1965**, *1*, 70.
(10) Tatsuno, Y; Yoshida, T.; Otsuka, S. *Inorg. Syn.* **1979**, *19*, 220-223.
(11) Dunn, B.C.; Kim D.J.; Webster, M.; Gasser, J.; Turpin, G.C.; Ernst, R.D.; Eyring, E.M. 19th Annual Technical Meeting CFFS C1 Chemistry, Roanoke, W.V., Jul 31-Aug 3, 2005.
(12) Albers, M.O.; Ashworth, T.V.; Oosthuizen, E.; Singleton, E. *Inorg. Syn.* **1989**, *26*, 68-69.
(13) Fu, Q.; Saltsburg, H.; Flytzani-Stephanopoulos, M. *Science* **2003**, *301*, 935-938.
(14) Qi, X.; Flytzani-Stephanopoulos, M. *Ind. Eng. Chem. Res*. **2004**, *43*, 3055-3062.
(15) Thundathil, M.A.; Lai, W.; Noailles, L.; Dunn, B.S.; Haile, S.M. *J. Am. Ceram. Soc.* **2004**, *87*, 1442-1445.
(16) Bickford, E.S.; Velu, S.; Song, C. *Catalysis Today* **2005**, *99*, 347-357.
(17) Gorte, R.J.; Zhao, S. *Catalysis Today* **2005**. *104*, 18-24

What C-13 chemical shift tensors can tell us about metal ligand interactions in catalysts

Ronald J. Pugmire and Zhiru Ma

Department of Chemistry and Department of Chemical Engineering

University of Utah

Introduction

Catalysts will play an increasingly important role in the development of C1 chemistry and the production of hydrogen. The NMR group at Utah is now focusing on understanding subtleties in catalyst structure and function.

Experimental

We have recently focused our research on catalyst systems with the goal to explore the feasibility of obtaining FIREMAT data on various metal-ligand complexes. The FIREMAT[1] experiment has proven to be a very useful tool for obtaining carbon-13 chemical shift tensor data.

Results

Twenty years ago low temperature shift tensor principal values were obtained in the Utah laboratory on a series of metal diene complexes[2] and some of these data were later included in an extended data set by Oldfield, et. al.[3] The earlier Utah data was obtained by fitting the powder patterns of the complexes and the error in these STPV's can be as high as 5-10 ppm. We have now begun to revisit this topic employing the high resolution FIREMAT technique. The additional resolution obtainable by this experimental technique has led to the discovery of additional resonance lines in the spectra of several metal-ligand complexes that we have recently studied. An illustrative example is found in the spectrum of (bicyclo[2.2.1]hepta-2,5-diene) dichloropalladium (II) (see Figure 1) in which the diene-carbons are split into a doublet separated by 2 ppm. This spectral feature is due to a break in the crystal symmetry arising from slight differences (~0.02 angstrom) in the palladium-diene bond lengths. The PVST data of these carbons are readily obtained from the FIREMAT data and these values are given in Table 1. Similar NMR data have been obtained in (1,5 cyclooctadiene) dimethylplatinum (II).

Table 1. Shift Tensor Principal Values in (bicyclo[2.2.1]heta-2,5-diene)dichoropalladium(II)

Carbon	δ_{iso}	δ_{11}	δ_{22}	δ_{33}
Diene (CH)	94.1	191.2	87.1	4.0
Diene (CH)	92.1	188.9	85.5	2.0
CH	66.1	100.1	68.7	29.6
CH2	52.4	66.1	56.0	35.0

Conclusions

These data illustrate the high degree of sensitivity to local structural variations. The data we have obtained at this writing have laid the ground work of a wider range of complexes that will be studied. We will begin modeling these data by means of quantum mechanical techniques in the

next few months. Exploration of the relativistic effects on the ligands will be included in our modeling efforts.

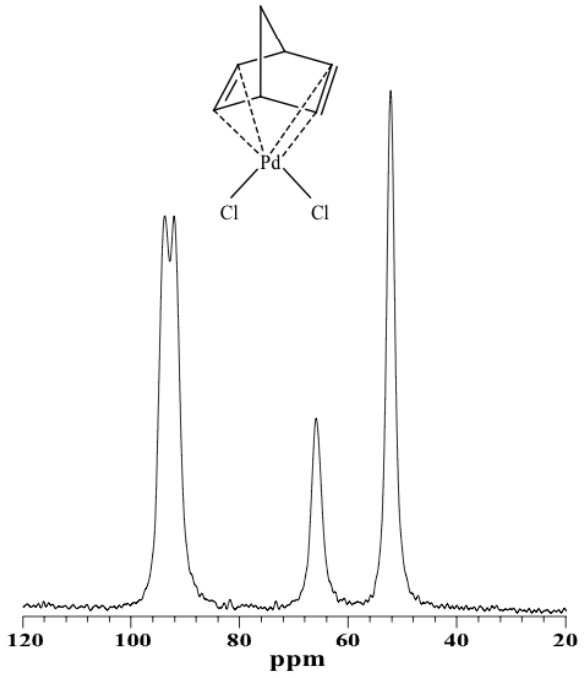

Figure 1. CP/MAS spectrum of (bicyclo[2.2.1]hetap-2,5- diene) dichloropalladium(II).

1. **References** A Sensitive High-Resolution Magic-Angle-Turning Experiment for Measuring Chemical-Shift-Tensor Principal Values. D.W. Alderman, G. McGeorge, J.Z. Hu, R.J. Pugmire and D.M. Grant, 1998**,** Mol. Phys., 95, 1113-1126.
2. Low Temperature Solution Studies of Copper(I) Complexes and Trans-Cycloalkenes and Solid State ^{13}C NMR Studies of Metal-Diene Complexes, Gregory Michael Wallraff, Ph.D. thesis, Department of Chemistry, University of Utah, 1985.
3. Solid-State NMR and Density Functional Investigation of Carbon-13 Shielding Tensors in Metal-Olefin Complexes, R. Havlin, M. McMahon, R. Scinivasan, H. Le, and E. Oldfield, J. Phys. Chem. A **1997**, 101, 8908-8913.

Development of an Advanced Gas-To-Liquid Technology Based on Near-Critical and Supercritical Fischer-Tropsch Synthesis Operation

Nimir O. Elbashir*, Joseph E. Durham, Christopher B. Roberts

230 Ross Hall, Department of Chemical Engineering, Auburn University, AL 36849

*Current Address: Environmental Technologies R&D, Engelhard Corp., Iselin, NJ 08830

Introduction

The objective of this research is to establish optimum operating conditions for Fischer Tropsch synthesis within the supercritical region that would maximize the production of value added chemicals and middle distillate hydrocarbons (gasoline fuel, jet fuel, and diesel fuel fractions) and at the same time minimize the production of methane and carbon monoxide. The first phase of our project was focused on highlighting the advantages of utilizing near critical and supercritical phase as reaction medium for the FTS technology. As concluded in our first annual report, the superior properties of the near-critical and supercritical fluids (liquid-like density and heat capacity, and gas-like diffusivity) can be used to advance the 80-year old FTS technology. In the second phase of our project we have examined the effects of supercritical fluid (SCF) (*n*-pentane or hexane) on FTS over an alumina supported cobalt catalyst in a fixed-bed-reactor. The influence of reaction conditions (such as temperature (210-260 °C), pressure (20-80 bar), syngas feed ratio (H_2/CO ratio of 0.5-2), contact time and space velocity (50-150 sccm/g_{cat})) on the FTS activity, selectivity, and hydrocarbon product distributions in the supercritical fluids (SCF) media was studied. Our results show that the adjustable thermophysical properties of the SCF significantly impact the FTS reaction performance and in most cases the SCF-FTS operations yield higher activity and better selectivity towards the most desired products compared to conventional gas-phase FTS operations. In the third phase of the project we have addressed the excellent opportunity to maximize the production of desired fuel fractions, through a simple tuning process of the reaction environment from liquid-like properties to vapor-like properties. An approach to understand the enhanced chain growth probability in SCF-FTS conditions was also addressed. This phenomenon was attributed to the enhanced α-olefins incorporation in the chain growth process. In the fourth phase of the project we have covered a preliminary examination of the kinetics of the FTS reactions under high-pressure high-temperature conditions in both conventional gas-phase FTS and supercritical hexanes FTS (SCH-FTS). Our findings illustrated that the classical surface reaction kinetics model that successfully estimates the reaction parameters in the gas phase FTS conditions fails to predict the rates in the SCH-FTS.

The role of the cobalt catalysts surface characteristics on the reaction performance in both conventional gas-phase FTS and SCF-FTS was addressed in the fifth phase of our project. This study was conducted in cooperation with Prof. Seehra's group at West Virginia University. The surface characteristics of these catalysts were measured by N_2 physisorption using a TriStar 3000 gas adsorption analyzer. Room temperature X-ray diffraction (XRD), temperature and magnetic field (*H*) variation of the magnetization (*M*), and low-temperature (5 K) electron magnetic resonance were used for determining the electronic states (Co^0, CoO, Co_3O_4, Co^{2+}) of cobalt for the calcined, reduced (before the reaction), and used samples (after the reaction). Our findings

also showed that the cobalt-based catalytic systems show excellent stability in terms of activity and selectivity as well as their structure under the SCF-FTS conditions for relatively long time-on-stream (up to 13 days). In the sixth phase of our project we have investigated the performance of iron-based catalytic systems and ruthenium-based catalytic systems on SCF-FTS. The ruthenium study was carried out in cooperation with Prof. Ernst's team at the University of Utah. The focus was on the role of catalyst type on the Enhanced Olefin Incorporation that was consistently observed on cobalt-based systems under near-critical and supercritical conditions. This annual report addresses our investigations of the cobalt-catalyst characteristics and their influence on the FTS performance (both in conventional gas-phase FTS and SCF-FTS), in addition to the hydrocarbon product distributions under SCF-FTS on ruthenium and iron catalysts.

Experimental Setup

The Fischer-Tropsch synthesis studies were carried out in our high pressure reaction unit that is connected to gas chromatography for reactant and product analysis. Our high pressure reactor is a conventional down-flow fixed bed stainless steel reactor (1.27 cm×25.4 cm; effective volume: 32 cm^3) purchased from HIP Equipment Company. The unit has been described in detail in our previous reports. The delivery system is composed of three mass-flow controllers (Brooks 5850E) for flow control of syngas (CO and H_2) and nitrogen (internal standard), CO, and H2, in addition to an HPLC pump (Acuflow Series III, Fisher) for the flow control of the supercritical solvent. The hexane and syngas are combined in a static mixer (OMEGA) before entering the reactor, where the high temperature results in a supercritical hexane phase. The reactor is situated in a furnace (Applied Test System Inc) with a programmed temperature controller system. The reaction pressure is controlled by a back pressure regulator (Tescom Inc.) located between the reactor and a hot trap. Two pressure indictors are located at the inlet and outlet of the reactor respectively to monitor the reaction pressure and pressure drop inside the reactor. After leaving the reactor, the products pass through a hot trap (200^oC) to condense very heavy components prior to sampling into the on-line GC analysis system. All lines between the reactor outlet and the GC are heated to 200^oC to prevent product condensation. Two GCs are used in the analysis system. A Varian 3300 GC with capillary column (DB-5) and a FID will be used for the analysis of C2-C30 hydrocarbons and oxygenates. A Varian CP-3800 with a packed column (Hayesep-DB100/120) and TCD will be used for the analysis of permanent gases and C1-C3 hydrocarbons.

Two of our cobalt catalytic systems were prepared in house using the impregnation technique. The 15% Co/SiO_2 (high surface area and low surface area) were prepared through impregnating fumed SiO_2 (99.0% purity purchased from Sigma-Aldrich) in an aqueous solution of cobalt nitrate (precursor $Co(NO_3)_2.6H_2O$ - 99.8% purity purchased from Aldrich Chemical Co). The low surface area catalyst (15% Co/ SiO_2 LSA) was supported in fumed silica of surface area 200 m^2/g, while the high surface area catalyst (15% Co/ SiO_2 HSA) was supported on 380 m^2/g fumed silica oxide. Before running the reaction our calcined catalysts were reduced in H_2 environment (50 sccm) at 320 °C and 1 atm for 4 hrs. This process took place in our high pressure reactor. Prior to initiating the reaction experiments the reduced catalyst was cooled in a helium blanket to room temperature. The alumina supported cobalt catalyst (15% Co/Al_2O_3) was obtained from United Catalysts, and the iron catalyst RLS 4.55 Si/isocyelan was obtained from SudChemie. The ruthenium catalyst 10% Ru/SiO2 (Aerogel) was prepared by Prof. Ernst's team at the University of Utah.

Results

A-Role of Cobalt Catalyst Characteristics

Three cobalt based catalytic systems were tested under a set of conditions that were selected to mimic that of industrial conditions (15% Co/ SiO_2 LSA, 15% Co/ SiO_2 HAS, and 15% Co/ Al_2O_3) that favor high conversion rate of CO and H_2 per single pass at an acceptable chain growth probability of α-value above 0.60). A summary of the catalyst characterizations is illustrated in Table 1. Table 2 show the catalysts activity and selectivity at a reaction temperature of 240 °C and pressure of 20±2 bar. The reported results in Table 2 have been collected after steady-state operation and prior to any deactivation of the catalyst taking place. A previous study has reported that the quasi steady state in reaction rates and selectivity of cobalt-based catalyst can be reached within as low as 4 hr of time-on-stream (TOS) [1]. In the current study, the reported activity and selectivity is for samples analyzed after long times (c.a. 40 hr TOS) to ensure stability of the catalysts under the studied conditions. Fig. 1 shows an example of the A1/C catalyst stability with time on stream at relatively high reaction temperature of 250 °C. No significant changes (up to 55 hr.) in both activity (CO conversion, H_2 conversion and syngas conversion) and selectivity (CH_4 and CO_2) with TOS are observed as shown in Fig. 1.

Under the studied conditions, the silica supported catalysts (A1/C and B1/C) were found to achieve higher CO and syngas conversions than the alumina supported one (C1/C) (see Table 2). This is also accompanied by higher methane selectivity of the silica supported catalysts (A1/C 21.3% and B1/C 18.9%) than that of the alumina supported one (C1/C 16%). In addition, the alumina supported catalyst (C1/C) gave much higher selectivity towards olefins (almost more than double of the silica supported ones, A1/C and B1/C). The C1/C catalyst also yields higher chain growth probability than the silica supported catalyst as shown in Table 2.

Initial inspection of the results suggests a correlation between the catalyst BET area and methane selectivity. A1/C catalyst has the highest surface area and shows the highest methane selectivity, followed by B1/C and C1/C. While a relation between catalyst surface area and methane selectivity has not been previously drawn, recent reports shows that the active phase reducibility of the cobalt catalyst is a function of the support's BET surface area [2]. Another characteristic that is known to give an indication of the methane selectivity is the size of Co particles [3]. The smaller the Co particles the higher would be the methane selectivity. Since the XRD pattern for the silica supported catalyst (A1/C and B1/C) showed almost the same crystallite size of Co_3O_4 (≈ 14 nm), one can not correlate the methane selectivity to the Co particle size from these results. Nevertheless, our EMR analysis shows interesting valence states of the cobalt particles on the catalyst surface. On the high surface area silica catalyst, A1/C, cobalt particles are present mainly as Co_3O_4 whereas in B1/C both Co_3O_4 and Co^{2+} are present on the catalyst surface. On the other hand, Co^{2+} is found to dominate the surface of the alumina supported catalyst (C1/C) and even after long use for 12 days TOS under mild reaction conditions (up to 260 °C and 30 bar) stable forms of Co^{2+} still exist accompanied by Co^0. As a result, lower methane selectivity accompanied by higher chain growth probability (α-value) and olefin selectivity and in the case of C1/C can be attributed to the presence of stable form of Co^{2+}. This is in agreement with previous findings of many cobalt-based catalytic systems, whereas a direct correlation between the extent of reduction and the catalyst selectivity was drawn [3-6]. Khodakov et al [3] reported that crystallite Co_3O_4 was observed in all partially reduced catalysts (cobalt supported on

mesoporous silica) of higher methane selectivity than the completely reduced. Reuel and Batholomew [4] suggested that the presence of stable unreduced oxide phases capable of catalyzing the water-gas shift reaction will result in higher methane selectivity.

Another interesting result is the relatively higher CO and syngas conversions in the silica supported catalysts (A1/C and B1/C) compared to that of the alumina supported catalyst (C1/C). In a previous study Reuel and Batholomew [4] reported the activity of different cobalt-based catalytic systems and they ranked their catalysts in the following order: Co/TiO_2>Co/Al_2O_3>Co/SiO_2>100% Co>Co/MgO. Such a ranking indicates that alumina supported catalyst should yield higher activity than the silica supported one. Nevertheless, Igelsia, et al. [7] have shown that the activity of cobalt catalysts is a function of the metal dispersion and mostly independent of the type of support. Our results also showed that the lower surface area catalyst (B1/C) yield higher activity than the higher surface area catalyst (A1/C) which suggests no correlation between the catalyst surface area and its activity.

B-Comparative Study between the Performance of Cobalt Catalysts in Gas-Phase FTS and Supercritical Phase FTS

Table 3 shows a summary of the activity and the selectivity of the three cobalt-based catalysts in both SCH-FTS and conventional GP-FTS at the same reaction temperature (240 °C) and syngas partial pressure (20 bar). Higher CO conversion and syngas conversion were obtained in SCH-FTS, except for the case of 15% Co/SiO_2 (HSA), where slightly higher conversions were achieved under GP-FTS conditions. Conducting the FTS reaction in the SCH medium results in a significant drop (more than 40%) in methane selectivity compared to that in conventional gas phase FTS as shown in Table 3. Similarly, the chain growth probabilities (α-values) are higher in SCH-FTS than gas-phase FTS, accompanied with higher α-olefins selectivities (results not shown). In order to see the influence of syngas conversion on selectivity towards CO_2 and CH_4, a plot of conversion versus the selectivity (collected from a broad range of reaction conditions) is shown in Figures 2a, and b. While data in Fig. 2a shows significant variations, the linear correlation suggests a decrease in methane selectivity as syngas conversion increases. Nevertheless, in the gas-phase FTS (Fig. 2b) the linear correlation exhibits an increase in methane selectivity with the syngas conversion. CO_2 selectivity is found to be less dependent on conversion in both SCH-FTS and gas-phase FTS. The interesting result shown in Fig. 2a indicates that operating FTS reaction in SCH media offers a better opportunity to minimize the selectivity of the most undesired product in the hydrocarbon products spectrum (i.e. methane) even at high syngas conversions.

Correlations of the catalyst activity and selectivity (as presented in Table 3) with the catalysts surface characteristics reveal that the pore radius of the catalyst has a direct influence on both syngas and CO conversions in gas-phase FTS. As shown in Fig. 3 the FTS activity increases with the pore diameter of the catalyst. This result is in agreement with the previous findings of Khodakov et al. [4] who showed that both the size of the supported Co_3O_4 and their reducibility is strongly dependent on pore diameter of mesoporous silica supports. They also suggested that small cobalt particles in narrow pores are more difficult to reduce than larger particles in wider pores. On the other hand, no direct correlation between the pore diameter and activity of the catalysts in SCH-FTS is observed as shown in Fig 3b. Because of the similarity in pore volume of the two silica-supported catalysts, investigations of pore volume effects on the activity and

selectivity in both gas-phase FTS and SCH-FTS is limited. An interesting result is that α-value in GP-FTS is found to decrease as pore volume increases, whereas, in SCH-FTS α-value increases with pore volume.

Pressure is known to affect both FTS termination rates and secondary reactions [8]. High gas phase pressure FTS operation could result in condensation of heavy hydrocarbons that normally exists as gases under atmospheric pressure operations. This condensation will cause diffusion limitations of CO reactant molecules resulting in an increase of the effective H_2/CO ratio, which usually leads to high methane selectivity and lower chain growth probability. These restrictions are obviously influenced by the catalyst pores structure. However, this scenario is changed for the SCH-FTS where the dense supercritical medium provides high solubility for heavy products and miscibility with reactant gases. This results in a single-phase operation for both reactants and products under the SCH operating conditions listed in Table 3 rather than two-phase operation (the phase boundaries for single phase operation of these mixtures has been measured and presented elsewhere [9]). Therefore, the SCH-FTS processes are not as impacted by mass transfer limitations as in conventional GP-FTS. As a result, neither pore radius nor pore volume has a significant influence on the SCH-FTS activity and selectivity. The slight increase in methane selectivity with the pore volume in SCH-FTS has not been accompanied by lower α-value as in the case in the GP-FTS. In a previous study [10], we have shown that classical surface reaction kinetics fails to predict the reaction rates (specifically, CH_4 formation rates) in SCH-FTS, because of the nonideality of the reaction mixture. Methanation rates are different from that of the FTS primary and secondary reaction rates and it is more likely to be influenced by the reaction conditions and the cobalt electronic states rather than the mass transfer limitations inside the catalyst pores. In our previous report we have shown that higher methane selectivity is observed in narrow pores due to either unreduced cobalt species or small cobalt particles, which produce higher relative amounts of methane than large cobalt particles. This is in agreement with the cobalt particle size (results not shown) where the sizes of silica supported catalysts are from 1-3 nm whereas that of the alumina supported catalyst is 12 nm.

C- Stability of the cobalt catalyst activity and structure after FTS reaction

Figs. 4 and 5 show an example of stability tests on the alumina-supported catalyst (15% Co/Al_2O_3) under different reaction conditions in the SCH-FTS and GP-FTS reactions at relatively long TOS. Syngas conversion is used to represent the activity of the catalyst, while methane selectivity is used to represent the selectivity. Under SCH (Fig.4), the initial catalyst stability test was conducted at 240 °C and 60 bar for 48 hrs TOS. During this time, the catalyst showed good stability in syngas conversion (~ 80%) and in CH_4 selectivity (~17%). The temperature was then decreased to 230 °C, while the pressure was kept constant at 60 bar. As a result, both syngas conversion and CH_4 selectivity decreased to ~58% and ~9%, respectively. A stable trend was observed under these conditions for more than 48 hrs TOS. The stability test was then followed by increasing the temperature to 250 °C and the pressure to 65 bar. At these conditions, syngas conversion reaches its highest level, 93%, at the initial 2 hrs TOS and then declined to ~87% for more than 100 hrs TOS. The trend of CH_4 selectivity with TOS shows good stability at ~20%. The aforementioned conditions were selected based on our previous investigations of the alumina-supported catalyst, whereby an optimum performance in both activity and selectivity was observed [9]. Upon returning to the initial conditions (240 °C and 60

bar), no significant changes in either syngas conversions or CH_4 selectivities were observed as shown in Fig. 4.

In the GP-FTS (Fig. 5), the stability test was initialized at 230 °C and 20 bar for 50 hrs TOS. The catalyst reached a steady value of activity and selectivity within 10 h of ~59% syngas conversion and ~23% CH_4 selectivity. Upon increasing the temperature to 250 C, significant increase in syngas conversion (~88%) and CH_4 selectivity (~37%) were obtained during the first 7 hrs. However, as the TOS was increased (up to 45 h) the syngas conversion decreased to reach 74% with negligible changes in CH_4 selectivity. Both the activity and the selectivity reached a steady value after 70 hrs TOS under the above conditions. Returning to the low temperature conditions (230 °C) resulted in a significant drop (c.a. 25%) in syngas conversion compared to the initial 50 hrs TOS; however, CH_4 selectivity is similar to the initial conditions.

Table 2 summarizes the characterizations of the catalysts used in the stability test (sample A1 is the used catalyst after the SCH-FTS conditions (Fig.4), whereas sample A2 is the used catalyst after the gas-phase FTS conditions (Fig.5). The characterizations of the calcined samples (before the reaction) are also included in the last column of Table 2. The XRD and magnetic characteristics of sample A3, which represents the un-used but reduced 15% Co/Al_2O_3, are considered as the baseline for the comparison of the catalyst characteristics before and after the FTS reaction. The characterizations of the calcined but un-used alumina-supported catalyst sample indicates the presence of Co_3O_4 and Al_2O_3 (γ, ε). As discussed earlier, upon reduction (sample A3), Co_3O_4 is partly reduced to hcp Co^0 and CoO; this is attributed to either incomplete reduction in the CO environment or the low reduction temperature (280°C). This is a reasonable conclusion since reduction usually follows the path $Co_3O_4 \rightarrow CoO \rightarrow Co^0$. The characteristics of sample A1 catalyst show the existence of hcp Co^0, CoO and two forms of Al_2O_3 with a negligible amount Co_3O_4. On the other hand, the XRD and magnetic characterizations of the A2 sample reveal that electronic state Co^0, with a larger amount of the fcc phase, and a smaller amount of the hcp phase is present in the used catalyst. This indicates that during both SCH-FTS and GP-FTS reaction, an in situ reduction of the Co_3O_4 to hcp Co^0 or fcc Co^0 is taking place. Another observation is that two phases of alumina are detected in A1 (γ-Al_2O_3, ε-Al_2O_3), while only one phase is detected in A2 (γ - Al_2O_3).

Detailed discussion on the causes of the catalyst stability under the supercritical phase FTS versus conventional gas phase FTS can be found elsewhere [11-12].

D- Hydrocarbon Product Distribution on Ruthenium and Iron Catalysts

The performance of Ru/SiO_2 (aerogel) (prepared by Prof. Ernst's Team) was investigated under near-critical conditions. The stability test of the catalyst at two temperatures is similar to that observed on the cobalt-based catalysts as shown in Fig. 6 (no significant drop in activity). Decreasing the temperature from 250 C to 230 C resulted in lower syngas conversion, however, CO conversion showed slight decrease with temperature under the supercritical conditions. The hydrocarbon product distribution over the ruthenium catalyst has shown a deviation from the standard ASF product distribution under the supercritical phase operation similar to that observed on the cobalt based catalytic systems. Figs. 7&8 show that as the pressure is increased from 35 bar (Fig. 7) to 43.8 bar (Fig. 8) the α-value increases from 0.73 to 0.83 accompanied by

significant deviation from the standard ASF distribution in the middle distillate hydrocarbon range (α-value $\approx$ 0.97).

The iron-based catalyst (RLS 4.55 Si/isocyelan) resulted in different trend than that observed with the cobalt-based catalysts and the ruthenium catalyst. The hydrocarbon product distribution was found to be in a good agreement with the standard ASF product distribution in near-critical and supercritical FTS conditions. Typical hydrocarbon product distribution in near-critical hexane-FTS (230 °C and 45 bar) is shown in Fig. 9. The α-value was found to be relatively high at 0.86. At higher temperature 250 °C and 45 bar no significant changes in the overall α-value was observed ($\approx$0.84).

The results of the iron catalyst compared to both the cobalt and ruthenium catalysts are in excellent agreement with previous studies involving the underlying the mechanism of FTS reactions. It is well known that on the iron catalyst the participation of an oxygenate intermediate plays a major role in the chain growth process [13]. It is also clear that a carbide is the more active form of the iron catalyst. However, the intermediate leading to the 1-alkenes remains to be identified. In general, most of the kinetic models have shown that the mechanism for FTS on the iron catalyst is different than that on the cobalt and ruthenium catalysts. This suggests that the enhanced olefin incorporation mechanism [9] is more likely to take place on the surface of cobalt and ruthenium catalyst rather than the iron-based catalyst. This conclusion is in agreement with our experimental findings so far.

Conclusions

The conclusions of the investigations covered in this report can be summarized as follows:

- The cobalt-based catalyst characteristics play a significant role in the FTS synthesis process. The characterization (BET surface characterizations, XRD, magnetization, and EMR) of six cobalt-based FTS catalysts (alumina and silica supported catalysts with 15% cobalt loading) shows different electronic states of the cobalt (fcp-Co^0, hcp-Co^0, CoO, Co_3O_4, Co^{2+}) and the supports (SiO_2 (quartz, cristobalite, tridymite); δ-Al_2O_3, and γ - Al_2O_3, and ε-Al_2O_3). The cobalt and the support material's electronic states are found to change with calcination, reduction, and reaction conditions. Correlations of the catalysts characteristics with activity and selectivity reveals that the presence of Co_3O_4 yield higher methane selectivity whereas the presence of Co^{2+} species yields lower methane selectivity but higher olefin selectivity.

- The cobalt-based catalytic systems show excellent stability in terms of activity and selectivity under high-pressure, high-temperature supercritical phase FTS for relatively long time-on-stream (up to 15 days). No significant changes of either cobalt particle size, electronic state, or surface structure (BET areas, pore radius, and pore volume) was observed after SCF-FTS operation. This indicates that no serious modification of the catalyst structure is taking place as well as no coke deposition.

- The deviation from the standard ASF product distribution observed in case of cobalt-based catalysts and ruthenium catalyst is attributed in part to the enhanced solubility of heavy products in the dense supercritical solvent medium yielding enhanced availability of vacant sites. Such an environment has a significant impact on the dynamic adsorption/desorption equilibrium of active species inside the catalyst pores. It also enhances the adsorption rates of olefins within light and middle hydrocarbon ranges and hence increases the possibility for their incorporation in the chain-growth process. An enhanced-olefin incorporation model for FTS in SCH including a

synthesis pathway and chain growth mechanism is suggested to provide explanation for deviations within the middle hydrocarbon products. Unlike the cobalt and ruthenium catalysts the iron catalyst production distribution was found to be in good agreement with the standard ASF distribution.

References

1. S. Sun, N. Tsubaki, and K. Fujimoto, *Appl. Catal. A: Gen.l* **202**, 121 (2000).

2. D. I. Enache, M. Roy-Auberger, R. Revel *Appl. Catal. A: Gen.* In press (2004).

3. A. Y. Khodakov, A.Griboval-Constant, R. Bechara, and V. L. Zholobenko, *J. Catal.* **206** 230 (2002).

4. R. C. Reuel. and C. H. Batholomew *J. Catal*. **85**, 78 (1984).

5. L. Fu, and C. H. Bartholomew *J. Catal.* **92**, 376 (1985).

6. B. S. Ernst, S. Libs, P. Chaumette, and A. Kiennemann *Appl. Catal. A: Gen.***186**, 145 (1999).

7. E. Iglesia, S. L. Soled and R. A. Fiato *J. Catal.* **137**, 212(1992).

8. E. Iglesia, Reyes, S. C., Madon, R. J., and Soled, S. L., *Adv. Catal.*,. **39**: p. 221-302 (1993).

9. N. O. Elbashir, and Roberts, C. B., *Ind. Eng. Chem. Res.,* **44**: p. 505-521 (2004).

10. N. O. Elbashir, and Roberts, C. B., *ACS Div. Petr. Chem. Prep.*, **49**(2): p. 157-160 (2004).

11. Dutta, P., Elbashir, N. O., Manivannan, A., Seehra, M. S., and Roberts, C. B., *Catal. Letters*,. **98**(4) 203-210 (2004).

12. N. O. Elbashir, Dutta, P., Manivannan, A., Seehra, M. S., and Roberts, C. B *Appl. Catal. A: Gen,* 285, Pages 169-180 (2005).

13. Davis, B. H. Fuel Proc. Technol., 71, Pages 157-166 (2001).

Table I. Results of characterization of the cobalt-based catalytic systems.

Sample	Description	BET SA (m^2/g)	XRD	Magnetic	EMR
A1	15% HSA Co/SiO_2-Fresh	-	SiO_2	Curie-Weiss, Co^{2+}	Co^{2+} line $g \approx 4.3$
B1	15% LSA Co/SiO_2-Fresh	-	SiO_2	Curie-Weiss, Co^{2+}	Co^{2+} line $g \approx 4.3$
A1/C	Calcined A1	256	SiO_2, Co_3O_4	Co_3O_4	No line
B1/C	Calcined B1	158	SiO_2, Co_3O_4	Co_3O_4	Co^{2+}-weak line $g \approx 4.3$
C1/C	15%Co/Al_2O_3-calcined	95	Co_3O_4, δ-Al_2O_3	Co_3O_4	Co^{2+}-line,$g \approx 4.3$ with sharp line
C1/U	C1 used in FTS reaction for 12 days	-	Co_3O_4, $Al_2O_3(\alpha,\delta,\chi)$	Co^0, Co^{2+}	Co^{2+}-line. Co^0-line

Table 2: Activity and selectivity of three cobalt-based catalysts at 240 °C and pressure 20±2 bar. H_2/CO ratio is 2, and the syngas flowrate is 50 sccm/gcat.

Catalyst	A1/C	B1/C	C1/C
Activity			
CO Conversion%	83.2	87.9	76.8
Syngas (H_2+CO) conversion %	71.9	80.8	65.4
Selectivity			
CH_4 select.%	21.3	18.9	16
CO_2 Select. %	5.1	5.1	3.3
Alkanes select.% *	63	66	58
Alkenes select.%*	10.6	10	22.7
Chain growth probability (α)	0.65	0,71	0.78

* Alkanes and alkene selectivity include the isomers for hydrocarbon range of C2+.
** α determined from ASF distribution: $\ln(W_n/n) = n\ln\alpha + \ln[(1-\alpha)^2/\alpha]$; W_n = weight of hydrocarbons of carbon number n. C_{35} is the heaviest hydrocarbon analyzed in our GC.

Table 3 Activity and selectivity of the cobalt-base catalysts under both supercritical-hexane FTS and gas-phase FTS.

	15% Co/SiO_2 HSA		**15% Co/SiO_2 LSA**		**15% Co/ Al_2O_3**	
	SCH[a]	Gas-Phase[b]	SCH[a]	Gas-Phase[b]	SCH[a]	Gas-Phase[b]
CO Conversion %	78.3	83.2	88.4	87.9	79.6	76.8
Syngas (H_2+CO) Conversion %	69.1	71.9	81.7	80.8	74.2	65.4
CH_4 Selectivity %	14.2	21.3	17.2	18.9	9.8	16
□-value	0.87	0.65	0.83	0.71	0.81	0.78

[a]SCH: Supercritical-Hexane FTS. Reaction conditions: temperature = 240 °C, total pressure = 60 bar (P_{syngas}= 20 bar, P_{hexane} = 40 bar), syngas flowrate 50 sccm/g_{cat}, hexane flowrate = 1mL/min.

[b]Gas-Phase FTS at 240 °C and 20±2 bar.

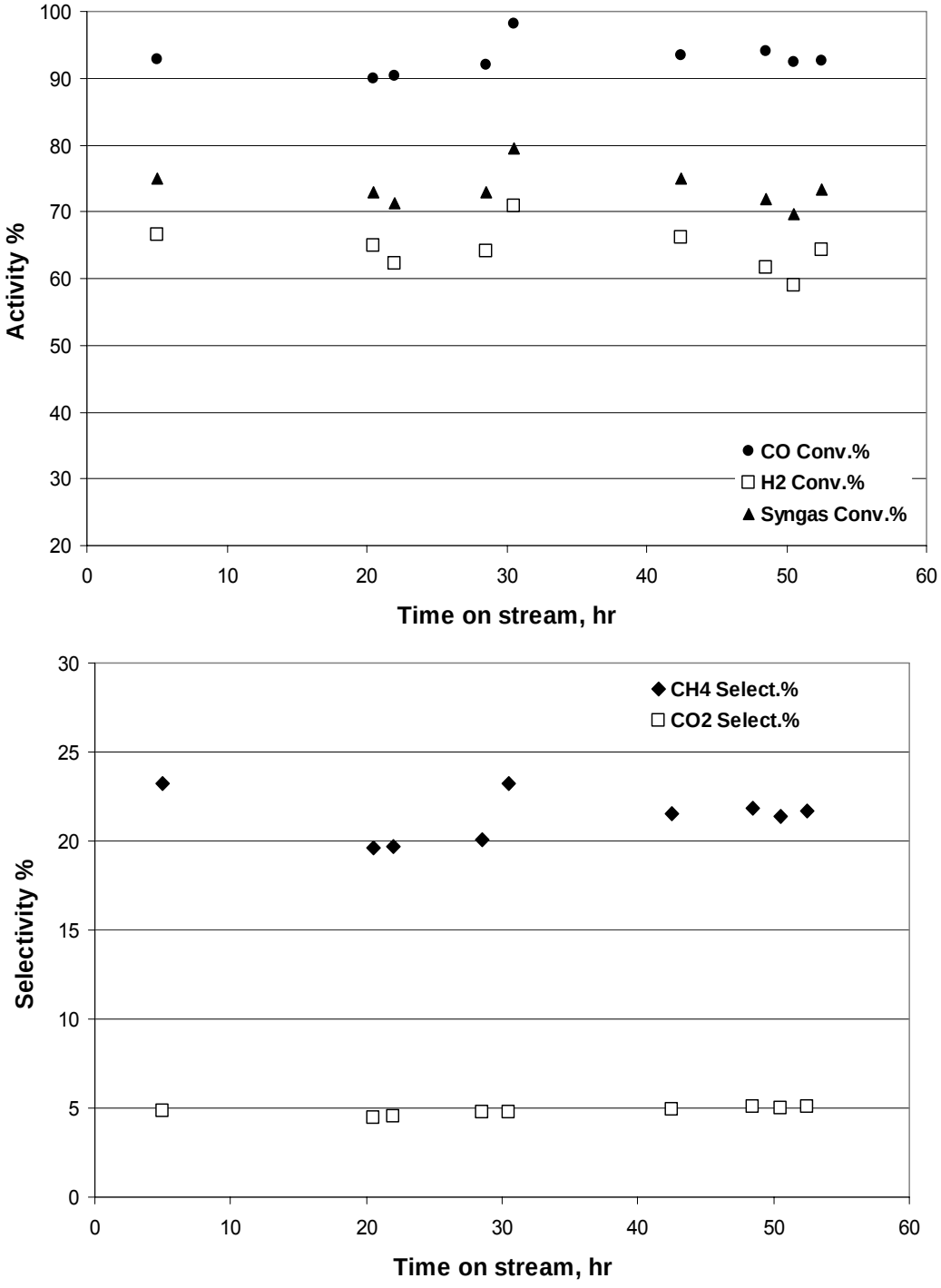

Fig. 1. Stability of the activity and selectivity of the silica supported catalyst (A1/C) with time-on-stream.

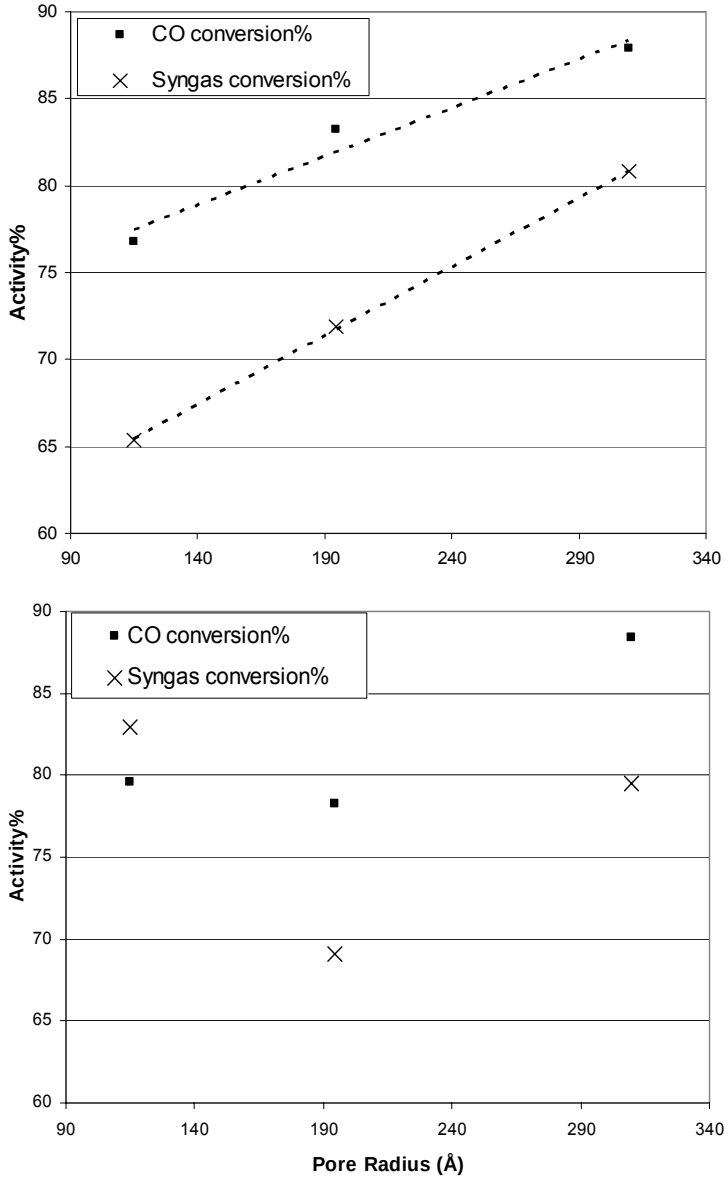

Fig. 3 Influence of pore diameter on the activity of cobalt-base catalysts under (a) gas-phase FTS, and (b) SCH-FTS at 240 °C and P_{syngas} of 20 bar.

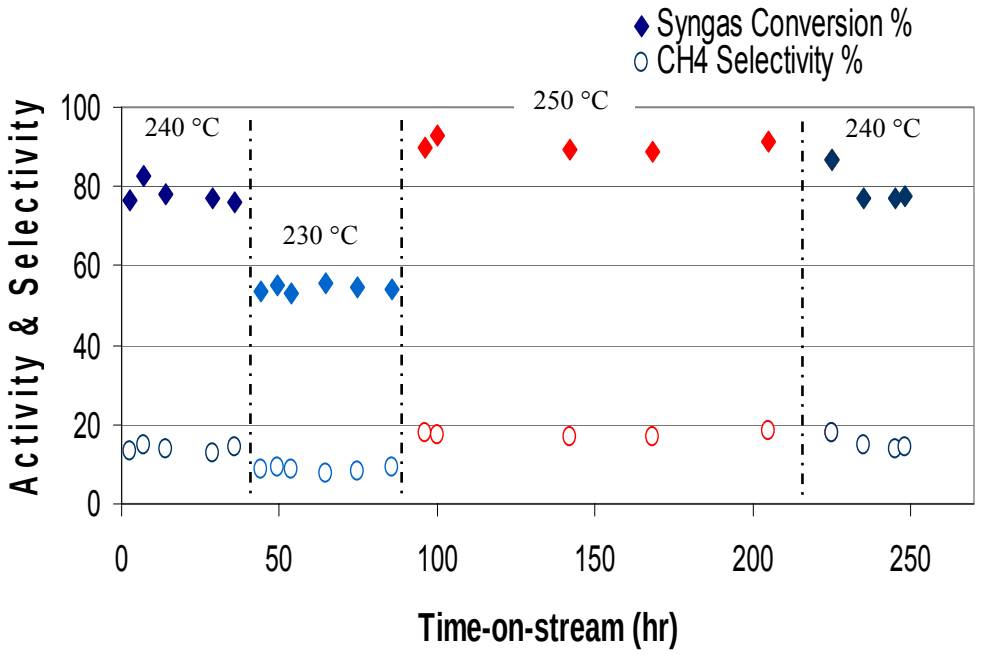

Fig. 4 Stability of the 15% Co/Al_2O_3 with TOS in SCH-FTS at different reaction conditions (240 °C and 60 bar; 230 °C and 60 bar; 250 °C and 65 bar; and 240 °C and 60 bar). P_{syngas} = 20 bar, syngas flowrate 50 sccm/g_{cat}, and hexane/syngas molar ratio is 3.

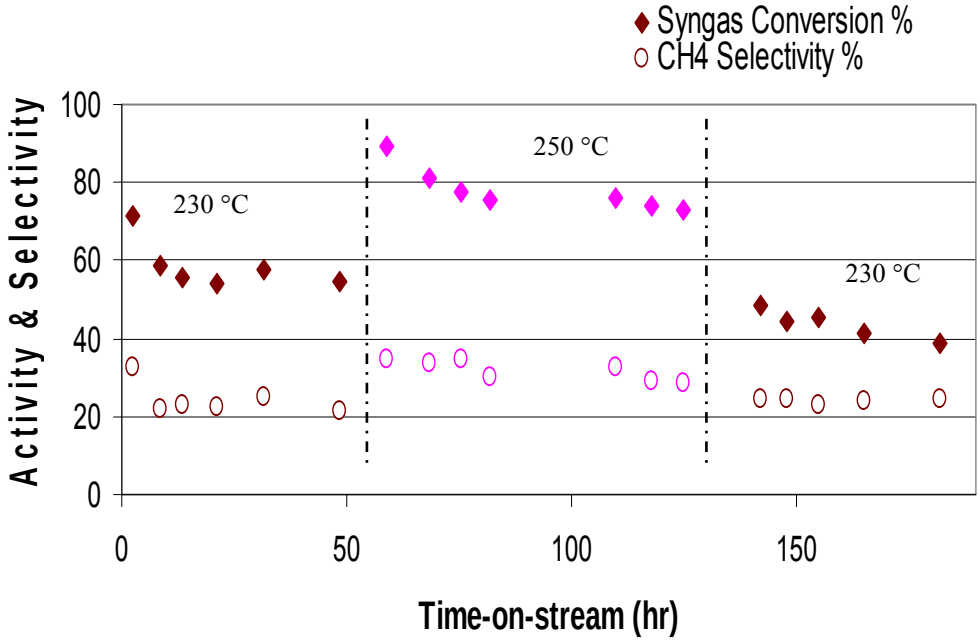

Fig. 5 Stability of the 15% Co/Al_2O_3 with TOS in gas phase-FTS at different reaction conditions (230 °C and 20 bar; 250 °C and 20 bar; and 230 °C and 20 bar). P_{syngas} = 20 bar, syngas flowrate 50 sccm/g_{cat}.

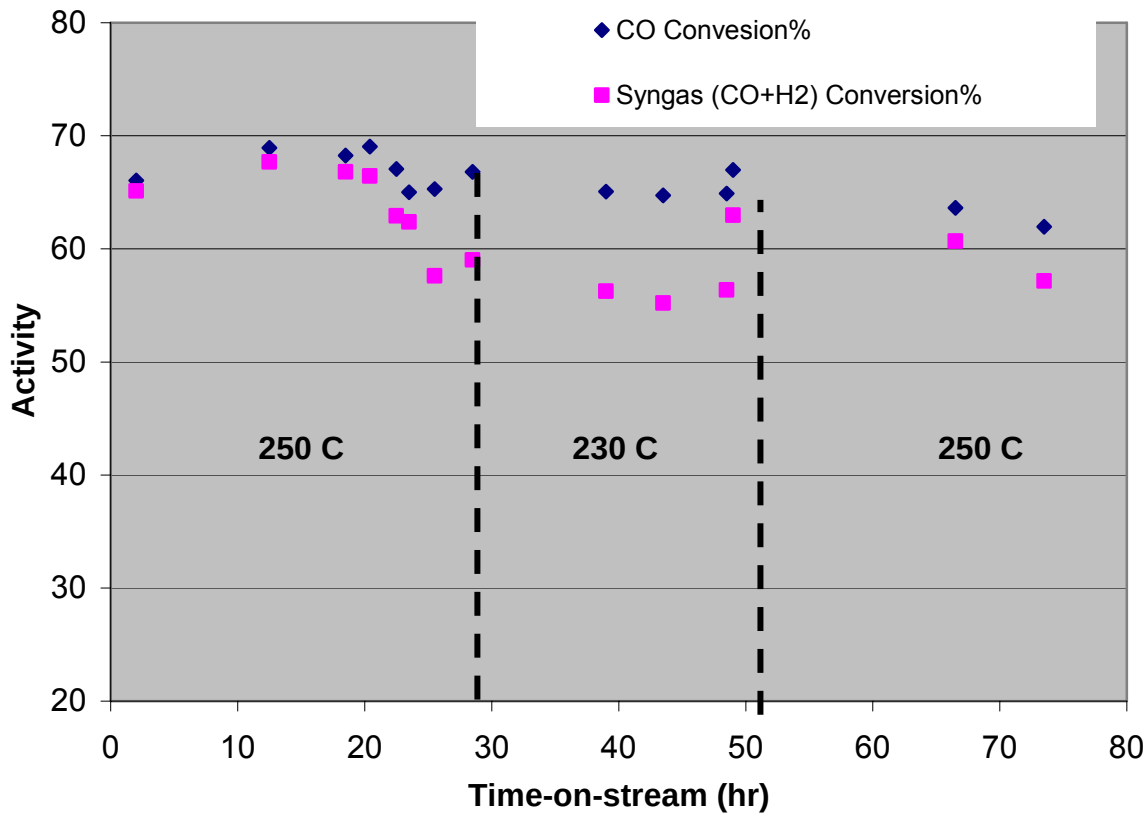

Fig. 6 Stability of Ruthenium Catalyst with TOS in near-critical phase FTS at different conditions (250 °C and 230 °C). P_{syngas} = 20 bar, syngas flowrate 50 sccm/g_{cat}.

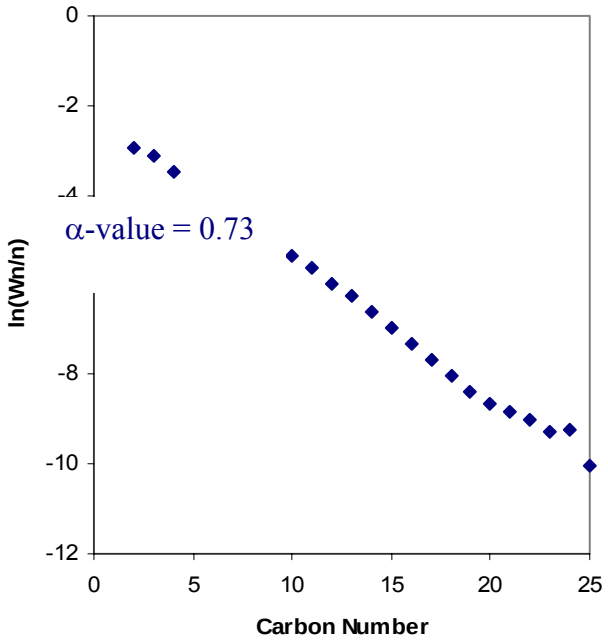

Fig. 7 Hydorcarbon product distribution on 10% Ru/SiO_2 catalyst at 250 °C and total pressure of 35 bar on SCF (hexane)-FTS (Run# Ru-07).

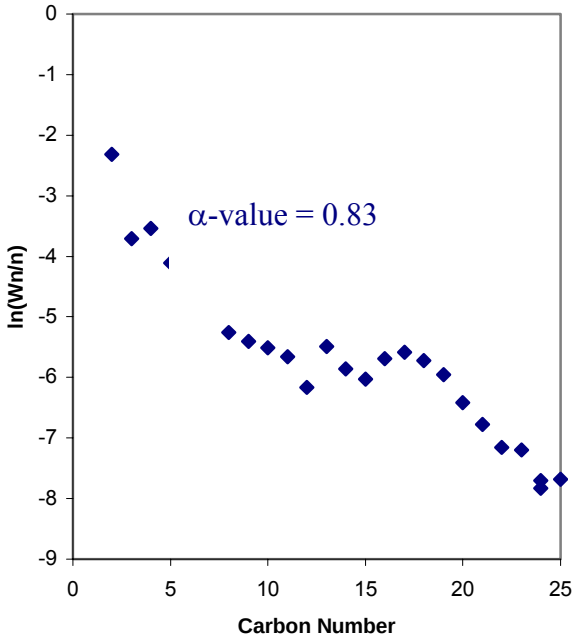

Fig. 8 Hydrocarbon product distribution on 10% Ru/SiO_2 catalyst at 250 °C and total pressure of 35 bar on SCF (hexane)-FTS (Run# Ru-15).

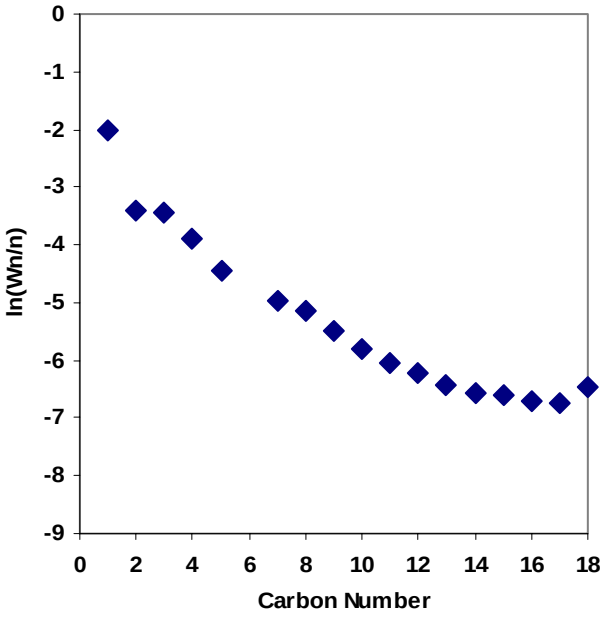

Fig. 9 Hydrocarbon product distribution on the iron catalyst, 230 °C, 45 bar in SCF (hexane)-FTS.

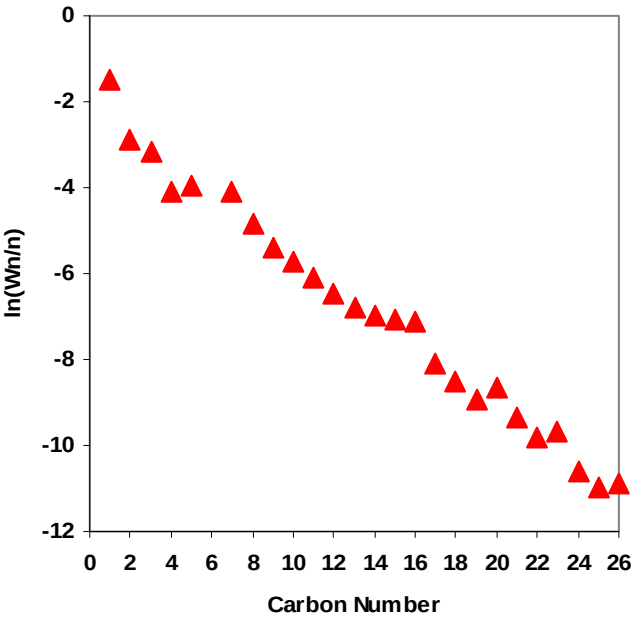

Fig. 10 Hydrocarbon product distribution on the iron catalyst at 230 °C and 45 bar in SCF (hexane)-FTS.

Science behind Catalysis in C1 Reactions: Catalyst Characterization and Determination of Active Species

M. S. Seehra, and P. Dutta
Physics Department, West Virginia University.

Final Technical Report, January, 2006

I. Introduction

The objectives of our research have been to characterize analytically various catalysts used by CFFS researchers (before and after their conversion experiments) in order to determine the active species for catalysis and to relate their properties to yields and product distributions. Since catalytic reactions occur at the nanoscale, we also have a strong program in nanomaterials.

In this report, we summarize the results of our investigations in these areas during the past year or so. The CFFS researcher have reported a number of studies of Fischer-Tropsch (FT) synthesis using cobalt catalyst supported on high surface area xerogel [1], aerogel [2,3], SiO_2 and Al_2O_3 [4,5]. The factors that effect the yields and product distribution of the FT products include operating temperature and pressure, surface area and pore size of the support, particle size and dispersion of cobalt and its electronic state (Co^0, Co^{2+}, Co^{3+}). To prepare the Co loaded catalyst, Co is usually impregnated as an oxide, followed by reduction and/or calcination to produce the desired Co^0 state which is the active catalyst. In order to compare the yield and product distribution with Co loading, it then becomes essential to determine the concentration of the various electronic states and phases of Co present in the catalyst. Here we summarize the results of our recent investigations for determining the different oxidation states of Co and their concentrations in Co/xerogel, Co/aerogel, Co/SiO_2 and Co/Al_2O_3 catalysts. Only summary of these results is presented below, with the details given in the quoted papers [1-8]. Structural and electronic properties nanoparticles of NiO, γ-Fe_2O_3, and FeOOH have also been reported [9-11].

II. Experimental

The crystalline phases present in a catalyst were determined by room temperature x-ray diffraction (XRD) in a Rigaku diffractometer using CuK_α radiation ($\lambda = 0.15418$ nm). The XRD technique is able to detect phases with concentration ≥ 3 %. The magnetic phases such as Co^{2+}, Co^{3+},Co^0, CoO, and Co_3O_4 were determined by magnetic measurements which were done using a commercial SQUID (superconducting quantum interference device) magnetometer. Additional information on states such as Co^{2+} was also determined by EMR (electron magnetic resonance) spectroscopy at the X-band frequency f = 9.28 GHz with a variable temperature (4 K to 300 K) cryostat. The important information on the electron state is contained in the g-value given by the EMR resonance condition $hf = g\mu_B H_0$, where h is the Planck's constant, μ_B is the Bohr magneton and H_0 is the resonance field of the EMR lines.

III. Results and Discussion

An example of the information obtained from the XRD studies is given in Fig. 1.Here we have shown the XRD patterns of Co/xerogel catalyst in which clear identification of Co^0, CoO and the support SiO_2 (xerogel) is made. (This figure is from the supporting materials of Ref. 1). In the Co/SiO_2 catalysts of Ref. 4, the XRD studies could only detect Co_3O_4, and Co^0 and CoO were absent [4]. Thus which phases of Cobalt (Co^0, CoO or Co_3O_4) are present in a catalyst depend on the experimental conditions the catalyst is exposed to and these different states can usually be detected by XRD.

Careful analysis of the temperature (T) and magnetic field (H) variation of the magnetization (M) provide additional details about the electronic states of cobalt and their concentrations. The presence of CoO and Co_3O_4 are detected from the peaks in susceptibility χ = M/H at temperatures T ≈ 300 K and T ≈ 40 K respectively [3-5] whereas if Co^0 is present, it dominates the measured magnetization from which its concentration can be determined [3]. In Fig. 2, we show our recent data from Ref. 3 on the χ vs. T variation in 10% Co/aerogel catalyst. The peak in χ near 20 K is due to Co^0 nanoneedles with diameter d ≈ 1 nm, whereas the peak in χ near 300 K (Fig. 3) is due to the presence of CoO. From the magnitude of the saturation magnetization of this sample at 5 K, the concentration of Co^0 was determined to be around 8%. If Co^0 is simultaneously present with either CoO or Co_3O_4, then from the behavior of the hysteresis loop of Co^0 in a field cooled sample, it can be determined whether Co^0/CoO or Co^0/Co_3O_4 are present as composite systems in core-shell structures or as individual phases. A shifted hysteresis loop under field-cooled conditions represents a core/shell structure [1]. An example of this is given in Fig. 4 for the 5% Co/xerogel sample. Here the hysteresis loop is shifted by 55 Oe when the sample is cooled in 10 kOe suggesting a core/shell structure for Co and CoO in this sample.

Another possibility for the cobalt state is that cobalt is incorporated substitutionally into the support (e.g as $Co_xSi_{1-x}O_2$) or chemisorbed on the surface of the support with bonding provided by surface absorbed H_2O and O_2. In such cases, the χ vs. T data follows the Curie-Weiss law: $\chi = \chi_0 + [C/(T-\theta)]$ where C gives the concentration of the Co^{+n} ions [4]. Furthermore, the variation of M vs. H at a low temperature (2 K) can be used to distinguish between Co^{2+} and Co^{3+} ions [4]. In the EMR studies of such materials, the presence of an EMR line at g = 4.3 is definite confirmation of the presence of Co^{2+} ions [6].

Next, the relationship between the different electronic states of cobalt and their concentrations with the F-T products and their distributions is discussed briefly. In the conventional gas-phase FT synthesis at 240^0C and 20 bar pressure, it was found that the presence of Co_3O_4 yields higher methane selectivity whereas the presence of Co^{2+} species yielded lower methane selectivity but higher olefin selectivity [4]. Similarly why the FT activity of 10 % Co/aerogel catalysts is not much better than that of 6 % Co/aerogel [2] has been explained in our recent work [3] in that the 10% Co/aerogel contains unreduced CoO and a complex cobalt silicate in addition to the desired Co^0.

To determine the morphology of the nanophases in the catalysts, we have used transmission electron microscopy, courtesy of the University of Kentucky and NIST (National Institute of Standards and Technology, Gaithersburg, MD). In the Figs. 5, 6 and 7, we show the TEM micrograph of the nanoparticles of NiO [11], γ-Fe_2O_3 [9] and 10%Co/aerogel [3]

respectively. Whereas the NiO particles are in the form of nanorods, γ-Fe_2O_3 have nearly spherical particles and the Co/aerogel samples of Co nanoneedles are of diameter ≈ 1 nm. Thus nanoparticles and nanocatalysts come in various shapes and sizes which do affect their properties and applications since different shapes represent different surface areas per unit volume. In the cited publications, we have correlated the measured properties with the morphologies of the particles. Thus a variety of experimental techniques are needed (and have been employed here) to properly characterize the catalysts used by the CFFS researchers. The availability of these techniques along with the collaborations among the CFFS researchers is a major strength of this program.

V. Papers Published/References

1. Silica Xerogel Supported Cobalt Metal Fischer-Tropsch Catalysts for Syngas to Diesel Range Fuel Conversion: B. C. Dunn, D. J. Covington, P. Cole, R.J. Pugmire, H.L.C. Meuzelaar, R.D. Ernst, E.C. Heider, E. M. Eyring, N.Shah, G.P. Huffman, M. S. Seehra, A. Manivannan, and P. Dutta; Energy & Fuel, 18, 1519-1521, (2004).

2. Silica aerogel supported catalysts for Fischer-Tropsch synthesis: B. C. Dunn, P. Cole, D. J. Covington, M.C. Webster. R.J. Pugmire, R.D. Ernst, E. M. Eyring, N.Shah, and G.P. Huffman; Appl. Catal. A: General, 278, 233-238 (2005).

3. Characteristics of Cobalt nanoneedles in 10% Co/aerogel Fischer-Trosch catalyst: P. Dutta, B.C. Dunn, N. Shah, E. M. Eyring, G. P. Huffman, A. Manivannan and M.S. Seehra; Chem. Materials, 17, 5183-5186 (2005).

4. Characterization of Fischer-Tropsch Cobalt-based Catalytic Systems (Co/SiO_2 and Co/Al_2O_3) by X-ray Diffraction and Magnetic Measurements: P. Dutta, N.O. Elbashir, A. Manivannan, M.S. Seehra, and C.B. Roberts; Catalysis Letters 98, 203-210 (2004).

5. Impact of Cobalt-based Catalyst Characteristics on the Performance of Conventional Gas-Phase and Supercritical-Phase Fischer-Tropsch Synthesis: N.O. Elbashir, P. Dutta, A. Manivannan, M.S. Seehra, and C.B. Roberts; Applied Catalysis A : General; 285, 169-180, (2005).

6. Nature of the reversible paramagnetism to ferromagnetism state in cobalt-doped TiO_2: A. Manivannan, G. Glaspell, P. Dutta and M. S. Seehra, J. Appl. Phys. 97, 10D325 (3 pages) 2005.

7. Determination of different electronic states of cobalt in Fischer-Tropsch catalysts: M. S. Seehra, P. Dutta and A. Manivannan; Prepr. Paper – Am. Chem. Soc. Div. Fuel Chem. 50, 638-639 (2005).

8. Stability and structure of cobalt catalytic systems in Fischer-Tropsch synthesis: Supercritical fluid media versus convensional gas-phase media; N.O. Elbashir, P.

Dutta, M.S. Seehra, and C.B. Roberts; Prepr. Paper – Am. Chem. Soc. Div. Fuel Chem. 50, 638-639 (2005).

9. Magnetic properties of nearly defect-free maghemite nanocrystals: P. Dutta, A. Manivannan, M. S. Seehra, N. Shah and G. P. Huffman; Phys. Rev. B, 70, 174428 (7 pages) (2004).

10. High frequency electron magnetic resonance and magnetic studies of ferrihydrite nanoparticles and evidence of a phase transition: A. Punnoose, M. S. Seehra, J. van Tol and L. C. Brunel; J. Magn. Magn. Mater. 288, 168-172 (2005).

11. Interparticle interaction effects in the magnetic properties of 5 nm NiO nanorods: M. S. Seehra, H. Shim, P. Dutta, A. Manivann, J. Bovevich; J. Appl. Phys. 97, 10J609 (3 pages) (2005).

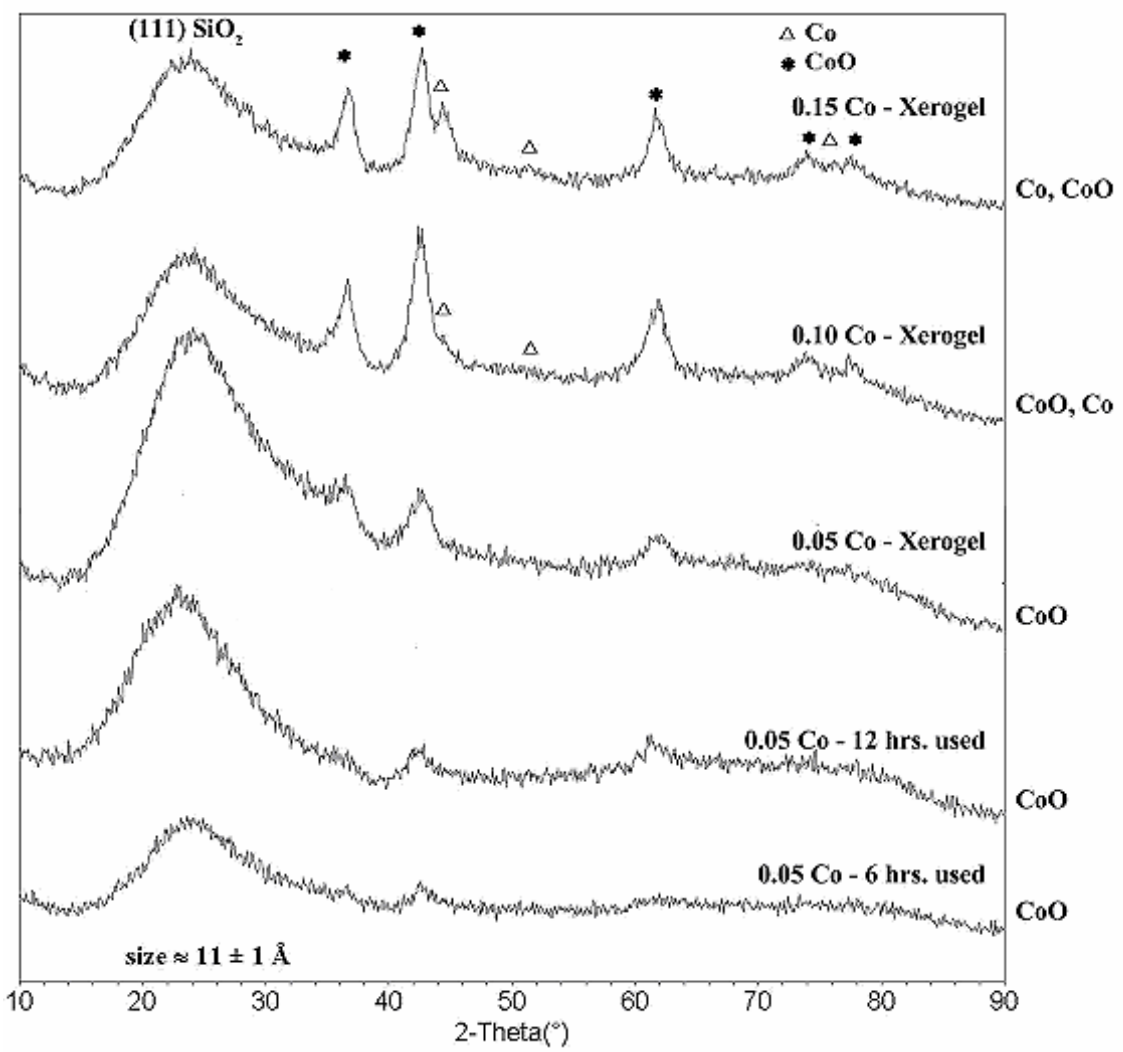

Figure 1. Room Temperature x-ray diffractograms of five samples of Co/xerogel with the peaks for Co^0, CoO and SiO_2 identified. The size ≈ 11 Å is for SiO_2 [Ref. 7].

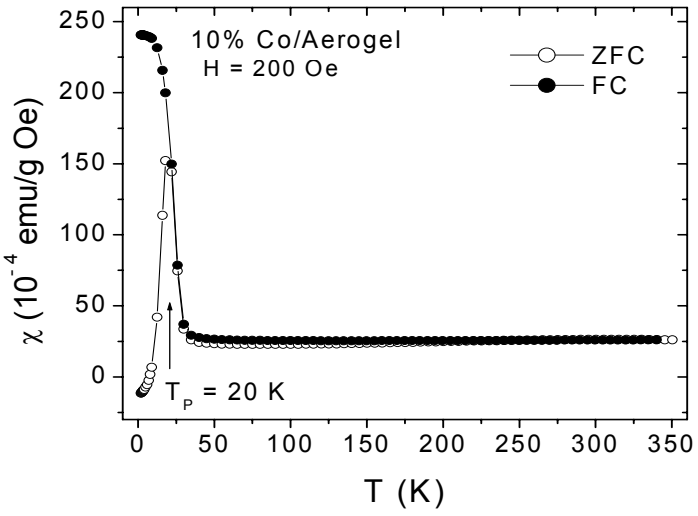

Figure 2. Temperature dependence of the magnetic susceptibility χ of 10% Co/aerogel catalyst for the ZFC (zero-field cooled) and FC (field-cooled) cases [Ref. 3].

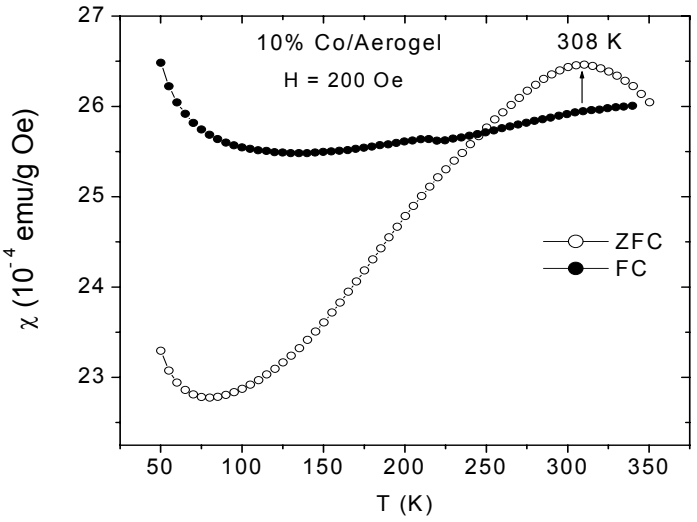

Figure 3. Expanded version of the χ data of Figure 2 for higher temperatures [Ref. 3].

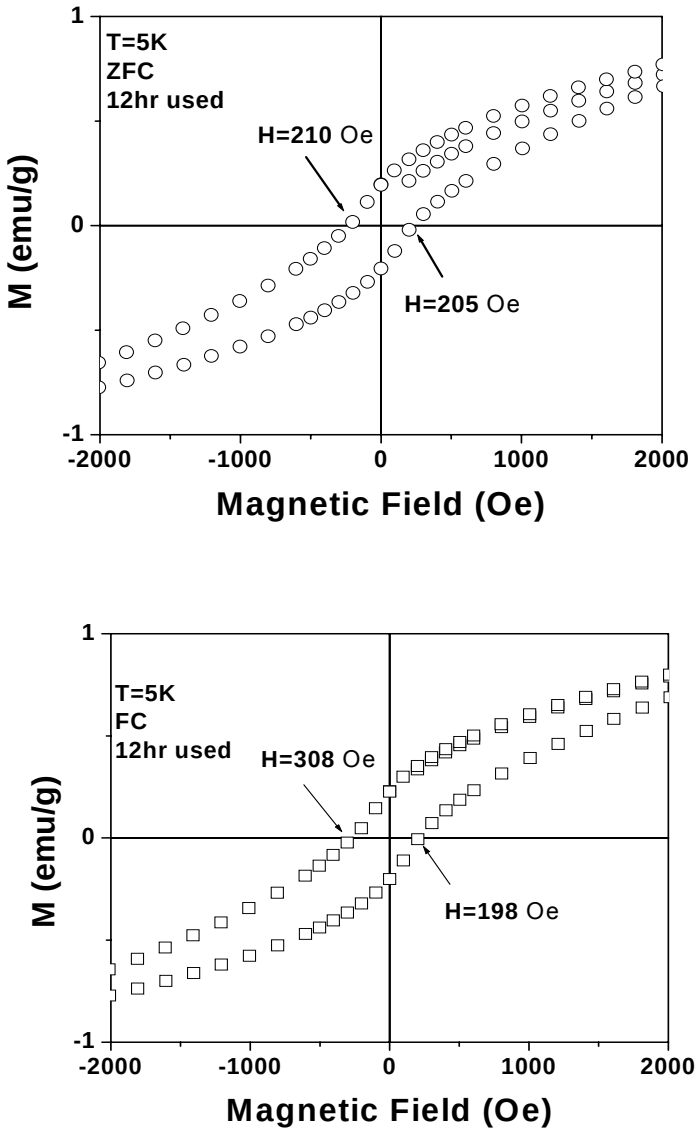

Figure 4. Hysteresis loops measured at 5 K for the 12-hr sample of 0.05 Co/aerogel under the ZFC and FC (H = 10 kOe) conditions. The loop shift for the FC case supports the core/shell model discussed in the text [Ref. 7].

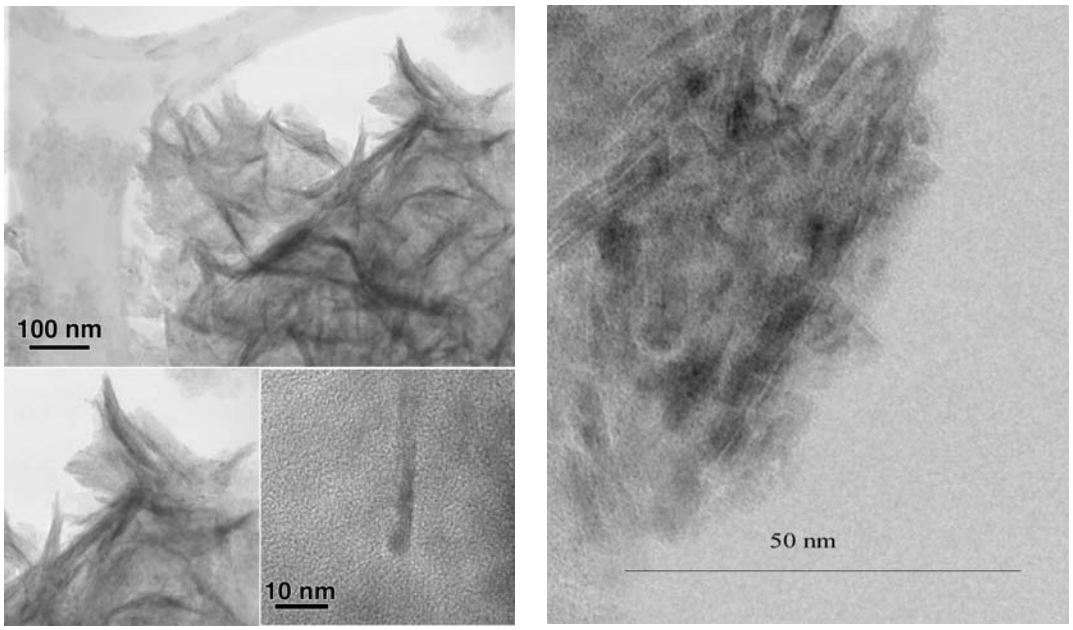

Figure 5. TEM micrographs of the NiO nanorods of diameter ≈ 5 nm [Ref. 11].

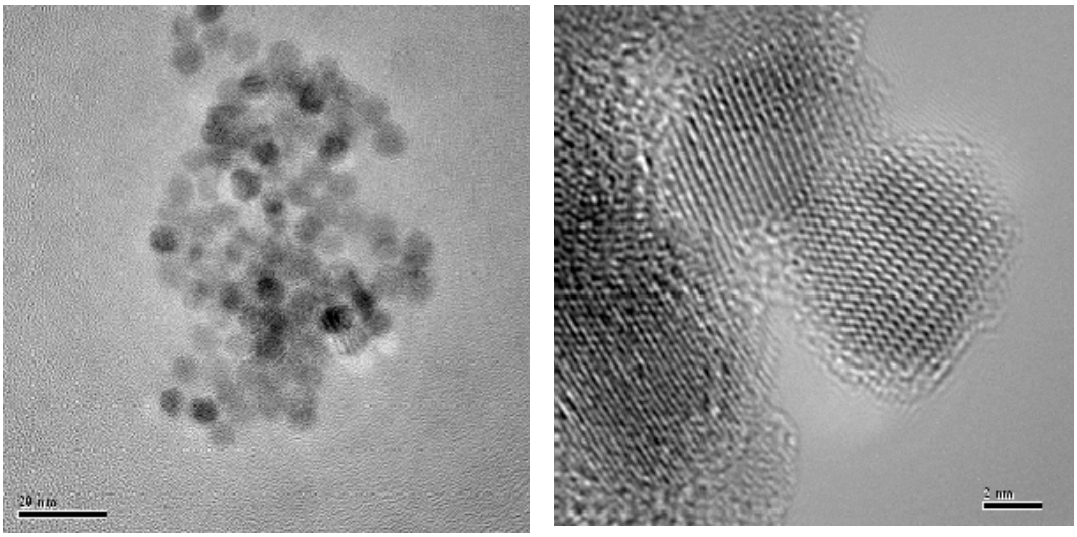

Figure 6. TEM micrographs of the γ–Fe_2O_3 nanocrystals at two different magnifications. The bar length on the left (right) picture is 20 nm (2 nm) [Ref. 9].

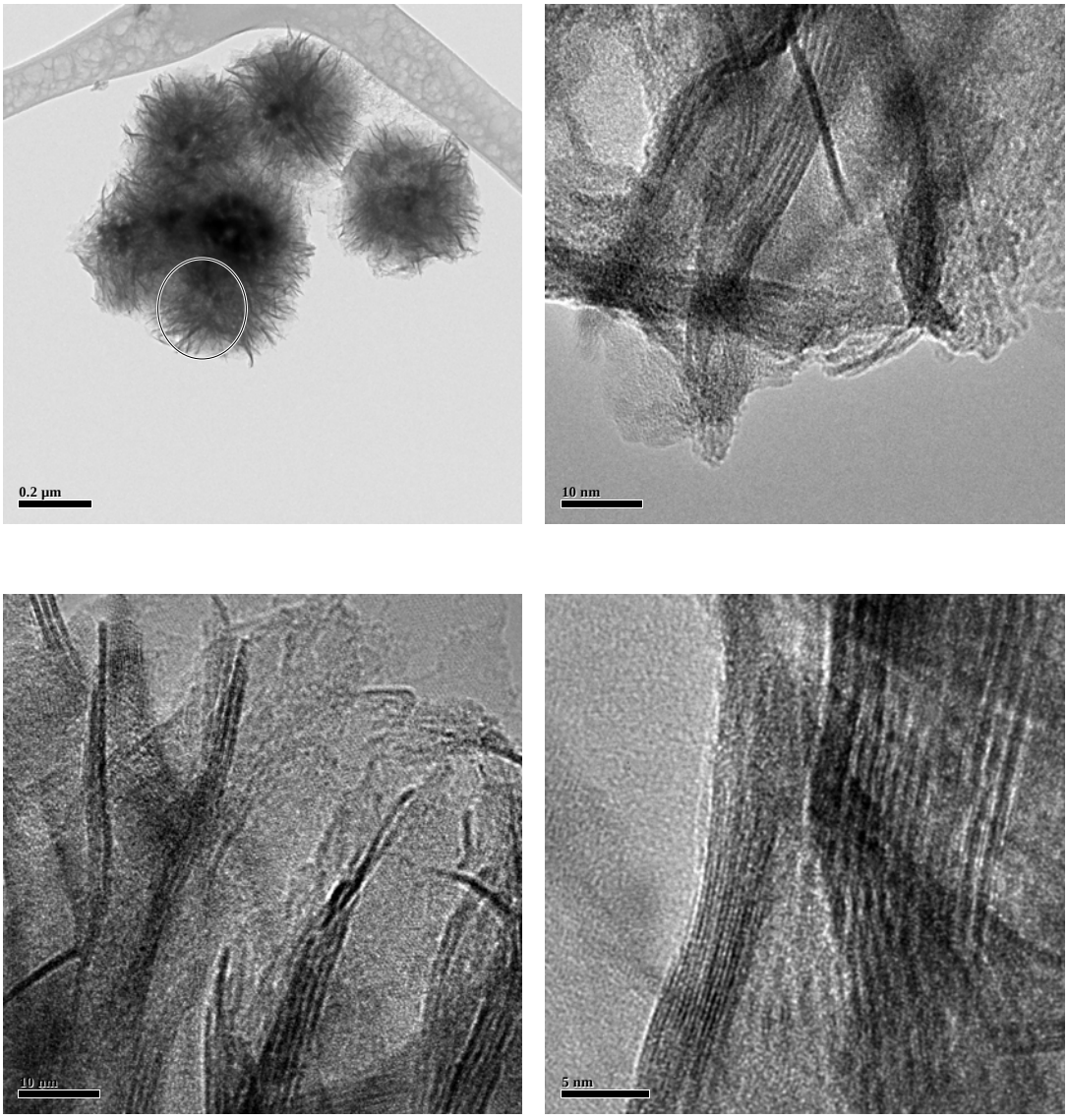

Figure 7. TEM micrographs of the 10% Co/aerogel sample with different magnifications [Ref. 3]. Co nanoneedles with diameter ≈ 1 nm are observed.

**New Catalysts for the Production of Chemicals,
Light Olefins and Hydrogen via C-1 Chemistry**

Xiwen Huang, Luckner Jean, and James A. Guin
Department of Chemical Engineering
Auburn University, Auburn, AL, 36849-5127

Introduction.

Our final report for this contract discusses research in two areas: (1) The production of light olefins and chemicals from methanol using SAPO catalysts, and (2) the production of hydrogen by dehydrogenation of cyclohexane over SBA supported Pt and Ru catalysts.

Light Olefins Production with SAPO catalysts. The motivation for our studies in this area is that high value chemicals can be produced from remote flared methane, coal, and other sources of biomass by first converting these raw materials to syngas (CO/H_2). The syngas can then be converted directly to chemicals, e. g. Fisher-Tropsch, or can be converted to methanol and then to chemicals by processes such as the methanol-to-olefins (MTO) process. A demonstration plant for this MTO process has been operated by UOP/Hydro in Norway for about 10 years at a capacity of about 1 ton/day using a catalyst based on SAPO-34. It has been stated that Eurochem is planning to build an MTO plant in Nigeria, which will convert the olefins produced to polymers at about a 0.5 million tons/year capacity. While these developments are interesting, there is apparently no currently operating commercial plant using SAPO catalysts to produce olefins from methanol or syngas. We have been performing research to develop and further understand the chemical and process variable effects of MTO reactions over various SAPO catalysts.

As noted by Dahl, several mechanisms, such as the "hydrocarbon pool mechanism" have been proposed for the MTO reaction[1]. One of the simplest pathways is the simple series pathway:

$$\text{Methanol} \rightarrow \text{DME (dimethylether)} \rightarrow \text{olefins}$$

The olefins can be further converted to fuels, or higher molecular weight products such as polymers. The main interest in our research is the lower C2 – C4 olefins. We have been studying the effects of process and catalytic variables on the process. As summarized in our previous reports in this series, we have been focusing on the so called SAPO (silicoaluminophosphate) molecular sieve (microporous) catalysts with crystal structures and pore sizes of less than 1 nm. These catalysts are a variation of the aluminophosphate catalysts developed by Wilson, et al. in which silicon atoms are substituted for some of the framework phosphorous atoms[2,3]. The SAPO catalysts exhibit Bronsted acidity and are typified by SAPO-5, SAPO-31, and SAPO's 34, 44, 47, and 56 with pore sizes of ca. 0.8 nm, 0.6 nm, and 0.4 nm respectively. A recent review concerning these catalysts is given by Pastore, et al.[4].

In our previous research, we have investigated the effects of catalyst acidity (Si content), presence of heteroatoms, e. g. Ni, Co, Ru, Fe, etc., and process variables such as temperature, space velocity, and water content of the methanol feed [5-7]. This year, we have concentrated our work on the effects of catalyst particle size on the lifetime and selectivity of the small pore SAPO catalysts on the MTO reaction. In addition, some of these catalysts were modified by Ru

addition using a vapor-phase addition technique developed by Dr. Ernst and colleagues at the University of Utah [8].

Hydrogen Storage and Production. In addition to the SAPO catalyst work noted above, we have also performed some work in the production of H_2 by dehydrogenation of cycloalkanes. In order to produce H_2 locally for fuel cells or for transportation purposes, many different methods have been attempted. These methods include pressurized H_2, cryogenic storage, adsorption on carbons, nanotubes, zeolites and other materials, storage in glass microspheres, reforming reactions, metal hydrides, and MOF's. All of these methods have various shortcomings, based primarily on economic or safety problems. Another method which has been proposed for the local production of H_2 is the dehydrogenation of cycloalkanes such as cyclohexane (CH), methylcyclohexane, tetralin, decalin, etc. This method has the advantages of no CO or CO_2 production, carrier compounds which are relatively cheap and nontoxic, and it can use current infrastructure for distribution by way of barge, rail, pipeline, or truck. Regeneration of the aromatic carrier compound can be performed at a central or remote location. Of course this method of H_2 distribution and storage produces no net H_2, but only acts as a distribution method. Several relevant references exist on the above methods of H_2 production, storage and distribution [9-16].

A disadvantage of using cyclohexanes to store hydrogen is the requirement of a chemical reaction to release, and regenerate, the hydrogen from the carrier. This reaction will require an efficient catalyst. One type of promising catalysts is based on metals supported on mesoporous silica sieves. Such seives are typified by the M41S family, of which the most notable is MCM-41. This particular support possesses an ordered honeycomb pore structure of hexagonal pores of 1-10 nm, and a surface are of 500-1000 m^2/g with low acidity [17]. A related group of mesoporous catalysts is the SBA catalysts developed by Stucky and coworkers [18]. This latter family is typified by SBA-15 which is similar to MCM-41, except that it has somewhat thicker Si pore walls, containing an associated microporosity [19]. These mesoporous catalyst supports are made by a templating procedure using a PEO-PPO-PEO triblock copolymer, or alkyl PEO surfactants, which are nontoxic, commercially available surfactants, at temperatures from 25 -100 ^oC in acidic solution. The silica source in our work is TEOS, although other sources may be used. The solids are recovered, dried, calcined, and metals are added. In the synthesis process, the EO/PO copolymer ratio affects the mesophase type and an organic cosolvent, 1,3,5 trimethylbenzene, allows pore expansion. There are also many other mesoporous silicas among which are HSM, PCH, KIT, FSM, MSU-n, etc.[20]. The mesoporous silicas have been used for catalyst supports in many chemical reactions such as Co-Ru/MCM-41 for F-T reactions, Pd/SBA-15 for hydrodechlorination of 1,1,2 trichloroethane, VO_x/SBA-15 for oxidative dehydrogenation of propane, and P-W-Zr oxides/SBA-15 and MCM-41 for n-pentane isomerization [21-25]. As yet, however, these mesoporous silicas have found little commercial utilization due to their lack of mechanical and hydrothermal stability. Thus more work is needed before these catalysts obtain widespread application.

In our research we have studied the development of the above mesoporous silicates, such as SBA- n, as possible supports for metal, e. g. Pt, Ru, catalysts to be used as dehydrogenation catalysts. As noted above, mesoporous sieves possess high surface areas (700-1500 m^2/g), pore volumes (0.8-1.2 cm^3/g) and ordered pore structures with narrow size distribution and the pore diameter can be tailored from 2 to 50 nm [18, 26-29].

Experimental.

Catalyst Synthesis. The synthesis of mesoporous SBA-11, -12, -15, and -16 was performed per literature methods [18]. Chemicals used include the following: tetraammine palladium(II) chloride monohydrate ($Pt(NH_3)_4Cl_2 \cdot H_2O$), tetraethoxysilane (TEOS); 1, 3, 5-trimethylbenzene(TMB); Brij 56($C_{16}EO_{10}$); Brij 76 ($C_{18}EO_{10}$); poly(ethylene glycol)-poly(propylene glycol)-poly(ethylene glycol) triblock copolymer, $EO_{20}PO_{70}EO_{20}$ (Pluronic 123), 2M HCl solution; $H_2PtCl_6.6H_2O$; $Pt(NH_3)_4Cl_2$; methanol (MeOH), were used as received. Deionised water was employed during the synthesis. All chemicals were from Aldrich. A typical synthesis was performed as follows for SBA-11: 80 g 2M HCl solution (0.16 mol) and 20 g H_2O (5.23 mol) are added into a 250 ml beaker, then 4.0g Brij 56(0.005856 mol) is added to the above solution with stirring for 1hr until the Brij 56 dissolve completely. Leave the solution stable for 10 min, then 8.80g TEOS (0.0422 mol) is added to that homogeneous solution with stirring at room temperature for 24 hrs. The produced solid is then recovered by centrifuge, washed and air dried at room temperature. Calcination of the SBA-11: 1g SBA-11 product is introduced to the furnace, temperature in the furnace is slowly increased to 500^oC at ramp of 1^oC/min, and kept at 500^oC for 6hr with air flow of 20 cc/min.

For our MTO work, SAPO's 34, 44, 47, and 56 (0.3, 0.6, and 0.9 mol Si/mol P_2O_5) catalysts synthesized previously by Dr. Prakash M. Adekkanattu as reported earlier under this contract were utilized [30, 31].

Metals addition: Three methods were used to add Pt to the mesoporous SBA silica supports. These were impregnation, ion exchange, and a vapor phase method developed by Dr. Ernst and co-workers at the University of Utah [8]. For impregnation, we used hydrogen hexachloroplatinate hydrate, $H_2PtCl_6 \bullet 6H_2O$; for ion exchange, tetraamine platinum chloride, $Pt(NH_3)_4Cl_2$ and for sublimation impregnation, bis (2,4dimethylpentadienyl)ruthenium. Additional details regarding metals addition are provided in our previous 6-month progress report available on the CFFS website.

Characterization. TEM was performed at the University of Kentucky by Dr. Shah and co-workers to characterize mesoporous SBA structure. SEM micrographs were obtained at Auburn University by Jean [32].

Reactions. Both cyclohexane dehydrogenation and MTO reactions were performed in fixed bed reactors with products analyzed by gas chromatography. Detailed reaction conditions and reactor diagrams were provided in our previous reports and by Jean [32]. For particle size reduction, samples were ground for 5, 10, and 15 min. time intervals with a Wig-L-Bug® grinder (Figure 1). All analyses were by Varian 3000 GC and analyzed by computerized software and spreadsheets. (Figures 2 and 3). The spreadsheet in Figure 3 also indicates a carbon balance for the reaction period.

Results and Discussion.

Micrographs. The TEM micrographs obtained at the University of Kentucky by Dr. Shah and colleagues for various SBA supports showed several mesoporous structures as pictured in Figure 4. Both end-on and side views are shown for the SBA-15. The presence of hexagonal two-dimensional mesoporous structure is apparent for the SBA-15 in the first 3 images. The last image (lower right) shows the mesostructure for SBA-11. Other TEM meso-structures observed

were shown in our previous 6 month report. As noted there, the SBA-16 preparation did not appear to have an ordered pore structure. It also appeared that some of the SBA supports lost their ordered pore structure on Pt impregnation, however good catalytic activity was observed in most cases. Figure 5 shows SEM micrographs of SAPO-34 crystals taken by Jean [32]. In this case the crystals are *ca*. 13 μm in size. This dimension was reduced by grinding for various times in the grinder in Figure 1. The effect of the grinding process on the crystallinity was not determined, but this could be examined by X-Ray diffraction if desired. Nonetheless, the reduction in crystal particle size usually resulted in some, albeit slight, increase in catalyst activity and lifetime.

Light Olefins Production. Figure 6 shows the effect of grinding on MTO reactions using SAPO-34 crystals shown earlier in Figure 5. Comparing the original crystals (top) with the same reaction using crystals after 5 min of grinding (bottom), it is apparent that there is a slight increase in production of C2-C4 olefins with the ground crystals. For example about 55% C_2-C_4 olefins production remains at 4 hrs. with the ground catalyst vs. as compared to no light oelfins production with the original catalyst. Similar results were shown in our 6 month report for SAPO-44. The effect of grinding for additional time periods on C_2-C_4 olefins production with SAPO-34 is shown in Figure 7**.** The particle size reduction results in a doubling of catalyst lifetime from about 4 to 9 hours for light olefins production. The exact reasons for the beneficial effects of grinding are not completely clear, but could be related to the greater effectiveness factors for the smaller particles and the greater ratio of external surface to volume.

Figure 8 shows the effect of temperature on the MTO performance of SAPO-56 with a 0.6 Si ratio. In this experiment, the temperature was ramped from 300 to 500 C with a single catalyst charge and 1 hr holding time at each 50 ^{o}C temperature increment. In general, the production of methane (C1) increases up to a temperature of *ca*. 450 C; however, at 500 ^{o}C the catalyst is essentially deactivated as noted by the presence of DME and MeOH as main products. Figure 9 shows the effect of Si content on MTO reactions for SAPO-56. It appears that the intermediate Si content (0.6 Si ratio) is most beneficial for the production of C_2-C_4 olefins. The effect of Si is possibility related to the acidity of the catalyst and hence the rate of coke formation, which causes the deactivation. Results of an attempt to regenerate the spent SAPO-56 catalyst by grinding are shown in Figure 10. These results show that grinding alone is ineffective in catalyst regeneration, perhaps because the coking process is not confined to the outer perimeter of the particles. However, oxidation is effective in regeneration of the catalyst, as shown by our earlier work.

Figure 11 shows the effect of Ru addition on the MTO performance of SAPO-34. As a comparison of Figure 7 (top) and Figure 11 reveals, SAPO-34 yield, activity, and selectivity diminished somewhat after Ru modification. Similar data for the effect of Ru modification of SAPO-44 was shown in our previous report. Likewise, results for modified and unmodified 56 indicated the Ru modified-SAPO catalyst activity was about the same as the unmodified SAPO catalyst activity.

Hydrogen Production by Cyclohexane Dehydrogenation. Our work in this area was summarized in detail in the previous 6-month report. For the readers convenience, we show here Figure 12 which is a summary of this work. As this figure shows**,** among the Pt SBA's which were made in our laboratory, and two commercial catalysts, 1% Pt/C and 1%Pt/Al_2O_3, the 1% Pt/SBA-15 gave highest conversion and is actually higher than the two commercial catalysts. These results show that the SBA supports offer considerable promise for the production of

hydrogen by dehydrogenation of cyclic alkanes, although more work will be required prior to the commercialization of these materials.

Conclusions.

Although SAPO catalysts have been in known for over 25 years, many studies are still being conducted to make them more efficient. Such studies include incorporation of various metals into their framework as one method often employed to seek improved performance. Process conditions have been investigated very thoroughly by various groups in order to systematically understand the optimum conditions in regard to product distribution, olefins selectivity, catalysis yield and catalytic activity. In our research we performed experiments over several microporous SAPO catalysts under various process conditions including temperature, particle size, and other catalyst modifications.

Results from scaling experiments using both 0.3 and 0.5 g SAPO catalysts at the same WHSV revealed almost identical product selectivity profiles with negligible differences in catalyst lifetime and MeOH conversion. This finding confirmed our original hypothesis that maintaining WHSV at 0.5 hr^{-1} by reducing all operating conditions by the same factor would not greatly change the reaction products. Results from our early studies led us to believe that when catalyst particles were ground, the ability for catalysts to resist rapid deactivation might be improved. This hypothesis was tested and some, but not all, catalysts were improved by the particle size reduction. Of the three SAPOs tested, SAPO-44 turned out to be better in terms catalytic performance and catalyst yield after grinding treatments. SAPO-56 (0.6 Si) maintained a similar activity level before and after grinding treatment, while SAPO-56 (0.9 Si) gave a slight improvement. On the other hand, SAPO-34, did not perform as well in any of the categories studied compared to the other samples. Further, results from this study indicated an optimum operating temperature condition yielding the greatest C_2 to C_4 light olefins production between 400 ^oC to 450 ^oC. This finding is in agreement with our earlier work in Dubois et al. [7].

Various SAPOs incorporated with ruthenium using a gas phase deposition method were tested for catalytic activity; however, data for these samples did not show much improvement for any of the categories analyzed: yield, product distribution or lifetime. These catalysts were incorporated with only 1% Ru loading, and it is possible an increase in loading or a change to alternative metals such as Pd and Pt and/or perhaps lower calcination temperatures could give better metal dispersion and performance. We also looked at the possibility of whether a spent catalyst would show any improvement in activity after grinding. Along these lines, results from an experiment with SAPO-56 (0.6 Si) did not show any evidence of regeneration or restored activity following grinding, as DME was the only product observed in significant amounts.

The dehydrogenation of cyclohexane over different kinds of Pt/SBA catalysts was carried out in a continuous fix-bed system at various reaction conditions. Reaction temperature imposed a significant impact on the cyclohexane conversion. Within our reaction temperature range, increases in the reaction temperature enhanced the dehydrogenation process leading to higher cyclohexane conversion. The effect of catalyst loading on cyclohexane conversion demonstrated that a moderate increase in the Pt loading on SBA-15 catalyst increased cyclohexane conversion, but there was an optimum loading point, where further increases in Pt loading had a detrimental effect on the dehydrogenation process. Under our experimental conditions, *ca*. 1% Pt/SBA-15 had the highest activity compared to other Pt loadings. SBA-15 mesoporous support was found

to have the best activity as a catalyst support among SBA-11, 12, 16, Al_2O_3 and C. At 250^{o}C, cyclohexane conversion was 96% over 1%Pt/SBA-15 catalyst. The effect of catalyst pore size on cyclohexane conversion illustrated that there was not much difference in cyclohexane conversion when the nominal pore size increased from 8.6nm to 12 nm, however, the conversion significantly decreased when the pore size increased to 30nm. Under our experimental conditions, when cyclohexane flowrate was less than 0.01cc/min, there was no significant influence of reactant flowrate on cyclohexane conversion; however, when liquid reactant flowrate further increased, the cyclohexane conversion began to decrease. Roughly equal catalyst activity existed for catalysts prepared by ion-exchange or impregnation; although, for low temperature reactions, there was some difference in cyclohexane conversion with the catalyst prepared by ion-exchange showing slightly better activity than the catalyst prepared by impregnation. Ru/SBA-15 catalyst did not demonstrate as much activity in the cyclohexane dehydrogenation process as the Pt catalyst.

Publications in 2004-2005

1. Jean, Luckner; Huang, Xiwen; Guin, James A.; Turpin, Gregory C.; Ernst, Richard D. Preprints of Symposia - American Chemical Society, Div. Fuel Chem. (2005), 50(2), 596-597.
2. Huang, Xiwen; Jean, Luckner; Guin, James A.; Shah, Naresh; Huffman, Gerald P.; Turpin, Gregory C.; Ernst, Richard D. Preprints of Symposia - American Chemical Society, Division of Fuel Chemistry , 230th ACS National Meeting, Washington, DC, Aug. 28-Sept. 1, 2005 (2005),
3. Huang, Xiwen; Jean, Luckner; Guin, James A.; Shah, Naresh; Huffman, Gerald P.; Turpin, Gregory C.; Ernst, Richard D. Abstracts of Papers, 230th ACS National Meeting, Washington, DC, United States, Aug. 28-Sept. 1, 2005 (2005),
4. Guin, James A.; Jean, Luckner; Huang, Xiwen; Turpin, Gregory C.; Ernst, Richard D. Abstracts of Papers, 230th ACS National Meeting, Washington, DC, United States, Aug. 28-Sept. 1, 2005 (2005).
5. Wang, Shaobin; Guin, James A. Studies in Surface Science and Catalysis (2004), 147 (Natural Gas Conversion VII), 439-444.
6. Dutta, P.; Manivannan, A.; Seehra, M. S.; Adekkanattu, P. M.; Guin, J. A.. Catalysis Letters (2004), 94(3-4), 181-185.

References.

1. Dahl, I.M., Mostad, H., Akporiaye, D., Wendelbo, R, Micro.Meso. Mater. 29 (1999) 185.
2. Wilson, S. T. et al., J. Am. Chem. Soc., 104 (1982) 1146.
3. Lok, B. M. et al., J. Am. Chem. Soc., 106 (1984) 6092.
4. Pastore, H. O. et al. Annu. Rev. Mater. Res. 35 (2005) 351.
5. Dutta, P.; Manivannan, A.; Seehra, M., Adekkanattu, P., Guin, J., Catal. Lett. (2004), 94, 181.
6.Obrzut, D.; Adekkanattu, P.; Thundimadathil, J.; Liu, J. Dubois, D., Guin, James A. Reaction Kinetics and Catalysis Letters (2003), 80(1), 113-121.
7. Dubois, D. R.; Obrzut, D. L.; Liu, J. Thundimadathil, J. Adekkanattu, P. M.; Guin, J. Punnoose, A. Seehra, M. Fuel Proc. Tech. (2003), 83(1-3), 203-218.
8. Wilson, D.R., Stahl, L., Ernst, R. D., Organometallic Synthesis, 3, 1986, 136.
9. Giordano, N. et al., Indian J. Technol. 21 (1983) 398.
10. Chaouki, J. et al. Chem. Eng. Sci., 49, (1995) 4639.
11. Ali, et al. Appl. Catal. A: General 177 (1999), 99.

12. Newson, E. et al. Hydrogen Energy Progress XII: Proceed. 12th World Hydrogen Energy Conf. (1998), 935.
13. Kariya, N. et al. Appl. Catal. A: General 233 (2002) 91; 247 (2003) 247.
14. Wang, Y., Shah, N., Huffman, G.P., *Energy & Fuels,* 18(5), (2004), 1429
15. Hodoshima, S. Appl. Catal. A: General 283 (2005) 235.
16. B. Bockrath, C. Matranga, J. Culp, E. Bittner, M. Smith, and S. Natesakhawat **"New Materials for the Separation and Storage of Hydrogen"**, NETL U.S. DOE presentation at 2005 Annual CFFS meeting, Stonewall Resort, WV, Aug 1, 2005.
17. Beck, J., et al. Mobil Corp., J. Am. Chem. Soc., 114 (1992) 10834.
18. Zhao, et al. J. Am. Chem. Soc. 120 (1998) 6024.
19. Ryoo, et al. J. Phys. Chem. B, 104 (2000) 11465.
20. K. Cassiers, T. Linssen, M. Mathieu, M. Benjelloun, K. Schrijnemakers, P. Van Der Voort, P. Cool, and E. F. Vansant , Chem. Mater. 14 (2002) 2317.
21. Parpranot, J. et al. J. Catal. 211 (2002) 530.
22. Lee, J et al.,J. Mater. Chem. 14 (2004) 1050.
23. Liu, Y. et al. J. Catal. 224 (2004) 417.
24. Yuranov, I. et al., Chem. Mater. 16 (2004) 760.
25. Li, T. et al. Appl, Catal. A: General 261 (2004) 211.
26. Kresge, C., Leonowicz, M., Roth, W., Vartuli, J., Beck, J. S., Nature, 359, 1992, 710.
27. Cai, Q., Lin, W., Xiao, F., Pang, W., Chen, X., Zhou, B., Micro. Meso. Mater., 32, 1999, 1.
28. Huo, Q., Margolese, D.I., Ciesla, U., Demuth, D.G., Feng, P., Gier, T.E., Sieger, P., Firouzi, A., Chemelka, B.F., Schöth, F., Stucky, G.D., Chem. Mater., 6, 1994, 1176.
29. Zhao, D., Feng, J., Huo, Q., Melosh, N., Fredrickson, G., Chemelka, B., Stucky, G., Science, 279, 1998, 548.
30. Annual Report for Period May 2001- May 2002, DOE Cooperative Agreement No. DE-FC26- 99FT40540, Consortium for Fossil Fuel Science, University of Kentucky.
31. Annual Report for Period May 2002- May 2003, DOE Cooperative Agreement No. DE-FC26- 02NT41594, Consortium for Fossil Fuel Science, University of Kentucky.
32. Jean, Luckner, Masters Thesis, Auburn University, Auburn, AL 2005.

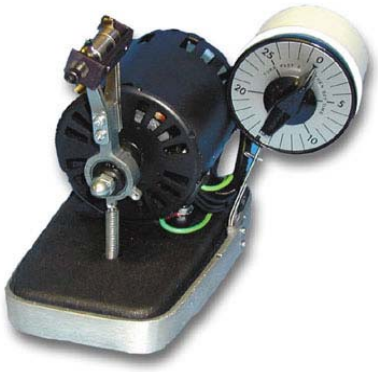

Figure 1. Picture of the Wiggle Bug® Grinder used to reduce to particle size of SAPO catalysts for MTO reactions testing

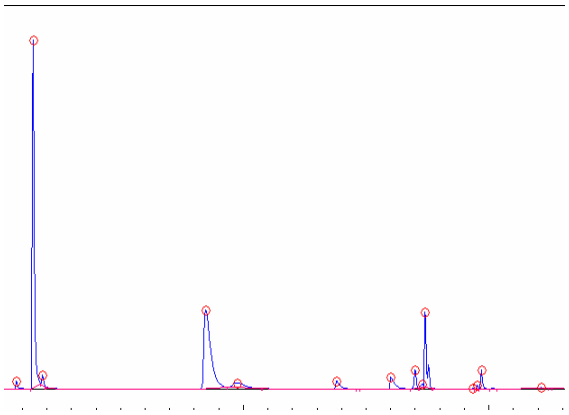

Figure 2 . Typical GC Product Distribution Profile Over SAPO-47, (Finer Particles), Temp=400°C. Major peaks left to right are C1, C2=, C2, C3=, C3, DME, MeOH, C4=, C4, C5=, C5 and C6=.

16-Nov		1	TOS hr	StopWatch Time	16.3	s	WHSV	0.5	hr^{-1}
MeOH flow	0.003	mL/min		Outlet Gas Flowrate	36.81	ml/min			
Catalyst weight	0.306	g		Outlet molar flowrate	0.00150	mol/min			
peaks	name	Retention Time	standard ppm	Standard Area for 100µL	Sample peak area 100µL	ppm of sample product	% of compound	mol/min of compound	mol C / min
C1	methane	0.75	1000	50.888	40.716	800	4.00	1.20E-06	1.20E-06
C2	ethane	1.85	1000	88.531	26.309	297	1.48	4.47E-07	8.94E-07
C2=	ethylene	1.433	1000	89.003	724.24	8137	40.64	1.22E-05	2.45E-05
C3	propane	10.133	1000	134.783	198.033	1469	7.34	2.21E-06	6.63E-06
C3=	propene	8.933	1000	125.471	816.379	6507	32.50	9.79E-06	2.94E-05
C4	C4	17.55	1000	149.33	207.026	1386	6.92	2.09E-06	8.34E-06
C4=	1-butene	17.166	1000	161.497	79.006	489	2.44	7.36E-07	2.94E-06
C4=			1000	161.497	32.742	203	1.01	3.05E-07	1.22E-06
C5	C5	21.233	1000	152.396	63.165	414	2.07	6.24E-07	3.12E-06
C5=		20.933	1000	174.431	17.209	99	0.49	1.48E-07	7.42E-07
C6	C6	24.316	1000	127.193	20.715	163	0.81	2.45E-07	1.47E-06
C6=		24.066	1000	166.067	9.33	56	0.28	8.45E-08	5.07E-07
DME		13.183	33670	1457.09	0	0	0.00	0.00E+00	0.00E+00
MeOH		15.433	40075	1252.2	0	0	0.00	0.00E+00	0.00E+00
Total					2234.87	20021		3.01E-05	8.09E-05
		mol/min					total products, moles	3.01E-05	
Methanol IN (moles/min)		7.416E-05					methane sel	4.00	
Carbon IN (mol/min)		7.416E-05		SUM of C2= to C4=			ethylene sel	40.64	
Carbon OUT (mol/min)		8.094E-05		76.60			Propylene sel	32.50	
Carbon OUT - Carbon IN		6.781E-06					others sel	22.09	
% Gain		9.1					C2-C4 sel	76.598847	
							Methanol conv	100.00	

Figure 3. Spreadsheet showing product distribution from a typical MTO reaction.

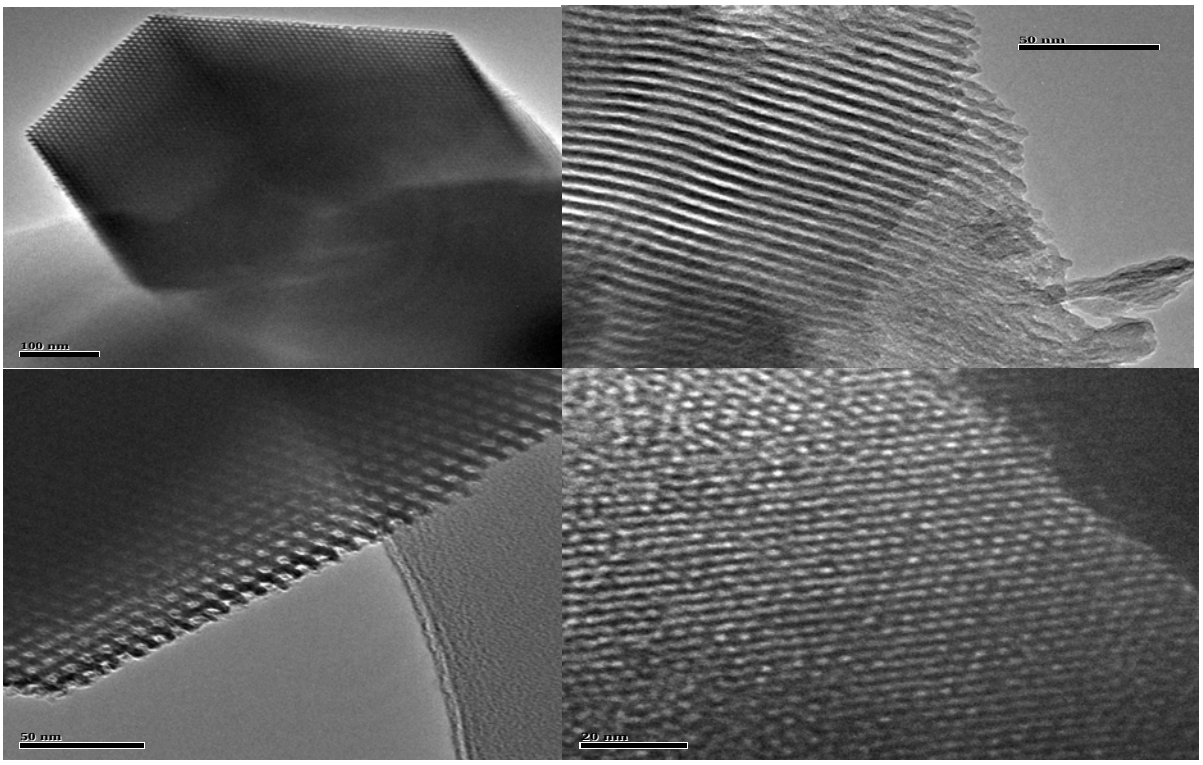

Figure 4. From top left to right, three TEM micrographs of SBA-15 and SBA-11 (lower right).

.

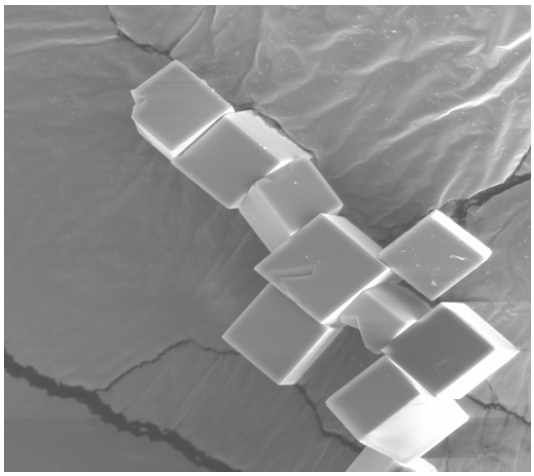

Figure 5. 13 µm particles, SAPO-34, X1000, 10kV, 14mm

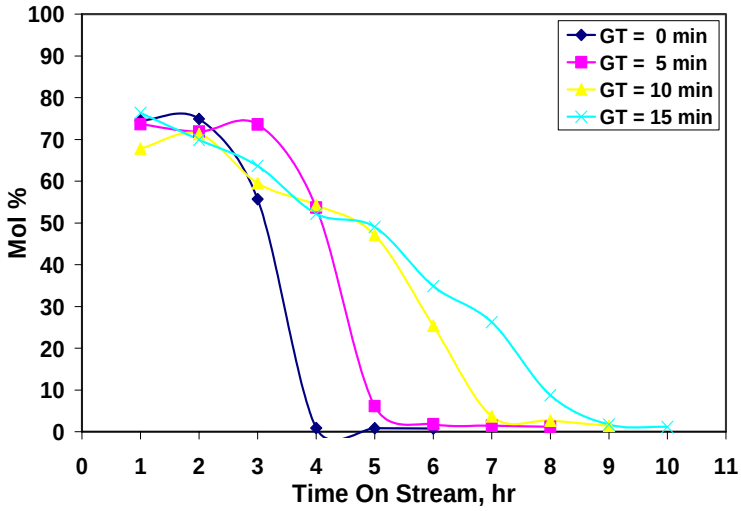

Figure 6. Effect of grinding time on product distribution from MTO reaction with SAPO-34 at 400^{o} C.

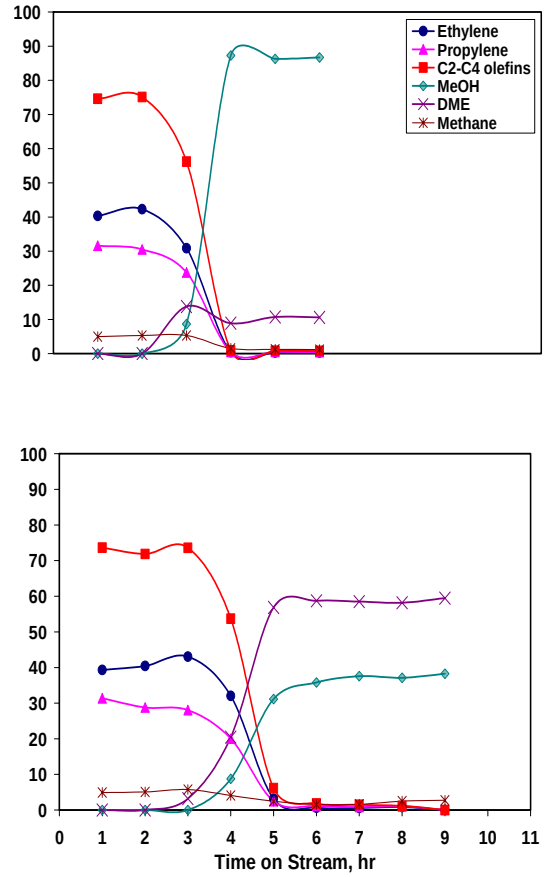

Figure 7. Effect of grinding on MTO reaction with SAPO-34. Top Figure (no grinding), Bottom (5 min grinding).

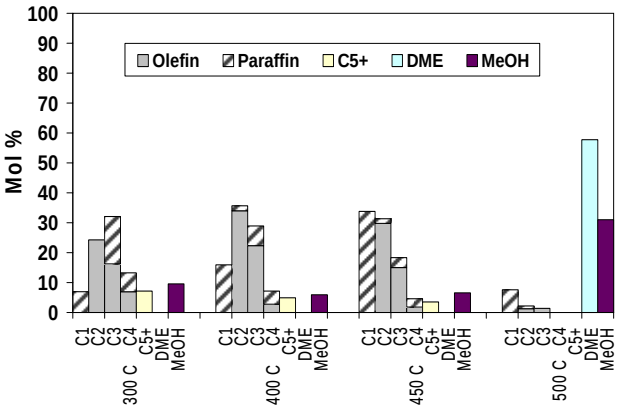

Figure 8. Effect of Temperature on MTO with SAPO-56 (0.6 Si ratio).

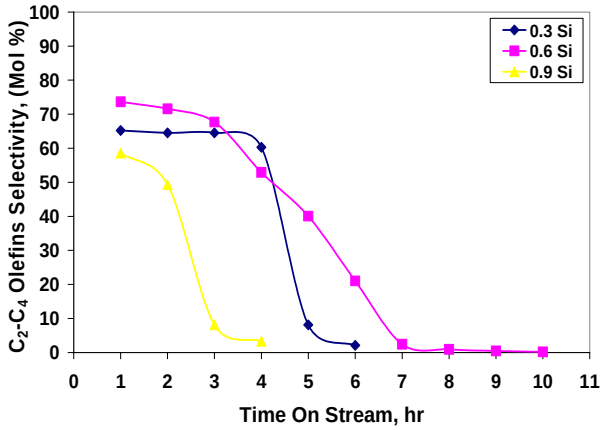

Figure 9. Effect of Si Content on Olefins Production using SAPO-56

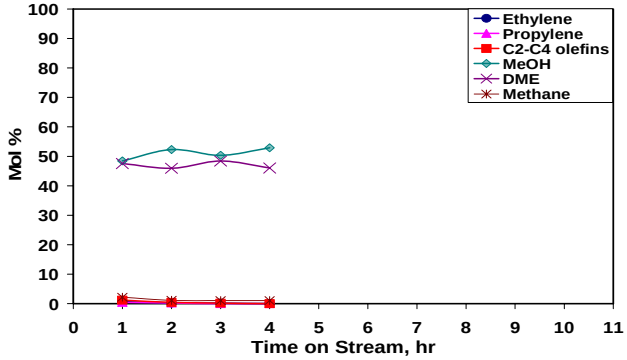

Figure 10. Product Distribution on SAPO-56, 0.6Si), 400°C, Spent Catalyst Ground for 15 min.

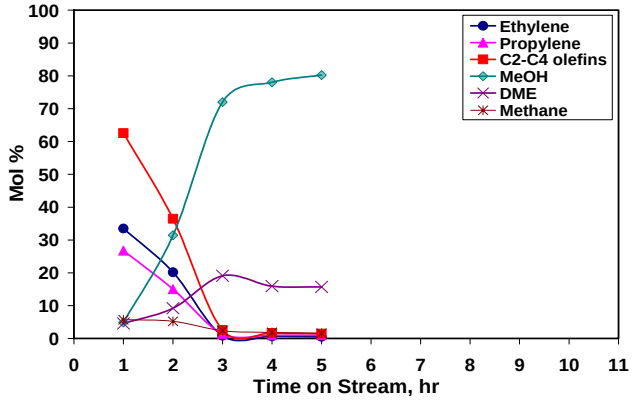

Figure 11. Distribution of Olefins, MeOH, and DME over Ru impregnated SAPO-34 at 400 °C.

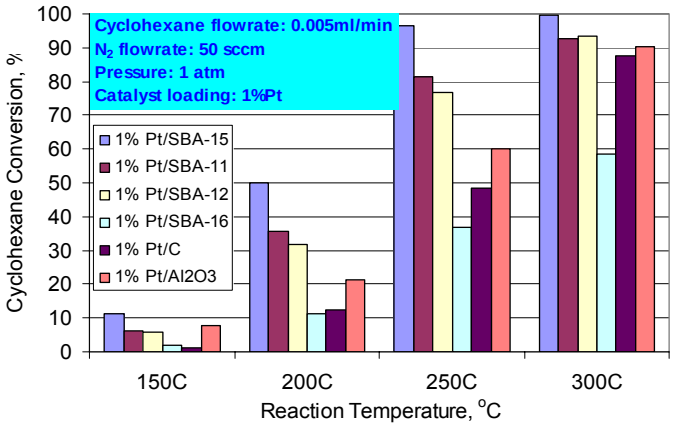

Figure 12. Cyclohexane dehydrogenation with various supported Pt catalysts at different temperatures.

HYDROGEN PRODUCTION FROM METHANOL IN SUPERCRITICAL WATER

Ram B. Gupta
Department of Chemical Engineering
Auburn University, Auburn, AL 36849-5127.

Introduction

The development of proton exchange membrane fuel cells for various transportation applications has resulted in a need of on-board and stationary reformers which can supply high purity hydrogen at low cost. Designing a process to produce H_2 at a very high pressure is an attractive approach for mobile and portable applications owing to its low storage volume. The reforming of hydrocarbons can be carried out in the presence of supercritical water instead of steam as used in the conventional processes, to produce H_2 at a very high pressure.

There are several advantages of carrying out the reforming reactions in supercritical water over the conventional processes. The density of supercritical water is higher than that of steam which results in a high space-time yield and the higher values of thermal conductivity and specific heat of supercritical water are beneficial for the endothermic reforming reaction. H_2 is available at a high pressure which can be stored directly, thus avoiding the problems associated with its compression. The process becomes economical as the compression work is reduced owing to the low compressibility of liquid feed as compared to that of gaseous H_2. [1] Hydrocarbons are completely soluble in supercritical water which minimizes the formation of char or slag which may otherwise cause catalyst deactivation. This is particularly important in the generation of H_2 from heavy oils such as diesel. The generation of H_2 by the steam reforming of biomass leads to the formation of significant amounts of tar and char which limits the yield of H_2 and the gaseous product contains higher hydrocarbons in addition to the desired light gases. Researchers have carried out the catalytic gasification of biomass or its model compounds in supercritical water to produce H_2-rich gas with effectively no tar or char formation. [2]

Methanol is chosen as feedstock for reforming because of its high hydrogen-to-carbon ratio and absence of carbon-carbon bonds. It is in the liquid state under normal conditions and hence can be stored and pumped easily. The major reactions involved in the methanol reforming are:

Methanol decomposition: $CH_3OH \Leftrightarrow CO + 2H_2$ (1)
Water-gas shift reaction: $CO + H_2O \Leftrightarrow CO_2 + H_2$ (2)
Methanation of CO: $CO + 3H_2 \Leftrightarrow CH_4 + H_2O$ (3)
Methanation of CO_2: $CO_2 + 4H_2 \Leftrightarrow CH_4 + 2H_2O$ (4)

To study the impact of pressure on the H_2 yield, equilibrium calculations were performed using Gibbs free energy minimization method and Peng-Robinson equation of state. **Figure 1** shows that as pressure increases, there is an increase in the CH_4 moles and decrease in the H_2, CO and CO_2 moles. It suggests that methanation of CO (reaction 3) and CO_2 (reaction 4) is favored at higher pressures. Methanation of CO results in a loss of 3 moles of H_2 while methanation of CO_2 results in a loss of 4 moles of H_2. To enjoy the benefits of the reforming of methanol in supercritical water which are mentioned before, it becomes important to prevent the loss of H_2 by minimizing the methanation reactions.

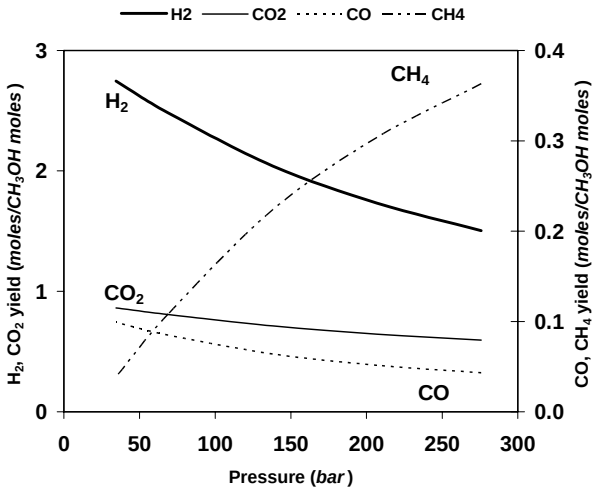

Figure 1. Dependence of gas yield on pressure using ASPEN+ equilibrium calculations. (10 wt.% methanol, 700 °C)

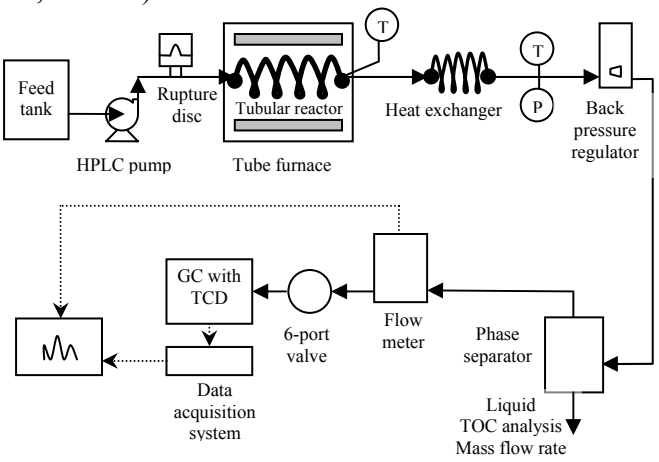

Figure 2. Schematic of the experimental setup used for methanol reforming in supercritical water.

Experimental

Materials. Methanol (99.9%), KOH (88.7% assay) and K_2CO_3•1½H_2O (99.9% assay) were obtained from Fisher.

Apparatus. Figure 2 shows schematic of the apparatus used in the study. A tubular reactor made of Inconel 600 (Microgroup) having a composition of 73% Ni, 18% Cr, 9% Fe was used. The reactor wall provides the catalytic surface area for the reactions. Later the reactor was replaced with a Ni-Cu tubing (Supelco) having a composition of 67% Ni, 33% Cu.

Aqueous methanol from the feed tank was pumped to the reactor using an HPLC pump (Waters 590). The reactor was heated using a tube furnace equipped with a temperature controller (Thermolyne 21100). The gas mixture exiting the reactor was cooled using an air-cooled heat exchanger made of SS 316 tubing. Pressure was measured by a pressure gauge P. The pressure was let down to the ambient by means of a back pressure regulator (Straval). The gas-liquid mixture was separated in a glass phase separator having gas tight valves to prevent the

escape of gases. The gas flow rate was measured using a gas flow meter (Omega FMA-1600). A six-port injection valve (Valco) having a 100 μL sample loop was used for the online sample injection. The gas composition was measured using a gas chromatograph (Varian 3700) equipped with a TCD and 60/80 Carboxen-1000 carbon molecular sieve column. (Supelco) The mass flow rate of the liquid coming out of the phase separator was measured using a balance. The total organic carbon (TOC) content of the liquid was analyzed using a TOC analyzer (OI Analytical Model 700).

Results and Discussion

Figure 3 shows that as pressure is raised from 34 to 276 bar, the H_2, CO and CO_2 moles decrease while the CH_4 moles increase as anticipated, suggesting that the methanation reactions, of both CO and CO_2 are favored at the higher pressures. The H_2 yield (H_2 moles/ CH_3OH moles) has dropped from 2.75 at 34 bar to 1.50 at 276 bar. The increase in density at the higher pressures leads to an increase in the residence time which ranged from 7 seconds at 34 bar to 59 seconds at 276 bar which resulted in the near-equilibrium yields.

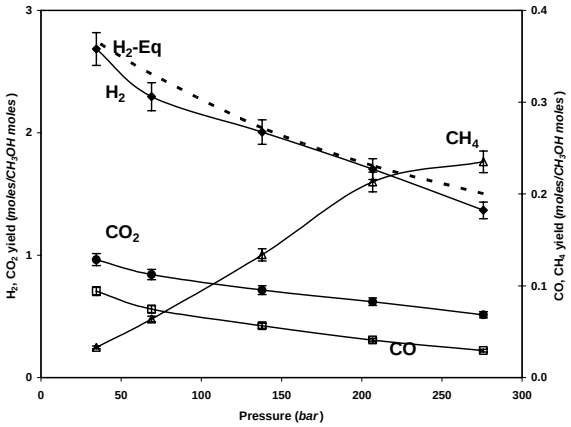

Figure 3. Effect of pressure on gas yield. (10 wt.% methanol, 0.5 mL/min, 700 °C, reactor length = 2 m)

The pressure variation was studied again in the Ni-Cu reactor at a lower residence time. **Figure 4** shows that the increase in pressure has a very little effect on the gas yields in this case. The H_2 yields which are higher than the equilibrium H_2 yields, remain fairly constant over the entire pressure range. The CH_4 yield is found to be almost negligible. This could be the combined effect of the low residence time, which ranged from 2 seconds to 17 seconds in this case and possibly the catalytic activity of the Ni-Cu reactor.

This behavior of the Ni-Cu reactor can be explained based on the mechanism of CO methanation. It proceeds via dissociative chemisorption of CO and H_2 to form intermediates which combine to form CH_4 as shown in reactions 5 to 7.

$CO \rightarrow C_s + O_s$ (5)

$H_2 \rightarrow 2H_s$ (6)

$C_s + H_s \rightarrow (CH)_s$ (7)

Alloying Ni with Cu results in the dilution of active Ni in an inactive matrix which diminishes the number and size of Ni clusters which are necessary for the dissociation of CO and deposition

of C_s on the surface. The Ni-Cu tubing reduces the number of places where C_s can be formed and held and decreases the extent of methanation of CO and CO_2. [3]

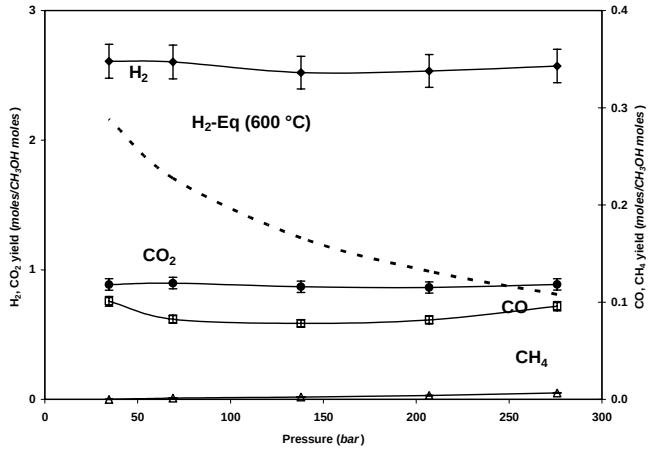

Figure 4. Effect of pressure on gas yield with Ni-Cu reactor. (10 wt.% methanol, 1 mL/min, 600 °C, reactor length = 1 m)

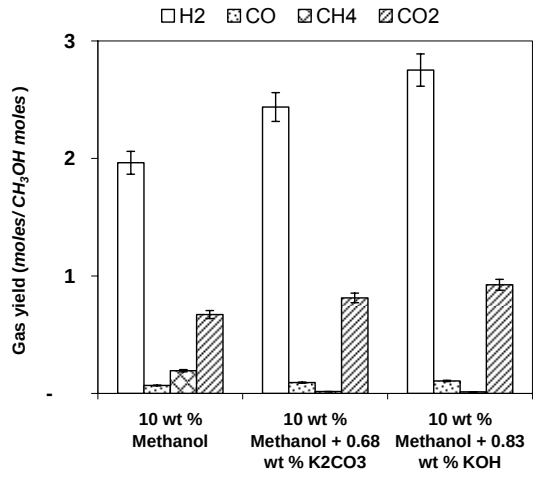

Figure 5. Effect of K_2CO_3 and KOH addition. (10 wt.% methanol, 1 mL/min, 700 °C, reactor length = 2 m)

The performance of the Inconel 600 reactor can be improved by adding K_2CO_3 or KOH in aqueous methanol. **Figure 5** shows the increase in the H_2 yield and the decrease in the CH_4 yield.

Conclusions

CH_4 formation during reforming of methanol in supercritical water can be suppressed by (1) operating at a low residence time, (2) using Ni-Cu reactor or (3) adding K_2CO_3 or KOH in the feed. This provides a high yield of hydrogen. The results have been published in the following paper:

> Gadhe, Jayant B.; Gupta, Ram B., "Hydrogen Production by Methanol Reforming in Supercritical Water: Suppression of Methane Formation" *Industrial & Engineering Chemistry Research* (2005) 44, 4577-4585.

References:

1. Boukis, N.; Diem, V.; Habicht, W.; Dinjus, E. *Industrial & Engineering Chemistry Research* **2003**, 42(4), 728-735.
2. Antal, Michael Jerry, Jr.; Allen, Stephen Glen; Schulman, Deborah; Xu, Xiaodong; Divilio, Robert J. *Industrial & Engineering Chemistry Research* **2000**, 39(11), 4040-4053.
3. Araki, M.; Ponec, V. *Journal of Catalysis* **1976**, 44(3), 439-48.

Coproduction of Hydrogen and Chemicals by Dehydrogenation of Methanol

F. Shi, Y. Zhang, J. W. Tierney and I. Wender

Department of Chemical Engineering, University of Pittsburgh

Introduction

Methanol is produced in huge amounts from synthesis gas derived chiefly from natural gas. In 2003 world capacity for methanol production was over 50 million tons. Very large plants are being built near resources of cheap natural gas. Methanol is a hydrogen-rich liquid, and provides a great deal of convenience in storage, transport and handling as a source of hydrogen.

Hydrogen can be generated from methanol in several ways:

Decomposition $CH_3OH = CO + 2H_2$

Steam reforming $CH_3OH + H_2O = CO_2 + 3H_2$

Dehydrogenation $2CH_3OH = HCOOCH_3 + 2H_2$

Coproduction of fuel and high value chemicals attracts more attention and potential industry investment because of high profitability. Dehydrogenation of methanol produces hydrogen as well as methyl formate (MF). MF has been proposed as a building block for chemicals. It is a stable liquid and can be catalytically converted to important chemicals including dimethyl formamide, formamide, ethylene glycol, acetic acid, dimethyl carbonate and formaldehyde. [1-4]

Since MF is an intermediate in a series of reactions, fast desorption and diffusion are essential for high selectivity to MF and hydrogen. In this study, work has started on the gas phase dehydrogenation of methanol to produce hydrogen and MF on a series of copper-based catalysts. The effects of supports and promoters are under investigation. The formation of hydrogen via steam reforming is also of interest.

Experimental

Catalyst preparation.

A series of copper-based catalysts were prepared by incipient wetness impregnation of aqueous $Cu(NO_3)_2$ solution onto various supports: ZSM-5, Al_2O_3, SiO_2, ZrO_2, TiO_2, and MgO. The impregnated samples were dried at 110˚C for at least 8 hours prior to calcination at 350˚C in air for 3h. Catalysts were pelletized to 60-80 mesh for testing. Before reaction, catalysts were reduced at 250˚C with 70 ml/min H_2/Ar (5:2) gases for 3 h.

Catalyst testing.

The equipment shown as Figure 1 was built for testing the dehydrogenation and the steam reforming of methanol. Temperature, flow rate and sampling procedure are programmable. The reactor is a U-shape quartz microreactor with maximum 2 ml catalyst loading. Liquid methanol is fed using a syringe pump (100DX, ISCO). In this study, 0.6 to 0.8 g of catalyst is loaded and reduced at 250˚C with 70 ml/min H_2/Ar (5:2) gases for 3 h. Methanol is fed at the rate of 3 ml/h. The feed is evaporated at 150˚C and mixes with 20 ml/min of Ar preheated to the same

temperature. Gas lines before entering the microreactor and the GC are heated to 150˚C with electrical tapes. Products are analyzed by two on-line Hewlett Packard GCs: one is equipped with a TCD detector and with a Carbonsphere packed column (6 feet, 3/8 in) for analysis of H_2, CO, CH_4, CO_2; another is equipped with a FID and HP-5 capillary column for analysis of methanol, methyl formate, dimethyl ether and other organic products. Liquid products are also collected with a cold trap at –80˚C and then are analyzed using GC-MS.

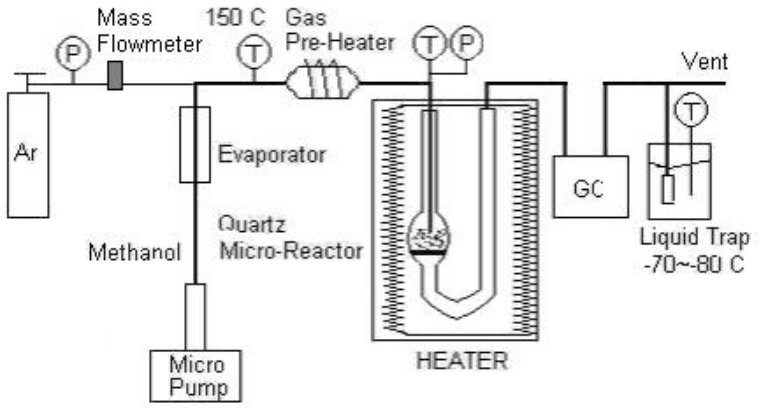

Figure 1 A Schematic of Methanol Dehydrogenation Apparatus

Results and Discussion

Characterizations of catalysts

The BET surface area of catalysts were measured by an ASPS-2010 Analyzer (MicroMeritics) using a liquid nitrogen adsorption method. Results are summarized in Table 1.

Table 1. A Summary of BET surface area of catalysts*

Support	Surface Area, m^2/g
MgO	47.3
Al_2O_3	110.5
TiO_2	36.5
ZrO_2	76.6
ZSM-5	307.4

* 10 wt% Cu for each catalyst

Temperature Programmed Reduction (TPR) was carried out using a TGA with a carrier gas of 5% H_2 in Ar, with a temperature ramping from room temperature to 500ºC at 5ºC/min. Only one reduction peak was observed for each catalyst, indicating reduction of Cu^{2+} to Cu^0. The peak temperatures are 30 to 60^{o}C lower than unsupported CuO, probably caused by decrease in crystal sizes of Cu on supported catalysts. XRD analysis was also conducted; the results showed that

CuO on the above supports is highly dispersed. Cu on a ZrO_2 support has the smallest particle size, coincident with lowest reduction temperature in TPR.

Thermodynamic calculations.

Thermodynamic calculations for methanol dehydrogenation and steam reforming (methanol/water=1) were conducted using ASPEN Plus 12, based on a Gibbs free energy minimization method. Results for hydrogen and MF production are shown in Figure 2. At temperatures below 200˚C, methanol dehydrogenation to MF and hydrogen is favored; at temperatures above 300˚C, complete decomposition of methanol to H_2 and CO dominates. Although steam reforming can produce more hydrogen than methanol dehydrogenation, it decreases the formation of MF.

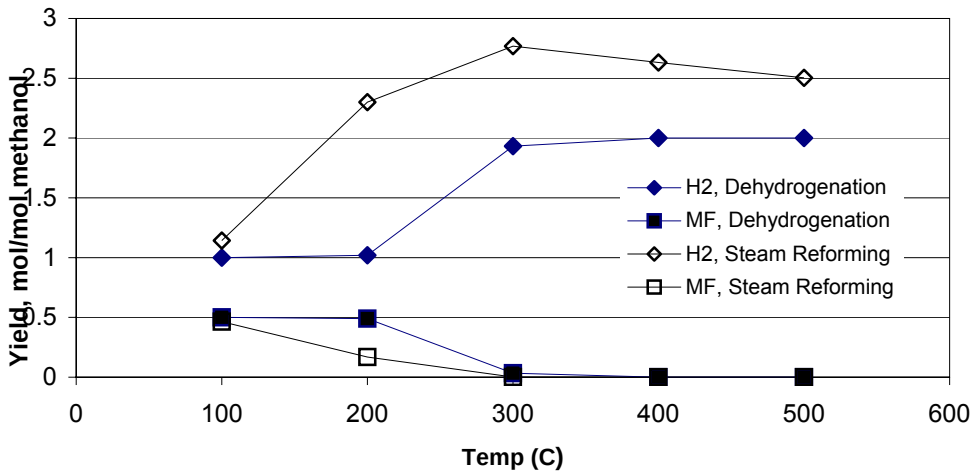

Figure 2. Calculated H_2 and MF production by methanol dehydrogenation.

Catalyst performance

Methanol dehydrogenation experiments were carried out on copper-based catalysts at 20ºC intervals from 160˚C to 300˚C. Methanol conversion and hydrogen production at various temperatures are shown in Figures 3 and 4, respectively. In Figure 3, methanol conversions increase with increase in temperature, rising rapidly above 240˚C. The Cu/Al_2O_3 catalyst has a steeper slope than the other catalysts due to formation of a large amount of dimethyl ether at higher temperatures. The Cu/MgO catalyst showed the highest activity and gave the highest yield of hydrogen. However, production of methyl formate on Cu/MgO was low, as shown in Figures 5 and 6.

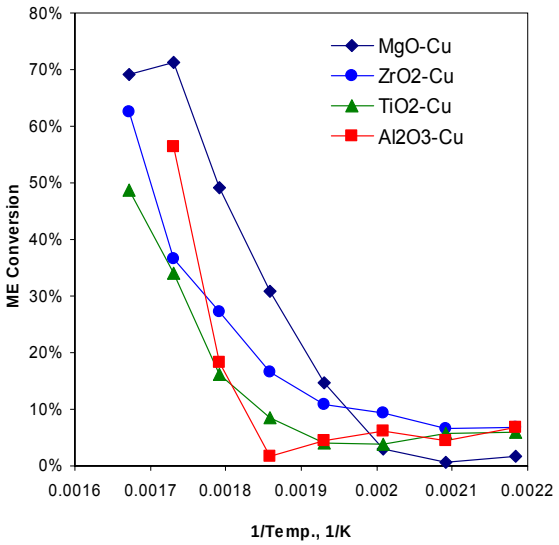

Figure 3. Methanol conversion vs temperature

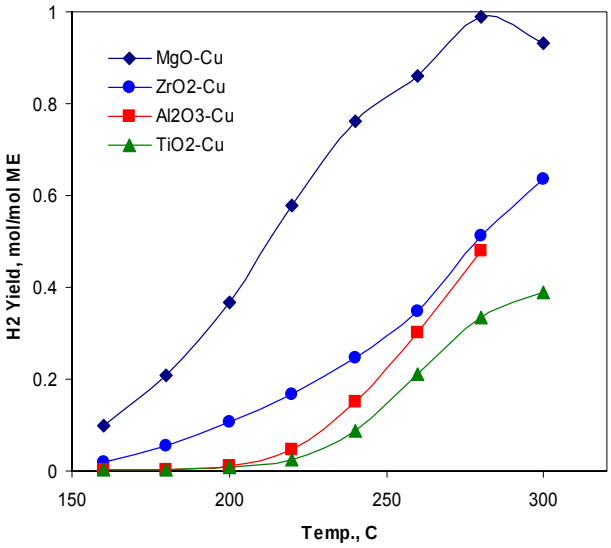

Figure 4. Hydrogen production vs temperature

Cu/ZrO_2 gave a moderate conversion of methanol and the yield of methanol was also moderate. As shown in Figure 5, Cu/ZrO_2 exhibited higher methyl formate production and moderate hydrogen production between 200 to 260˚C. Figure 6 shows that methyl formate selectivity is in the order of Cu/TiO_2>Cu/ZrO_2>Cu/MgO. Cu/TiO_2 showed the highest yield of methyl formate, while the methanol conversion was the lowest.

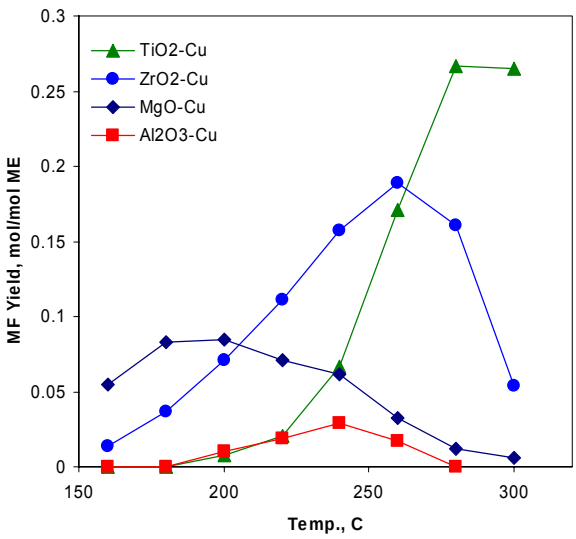

Figure 5. MF yield versus temperature

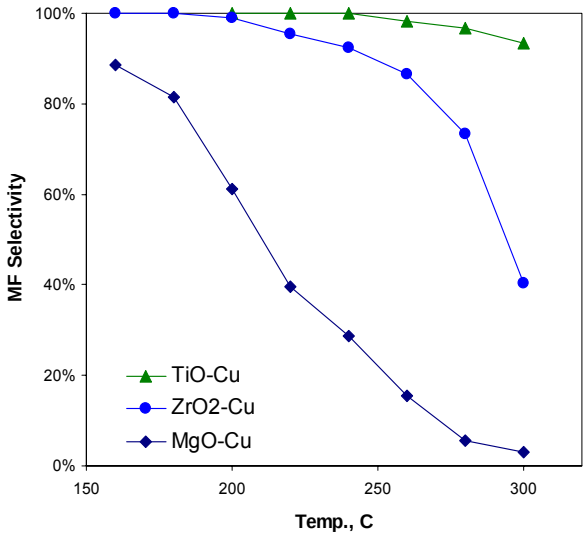

Figure 6. MF selectivity versus temperature

The decomposition of methanol proceeds in several ways. Route 1 is the reverse reaction of the synthesis of methanol and produces CO and H_2. Route 2 is partial dehydrogenation to form methyl formate and hydrogen. Methyl formate then could decompose to form CO and H_2. A Cu/MgO catalyst may catalyze Route 1 to produce more hydrogen and less methyl formate. Cu/ZrO_2 and Cu/TiO_2 could mainly catalyze Route 2 reactions to form methyl formate and

hydrogen. The Cu/Al_2O_3 produced less methyl formate and hydrogen because of the formation of large amounts of dimethyl ether.

Conclusions

Thermodynamically, coproduction of hydrogen and methyl formate is favored at temperatures below 220˚C. At temperatures higher than 250˚C, complete methanol decomposition is favored to form syngas with a ratio of $H_2/CO=2$. The presence of steam favors hydrogen but decreases methyl formate production. A Cu/MgO catalyst produced more hydrogen but less methyl formate. The Cu/TiO_2 catalyst has a higher selectivity to methyl formate but lower activity. The Cu/Al_2O_3 produced less hydrogen and methyl formate but high dimethyl ether. Cu/ZrO_2 show good activity for coproduction of hydrogen and methyl formate and will be pursued in future. This catalyst shows high promise and is being more thoroughly investigated.

References

1. Iwasa, N.; Takezawa, N. *Top. Catal.* **2003**, 22, 215.
2. Hashimot, K.; Toukai, N. *J. Mol. Catal. A* **2002**, 186, 79.
3. Shreiber, E. H.; Roberts, G. W. *Appl. Catal. B* **2000**, 26, 119.

Lee, J. S.; Kim, J. C.; Kim, Y. T. *Appl. Catal.* **1990**, 57, 1.

Hydrogen by Catalytic Reforming of Polyols

B. Liu, Y. Zhang, J.W. Tierney and I. Wender
Department of Chemical Engineering, University of Pittsburgh

Introduction

Hydrogen is a clean and efficient fuel and it will be the ultimate fuel in the future. Currently, hydrogen is made mainly from fossil fuels by steam-reforming, partial oxidation, or gasification.[1] Production of hydrogen by steam-reforming of hydrocarbons requires a complex combination of multiple processes to achieve low carbon monoxide levels (e.g., 10–100 ppm) to be used in PEM fuel cells. An important step toward a simple process for the production of hydrogen containing low levels of carbon monoxide may be made possible by the discovery that hydrogen can be produced by catalytic reforming of polyols in the liquid phase at temperatures near 240°C.[2-7] This process has the advantage that reforming of the oxygenated hydrocarbon and the water–gas shift (WGS) are both thermodynamically favorable at the same low temperatures, thus making it possible to conduct both reactions in one reactor. The process eliminates the need to vaporize water and glycol and leads to low levels of carbon monoxide.

In our studies we focused on ethylene glycol (EG), a chemical found in the cooling system of most vehicles, and on glycerol, a by-product of the hydrolysis of fats and oils to make biodiesel.[8] The production of glycerol is greater than demand as biodiesel production has been increasing rapidly. We found both EG and glycerol could be reformed to hydrogen and carbon dioxide at a temperature starting as low as 220°C. Hydrogen yields from reforming EG and glycerol were 82% and 70%, respectively.

Experimental

Catalyst preparation

Alumina-supported platinum catalysts were prepared by incipient wetness impregnation with aqueous solutions of tetraammineplatinum nitrate ($Pt(NH_2)_4(NO_3)_2$), followed by drying in an oven at 100°C for 12 hours. The catalysts were calcined at 260˚C for 2 hours. Experiments were carried out on these catalysts and a commercial Pt/Al_2O_3 catalyst with 1 wt% Pt purchased from Aldrich. The preparation of various Pt and Ni catalysts on different supports and with the addition of promoters is ongoing.

Catalyst testing

A continuous fixed-bed liquid phase microreactor with computer control as described in previous reports has been built and is currently in operation. The reactor is a 3/8 inch od and 1/4 inch id stainless-steel tube with a packed bed of catalyst about 10mm long. A thermocouple inserted into the middle of the catalyst bed in the reactor insures accurate measurement of temperature. In this study, one gram of platinum on alumina powder was loaded into the reactor, and activated by hydrogen at a rate of 50 ml/min, with a temperature program ramping from room temperature to 250°C at 1°C /min, holding at 250°C for 2 hours. A liquid solution of 10 wt% ethylene glycol (or glycerol) was introduced in an up flow configuration at 6.0ml/h with a syringe pump. The total pressure of the system was regulated to 350psi-680psi with nitrogen. For each experiment, reaction temperature was gradually increased from 220°C to 270°C in 10 degree intervals. The system pressure was kept at 50psi over the vapor pressure of water at that

temperature to keep the system in the liquid phase. For each temperature, the system was operated for more than six hours to reach steady state. Liquid products were collected in a cold trap and analyzed by GC and GC-MS. The effluent gas went through two automatic sampling valves and was analyzed by an online GC (HP5890) equipped with two packed columns: Porapak Q with FID for analysis of light organic products and Carbonsieve with TCD for analysis of H_2, CO, CO_2.

Results and Discussion

Aqueous-phase reforming (APR) of 10 wt% of EG or of glycerol solutions was carried out in the fixed bed tubular reactor. At temperatures below 260˚C, hydrogen and carbon dioxide constitute more than 99% of the gas. Methane, ethane and propane products constitute less than 1% in most cases and increase with reaction temperature. Carbon monoxide could not be detected at low feed rates. Liquid phase products contain small amounts of alcohols (methanol and ethanol), organic acids (acetic and glycolic acids), and acetaldehyde.

Figure 1. Hydrogen yields from aqueous-phase reforming of ethylene glycol.

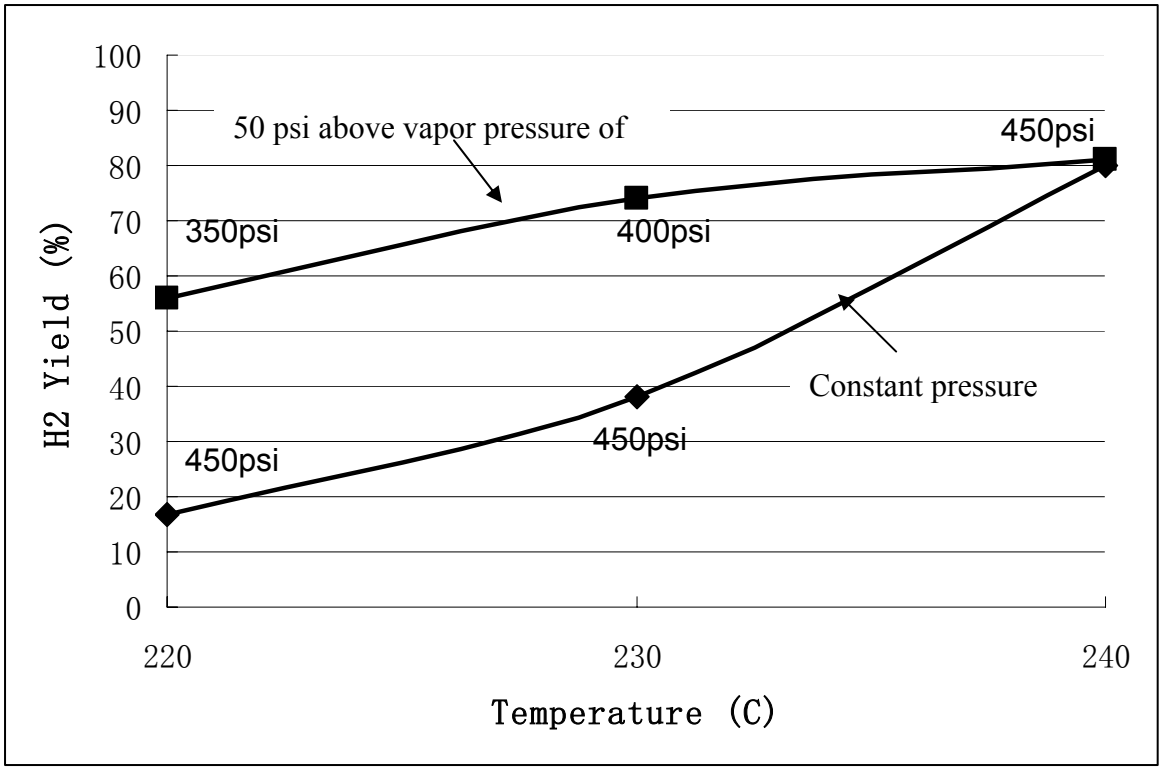

The hydrogen yield is dependent on system temperature and pressure; its yield increases with temperature below 250˚C and becomes flat above that temperature. Hydrogen yields from reforming of EG at different pressure are shown in Figure 1. High hydrogen yields can be achieved when the system pressure is kept slightly above the vapor pressure of water at the same temperature

Polyethylene glycol 200 (PEG 200) was used as a model compound to study the reaction pathways of aqueous phase reforming of polyols. Mass spectroscopic analysis of PEG 200 before and after the reaction suggests that C-C chain breakage may be the main pathway in the APR of polyols.

Different polyols have different hydrogen production capabilities. The results of hydrogen production from oxygenated hydrocarbons are shown in Table 1

	H_2 %	CO_2 %	Total hydrocarbon %	H_2 rate ml/min
EG $HOCH_2$-CH_2OH	66.8	31.8	1.4	15.9
Glycerol $HOCH_2$-CHOH-CH_2OH	61.5	33.3	5.2	7.7
1,2-Propanediol $HOCH_2$-CHOH-CH_3	58.9	30.7	10.4	4.1
1,3-Propanediol $HOCH_2$-CH_2-CH_2OH	46.5	32.6	20.9	3.4
1-Propanol $HOCH_2$-CH_2-CH_3	45.4	26.6	28	3.2

Reaction conditions: 10 wt% in water solution, 6 ml/h, 1 gram Pt/Al_2O_3 catalyst with 1% Pt, 270^{o}C and 680psi

Table 1 Hydrogen production from selected oxygenated hydrocarbons

At the same conditions, EG produced more hydrogen than glycerol, propylene glycol or propanol. Addition of a methyl or methylene group to EG decreases H_2 production; polyols with adjacent hydroxyl groups yield more H_2. Glycerol contains a secondary hydroxyl group which is easy to break from the carbon chain, resulting in a decrease in hydrogen yield.

Conclusions

1. Aqueous-phase reforming of polyols in a continuous system produced significant amounts of hydrogen with low CO.
2. The H_2 yield is dependent on system temperature and pressure. The hydrogen yield increases with rising temperature; above 250ºC , it increases slowly. To obtain a high hydrogen yield, the system pressure should be kept slightly above the bubble point pressure. Increasing pressure inhibits aqueous-phase reforming.
3. Effect of hydroxyl groups: Addition of a methyl or methylene group to polyols decreases H_2 production; polyols with adjacent hydroxyl groups yield more H_2 than molecules containing separated hydroxyl groups.

4. Aqueous-phase reforming of polyols may be useful for H_2 generation from renewable materials for use in PEM fuel cells

References

1. J. Rostrup-Nielsen, *Phys. Chem. Chem. Phys.* 3 (2001) 283.
2. R. R. Davda, J. W. Shabaker, G. W. Huber, R. D. Cortright and J.A. Dumesic, *Applied Catalysis B: Environmental* 43 (2003), 13–26.
3. J. W. Shabaker, G. W. Huber, R. R. Davda, R. D. Cortright and J. A. Dumesic, *Catalysis Letters* 88 (2003), 1–2
4. J. W. Shabaker, R. R. Davda, G. W. Huber, R .D. Cortright and J. A. Dumesic, *Journal of Catalysis* 215 (2003), 344–352.
5. R. D. Cortright, R. R. Davda and J. A. Dumesic, *Nature*, 418 (2002), 964-967.
6. G. W. Huber, J. W. Shabaker and J. A. Dumesic, *Science*, 300 (2003), 2075-2077
7. J. W. Shabaker, D. A. Simonetti, R. D. Cortright, J. A. Dumesic, *Journal of Catalysis*, 231 (2005), 67–76.
8. L. Bournay, D. Casanave, B. Delfort, G. Hillion and J.A. Chodorge, *Catalysis Today,* 160 (2005), 190-192

Production of hydrogen and carbon nanotubes by catalytic decomposition of lower alkanes

Naresh Shah, Yuguo Wang, and Gerald P. Huffman
University of Kentucky

Introduction

The U.S. currently produces 9 million tons of hydrogen per year. This will need to increase by an order of magnitude to fully implement the hydrogen economy. Traditionally, hydrogen is produced by reforming or partial oxidation of hydrocarbons to produce synthesis gas, followed by the water-gas shift reaction to convert CO to CO_2 and produce more hydrogen, followed by separation procedures. However, further purification steps are required to reduce CO to levels tolerable by the catalysts used in fuel cells. Non-oxidative, catalytic decomposition of hydrocarbons is an alternative, one-step process to produce pure hydrogen.

Nanoscale, binary, Fe-M catalysts supported on alumina (0.5%M-4.5%Fe/γ-Al_2O_3, M=Mo, Ni, or Pd) were shown to decrease the decomposition temperature of methane, ethane, and propane by 400 - 500 °C.[1, 2, 3] The most active temperature range for all three feed gases is 650-800 °C, where 70-90% of the product is pure hydrogen and the remainder is unreacted alkane feed.

One of the problems with non-oxidative dehydrogenation is coking of the catalyst and reactor due to carbon build up. Under proper reaction conditions, however, these binary catalysts promote the growth of carbon nanotubes that transport carbon away from the catalyst surfaces, thereby preventing catalyst deactivation by coking as well as producing a potentially valuable by-product. High resolution TEM has been used to investigate the structures of the CNT. Multi-walled nanotubes (MWNT) with parallel, concentric, graphene walls are produced at high temperatures (650-700 ºC). At low temperatures (450-500 ºC), a stacked–cone nanotube (SCNT) structure is produced in which the graphene sheets lie at an angle to the tube axis, which results in extensive graphene layer openings and edge sites on the surface of the SCNT.

The SCNT produced by lower temperature dehydrogenation of ethane and propane is an excellent catalyst support material. Cyclohexane is completely converted to benzene and hydrogen at 315 ºC using a catalyst consisting of only 0.25 wt% Pt supported on SCNT. SCNT also exhibit some promise as a hydrogen storage medium. Alkali washed (to remove alumina support) SCNT indicated greater than one weight percent hydrogen uptake at ambient temperature and 700 psig pressure.

Characterization of the catalysts by XAFS and Mössbauer spectroscopy, TEM, and XRD indicates that the active phase is an Fe–M–C austenitic metal alloy and that the catalyst particles are anchored to the alumina support by an Fe-aluminate, hercynite.[4] The catalysts exhibit good time on stream behavior because the Fe-M-C phases are very effective in stabilizing carbon in the form of CNT, which efficiently carry the carbon away from the active alloy particle surfaces.

In order to increase the value of the CNT produced by this method, it is essential that all catalytic metals as well as alumina support be removed. Vigorous boiling in concentrated NaOH solution was able to dissolve some alumina support. Using this washing technique, we have previously reported obtaining SCNT with as much as 88 weight% carbon purity. Unfortunately, this purity is not sufficient for many applications. Therefore, we have synthesized and tested a

new high surface area support which is highly soluble in 1M nitric acid. Here we report hydrogen production results from methane and ethane decomposition using this support

Preparation of Mg(Al) oxide support

The Mg(Al) oxide support was prepared by co-precipitation from a mixture of 1 M solutions of magnesium and aluminum nitrates (Mg:Al=5:1). While stirring at 60°C, a solution of potassium carbonate and potassium hydroxide was slowly added to the nitrate solution to precipitate aluminum-magnesium-hydroxycarbonate ($Mg_6Al_2(CO_3)(OH)_{16}{\cdot}4(H_2O)$ – hydrotalcite). The precipitate was dried overnight in a vacuum oven at 95°C. On calcination at 550°C for 4~5 hours, the hydroxytalcite structure breaks down, releasing steam and CO_2.and producing a high surface area (~200 m^2/gram) Mg(Al)O support. The catalytic metals were added to this support by the same incipient wetness procedure used previously.

Results

Figure 1 is a plot of hydrogen production as a function of time by using two different catalysts on Mg(Al)O supports at two different reaction temperatures. Both 5 wt% Ni and binary 3.25 wt%Fe-1.75 wt% Ni (total 5 wt% metal) catalysts yield high hydrogen volume percent in the effluent stream initially for higher (700C) reaction temperature, but are deactivated fairly quickly. On the contrary, the same two catalysts generate lower but longer lasting amounts of hydrogen at a lower (500 C) reaction temperature

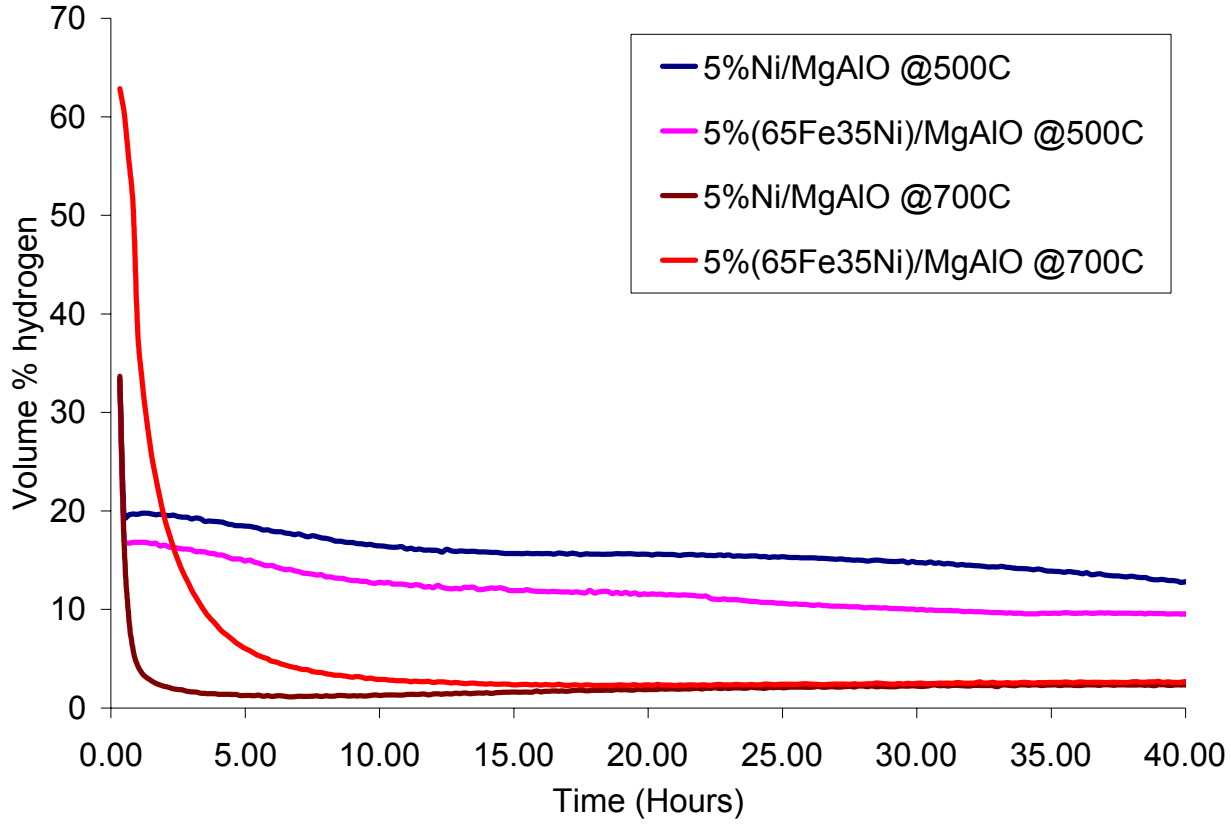

Figure 1. Time-on-stream hydrogen production by decomposition of undiluted **methane** at two different temperatures using two different catalytic metal loadings on the same Mg(Al)O support

Figure 2 is a similar plot of time on stream hydrogen production using undiluted ethane as a feed. In this case, also the initial hydrogen production is higher at a higher reaction temperature which drops to less than half in a few hours. However, in the case of ethane, even the reduced hydrogen volume percent in the effluent stream is higher than the hydrogen concentration at the lower reaction temperature.

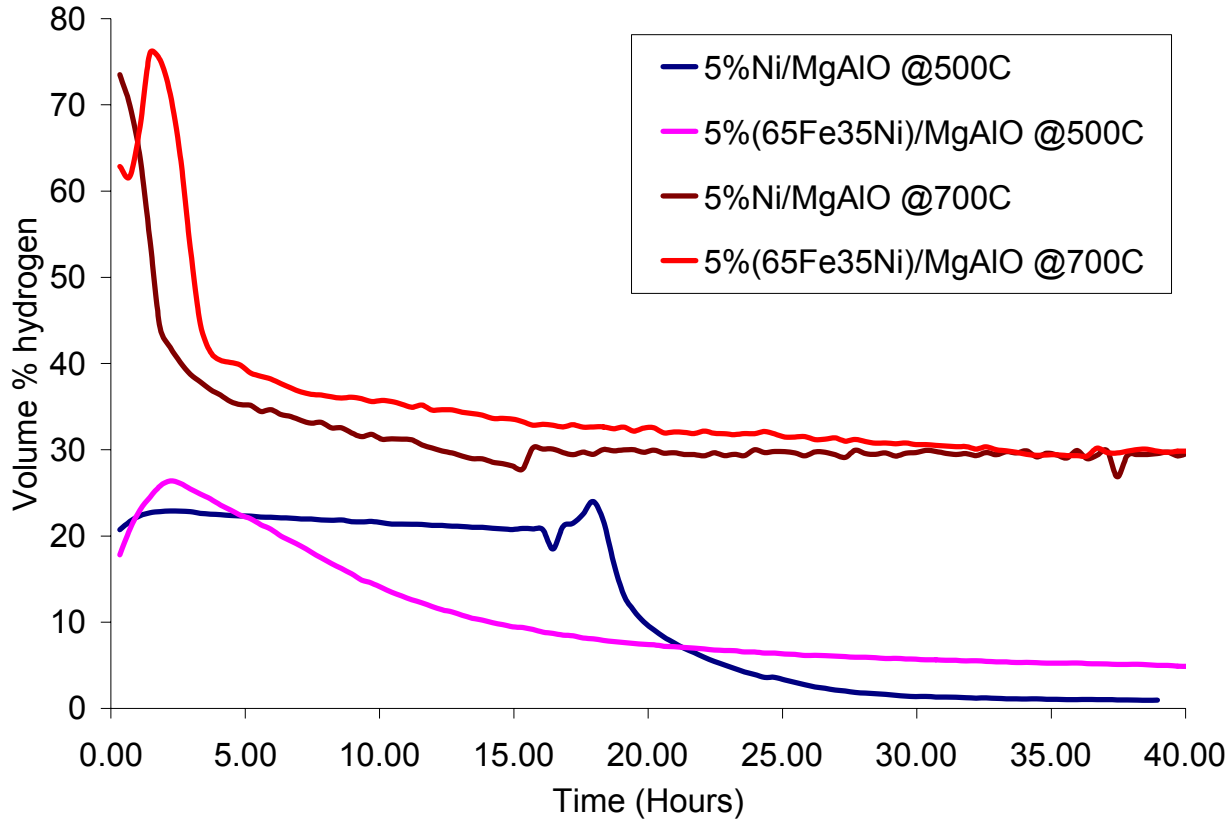

Figure 2. Time-on-stream hydrogen production by decomposition of undiluted **ethane** at two different temperatures using two different catalytic metal loadings on the same Mg(Al)O support

In both methane and ethane decomposition experiments, it was noted that 5 wt% Ni is a better catalyst (yields more hydrogen) than a binary 3.75 wt%Fe-1.25 wt% Ni catalyst for lower (500 C) reaction temperature, while 3.75 wt%Fe-1.25 wt% Ni catalyst yields more hydrogen than 5 wt% Ni at a higher (700C) reaction temperature.

Publications and other significant communications (2002-2005):

1. M.R. Smith Jr., W.W. Hedges, R. La Count, D. Kern, N. Shah, G.P. Huffman, and B. Bockrath, "Selective oxidation of single-walled carbon nanotubes using carbon dioxide", *Carbon*, **41** (2003) 1221-1230.

2. Naresh Shah, Sidharta Pattanaik, Frank E. Huggins, Devadas Panjala, and Gerald P. Huffman, "XAFS and Mössbauer spectroscopy characterization of supported binary catalysts for non-oxidative dehydrogenation of methane", *Fuel Processing Technology*, **83** (2003) 163-174.

3. A. Punoose, N. Shah, G.P. Huffman, and M.S. Seehra, "X-ray diffraction and electron magnetic resonance studies of $M/Fe/Al_2O_3$ (M=Ni, Mo, and Pd) catalysts for CH_4 to H_2 conversion", *Fuel Processing Technology*, **83** (2003) 263-274.

4. Alex Punnoose, T. Phanthavady, M.S. Seehra, N. Shah, and G.P. Huffman, "Magnetic properties of ferrihydrite nanoparticles doped with Ni, Mo, and Ir", *Phys. Rev. B*, **69** (2004), 054425-054434.

5. N. Shah, Y. Wang, D. Panjala, and G.P. Huffman, "Production of pure hydrogen and carbon nanostructures by catalytic non-oxidative dehydrogenation of ethane and propane", *Energy & Fuels*, **18** (2004) 727-736.

6. Yuguo Wang, Naresh Shah, and Gerald P. Huffman, "Simultaneous production of hydrogen and carbon nano-structures by decomposition of propane and cyclohexane over alumina supported binary Fe-based catalysts", *Catalysis Today*, **99** (2004) 359-364.

7. Gerald P. Huffman, Naresh Shah, Yuguo Wang, and Frank E. Huggins, "Catalytic dehydrogenation of hydrocarbons: alternative one-step process to produce pure hydrogen and carbon nanotube byproducts", *ACS Fuel Chemistry Division Preprints*, **49(2)** (2004) 731-732; invited presentation at the ACS Presidential symposium: Fuels for the Future: Leading the Way with Chemistry, ACS National Meeting, Philadelphia, PA, August 24, 2004.

8. P. Dutta, A. Manivannan, M. S. Seehra, N. Shah, and G. P. Huffman, "Magnetic properties of nearly defect-free maghemite nanocrystals", *Physical Review B* (2004) 174428-1 – 174428-7.

9. P. Dutta, A. Manivannan, M.S. Seehra, N. Shah, and G.P. Huffman, "Magnetic and structural properties of a DNA-maghemite nanocomposite", *J. Appl. Phys.*, **99** (2006), in press.

Patent: Naresh Shah, Devdas Panjala, and Gerald P. Huffman, U.S. Patent No. 6,875,417 B1, "Catalytic Conversion of Hydrocarbons to Hydrogen and High-Value Carbon", April 5, 2005.

References:

1. Shah, N.; Panjala, D.; Huffman, G.P. *Energy & Fuels,* 15(6), 1528-34 (2001).

2. Shah, N.; Panjala, D.; Huffman, G.P. *Energy & Fuels,* 15(6), 1528-34 (2001).

3. Wang, Y.; Shah, N.; Huffman, G.P. *Energy & Fuels* 18(5), 1429-1435 (2004).

Shah, N.; Pattanaik, S.; Huggins, F.E.; Panjala, D.; Huffman, G.P., *Fuel Processing Technology*, 83, 173-183 (2003).

Continuous Hydrogen Production by Catalytic Dehydrogenation of Tetralin and Decalin over Stacked Cone Carbon Nanotube Supported Pt Catalysts

Yuguo Wang, Naresh Shah, Frank E. Huggins, and Gerald P. Huffman, University of Kentucky

Introduction

The U.S. Department of Energy has recently announced its intention to develop the "FreedomCar", a hydrogen-powered vehicle. Such vehicles would likely use polymer electrolyte membrane (PEM) fuel cells, which require very pure hydrogen and operate in the temperature range of 80-90°C. Currently, most of the processes for producing hydrogen are conducted at much higher temperatures. The most popular method is steam methane reforming at temperatures >700°C, followed by the water gas-shift (WGS) reaction and various purification steps to reduce the residual CO to ppm levels.

An alternative route is direct dehydrogenation of cycloalkanes, which produces pure hydrogen and aromatic products at much lower reaction temperatures, ~300°C. Moreover, the aromatic products produced from cycloalkanes (benzene, toluene, naphthalene, etc.) can be re-hydrogenated. Recently, we reported results for the dehydrogenation of cyclohexane and methylcyclohexane in a continuous flow reactor under steady state conditions using Pt and Pd supported on stacked cone carbon nanotubes (SC-CNT). [1] The Pt/SC-CNT catalysts exhibited the highest activity for the dehydrogenation of cyclohexane and methylcyclohexane to produce hydrogen and benzene or toluene, respectively. HRTEM images showed that the Pt particles were highly dispersed with mean sizes ~2-3 nm after time on stream of over six hours at 315°C.

Cooper et al. [2] have also studied the possibility of using liquid-phase cycloalkane hydrogen carriers (cyclohexane, methylcyclohexane, tetralin, decalin etc.) to supply and store hydrogen. Their analysis integrates the fuel distribution with onboard vehicle storage technology into a total system approach that indicates excellent energy efficiency. Tien et al [3, 4, 5] studied the dehydrogenation of tetralin to produce hydrogen and naphthalene using palladium catalysts supported on activated carbon fibers using both a batch reactor and a continuous flow, fixed-bed reactor. Their results show effective hydrogen evolution from tetralin at 300°C. The relatively high surface area of the activated carbon fibers seems to improve the high activity of their reusable palladium catalyst. Several other groups have reported that dehydrogenation of cyclohexane, methylcyclohexane and decalin can be conducted effectively in the presence of Pt catalysts under "liquid-film" or "wet-dry" conditions. Hodoshima et al.[6, 7, 8] have studied the system of decalin dehydrogenation/naphthalene hydrogenation pair as a hydrogen source for fuel-cell vehicles using a liquid-film type reactor at around 210°C with carbon-supported Pt and Pt-Re composite catalysts. Under liquid-film conditions, hydrogen was evolved from decalin more efficiently than under liquid-phase conditions due to the superheated states of the dehydrogenation catalysts. Kariya et al. [9, 10] studied the hydrogen evolution from liquid cycloalkanes over Pt-containing catalysts supported on activated carbons under "wet-dry multiphase conditions" and by pulse-spray mode reactor with Pt catalysts. In both of these reaction modes, the catalyst surface experiences wet and dry conditions alternately during the reactions, which creates a higher catalyst surface temperature that is advantageous to the endothermic dehydrogenation reaction.

In this paper, we report results for the dehydrogenation of tetralin and decalin using Pt/SC-CNT and Pt, Pd and Rh on other carbon supports and on alumina. The Pt/SC-CNT catalysts are found to be significantly more active for the continuous production of hydrogen at 240°C in a continuous flow reactor than the other catalysts tested.

Experimental

The SC-CNT used as catalyst supports in this work were produced by ethane decomposition in a continuous flow reactor at 500°C over a (0.5wt.%Pd-4.5wt.%Fe)/Al_2O_3 catalyst, using the procedures discussed in detail elsewhere.[1, 11, 12] The purified SC-CNT had a BET surface area of 280 m^2/g. Typical images of the SC-CNT structure are shown in Figure 1.

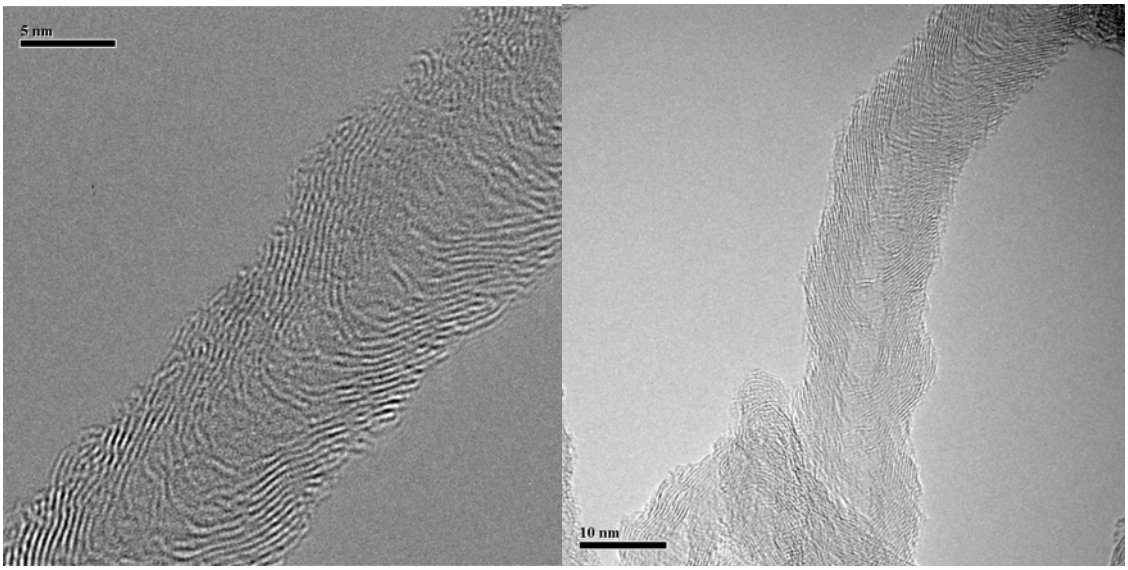

Figure 1. HRTEM images of SC-CNT produced by dehydrogenation of ethane (left) and propane (right) with an Fe-Pd/Al_2O_3 catalyst at 500°C and 475°C, respectively.

The purified SC-CNT were impregnated with $Pt(NH_3)_4(NO_3)_2$ solution to prepare the Pt loaded SC-CNT catalysts. Pt/SC-CNT catalysts with Pt loadings ranging from 0.25 to 1.0 wt.% were prepared. For comparison purposes, 1.0 wt.% Pt/Al_2O_3, 1.0 wt% Pd/Al_2O_3, 1.0 wt.% Rh/Al_2O_3, and 1.0 wt.% Pt/granular carbon were purchased from Alfa Aesar, and a 1.0 wt.% Pt/carbon black(acetylene soot) catalyst was prepared. The impregnated catalysts were calcined before use in N_2 at a flow rate of 50 mL/min for 12 hours at 500°C to decompose the metal nitrates.

The dehydrogenation experiments for tetralin and decalin were carried out in a fixed bed plug-flow stainless steel reactor. Tetralin and decalin with purities of over 98% were purchased from Alfa Aesar. For each run, 0.5 gram of catalyst was used. Prior to reaction, the catalysts were reduced in a hydrogen flow of 50 ml/min for 2 hours at 500°C. No methane was produced during this treatment, indicating that the graphitic layers of the SC-CNT do not undergo any gasification reaction under these reduction conditions. After reduction, the reactor was flushed with an inert gas until the GC showed no residual hydrogen peak (~15 minutes.). Liquid tetralin or decalin were then pumped into the reactor using a syringe pump at a flow rate equivalent to 5 ml/min of gaseous tetralin or decalin flow calculated at 25°C. The thermodynamic Gibbs free

energies for the dehydrogenation of tetralin, *cis*-decalin and *trans*-decalin to hydrogen and naphthalene in the ideal gas state without catalysts go to zero at 262, 231 and 257ºC, respectively, using the formulas given in Yaw's book, which are shown in Table 1. [13] In the current experiments, the dehydrogenation reactions shown in table 2 were investigated at atmospheric pressure at a temperature of 240ºC. The reaction products were first trapped in a condenser cooled by a mixture of ice and water. Liquid products in the condenser were later analyzed using a HP 5890 FID GC. The gaseous reaction products were analyzed online using a Perkin-Elmer GC with a TCD detector for hydrogen and light hydrocarbons (C1-C3) analysis, which were the only gaseous products observed after the liquid condenser. All the experiments were run for 90 minutes before termination.

Table 1. Parameters used for calculation of the Gibbs energy of formation (ΔG_f) for tetrahydro-napthalene, decalin and naphthalene. ΔG_f (kJ/mole) = $A + BT + CT^2$ (T=298 K-1000K).[13]

name of molecule	A(kJ/mole)	B(kJ/(mole·K)	C(kJ/(mole·K^2)
tetralin	23.033	4.6879E-01	4.3036E-05
decalin-cis	-175.788	8.5412E-01	9.0650E-05
decalin-trans	-189.001	8.5677E-01	6.9466E-05

Table 2. Dehydrogenation reactions of tetralin and decalin.

Tetralin reaction: $C_{10}H_{12}(g) \rightarrow C_{10}H_8(g) + 2\ H_2(g)$
Cis-decalin reaction: $C_{10}H_{18}\ (g) \rightarrow C_{10}H_8(g) + 3H_2(g)$
Trans-decalin reaction: $C_{10}H_{18}\ (g) \rightarrow C_{10}H_8(g) + 3H_2(g)$

Results and discussion

Dehydrogenation of tetralin

The catalytic reaction of dehydrogenation of cycloalkanes to produce hydrogen and aromatics suffers two disadvantages for automotive applications: the first is the relatively high temperature required to provide enough energy for this endothermic reaction; the second is that the aromatic products produced compete with the reactants for adsorption on the catalysts surface. [2, 3] The already existing aromatic ring in tetralin molecule may lead to advantageous adsorption on the catalyst, making it a good candidate for hydrogen production.

The results obtained by catalytic dehydrogenation of tetralin with all of the catalysts tested are presented in table 3. Figures 2 and 3 compare the conversions obtained at 240ºC for Pt catalysts supported on different carbon supports. It is seen in Figures 2 and 3 that 1.0 wt% Pt/SC-CNT has the best activity for dehydrogenation of tetralin to hydrogen and naphthalene, with a 50.3 mole% conversion and a hydrogen generation rate of 5.31 ml/min. It is seen in Table 3 that the activity of the SC-CNT support is essentially negligible. For SC-CNT supported catalysts, as Pt

Table 3. Dehydrogenation of tetralin with different catalysts.

Catalyst	Conversion (%)	Hydrogen evolution rate (ml/min)	Turnover frequency (mole H_2/mole Pt)/s
SC-CNT	0.5	0.05	
1 wt.% Pt/granular	9.5	0.95	0.027
1 wt.% Pt/carbon black	18.0	1.8	0.052
0.25 wt.% Pt/SC-CNT	21.3	2.13	0.247
0.50 wt.% Pt/SC-CNT	35.9	3.59	0.208
1.0 wt.% Pt/SC-CNT	50.3	5.31	0.146
1.0 wt.% Pd/Al_2O_3	45.5	4.53	0.132
1.0 wt.% Pt/Al_2O_3	48.2	4.82	0.139
1.0 wt.% Rh/Al_2O_3	50.2	5.02	0.145

loading increases, the activity of the catalyst increases in nearly a linear fashion up to 1 wt.%. The higher activity for Pt on the SC-CNT supports undoubtedly reflects its higher dispersion. As shown previously, the mean Pt particle diameter on these supports is typically only 2-3 nm, [1] while the Pt particle diameter on granular carbon is 80-100 nm and that on carbon black is 10-15 nm, as shown by the TEM micrographs in Figure 4.

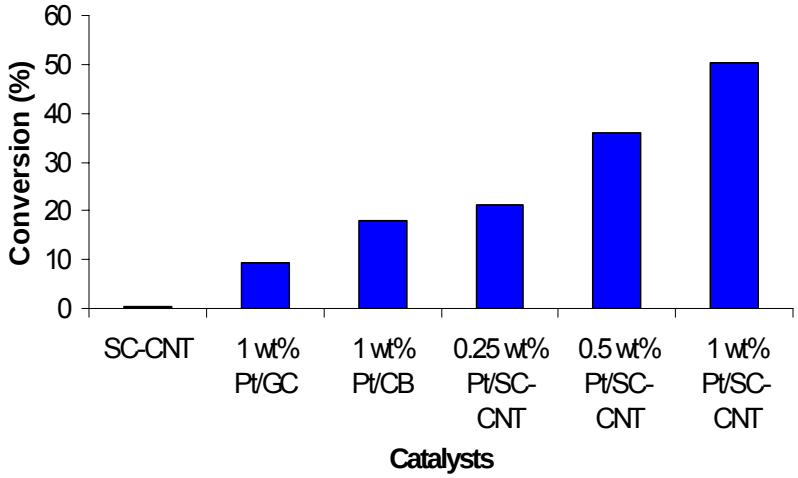

Figure 2. Conversion of tetralin with Pt catalysts supported on different carbon support at 240 °C

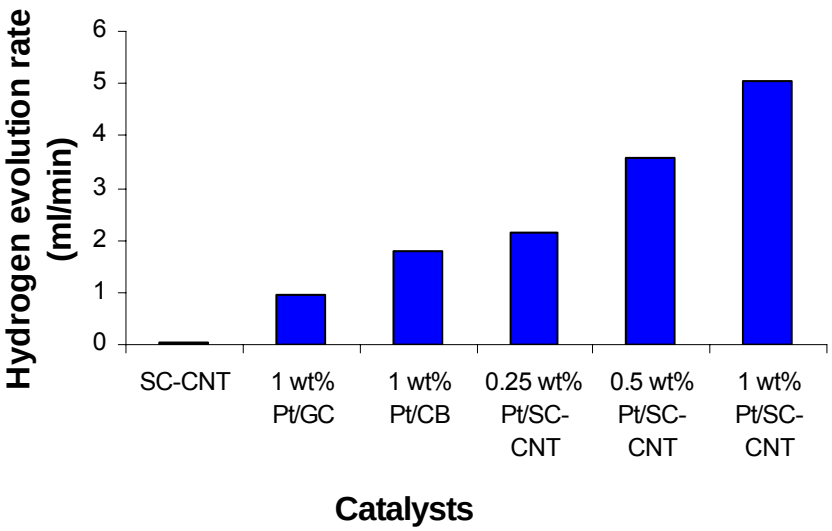

Figure 3. Hydrogen evolution rate for tetralin at 240 °C using Pt on different carbon supports.

Figure 3 shows the hydrogen evolution rate for different carbon supported Pt catalysts. The best catalyst 1.0 wt% Pt/SC-CNT generates hydrogen at a rate of 5.31 ml/min. Since one mole of tetralin produces two moles of hydrogen and one mole of naphthalene, the speed of hydrogen generation for a catalyst is proportional to its conversion, so figure 3 exhibits the same trend as observed in figure 2.

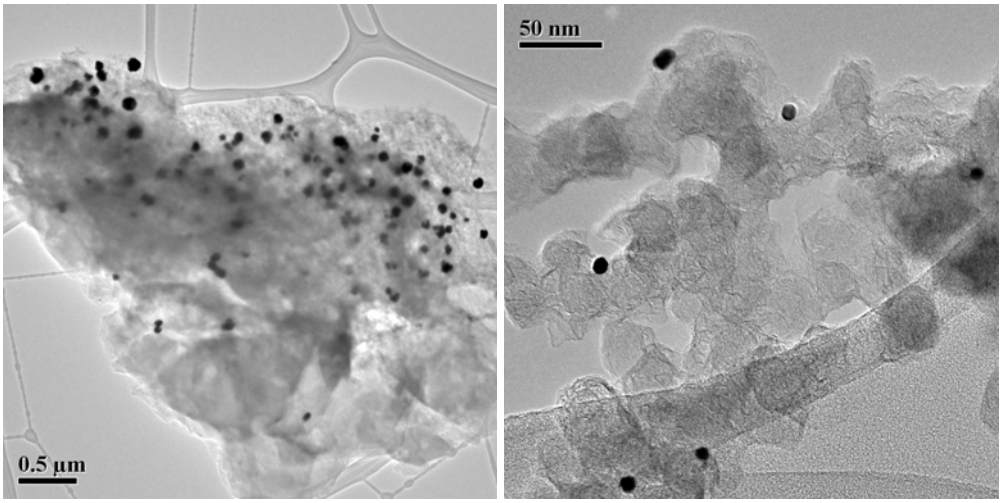

Figure 4. HRTEM images of used Pt catalysts for dehydrogenation of tetralin. Left: 1.0wt.%Pt/granular carbon Right: 1.0wt.%Pt/carbon black.

It should be noted from Table 3, however, that although the 1.0 wt% Pt/SC-CNT shows the best activity for hydrogen generation, the 0.25 wt% of Pt/SC-CNT has the highest hydrogen turn over frequency (TON) for per metal atom used. {TON = {2×(moles of tetralin converted)/(moles of metal present)/second}. The TON for each catalyst calculated is the average TON for the entire time on stream time of 90 minutes.

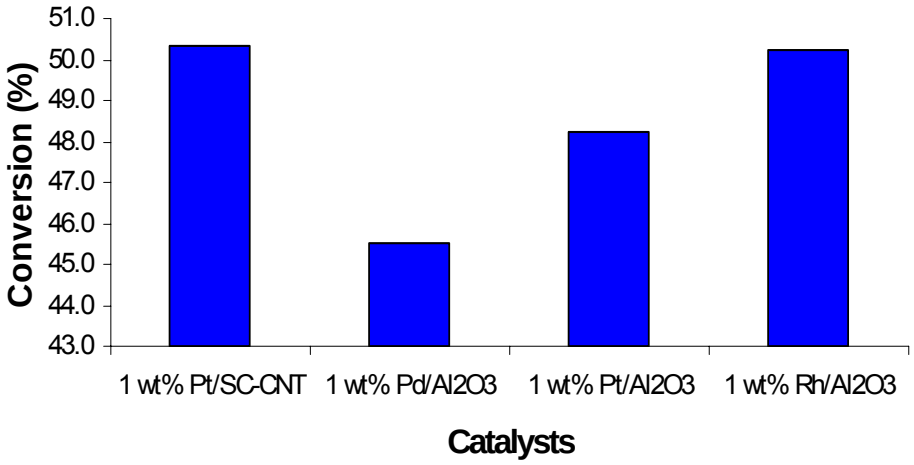

Figure 5. Comparison of tetralin conversion for Pt/SC-CNT to those of several alumina supported metals.

Figure 5 compares the conversion results for dehydrogenation of tetralin using 1.0 wt.% of several different metal catalysts supported on alumina to those obtained using the 1.0 wt.% Pt/SC-CNT catalyst. The Pt/SC-CNT exhibits the best activity of all these catalysts although the Rh/Al_2O_3 catalyst is nearly as good.

Dehydrogenation of decalin

Decalin has a hydrogen storage capacity of 4.3 wt.% and it has been proposed as a storage medium for fuel-cell hydrogen in mobile modes. Moreover, catalytic naphthalene hydrogenation to decalin was performed industrially as early as the 1940s and the existing liquid fuels infrastructure can be used for the transportation of decahydro-naphthalene. [14] In the cycle of dehydrogenation of decalin and hydrogenation of naphthalene, decalin is usually a mixture of cis- and trans- isomers. The cis-isomer has a flexible geometric structure while the trans-isomer has a rigid geometric structure as shown in figure 6. Figure 7 shows the dehydrogenation of a decalin mixture of 37% of cis- and 63% of trans- with different catalysts at 240 °C. The 1.0 wt.% Pt/SC-CNT again shows the highest conversion.

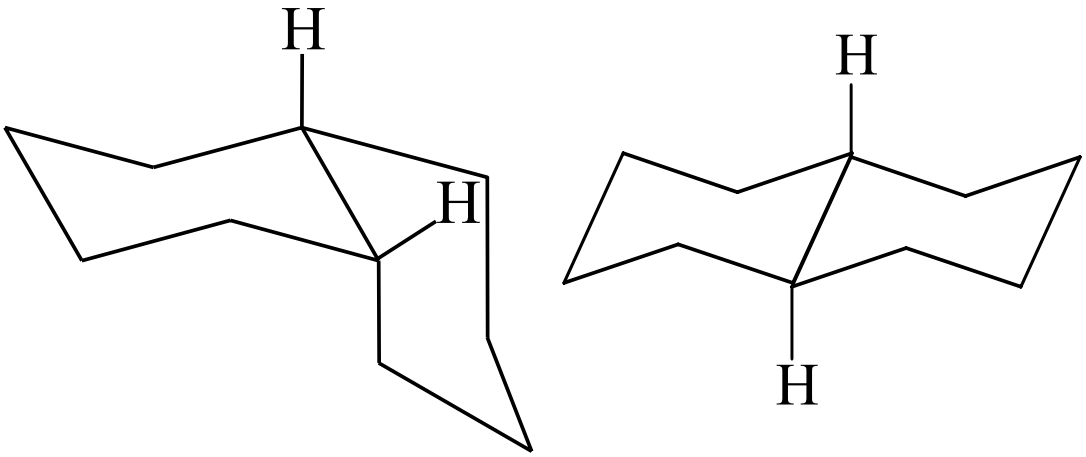

Figure 6. Structure of cis-(left) and trans-(right) decalin

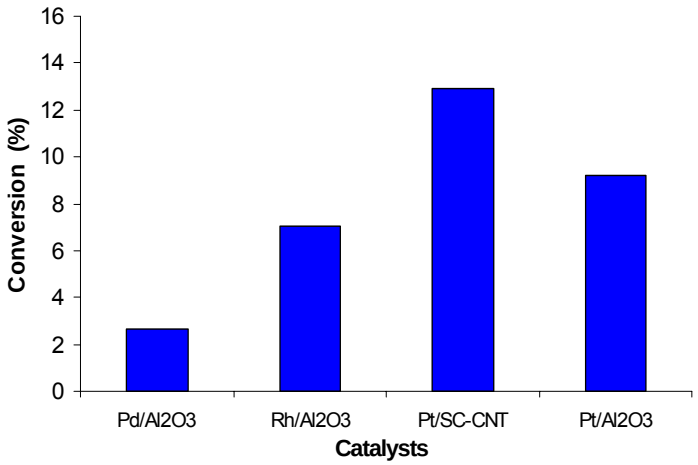

Figure 7. Dehydrogenation of decalin with different catalysts at 240 °C

Unlike the conversion results for tetralin, the decalin conversion for the Rh catalyst is significantly lower than that exhibited by the Pt/SC-CNT catalyst. Pd/Al_2O_3 again exhibits the worst activity among the three alumina supported catalysts. The activity order for dehydrogenation of decalin is as follows: 1.0wt.% Pt/SC-CNT > 1.0wt.% Pt/Al_2O_3 > 1.0wt.% Rh/Al_2O_3 > 1.0wt.% Pd/Al_2O_3. For the run with 1.0wt.% Pt/SC-CNT, after 90 minutes of time on stream, there were 19% cis-decalin, 68% trans-decalin, 4% tetralin and 9% naphthalene in the liquid products. The smaller amount of tetralin compared with the amount of naphthalene shows that the dehydrogenation of decalin to tetralin is the intermediate step for producing naphthalene and the reaction of dehydrogenation of tetralin to naphthalene and hydrogen is the faster step. On the other hand, the remaining 68% trans-decalin in the products compared with the remaining 19% cis-decalin is higher than the amount of trans-decalin in the starting mixture of 63% *trans*-decalin and 37% *cis*-decalin, which means that *trans*- decalin converts more slowly than *cis*-decalin. The more stable *trans*- structure may contribute to this because there is no steric strain between the two bridging hydrogen atoms in the *trans*- structure. Unlike the flexible *cis*-structure in which the two rings can be flipped, the rigid geometric structure of *trans*-decalin makes it more difficult for it to be adsorbed onto the catalyst surface.

In the dehydrogenation of cycloalkanes to generate aromatic products and hydrogen, the aromatic product desorbs slowly from the catalyst surface and there is a retardation effect on the conversion rate of cycloalkanes. [4-8] The aromatic ring in tetralin promotes its adsorption onto the catalyst surface in the competition with the naphthalene product. Therefore, although the Gibbs energy for dehydrogenation of cis-decalin to naphthalene and hydrogen in the ideal gas state goes to zero at 231°C while that of tetralin goes to zero at 262°C, the conversion of tetralin at 240°C by 1.0wt% Pt/SC-CNT is 35.6% and higher than that of cis-decalin, which is only 13%. Even at 300°C, the dehydrogenation of decalin in a membrane reactor gives only a very low conversion (~15%). However, the conversion is greatly enhanced by the selective separation of hydrogen by a membrane and its removal from the reactor.[15] Overall, it appears that for fast on-board hydrogen generation by catalytic dehydrogenation, tetralin is preferable to decalin despite its lower hydrogen storage capacity.

Summary and Conclusions

It has been shown that efficient production of pure hydrogen can be achieved by dehydrogenation of tetralin or decalin with catalysts consisting of 0.25-1.0 wt% Pt supported on SC-CNT. The catalysts exhibited 100% selectivity for the conversion of tetralin to hydrogen and naphthalene and close to 100% selectivity for the conversion of decalin to hydrogen and naphthalene. A 0.25 wt% Pt/SC-CNT catalyst has the highest turn over frequency for hydrogen production from tetralin. A 1 wt% Pt/SC-CNT catalyst exhibited greater conversion percentages for both tetralin and decalin than 1 wt% of Pt, Pd, or Rh supported on alumina The flexible geometric structure of *cis*-decalin contributes to its faster conversion to naphthalene and hydrogen than observed for *trans*-decalin. The aromatic ring in the tetralin structure appears to favor its adsorption to catalyst surfaces and may account for its significantly higher conversion rate than decalin.

Publications and other significant communications (2002-2005):

1. Yuguo Wang, Naresh Shah, and Gerald P. Huffman, "Pure hydrogen production by partial dehydrogenation of cyclohexane and methylcyclohexane over nanotube supported Pt and Pd catalysts", *Energy & Fuels*, **18** (2004) 1429-1433.

2. Brian C. Dunn, Daniel J. Covington, Paul Cole, Ronald J. Pugmire, Henk L.C. Meuzelaar, Richard D. Ernst, Emily C. Heider, Edward M. Eyring, Naresh Shah, and Gerald P. Huffman, "Silica aerogel supported cobalt metal Fischer-Tropsch synthesis", *Applied Catalysis A* (2004) in press.

3. Brian C. Dunn, Daniel J. Covington, Paul Cole, Ronald J. Pugmire, Henk L.C. Meuzelaar, Richard D. Ernst, Emily C. Heider, Edward M. Eyring, Naresh Shah, Gerald P. Huffman, M.S. Seehra, A. Manivannan, and P. Dutta, "Silica xerogel supported cobalt metal Fischer-Tropsch catalysts for syngas to diesel range fuel conversion", *Energy & Fuels*, **18** (2004) 1519-1521.

4. Yuguo Wang, Naresh Shah, and Gerald P. Huffman, "Simultaneous production of hydrogen and carbon nano-structures by decomposition of propane and cyclohexane over alumina supported binary Fe-based catalysts", *Catalysis Today*, **99** (2004) 359-364.

5. Gerald P. Huffman, Naresh Shah, Yuguo Wang, and Frank E. Huggins, "Catalytic dehydrogenation of hydrocarbons: alternative one-step process to produce pure hydrogen and carbon nanotube byproducts", *ACS Fuel Chemistry Division Preprints*, **49(2)** (2004) 731-732; invited presentation at the ACS Presidential symposium: Fuels for the Future: Leading the Way with Chemistry, ACS National Meeting, Philadelphia, PA, August 24, 2004.

6. Artur Braun, Jan Ilavsky, Brian C. Dunn, Pete R. Jemian, Frank E. Huggins, Edward E. Eyring, and Gerald P. Huffman, "Ostwald-Ripening of Cobalt Precipitates in Silica Aerogels? – An Ultra-Small X-Ray Scattering Study", *J. Applied Crystallography*, **38** (2004) 132-138.

7. P. Dutta, B. C. Dunn, E. M. Eyring, N. Shah, G. P. Huffman, A. Manivannan, M. S. Seehra, Characteristics of Cobalt Nanoneedles in 10% Co/Aerogel Fischer-Tropsch Catalyst, Chemistry of Materials, 17(20) (2005) 5183-5186.

References:

1. Yuguo Wang, Naresh Shah, and Gerald P. Huffman, Energy *& Fuels*, **18** (2004) 1429-1433.

2. Cooper, A. C.; Bagzis, L. D.; Campbell, K. M.; Pez, G. P., *ACS Div. Fuel Chem. Preprints*, **2005**, *50 (1)*, 271-273.

3. Tien, P. D.; Satoh, T.; Miura, M.; Nomura, M.; Energy & Fuels, **2003**, 17, 658-660.

4. Tien, P. D.; Satoh, T.; Miura, M.; Nomura, M.; Energy & Fuels, **2005**, 19, 731-735.

5. Tien, P. D.; Satoh, T.; Miura, M.; Nomura, M.; Energy & Fuels; **2005**, 19, 2110-2113.

6. Hodoshima, S.; Arai, H.; Saito, Y.; Int. J. Hydrogen Energy, **2003**, 28, 197-204.

7. Hodoshima, S.; Arai, H.; Saito, Y.; Int. J. Hydrogen Energy, **2003**, 28, 1255-1262.

8. Hodoshima, S.; Takaiwa, S.; Shono, A.; Satoh, K.; Saito, Y.; Appl. Catal. **2005**, 283, 235-242.

9. Kariya, N.; Fukuoka, A.; Ichikawa, M.; Appl. Catal. **2002**, 233, 91-102.

10. Kariya, N.; Fukuoka, A.; Ichikawa, M.; Appl. Catal. **2002**, 233, 91-102.

11. Shah, N.; Panjala, D.; Huffman, G. P., *Energy & Fuels*, **2001**, *15(6)*, 1528.

12. Shah, N.; Wang, Y.; Panjala, D.; Huffman, G.P., *Energy & Fuels,* **2004**, 18, 1429-1433.

13. Yaw, L. C., Chemical Properties Handbook: Physical, Thermodynamic, Environmental, Transport, Safety, and Health Related Properties for Organic and Inorganic Chemicals, McGraw-Hill, New York, 1999.

14. Weitkamp, A. W., Adv. Catal., 1968, 18, 1-110.

15. Loufty, R. O.; and Vekster, E. M. *In Proceedings of the International Hydrogen Energy Forum 2000*; Munich, 2000, pp. 335.

METAL-PROMOTED CERIA CATALYSTS FOR THE WATER-GAS-SHIFT PRODUCTION OF HYDROGEN

Edward M. Eyring

Department of Chemistry, University of Utah, Salt Lake City, UT 84112

I. Introduction

Metal-promoted ceria catalysts have been shown to be highly active for the production of hydrogen from carbon monoxide and water through the Water-Gas-Shift Reaction (WGSR).[1] One drawback to previously investigated ceria catalysts is the relatively low surface area of impregnated or precipitated catalysts.[2] The surface areas of impregnated catalysts are usually less than 100 m^2/g and precipitated catalysts can sometimes be as high as 165 m^2/g. A recent report suggests that high surface area ceria [3] (275 m^2/g) can be prepared via a sol-gel route, but the authors did not employ the ceria aerogel as a catalyst. Using the reported preparation method as a starting point, it should be possible to synthesize metal-promoted ceria catalysts with a much higher surface area.

II. Experimental

Research into new heterogeneous catalysts involves 3 distinct steps: synthesis, pretreatment, and measuring catalytic performance. The results from the first experiment are then used to guide the next experiment. This procedure is repeated for subsequent trials. Because catalytic performance requires many days to evaluate, the overall process can often be quite time-consuming. Therefore, we have designed and constructed a 6-channel microreactor that allows evaluation of 5 new catalysts and a reference catalyst simultaneously. This parallel arrangement increases our experimental throughput by five-fold without any loss in data fidelity.

The 6-channel microreactor is based on an 18-channel microreactor recently reported. [4] We have adapted the design to our specific requirements, namely the inclusion of a water vaporizer, heated gas-distribution manifold, and heated stream selection valve. The overall apparatus consists of several subassemblies that are described individually below and a block digram appears in Figure 1.

The focus of the microreactor is the six catalyst beds and heated block. Each reactor consists of a stainless steel tube with a stainless steel frit in the center to support the catalyst. The tubes pass through a stainless steel block to heat the catalyst beds to the desired reaction temperature. To ensure thermal homogeneity, the tubes are arranged in a circle surrounding one heating element and six additional heating elements surround the reactors. A thermocouple is located within each catalyst bed to monitor the reaction temperature.

Reactants are distributed to the reactors by splitting a single stream into six identical streams. The splitting is accomplished by using six matched orifices which ensure that the flow is identical in each reactor. The orifices are 63.5 μm in diameter and are protected from plugging by both an upstream and downstream 15 μm screen. The entire manifold assembly is heated in an oven to maintain all reactants in the gas phase. CO and N_2 are delivered into the manifold by means of electronic mass-flow controllers and water is delivered via a precision

syringe pump into a heated vaporizer. The N_2 gas purges the vaporizer and carries the water vapor downstream.

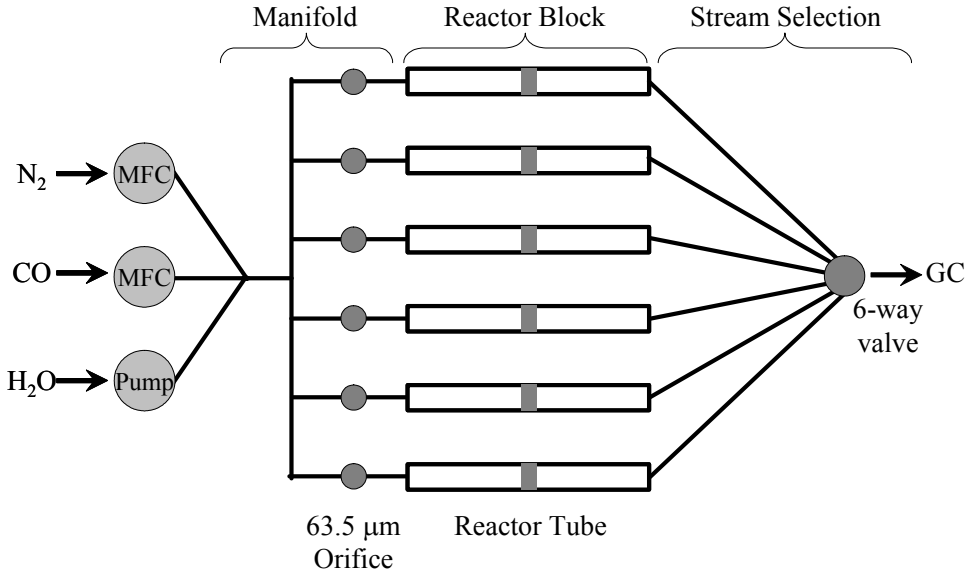

Figure 1. Block diagram of 6-channel microreactor. MFC ≡ mass flow controller. GC ≡ gas chromatograph.

The effluent of each reactor is connected to a six-way stream selection valve. This valve maintains isolation between streams and delivers a single stream to a GC for product analysis. Since only one stream can be analyzed at a time, the valve periodically advances so that another stream can be analyzed. The stream in maintained at elevated temperature by locating it within an oven.

The entire reactor assembly is computer-controlled for data logging and emergency shutdown. All reaction parameters (flow rates, internal reactor temperatures, external reactor temperatures, oven temperatures, manifold pressure, and valve position) are constantly monitored and an out-of-specification condition will trigger an emergency shutdown procedure. Electrical power to all heaters will be discontinued and must be reset manually before the reactor can be restarted. The flow of CO and H_2O will be halted, but the N_2 carrier gas will continue.

Ceria aerogels were prepared by adapting a published procedure. [3] Cerium(IV) methoxyethoxide, methoxyethanol, and water were combined under an inert atmosphere in a molar ratio of 1:36:9. The solution was manually mixed until homogeneous and air was bubbled through the solution until the purple solution became orange. Gelation occurred in approximately 2 hours after the color change. This oxidation step using air is the major deviation from the published procedure, but is necessary to achieve gelation. The alcogels were dried into aerogels using supercritical CO_2.

Gold and copper were incorporated into the ceria aerogel as preformed zero-valent nanoparticles. [5] The nanoparticles were added to the reaction mixture prior to gelation and were

retained within the gel through the supercritical drying step. Palladium was incorporated into the ceria aerogel by gas-phase impregnation using (η^3-allyl)(η^5-cyclopentadienyl) palladium.[6] A sample of the Pd precursor and ceria aerogel were physically mixed and kept under a dynamic vacuum overnight. The solid Pd precursor gradually disappeared as it sublimed into the ceria aerogel. All catalysts were calcined at 200 ^oC for four hours before testing. The surface area of each catalyst was determined using nitrogen adsorption (single-point BET method) at -196 ^oC using a Micromeritics Chemisorb 2720 that was purchased during the period of time covered by this report.

All catalysts were evaluated in the 6-channel microreactor at 5 different temperatures with at least 24 hours time-on-stream at each temperature. The amounts of H_2 and CO_2 produced and the amount of CO consumed were determined from online gas chromatography. Each reactor was sampled every two hours. The catalysts were evaluated in both their as-prepared and calcined state.

III. Results and Discussion

Because the 6-channel microreactor is an unconventional design (compared with a single-channel microreactor), qualifications tests were performed to ensure temperature and flow homogeneity. Figure 2 shows the flow rate through each reactor under four different experimental conditions: 1) 250 ^oC and 35 cm^3/min N_2; 2) 250 ^oC and 3.5 cm^3/min N_2; 3) 25 ^oC and 35 cm^3/min N_2; and 4) 25 ^oC and 3.5 cm^3/min. The flow rate in each channel was nearly identical and small variations are due to manufacturing differences in the orifice size.

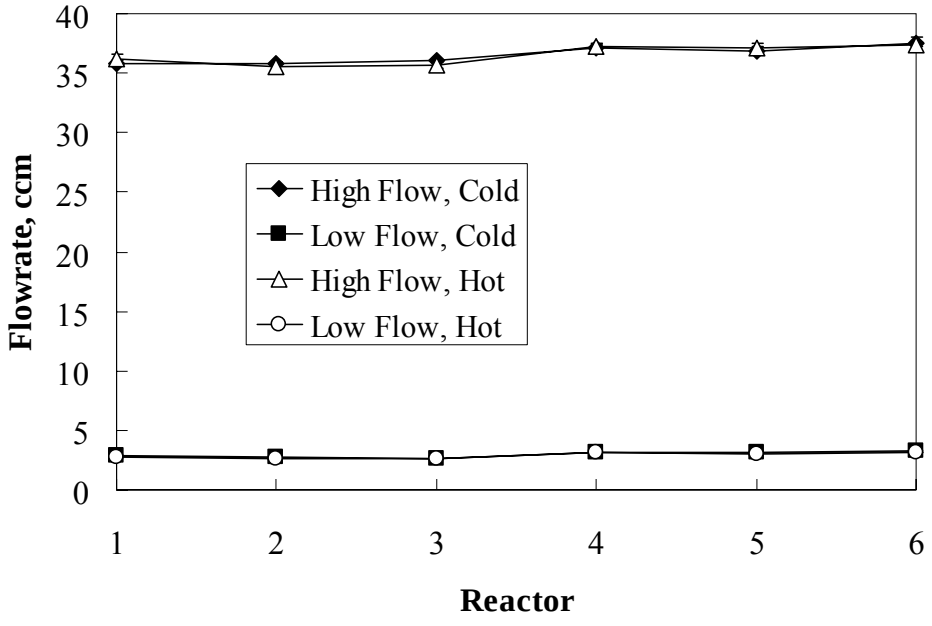

Figure 2. Measured flow rates though each reactor of 6-channel microreactor.

Figure 3 shows the temperature within each reactor during a typical heat-up step followed by maintaining the temperature at 160 ^{o}C for 30 minutes. Only small differences in temperature were observed among the 6 channels. Any small differences in temperature that might cause a change in catalytic reaction rate are of little concern because the actual catalyst bed temperature is measured.

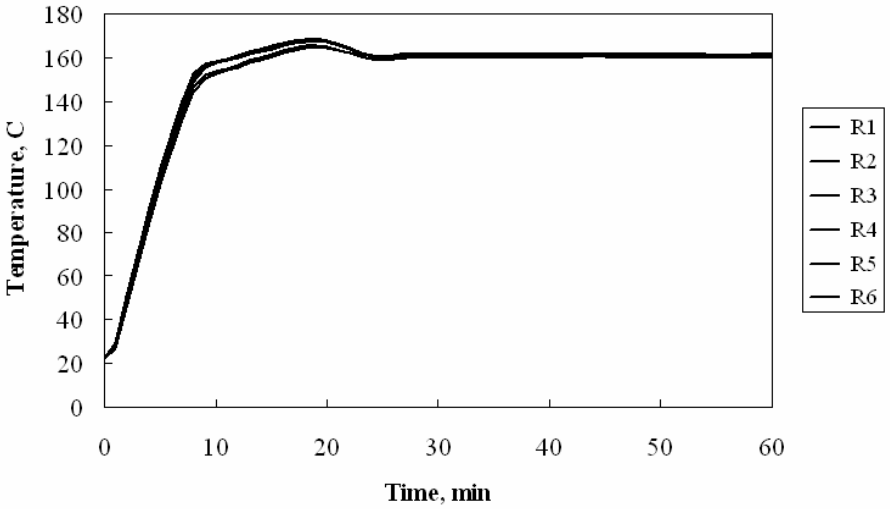

Figure 3. Internal temperature of each reactor during heating.

The specific surface area of 6 catalysts appears in Table 1 in both the as-prepared and calcined state. Some loss of surface area occurred during the four hour calcination at 200 ^{o}C, but the loss was limited to about 10%. Metal nanoparticle loading with gold and copper showed some loss in surface area while the gas-phase incorporation of palladium appeared to maintain the surface area of the pure ceria aerogel. This likely indicates that the palladium exists as an amorphous layer on the ceria surface or very small particles on the ceria surface.

Table 1. Specific surface area of 1% metal-promoter ceria aerogel catalysts.

Catalyst	Specific Surface Area, m^2/g
Ceria aerogel	275.0 ± 1.3
Au/ceria aerogel, as prep'd	229.1 ± 1.4
Au/ceria aerogel, calcined	193.0 ± 0.9
Pd/ceria aerogel, as prep'd	283.6 ± 1.2
Pd/ceria aerogel, calcined	not available
Cu/ceria aerogel, as prep'd	225.8 ± 4.1
Cu/ceria aerogel, calcined	195.5 ± 2.2

The six metal-promoted ceria aerogel catalysts as well as the pure ceria aerogel were evaluated for catalytic activity towards the production of hydrogen via the WGSR at five temperatures and the results are shown in Figure 4.

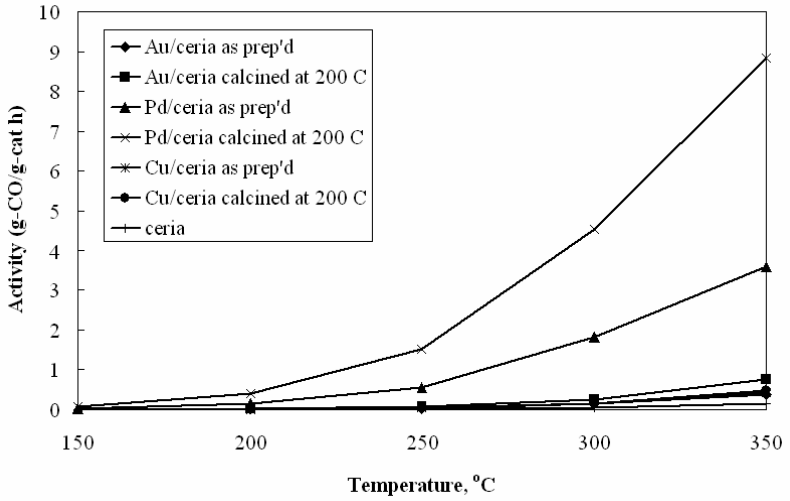

Figure 4. Specific activity of metal-promoted ceria aerogel catalysts.

Calcination typically resulted in an increase of catalytic activity by a factor of 2 and the palladium-based catalysts were the most active in both the as-prepared and calcined states. Some hydrogen was detected for each metal-promoted ceria aerogel catalyst and the pure ceria aerogel. These results are in agreement with previous reports that palladium is a more effective catalyst for low-temperature WGSR than either copper or gold. [7, 8] The activation energy for the catalyzed WGSR can be calculated from the temperature dependence of the measured reaction rate for each catalyst and the results are shown in Figure 5.

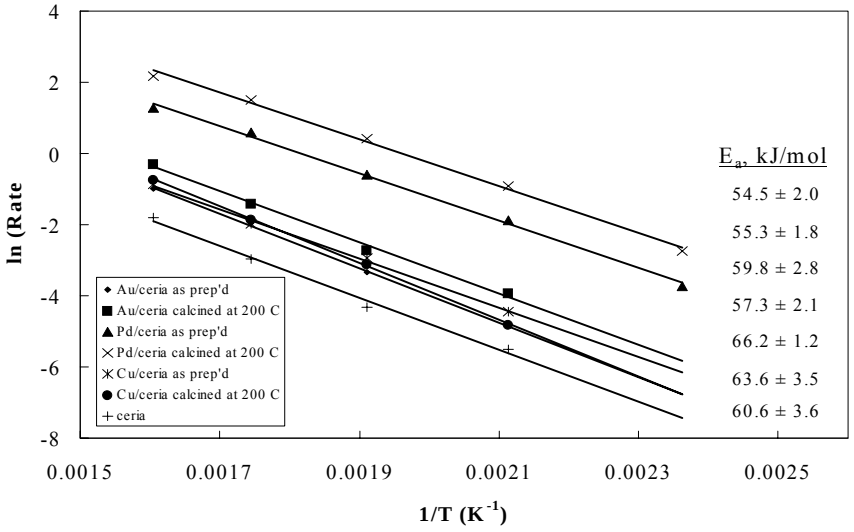

Figure 5. Arrhenius-style plots to calculate activation energy for the Water-Gas-Shift Reaction.

The activation energies are higher than those previously reported [7] in 2004 by Hilaire and coworkers. Further optimization of the catalyst synthesis and pretreatment conditions should provide lower activation energies and more active catalysts. One promising optimization [9] is the inclusion of copper into a palladium-based catalyst as this has been shown to be effective in increasing the catalytic activity.

IV. Conclusions

The sol-gel synthesis followed by supercritical CO_2 drying leads to ceria aerogel-based catalysts with much higher surface area than impregnated or precipitated catalysts. The catalysts are active towards the production of hydrogen through the WGSR. Gas-phase loading of palladium resulted in more active catalysts than the incorporation of either copper or gold zero-valent nanoparticles.

V. Publications and Presentations

1) "Characteristics of Cobalt Nanoneedles in 10% Co/Aerogel Fischer-Tropsch Catalyst," Dutta, P.; Dunn, B. C.; Eyring, E. M.; Shah, N.; Huffman, G. P.; Manivannan, A.; Seehra, M. S. *Chemistry of Materials* **2005**, *17*, 5183-5186.
2) "SBA-15 supported cobalt and iron catalysts for Fischer-Tropsch synthesis," Kim, D. J.; Dunn, B. C.; Kang, M.; Yie, J. E.; Eyring, E. M. 230th ACS National Meeting, Washington, DC, Aug. 28-Sept. 1, 2005.
3) "Aerogel-supported transition metal catalysts for Fischer-Tropsch and related reactions," Turpin, G. C.; Dunn, B. C.; Shi, Y.; Ma, Z.; Pugmire, R. J.; Eyring, E. M.; Ernst, R. D. 230th ACS National Meeting, Washington, DC, Aug. 28-Sept. 1, 2005.
4) "Enhancement in the reducibility of cobalt oxides on a mesoporous silica supported cobalt catalyst," Kim, D. J.; Dunn, B. C.; Cole, P.; Turpin, G. C.; Ernst, R. D.; Pugmire, R. J.; Kang, M.; Kim, J. M.; Eyring, E. M.. *Chemical Communications* **2005**, *11*, 1462-1464.
5) "Mesoporous silica supported cobalt catalysts for Fischer-Tropsch synthesis: Reducibility of cobalt oxides and catalytic activity," Kim, D. J.; Dunn, B. C.; Cole, P.; Turpin, G. C.; Ernst, R. D.; Pugmire, R. J.; Kang, M.; Lee, H. I.; Kim, J. M.; Eyring, E. M. 229th ACS National Meeting, San Diego, CA, March 13-17, 2005.
6) "Ostwald ripening of cobalt precipitates in silica aerogels? An ultra-small-angle X-ray scattering study," Braun, A.; Ilavsky, J.; Dunn, B. C.; Jemian, P. R.; Eyring, E. M.; Huggins, F. E.; Huffman, G. P. *Journal of Applied Crystallography* **2005**, 38, 132-138.
7) "Silica aerogel supported catalysts for Fischer-Tropsch synthesis," Dunn, B. C.; Cole, P.; Covington, D.; Webster, M. C.; Pugmire, R. J.; Ernst, R. D.; Eyring, E. M.; Shah, N.; Huffman, G. P. *Applied Catalysis, A: General* **2005**, 278, 233-238.
8) "Mesostructured silica supported cobalt catalysts for Fischer-Tropsch Synthesis,". Kim, D. J.; Dunn, B. C,; Cole, P.; Turpin, G. C.; Ernst, R. D.; Pugmire, R. J.; Kang, M.; Lee, H. I.; Kim, J. M.; Eyring, E. M. Poster Presentation, Gordon Research Conference (Hydrocarbon Resources), January 9-14, 2005, Ventura, CA.
9) "Silica aerogel as a Fischer-Tropsch catalyst Support," Dunn, B. C.; Cole, P.; Turpin, G. C.; Ma, Z.; Pugmire, R. J.; Ernst, R. D.; Eyring, E. M. Poster Presentation, Gordon Research Conference (Hydrocarbon Resources), January 9-14, 2005, Ventura, CA.

VI. References

1. Fu, Q.; Saltsburg, H.; Flytzani-Stephanopoulos, M. *Science* **2003**, *301*, 935.
2. Jacobs, G.; Crawford, A.; Williams, L.; Patterson, P. M.; Davis, B. H. *Appl. Catal. A: Gen.* **2004**, *267*, 27.
3. Thundathil, M. A.; Lai, W.; Noailles, L.; Dunn, B. S.; Haile S. M. *J. Am. Ceram. Soc.* **2004**, *87*, 1442.
4. Hendershot, R .J.; Lasko, S. S.; Fellmann, M. F.; Oskarsdottir, G.; Delgass, W. N.; Snively, C. M.; Lauterbach, J. *Appl. Catal. A: Gen.*, **2003**, *254*, 107
5. Slot, J.; Geuze, H. *J. Cell Biol.* **1981**, *90*, 533.
6. Tatsuno, Y; Yoshida, T.; Otsuka, S. *Inorg. Syn.* **1979**, *19*, 220.
7. Hilaire, S., Wang, X.; Luo, T.; Gorte, R. J.; Wagner, J.; *Appl. Catal. A: Gen.* **2004**, *258*, 271.
8. Li, Y.; Fu, Q,; Flytzani-Stephanopoulos, M. *Appl. Catal. B: Env.* **2000**, *27*, 179.
9. Bickford, E. S.; Velu, S.; Song, C. *Catal. Today* 2005, *99*, 347.

HYDROGEN PRODUCTION FROM PARTIAL OXIDATION OF PROPANE OVER PLATINUM-ON-CERIA CATALYSTS

Tapan K. Das, Vijaya Bansode, Edwin L. Kugler and Dady B. Dadyburjor

Department of Chemical Engineering
West Virginia University
Morgantown, WV 26505-6102

I. INTRODUCTION

The production of hydrogen has achieved increased importance in recent years especially in refineries due to new environmental laws demanding more environmental-friendly fuels with ultra low sulphur and nitrogen content and less aromatics [1, 2] [1,2]. The conversion of gasoline to hydrogen is an attractive option for fuel-cell feeds since no infrastructure for hydrogen fuel supply currently exists. The major technologies for reforming hydrocarbons into hydrogen, carbon monoxide and carbon dioxide are catalytic steam reforming, partial oxidation and autothermal reforming [3, 4] [3,4]. The commercial process for the production of hydrogen uses steam reforming process over a Ni catalyst at high temperatures. But the drawback is that this reaction is endothermic and, therefore, the reactor needs to be heated by combustion of fuels. Partial oxidation and autothermal reforming processes promise to have much better dynamics than steam reforming system since they do not require external heating and can be heated up internally by exothermic reaction of fuels. In this study, propane was used as a model reactant and the results obtained over propane feed can be extended to develop an on-board gasoline fuel processor.

The theoretical conditions for the formation of CO and H_2 from C_3H_8 are

$$C_3H_8 + 1.5O_2 = 3CO + 4H_2 \qquad \Delta H° = -227 \text{ kJ/mol}$$

Propane can react with O_2 to form complete combustion products:

$$C_3H_8 + 5O_2 = 3CO_2 + 4H_2O \qquad \Delta H° = -2043 \text{ kJ/mol}$$

Propane can react with steam to form CO and H_2

$$C_3H_8 + 3H_2O = 3CO + 7H_2 \qquad \Delta H° = 498 \text{ kJ/mol}$$

Finally, C_3H_8 can crack to form CH_4 and coke:

$$C_3H_8 = 2CH_4 + C \qquad \Delta H° = -47 \text{ kJ/mol}$$

Cerium oxide has been suggested to promote catalysis of oxidation reactions, due to its oxi-reduction potential and mainly due to the high capability of oxygen storage. We investigated the partial oxidation of propane using Pt/CeO_2 catalysts, with CeO_2 prepared by different techniques. These results are briefly described in this report.

II. EXPERIMENTAL

We prepared 1.0%Pt/CeO_2 catalysts using supports of different surface areas. All supports were loaded with platinum via incipient wetness impregnation using aqueous solution of platinum chloride. The CeO_2 support of lowest surface area was a commercial materials obtained from Aldrich. This support was designated as CeO_2(A). The CeO_2(B) support was prepared via homogeneous precipitation from $Ce(NO_3)_3.6H_2O$ solution with aqueous ammonia [5]. The precipitate was filtered, washed with deionized water and dried 100°C and finally calcined at 400°C for 4 hrs. The high surface area CeO_2 was prepared by decomposition of $Ce(NO_3)_3.6H_2O$ through calcination under air at 500°C using a method similar to Hilaire *et al.* [6]. This support designated as CeO_2(C).

The calcined catalysts were characterized using X-ray diffraction, N_2 adsorption at 77K (BET surface area), temperature programmed reduction (TPR), and O_2 pulse titration after reduction at 500°C in hydrogen. The partial oxidation of propane was carried in a fixed-bed reactor at atmospheric pressure over a temperature range 200-800°C and also over a range of O_2/C_3H_8 ratios using 0.1 g of catalysts. A flowsheet of fixed-bed reactor system is displayed in Figure 1. Results are reported as conversions and selectivities of H_2, CO and CO_2, where selectivity is defined as

S_{H2} = (moles of H_2 produced)/(4 × moles of C_3H_8 consumed)

$S_{CO[or\ CO2]}$ = (moles of CO [or CO_2] produced)/(3 × moles of C_3H_8 consumed)

III. RESULTS AND DISCUSSION

BET surface area measurements for supports and catalysts were conducted and the results are summarized in Table 1. The Pt/CeO_2(B) and Pt/CeO_2(C) have BET surface area 6 and 8 times larger than commercial Pt/CeO_2(A). TPR profiles reported in Figure 2 show two important features. The reduction of bulk ceria occurs at ~750°C. Reduction of surface shell of ceria, present as a large broad peak on the high surface area ceria support, occurs between 400 and 500°C. Pt catalyses the reduction of surface ceria and therefore the reduction peak shifts to the lower temperature, but has little effect on bulk. To further understand the degree of reduction, pulse reoxidation measurements of catalysts reduced at 500°C were performed. As shown in Table 1, high surface area supports and catalysts displayed high extent of reduction as compared commercial catalysts. The commercial catalysts showed significantly lower reducibility.

The effect of temperature on partial oxidation of propane for 1.0%Pt/CeO_2(C) catalyst is shown in Figure 3. The reaction occurs in two simultaneous stages. At the temperature range between 250°C to 500°C, propane oxidized exclusively into CO_2 and H_2O with little H_2. Above 500°C, O_2 is completely consumed and the selectivity of CO and H_2 increase steadily, peaking at 750°C. The activity and selectivity of different 1.0%Pt/CeO_2 catalysts are presented in Table 2. The higher surface area 1%Pt/CeO_2 catalyst shows higher propane conversion, higher H_2 selectivity and lower CO_2 selectivity. The effect of O_2/C_3H_8 ratio on the performance of the 1.0%Pt/CeO_2(C) at 700°C is investigated (Figure 4). Under the constant space velocity by keeping the flow rate of inert (270 ml min^{-1}) and the total flow rate (30 ml min^{-1}) of C_3H_8 and O_2 constant, the respective flow rate of C_3H_8 and O_2 are changed to obtain different O_2/C_3H_8 ratios. The propane conversion increases with increasing O_2/C_3H_8 ratio and it reaches to ~100% at O_2/C_3H_8 ratio 5.0. As the O_2/C_3H_8 ratio changes from 0.5 to 2.0, the H_2 selectivity decreases

slowly and the ratio above 2.0, the CO and H_2 selectivities decrease rapidly. The optimum O_2/C_3H_8 ratio is found to be 2.0 for moderately high conversion and high selectivity. The CO_2 selectivity increases with increasing O_2/C_3H_8 ratio.

IV. CONCLUSIONS

From the above results, the conclusion could be drawn that Pt catalyzes the reduction of surface CeO_2 and has little effect on reduction of bulk CeO_2. CeO_2 prepared by decomposition method exhibits highest BET surface area and reducibility. The $Pt/CeO_2(C)$, prepared by decomposition method, exhibits the highest catalytic activity toward partial oxidation at 700ºC. The reaction temperature below 500°C is total combustion regime produces only CO_2 and water. The temperature above 500°C is the partial oxidation regime along with total combustion. The optimum O_2/C_3H_8 ratio is 2.0 for moderately high conversion and high selectivity.

V. PAPERS PRESENTED

T.K. Das, V. Bansode, E.L. Kugler, and D.B. Dadyburjor, "Effect of Support on Autothermal Reforming of Propane," Conference Proceedings, AICHE Annual Meeting, Cincinnati, OH, October 30, 2005

V. Bansode, T. K. Das, E. L. Kugler and D. B. Dadyburjor, "Effect of Support on Hydrogen Production from Partial Oxidation of Propane over Pt Catalysts," CFFS Annual Meeting, Stonewall Jackson Resort, WV, August 1-3, 2005

T. K. Das, V. Bansode, E. L. Kugler and D. B. Dadyburjor, "Hydrogen Production from Partial Oxidation of Propane over Pt/CeO2 Catalysts," Pittsburgh-Cleveland Catalysis Society Spring Symposium, Pittsburgh, June 17, 2005

T.K. Das, V. Bansode, E.L. Kugler and D.B. Dadyburjor, "Autothermal reforming of propane over Pt/CeO_2 catalysts", 19th North American Chemical Society Meeting, Philadelphia, May 2005

T.K. Das, V. Bansode, E. L. Kugler and D.B. Dadyburjor, "Hydrogen Production from Partial oxidation of propane over Pt/CeO_2 catalysts", Gordon Research Conferences, Hydrocarbon Resources, Ventura, Los Angeles, January 9-14, 2005.

VI. REFERENCES

[1] M.A. Peña, J.P. Gómez, J.L.G. Fierro, "New Catalytic Routes for Syngas and Hydrogen Production", Applied Catalysis A, 144: 7-57, 1996.

[2] J.N. Armor, "The multiple Roles for Catalysis in the Production of Hydrogen", Applied Catalysis A, 176: 159-176, 1999.

[3] A.D. Little, "Muti-fuel Reformers Phase I, Final Report, DOE/CE/50343-2, 1994.

[4] S.G. Chalk, J. Milliken, J.F. Miller, S.R. Venkateswaran, "The US Department of Energy– investing in clean transport", Jounal of Power Sources, 71: 26-35, 1998.

[5] T. Shido, Y. Iwasawa, "Reactant-Promoted Reaction Mechanism for Water-Gas Shift Reaction on Rh-Doped CeO_2", Journal of Catalysis, 141: 71-81, 1993.

[6] S. Hilaire, X. Wang, T. Luo, R. J. Gorte and J. Wagner, "A comparative study of water-gas-shift reaction over ceria supported metallic catalysts" Applied Catalysis A, 215: 271-278, 2001.

Table 1: Results of BET surface area and pulse reoxidation measurements

Supports/ Catalysts	*BET SA (m^2/g)*	*O_2 consumption ($\mu mol/g_{cat}$)*
CeO_2(A)	17.3	21.1
CeO_2(B)	69.6	146
CeO_2(C)	84.7	180
1.0% Pt/CeO_2(A)	9.9	30.9
1.0% Pt/CeO_2(B)	65.8	199
1.0% Pt/CeO_2(C)	80.4	218

Table 2: Propane activity and selectivity of the catalysts

Catalysts	*X_{C3H8} (%)*	*S_{H2} (%)*	*S_{CO} (%)*	*S_{CO2} (%)*	*H_2/CO*	*H_2-Yield ($mol/h/g_{cat}$)*
1.0% Pt/CeO_2(A)	62.5	64.3	45.4	45.5	1.9	0.45
1.0% Pt/CeO_2(B)	71.1	72.5	53.8	38.0	1.8	0.58
1.0% Pt/CeO_2(C)	72.5	76.0	58.8	34.1	1.7	0.62

Figure 1: Flowsheet of down flow fixed-bed reactor

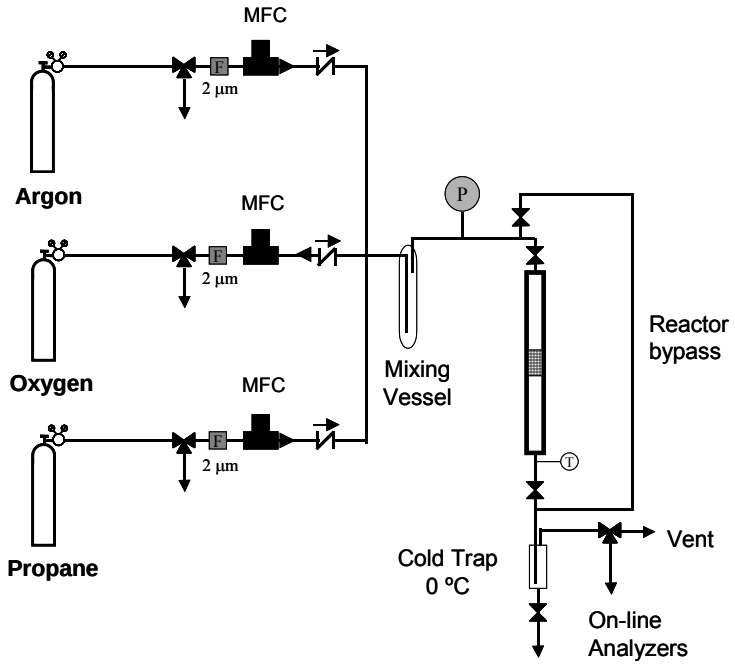

Figure 2: TPR profile of supports and catalysts

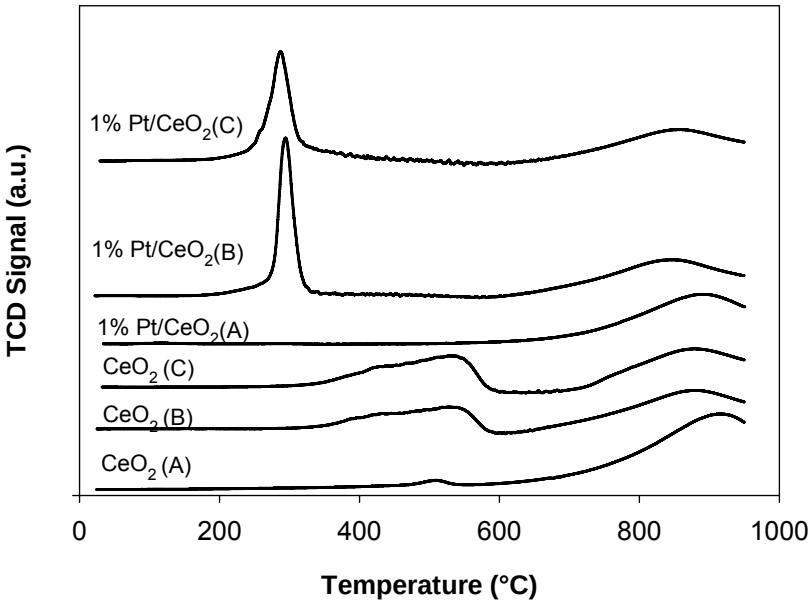

Figure 3: Effect of temperature on partial oxidation of propane over 1.0%Pt/CeO_2 (C) catalyst. (0.1 g cat; 700°C; 1 atm, feed: 300 sccm, 90% Inert[Ar + N_2 (Int. std.)], O_2/C_3H_8 = 1.8)

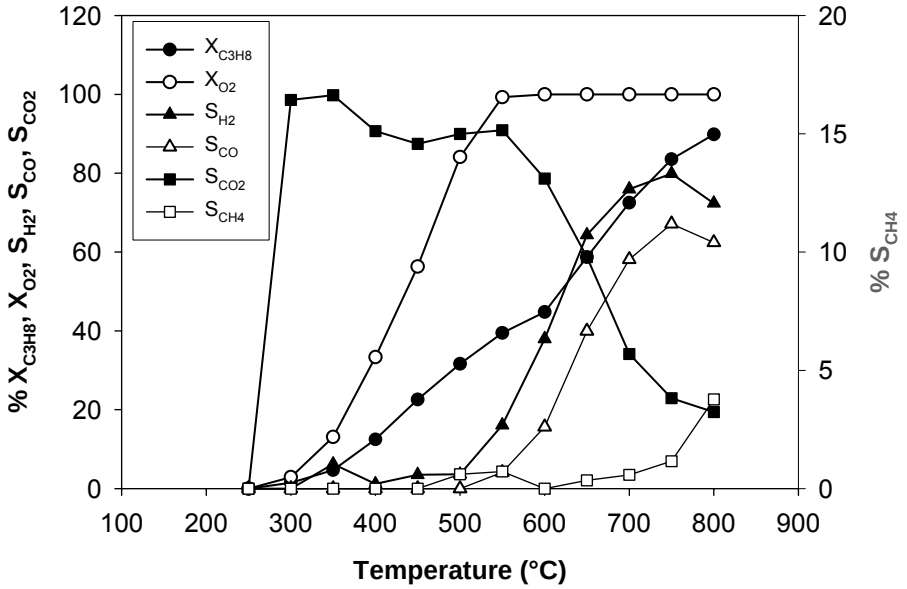

Figure 4: Effect of O_2/C_3H_8 ratio on partial oxidation of propane over 1.0%Pt/CeO_2 (C) catalyst (700°C, feed: 300 sccm, 90% Inert[Ar + N_2 (Int. std.)])